DIAGNOSIS AND MODELLING OF OPTICALLY THICK STRUCTURES IN THE LOWER SOLAR ATMOSPHERE

A THESIS SUBMITTED TO
THE DEPARTMENT OF PHYSICS AND APPLIED PHYSICS
OF THE UNIVERSITY OF STRATHCLYDE
FOR THE DEGREE OF
DOCTOR OF PHILOSOPHY

By
Gordon Anderson Fischbacher
March 2001

© Copyright 2001

Abstract

This thesis presents a study of escape probability and absorption factor techniques for describing the effects of opacity on atomic population structure and emergent spectral line intensities in the context of solar atmospheric plasmas. These techniques are presented and used in conjunction with data from the SUMER spectrometer onboard the SOHO spacecraft from which values of optical depth are directly extracted. From these, spectral lines of C II and C III are classified according to their disk centre and limb optical depths and also according to the influence of opacity on the upper level population density of each line.

Escape probability quantities are then used with the SUMER data to assess the applicability of simple stratified atmosphere models in describing spectral emission from the highly inhomogeneous solar transition region.

Following this, the assumptions underpinning the escape probability and absorption factor methods are comprehensively addressed to test the validity of the escape probability expressions and to develop them for use within non-stratified models which include plasma flow and line blending. It is found that for moderate optical depths ($\tau_0 <\sim 10$) the escape probability is an effective tool for accurately describing the effect of opacity on emergent spectral line intensities. Furthermore it is found that they may be used to extract optical depths directly from observational data *independently* of preconceived atmosphere model ideas. The analysis enables the detection of *unresolved* spicule-like structures at the solar limb.

Stratified models are re-addressed with the inclusion of line blending and instrumentally scattered light and it is found that they can be effective in predicting observed spectral emission at the solar limb.

Acknowledgements

Throughout the course of this work I have encountered many people, a number of whom I would now like to thank.

Firstly there is my supervisor, Prof. Hugh Summers, without whom I would neither have started nor finished this work. Since the beginning he has given me enough rope to be creative, but has stayed sufficiently close to make sure I didn't hang myself with it. I would also like to thank Drs Jim Lang and Richard Harrison at the Rutherford Appleton Laboratory for taking time to provide ideas and direction for this work. Thanks also to Dr Peter McWhirter for sharing some of his insights.

Throughout my PhD I have been fortunate to work in a supportive environment and have enjoyed encouragement from and friendship with with my fellow colleagues. I would especially like to thank (soon to be Dr) Stuart Loch who has been an excellent counsellor, advisor, source of inspiration, comedian and friend. He has never uttered a discouraging word and has always listened to and tolerated my lengthy monologues. Your help has been invaluable, thank you Stuart. Special thanks also to Dr David Brooks who, despite leaving Strathclyde near the beginning of my PhD, has maintained interest and contributed to the development of ideas and plans. Thanks also go to Dr Nigel Badnell, Prof. Geoff Duxbury, Prof. Gian-Luca Oppo and Dr Robbie Stewart for their interest and encouragement over the past few years.

My fellow cave dwellers, past and present, have injected humour and life into this place. Much appreciation goes to Harvey, Connor, Kathleen and Allan. I would also like to thank Kathleen for reading my thesis and helping to keep my spelling and grammar correct. A big task for a busy lady. Thanks Kathleen.

There have been occasions when work has been placed on hold, and time has been taken to enjoy a cup of tea and perhaps a biscuit. This has not been a lonely experience. So thanks to Gail, Hendy, Seanlyon, Jo, David and John for some fun and invariably bizarre tea times. Over the course of three years worth of tea breaks some truly crazy things have been uttered, the vast majority of which (at a rough guess I'd say 90%) have emanated from the mouths of Hendy and Gail. How it is

that I am the only one to have received a one tea break ban, I'll never know. Thanks guys, you're all nuts!

I would like to thank my family for their support especially in the early days.

Finally, I would like to acknowledge an EPSRC studentship.

To my Esther,

for your smile and the joy you've brought to my life.

Remembering mine affliction and my misery,
the wormwood and the gall.
My soul hath them still in remembrance,
and is humbled in me.
This I recall to my mind,
therefore have I hope.

It is of the LORD's mercies that we are
not consumed,
because his compassions fail not.
They are new every morning:
great is thy faithfulness.
The LORD is my portion,
saith my soul;
therefore will I hope in him.

Lamentations 3:19-24 (KJV)

Contents

List of Figures

List of Tables

Chapter 1

Introduction

The sun has been an object of scientific interest since the time of the ancient Greeks and an object of wonder since long before then. It is the centre piece of the solar system and its varied and powerful characteristics impinge markedly on life on earth, making detailed study of its processes both a useful and important effort. The earth exists in a delicate balance with a sensitive dependence on the behaviour of the sun. Any closer and it would be too hot for life. Any further away and it would be too cold. Long term solar cycles produce global warming and ice ages and planets that lack a protective magnetosphere have their atmospheres stripped away by the solar wind. This process is underway on Venus which has a solar wind induced comet-like tail that stretches as far as earth. On smaller timescales, coronal mass ejections, when oriented appropriately, are capable of simultaneously producing the beautiful aurorae and destroying satellites and power grids.

In these days when the depletion of fossil fuels and atmospheric pollution are critical issues and the potential of renewable energy sources is of key interest, the sun is an obvious choice of generator providing, for all practical purposes, limitless energy. The effective harnessing of such energy will benefit greatly from an increased understanding of the sun. Solar physics research also presents an opportunity to study a naturally magnetically confined plasma environment. It therefore provides useful knowledge and insight for the development of magnetically confined laboratory fusion plasmas, which are being developed around the world as abundant sources of

power.

The sun is a fairly average star and its proximity to the earth allows it to be resolved into subregions – other stars can only be seen as single objects. Consequently study of the sun provides much information pertinent to stellar physics.

The sun is an extremely diverse and dynamic creature which poses a whole host of rich physical questions and only the basics of solar physics are understood to any depth. The Solar and Heliospheric Observatory (SOHO - Domingo et al., 1995) is a joint NASA (National Aeronautics and Space Administration) and ESA (European Space Agency) spacecraft situated in orbit round the sun-earth L1-Lagrange point – the point where the gravitational force due to the sun is balanced by that of the earth. It has a payload of twelve instruments designed collectively to address three of the main unanswered questions in solar physics. Namely,

1. What is the detailed structure of the solar interior?

2. How is the solar corona heated?

3. How is the solar wind accelerated?

To address the question of coronal heating, SOHO carries six solar atmosphere remote sensing instruments, one of which is the Solar Ultraviolet Measurements of Emitted Radiation (SUMER) spectrometer (Wilhelm et al., 1995), data from which is discussed here.

Fig. 1.1 shows a model of the temperature structure of the solar atmosphere. The photosphere (heights $<$ 0 km) is relatively dense and cool ($\sim$ 6000K). Above the photosphere is a narrow layer called the chromosphere which spans a temperature range from the temperature minimum of $\sim$ 4,000 K just above the photosphere, up to $\sim$ 20,000 K at $\sim$ 2000km. Between the chromosphere and the corona a transition region of uncertain structure exists which spans the region $\sim$ 20,000 $\rightarrow$ $\sim$ 2,000,000K. Above the transition region is the corona which extends to many solar radii at a temperature of $\sim$ 2,000,000K.

The images shown in figs 1.2, 1.3 and 1.4 give some indication of the dynamic nature of the solar atmosphere. If the dynamics are to be understood it is necessary

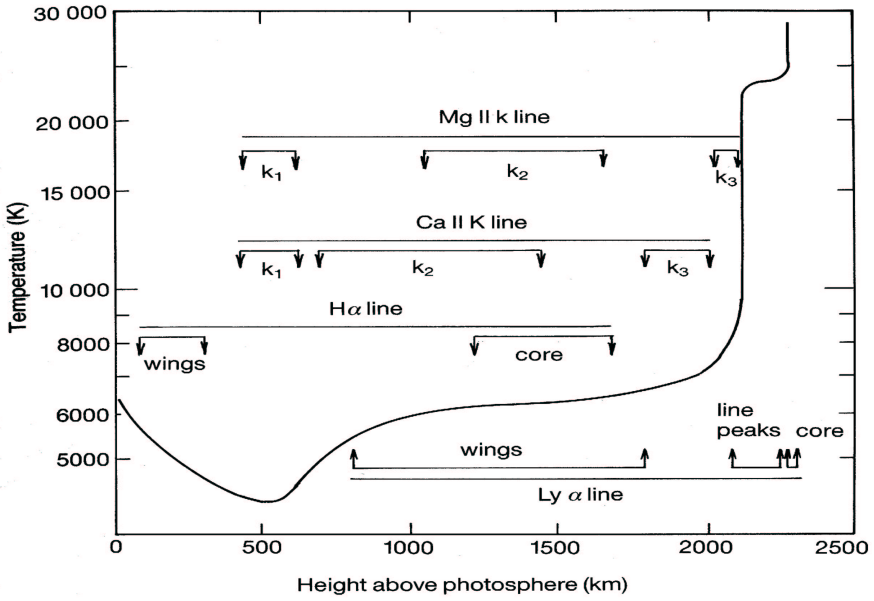

Figure 1.1: The variation in temperature with height in the solar atmosphere up to the transition region based on the hydrostatic equilibrium model of Vernazza et al. (1981). (Taken from Phillips, 1992).

to first probe the atmospheric and temperature structures of the *quiet sun* – i.e. the non-active sun – though, as the recent SOHO data bears testimony, even the quiet sun is dynamic on timescales less than that of ionisation equilibrium (Brooks et al., 1998). This thesis seeks to develop methods useful for both the diagnosis and modelling of plasma structure from observations of *optically thick* spectra.

1.1 The solar chromosphere and transition region

The regions of the solar atmosphere which are of particular interest in this work are the *chromosphere* and the *transition region* (TR). The solar chromosphere is a narrow part of the solar atmosphere visible during an eclipse or with special observing techniques. Its main characteristics are a rise in temperature with height and a complex dynamic structure. Hα and calcium H and K line spectroheliograms (eg. fig 1.2) of the sun show that the chromosphere is a highly non-uniform, structured region of the solar

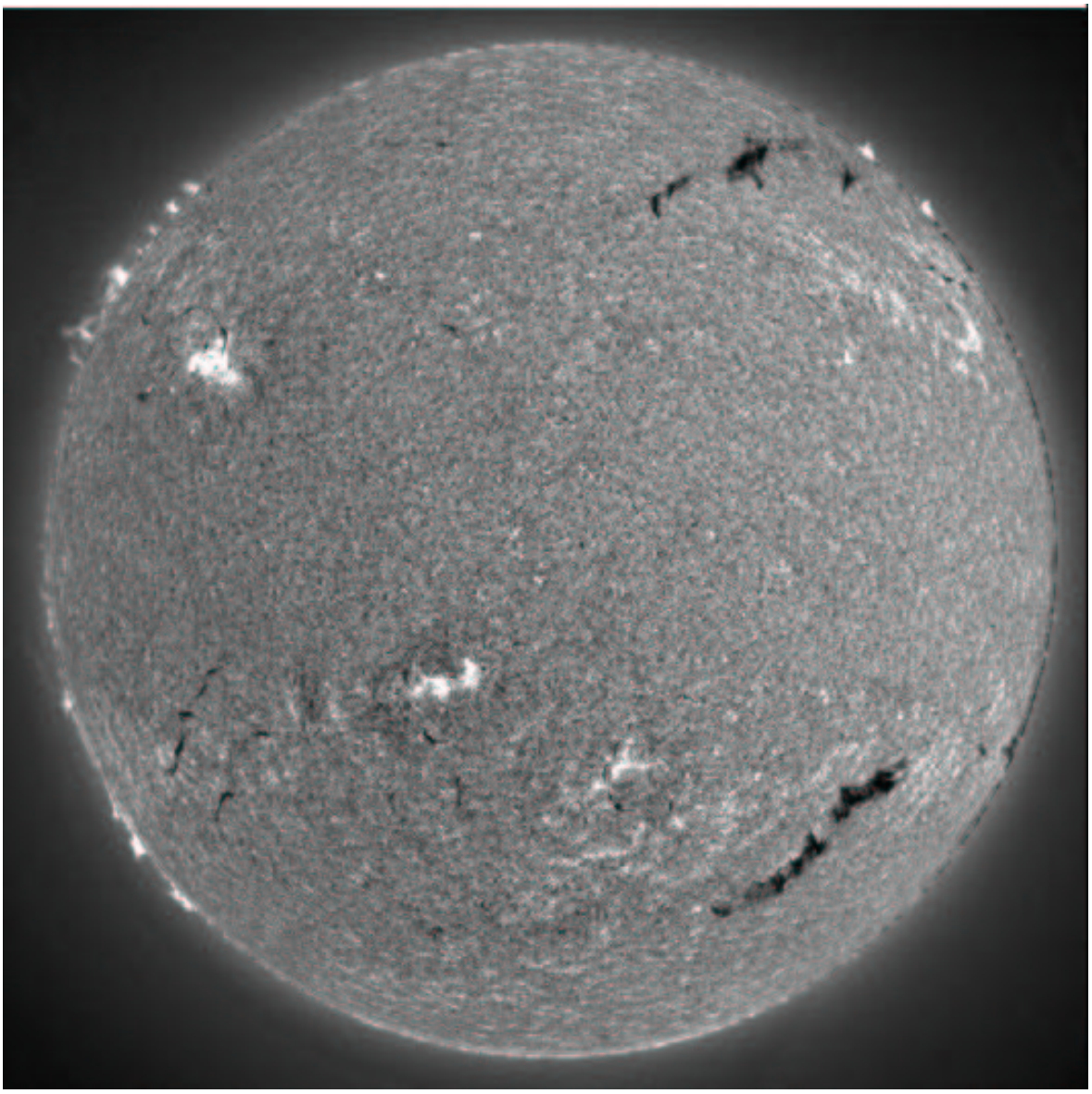

Figure 1.2: Image of the solar disk in hydrogen Hα at 6563 Å revealing the lower chromosphere. Several active regions are evident as well as many prominence filaments (see sec. 1.1.2). A number of prominences are visible at the limb.

atmosphere. In fig. 1.2 large bright zones called *active regions* are visible with bright patches in their vicinity known as *plages*. Evident also are long, dark structures called *filaments* (see sec. 1.1.2).

Fig. 1.3 shows the solar disk as seen in He II 304 Å which corresponds to a temperature of around 80,000 K. In this figure bright clumps that form a pattern can be seen. This pattern is known as the *chromospheric network* which is quite faint in quiet sun regions and more enhanced near active regions. An individual network cell is typically $\sim$ 30,000 km across and lasts about 1 day. The bright patches are called *floculi* or *coarse mottles*. A coarse mottle is made up of several bright *fine mottles* about 7000 km by 700 km, lasting about 1 day with both upward and downward velocities. Fine mottles are associated with *spicules* when viewed at the limb (see sec. 1.1.1).

Chromospheric features and the photospheric magnetic field are related on a small and a large scale. For example clumps of intra-network field within network cells are associated with bright cell points. This field appears at centres of supergranules and moves radially outwards to the supergranule edges where it either cancels or coalesces with the network field. On the larger scale, strong fields around sunspots are related to the plage structures.

Between the chromosphere and corona there is an even more narrow region known as the transition region (TR). This region has a complex structure with many features at or below the resolution limit of current observational instrumentation. Energy seems to be mostly supplied by thermal conduction and downflow of hot gas from the corona above. This means that dissipation of wave energy from the photosphere is not significant. This interpretation was questioned by Feldman & Lamming (1994). Measurements suggest that emission is due to tiny ($\sim$ 100 km) structures which are not resolvable. Feldman et al. postulate that much of the ultraviolet (UV) emission is due to these *unresolved fine structures* and only part is due to 'true' TR emission (i.e. chromosphere-corona interface).

Both the chromosphere and the TR are confined to the network which is steadily less sharply defined as temperature increases until the corona where it is not visible.

Plasma flow and photo-absorption affect spectral line profiles and so careful study

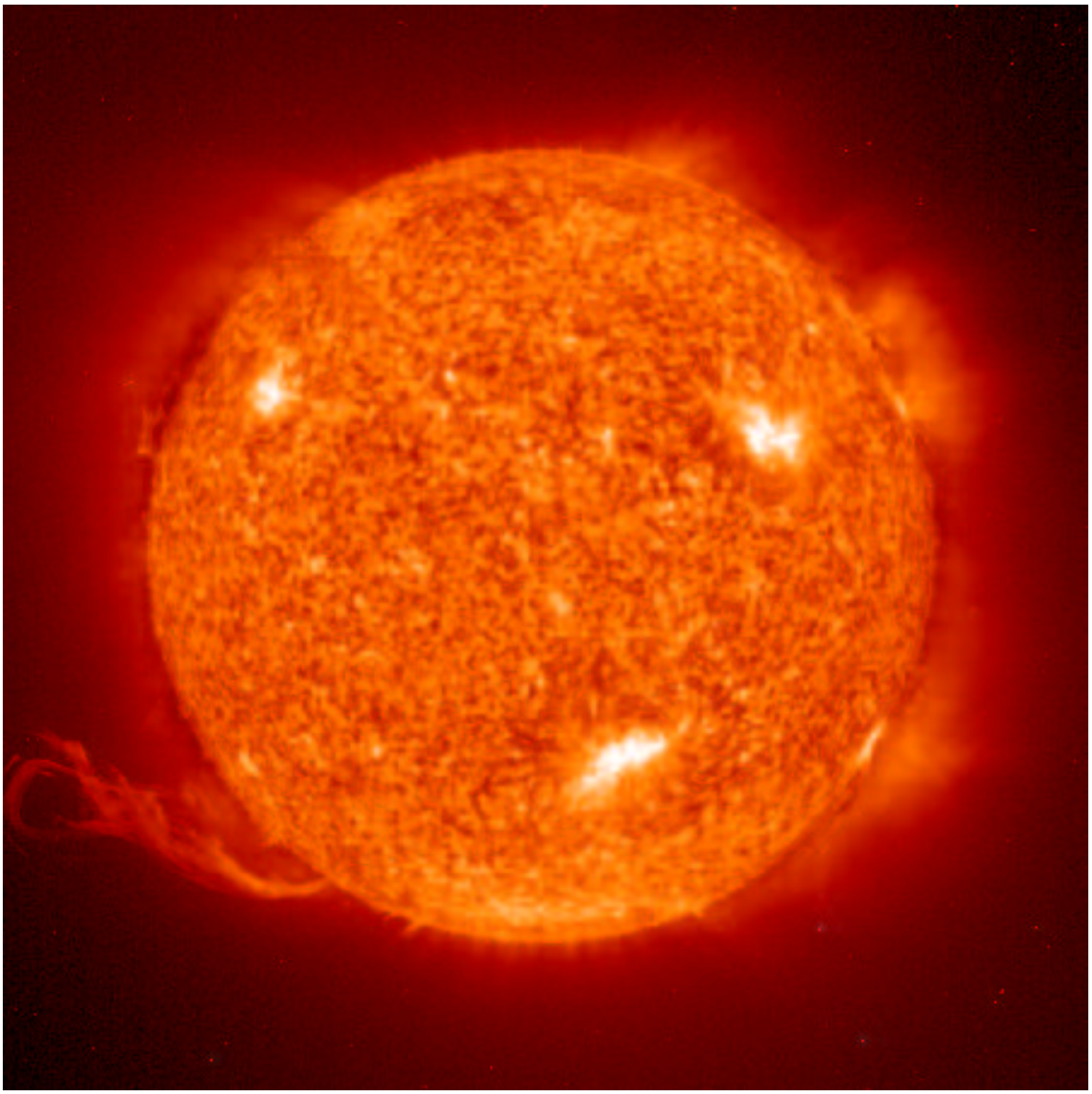

Figure 1.3: Image of the solar disk in He II 304 Å obtained using the Extreme-Ultraviolet Imaging Telescope (EIT) on SOHO, revealing the mid chromosphere ($\sim$ 80,000K). The bright patches on the disk are active regions which are situated above sunspots. The large structures above the limb are prominences and the spiky structures evident at the poles are macrospicules.

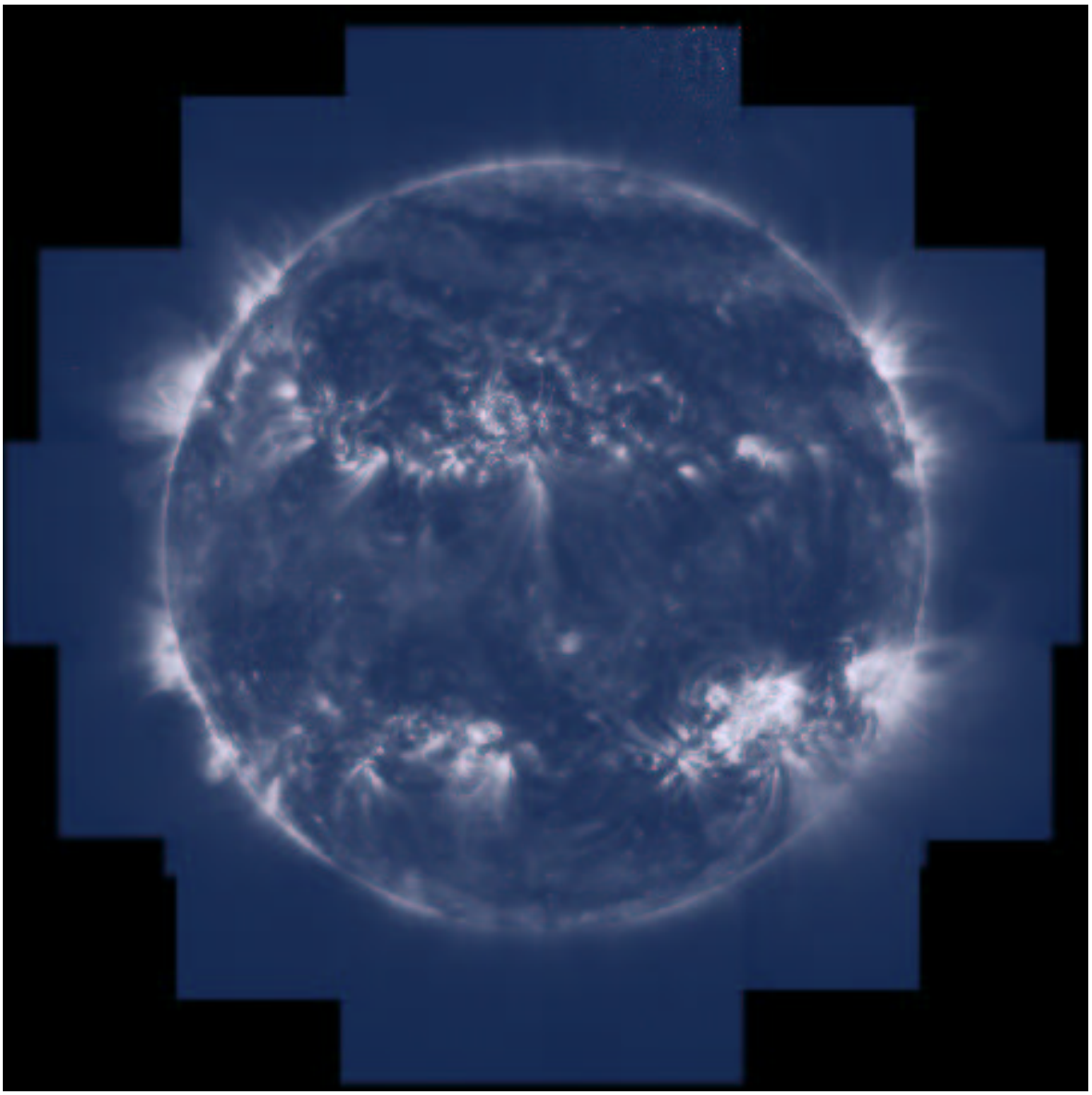

Figure 1.4: Image of the solar disk in Fe IX 171 Å obtained using the Transition Region and Coronal Explorer (TRACE) showing the upper transition region/lower corona at $\sim$ 1,000,000 K. Active regions are visible in two belts north and south of the equator. Plasma loops extending into the corona are also evident.

of TR spectral lines, many of which are optically thick (i.e. have non-negligible opacity) can provide information on mass motions and possible methods of energy transport.

1.1.1 Solar spicules

The edge of the chromosphere is made up of numerous fine jet-like structures known as *spicules*. These features are prevalent in the quiet sun and are significant in both disk and limb observations. The focus of this work is on the modelling of spectral emission from the chromosphere and the TR and so it is useful to consider these spicule structures and their spectral characteristics is some detail.

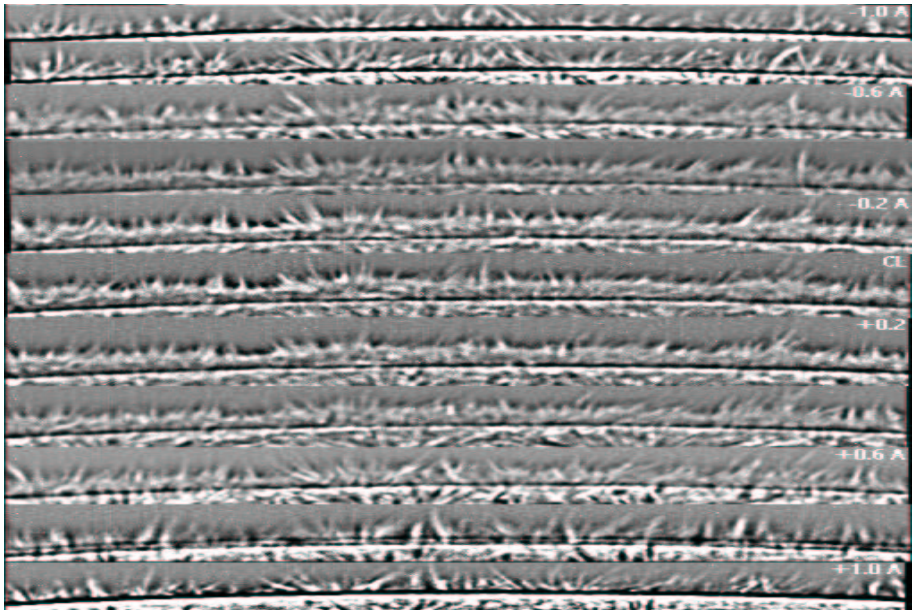

Figure 1.5: Eleven images of spicules at the limb obtained from different regions of the Hα line. The discontinuity between the spicules and the disk is due to the fact that an occulter was used to mask the disk to observe the spicules with the disk observations superimposed below.

Spicules were first described by Secchi (1877) and were named by Roberts (1945). They are jet-like structures with aspect ratios of about 20 (Lorrain and Koutchmy, 1996 – henceforth LK) which rise to heights of around 10,000 $\rightarrow$ 15,000 km with

diameters $\sim 150 \rightarrow 200$ km (eg. Withbroe, 1983; LK; Budnik et al., 1998). Thus they exist at the resolution limit of current instruments (SUMER spatial resolution is ~ 1 arc sec which corresponds to $\sim$ 1000km). The surface coverage of spicules is $\sim 1\%$ (Athay and Holzer, 1982) with about 70,000 of them being present at any one time (LK). They are most commonly observed in chromospheric spectral lines such as Hα (fig 1.5) but also in extreme ultraviolet (EUV) lines from the upper chromosphere and transition region (fig 1.3). Seen in Hα, upon reaching their maximum height their root disconnects from the surface, the proper motion of the cool radiation source becomes downward and they disappear (LK). Lifetimes are $\sim 5 \rightarrow 15$ mins and upward velocities are perceived as (and are generally accepted to be) $\sim$ 25 km/sec. This velocity is inferred from Doppler shifts measured at the limb and so is open to misinterpretation if transverse velocities are present as Beckers suggests. LK add that this velocity is also that perceived by the apparent motion of the spicule head and that the velocity can be much larger ($\sim$ 50-100 km/sec) during the *impulsive phase*.

It is clear that spicule structure, formation and propagation are intimately related to the magnetic field topology, with spicules, as discussed below, appearing within *magnetic elements* (Lorrain and Koutchmy, 1993) at the boundaries of supergranule cells. This link is evident when observing at the limb as well as on disk in the patterns and groupings that are found. A further connection with the magnetic field is evident in coronal holes (regions of very low coronal X-ray emission situated at the poles where the magnetic field lines are open) in the presence of *macrospicules* or *spikes* which extend to $\sim$ 30,000 km above the limb.

Spicules are observable in spectral lines at upper chromospheric and transition region temperatures. Budnik et al. (1998) observed typical "EUV inhomogeneities possibly associated with spicules" growing (if viewed at the limb) horizontally and vertically with increasing emission line temperature until $\sim$ 1–2 x 10^5 K where the structures appear totally diffuse.

Spicules On the Disk

Spicules have photoelectrically controlled spectroscopic characteristics, appearing in absorption when viewed on disk. Spicules at the limb are associated with dark, and

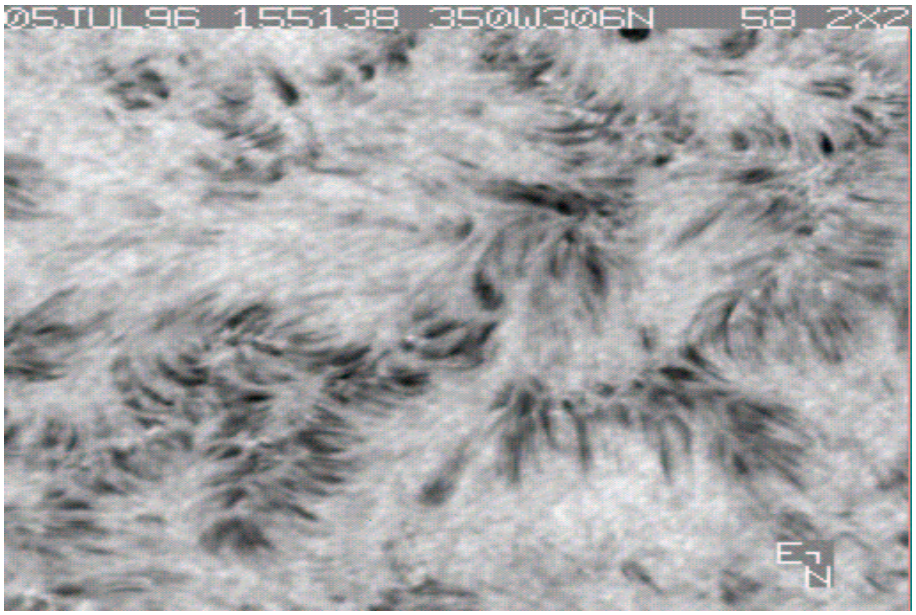

Figure 1.6: A region of the disk seen in Hα showing dark mottle features.

possibly also bright, mottles on the disk (fig. 1.6) which exist at the boundaries of supergranule cells. Dark mottles are absorption features seen against a brighter chromospheric background. Bright mottles are situated at lower heights than dark ones and occur in the same regions where they form groups of around 50 mottles in total forming coarse mottles, *rosettes* or *bushes*.

In mid chromospheric spectral lines, Doppler shifts corresponding to both upflows and downflows are observed whereas in upper chromospheric lines upflows are dominant (Doschek et al., 1976). In contrast, downflows are dominant in TR lines (Athay and Holzer, 1982). These flows provide a key point of interest in the spicule debate on the issues of chromospheric heating, coronal mass and energy balance, and the question of what happens to the TR as a spicule rises beneath it.

The Spectroscopy of Spicules

Spicules are most frequently observed in Hα – they are often referred to as Hα spicules to distinguish them from EUV inhomogeneities. In the visible range they are also often observed in Hβ and calcium lines. Spicules are observed in the upper chromosphere and TR in EUV lines of impurities such as C I $\rightarrow$ C IV. Model based hydrogen densities in spicules have been calculated as $\sim 10^{12}$ cm^{-3} at $T_e \sim 1.5 \times 10^4$ K (Papushev and Salakhutdinov, 1994). Athay & Holzer (1982), however, state that the average hydrogen density within spicules is $\sim 6 \times 10^{10}$ cm^{-3}. Spicules emit spectral radiation at a range of chromospheric and TR temperatures. It is generally assumed

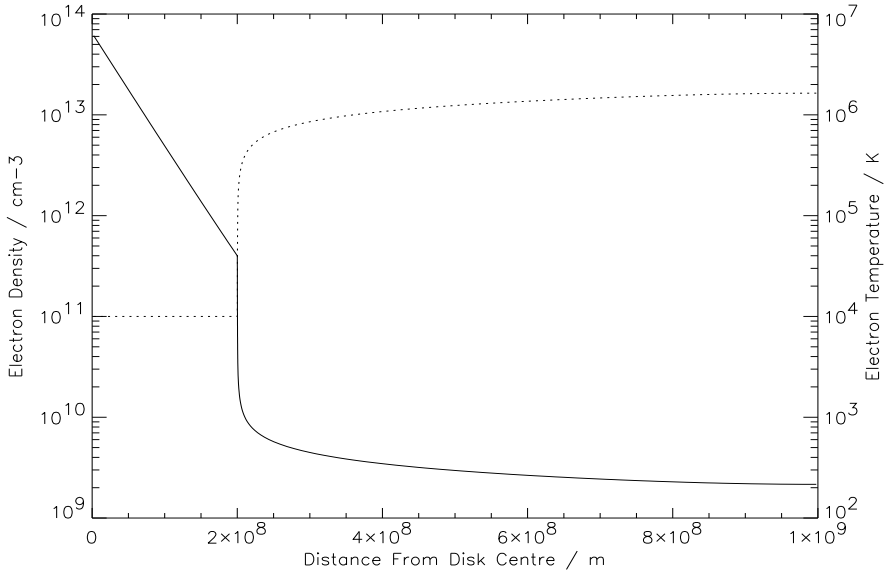

Figure 1.7: Model of the variation of electron temperature (c.f. fig 1.1) and electron density with height according to Vernazza et al. 1981.

that spicules have a 'cool' chromospheric core surrounded by a relatively hot TR sheath. LK suggest in their model, however, a 'hot' core surrounded by a relatively cool sheath (presumably surrounded also by a hot sheath). Instrumental resolution is not yet sufficiently fine to answer this question.

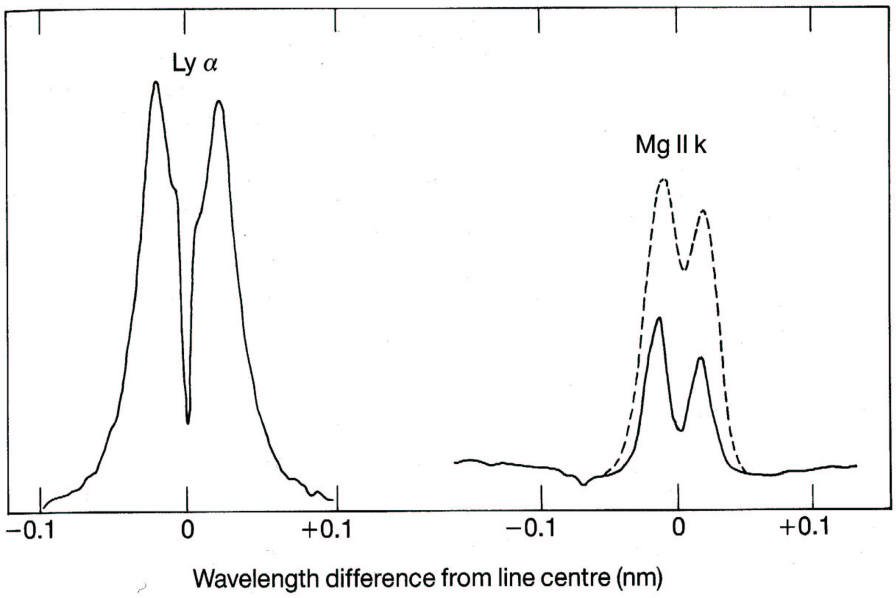

Figure 1.8: Two examples of spectral lines originating in the solar chromosphere. The solid lines correspond to quiet-sun conditions and the dashed line corresponds to active-sun conditions. (Taken from Phillips, 1992).

Many spectral lines originating from spicules and the chromosphere and TR in general are optically thick and can display marked deviation from Gaussian profiles (see fig. 1.8). Furthermore, plasma flow leads to the displacement of lines from their rest wavelengths and possibly also of absorption profiles from emission profiles due to Doppler motion. Thus asymmetries, Doppler shifts, self reversals and broadenings abound in the lines of the chromosphere and TR. A significant contribution to these features is made by large scale non-thermal motions such as rotations. Spicules may be classified as being one of two types (Beckers, 1972): type I – spicules with wide profiles; type II – spicules with narrow profiles. The distinction between these two may be interpreted as being related to rotation. Line profiles are also complicated, especially when viewed on disk, by spicule tilting, by the possible presence of unresolved spicules and the effects of scattered light – both instrumental and due to the inter-spicular medium which also possibly contains unresolved spicule structures.

Papushev and Salakhutdinov (1994) have added to this picture and talk of intricate changes in the Hα profile as the spicule rises. They say that all line profile parameters change by $\sim 30 \rightarrow 40\%$, with $30 \rightarrow 200$s duration during the evolution of the spicule. Furthermore they say that the profiles show asymmetries but that the 'middle' stage is characterised by Gaussian profiles.

Most authors seem to agree that spicule scale heights[1] are $\sim$ 1,500 km ($\sim$ 2,000 km in coronal holes). On the matter of spicule heights, however, there is less coherence. This is largely due to the ambiguous definition of height generally taken to be the maximum height above the limb at which a spicule may be seen. Nevertheless, most authors claim heights to be between 10,000 and 15,000km. The existence of spicules (or, at least, spicule associated inhomogeneity) is more difficult to verify in the case of coronal lines due to the relatively strong background emission. Budnik et al. (1998) used the high resolution SOHO data to identify such inhomogeneities directly by observing the variation of spectral line intensity with position in the vicinity of spicules. Withbroe (1983), on the other hand, approached this issue by comparing observed RMS fluctuations in the intensity with position with the expected statistical fluctuations.

Implications of Spicules to the Mass and Energy Balance of the Corona

As the chromosphere and the TR separate the cool photosphere from the hot corona, and spicules represent mass and energy flux upward from the chromosphere into the corona, it is reasonable to expect spicules to play a significant role in the mass and energy balance of the corona. Simple calculation of the upward mass flux reveals that it is two orders of magnitude greater than that of the solar wind (Athay and Holzer, 1982). Clearly the majority of this material must flow back down again but only 1% need remain to maintain the mass of the corona. Budnik et al. (1998) claim that their SOHO observations mentioned above do show evaporation of spicular material into the corona.

Views on the energy balance question are more varied. Beckers' calculation of

[1] Atmospheric pressure falls off, roughly speaking, as e^{-h/H_s}, where h is the height above the limb and H_s is the scale height

the kinetic energy of a spicule led him to believe that they do not contribute an appreciable amount of energy to the corona. Athay and Holzer (1982), on the other hand, calculated the gravitational potential energy gained by a spicules and found it to be sufficient to power the corona if that energy was dissipated as the spicules descended. They drew on the observed TR downflows as evidence for this. This calculation was, however, dependent on the assumption that spicules rise to greater heights than had been observed ($\sim 5\times10^4$km). Withbroe (1983) responded to the Athay and Holzer model by utilising EUV observations to show that spicules do not rise above 15,000 km. He then used DEM analysis to conclude that the observed transition region downflows do not support this model and concluded that spicules are probably not the primary source of heating of the corona.

1.1.2 Solar prominences

It is interesting to consider solar prominences, which are tongues of material that are suspended in the corona since they emit a spectrum at chromospheric temperatures and display optical depth effects. They exist at around 10,000 K, surrounded by 2,000,000 K coronal plasma and consequently have a TR sheath about them. Typical quiescent prominences are 10,000→600,000 km long and 5,000→10,000 km thick and sit at heights up to $\sim$ 50,000 km above the photosphere. Typical lifetimes are around a month. Their formation, structure, stability and ultimate eruption are the focus of much modelling and observational effort and many questions concerning them remain unanswered. Like spicules they appear in absorption when viewed on disk and are visible in fig. 1.2 as dark lanes called filaments. They are also evident in this figure as bright features at the limb. The temperature within the prominence is not sufficient to collisionally excite hydrogen atoms to produce Hα photons and so the presence of prominences in the Hα spectroheliogram seems surprising. The Hα photons arise due to excitation of neutral hydrogen via absorption of Lyman continuum photons from the underlying chromosphere and so do not have anything to do with the actual electron temperatures.

In fig. 1.3 prominences are present despite the fact that this image reveals the

sun at a temperature of $\sim$ 80,000 K – a temperature much greater than that of the prominence itself. This is due to emission from the prominence-corona transition region (PCTR) that exists around the prominence which spans the temperature range of $\sim$ 10,000 $\rightarrow$ 2,000,000 K.

Prominences present many challenging modelling problems since their emission spectrum and energy balance depend critically on photo-electric processes. Thus the details of radiation transport must be carefully computed to model radiative characteristics and power loss.

1.2 Spectral emission from plasmas

Plasmas are made up of atoms, ions and electrons which all radiate via different atomic processes. Understanding such processes is necessary for the modelling of plasmas and the interpretation of spectral data. This involves understanding the electronic structure of atoms and ions and the interactions between particles and photons that couple species, ionisation stages and energy levels to produce the resultant spectrum. This problem is complex but can be handled for a number of regimes.

It is of interest to understand the processes that generate and sustain the solar chromosphere and TR and that drive the processes therein. The principal, if not sole method by which this may be achieved is spectroscopy – i.e. by detailed interpretation and analysis of the light emitted from these regions. If the light emitting mechanisms are to be understood, all the atomic processes that lead to photo-emission must be accounted for. If an ion, A, of charge Z, with outermost electron in excited state i is denoted A_i^{+Z}, then these processes may be summarised as follows:

Radiative processes

1. Spontaneous emission:

$$A_i^{+Z} \rightarrow A_j^{+Z} + h\nu$$

2. photo-absorption:

$$A_j^{+Z} + h\nu \rightarrow A_i^{+Z}$$

3. stimulated emission:

$$A_i^{+Z} + h\nu \rightarrow A_j^{+Z} + h\nu + h\nu$$

4. photo-ionisation:

$$A_i^{+Z} + h\nu \rightarrow A^{+Z+1} + e$$

5. radiative recombination:

$$A^{+Z+1} + e \rightarrow A_i^{+Z} + h\nu$$

6. stimulated recombination:

$$A^{+Z+1} + e + h\nu \rightarrow A_i^{+Z} + h\nu + h\nu$$

7. dielectronic recombination:

$$\begin{aligned} A_i^{+Z+1} + e &\rightleftharpoons A_{j,nl}^{+Z} \\ A_{j,nl}^{+Z} &\rightarrow A_{i,nl}^{+Z} + h\nu \end{aligned} \tag{1.1}$$

Note that h is Planck's constant (6.62618×10^{-34} J s) and ν is the photon frequency in Hz. In dielectronic recombination an ion of charge $Z+1$ captures an electron which loses energy to a bound electron of the ion, exciting it from level i to level j, and leaves the captured electron in a highly excited state denoted nl. At this point the process may reverse in what is called *Auger breakup*, or the inner excited electron may relax via the emission of a photon as indicated. Following this the captured electron may cascade down to a lower level.

If an electron, e, in an energy state i is denoted $e(\varepsilon_i)$, then the collisional processes may be summarised as follows:

Collisional processes

1. Electron impact excitation and de-excitation:

$$A_i^{+Z} + e(\varepsilon_i) \rightleftharpoons A_j^{+Z} + e(\varepsilon_j)$$

2. Electron impact ionisation and 3-body recombination:

$$A_i^{+Z} + e(\varepsilon_i) \rightleftharpoons A_\rho^{+Z+1} + e + e$$

3. Charge exchange recombination:

$$A_i^{+Z+1} + H^0 \rightarrow A_j^{+Z} + p$$

If a plasma is sufficiently dense, as in the solar photosphere, then no radiation can escape except from very close to the outer edge. All photons within the plasma that are emitted are subsequently absorbed. Such a situation is termed *complete thermodynamic equilibrium* and the atom and ion excited state population densities are characterised by *detailed balance*. That is, every individual reaction is balanced by its inverse. In such circumstances the atoms, ions and electrons establish energy distributions with characteristic temperatures. Free particles have a *Maxwellian velocity distribution* given by

$$f(v) = 4\pi \left(\frac{m}{2\pi kT}\right)^{3/2} v^2 exp\left(-\frac{mv^2}{2kT}\right) \tag{1.2}$$

where v is the velocity, m is the mass; k is Boltzmann's constant, and T is the temperature. Bound states of atoms and ions have a Boltzmann distribution. Number densities (populations) of atoms and ions in bound levels i and j with statistical weights ω_i and ω_j, are related by

$$\frac{N_i}{N_j} = \frac{\omega_i}{\omega_j} exp\left(-\frac{E_i - E_j}{kT}\right) \tag{1.3}$$

where E_i and E_j are the energies of levels i and j respectively. For ions of the same species but adjacent ionisation stages, these populations are given by the *Saha-Boltzmann equation*, viz.

$$\frac{N_i^Z}{N_e N_j^{Z+1}} = \frac{\omega_i^Z}{\omega_j^{Z+1}} \frac{h^3}{2\left(2\pi m_e kT\right)^{3/2}} exp\left(-\frac{E_i}{kT}\right) \tag{1.4}$$

The deviation of plasmas from thermodynamic equilibrium is usually due to a deficit in the radiation field. However, there are circumstances where collisional processes

are so efficient that this deficit does not matter and collisional processes alone are sufficient to maintain thermodynamic equilibrium populations. This situation is called *local thermodynamic equilibrium* (LTE). LTE often holds for highly excited states due to their large cross-sections and low transition energies. Low lying levels, however, only achieve LTE at high densities.

Out of thermodynamic equilibrium, detailed balance does not hold. In this case, however, a plasma in equilibrium will have atomic and ion populations satisfying *statistical balance*. That is, the sum of all the processes which populate a level (labelled i) are balanced by those that depopulate it. Thus

$$\begin{aligned}
& \sum_{i'>i} \left[A_{i'\to i} + \int_{line} u(\nu) B_{i'\to i} d\nu + N_e q^{(e)}_{i'\to i} + N_e q^{(p)}_{i'\to i} \right] N_{i'} \\
+ & \sum_{i''<i} \left[\int_{line} u(\nu) B_{i''\to i} d\nu + N_e q^{(e)}_{i''\to i} + N_e q^{(p)}_{i''\to i} \right] N_{i''} \\
+ & N_e N_+ \alpha^{(r)}_i + N_e^2 N_+ \alpha^{(3)}_i + N_e N_+ \int u(\nu) B_{\kappa\to i} d\kappa \\
= & \left[\sum_{i'>i} \left[\int_{line} u(\nu) B_{i\to i'} d\nu + N_e q^{(e)}_{i\to i'} + N_e q^{(p)}_{i\to i'} \right] \right. \\
+ & \sum_{i''<i} \left[A_{i\to i''} + \int_{line} u(\nu) B_{i\to i''} d\nu + N_e q^{(e)}_{i\to i''} + N_e q^{(p)}_{i\to i''} \right] \\
+ & \left. \int u(\nu) B_{i\to\kappa} d\kappa + N_e q^{(e)}_{i\to\varepsilon} + N_e q^{(p)}_{i\to\varepsilon} \right] N_i + \frac{dN_i}{dt}
\end{aligned} \tag{1.5}$$

where

- $A_{i'\to i}$ - spontaneous emission from $i' \to i$
- $u(\nu)B_{i'\to i}$ - stimulated emission from $i' \to i$
- $u(\nu)B_{i\to i'}$ - photo-absorption from $i \to i'$
- $N_e q^{(e)}_{i'\to i}$ - electron collisional de-excitation from $i' \to i$
- $N_e q^{(p)}_{i'\to i}$ - proton collisional de-excitation from $i' \to i$
- $N_e q^{(e)}_{i\to i'}$ - electron collisional excitation from $i \to i'$
- $N_e q^{(p)}_{i\to i'}$ - proton collisional excitation from $i \to i'$

- $\int u(\nu) B_{i \to \kappa} d\kappa$ - photo-ionisation from i
- $N_e q_{i \to \varepsilon}^{(e)}$ - electron collisional ionisation from i
- $N_e q_{i \to \varepsilon}^{(p)}$ - proton collisional ionisation from i
- $N_e N_+ \alpha_i^{(r)}$ - radiative recombination
- $N_e^2 N_+ \alpha_i^{(3)}$ - three body recombination
- $N_e N_+ \int u(\nu) B_{\kappa \to i} d\kappa$ - stimulated recombination

There is such an equation for every level from the ground to $n = \infty$. The solution of these equations yields the *population structure*.

At low densities, such as those in the solar corona, radiation processes control the de-excitation of electrons. *Coronal equilibrium* describes this regime by neglecting the collisional de-excitation term in favour of spontaneous emission. Thus atoms are excited by electron collisions and de-excited by spontaneous radiative decay. They are collisionally ionised by electron impact, and recombine by electron collision. This model neglects collisional de-excitation by assuming that sufficient time elapses between collisions to ensure that excited electrons decay radiatively. Also if an atom is ionised, it has time to recombine before suffering collisions. Furthermore, photo-excitation and photo-ionisation processes are ignored. This is reasonable if the density is sufficiently low.

It is interesting to note that even at the low densities for which the coronal model is valid, highly excited levels may still be collisionally dominated, and so have LTE populations. This may be accounted for within the coronal model by treating such highly excited states as part of the continuum.

Both the solar chromosphere and transition region exist between the thermodynamic equilibrium and coronal regimes where all the radiative and collisional processes come into play. *Collisional-radiative* modelling, first introduced by Bates, Kingston & McWhirter (1962), caters for this middle ground and encompasses the low density coronal and high density LTE regimes. In this model all radiative and *electron* collisional processes are included. However, photo-induced ones (eg. photo-excitation and photo-ionisation) are not.

Collisional-radiative theory recognises the many indirect ways by which highly excited levels can influence the dominant low lying ones. For example, electrons may recombine into a highly excited state and then cascade down to lower levels. Or, following recombination there may be stepwise ionisation. These effects are combined with the direct *state resolved* ionisation and recombination coefficients to produce the collisional-radiative recombination and ionisation coefficients. Also included (Burgess & Summers, 1969) is dielectric recombination to produce *collisional-dielectronic* recombination and ionisation coefficients.

To solve the statistical balance equations the *quasi-equilibrium assumption* is invoked, whereby the highly excited states are assumed to be in equilibrium with the metastable and ground levels. Thus the population densities of all levels apart from the metastable and ground levels, may be found *relative* to the metastable and ground level populations. The quasi-equilibrium assumption follows from consideration of relaxation timescales. In general

$$\tau_{met} \sim \tau_g \sim \tau_{plasma} \sim \tau_{ion} \gg \tau_{ord} \gg \tau_{ee}$$

where these quantities are the metastable, ground, plasma diffusion/dynamic, ion, ordinary excited state and electron-electron equipartition timescales, respectively (see Spitzer, 1956; McWhirter & Summers, 1984; Brooks, 1997). The metastable and ground timescales are similar to the plasma dynamic timescale and so their populations may only be calculated within a transport model which includes these dynamics. However, the ordinary excited state timescale is much smaller than all three and so it is reasonable to assume that at any time the ordinary excited states are in equilibrium with the ground and metastables.

1.3 The problem of opacity

1.3.1 The radiative transfer equation

In the solar chromosphere and transition region the photo-induced effects that are not handled within collisional-radiative theory become important. The plasma is said

to be *optically thick* which means that on average emitted photons have a significant probability of being absorbed before they are able to escape the plasma. This leads to a loss of photons from the line-of-sight. Additionally, absorbed photons affect the population structure which in turn affects the emitted radiation. Thus the system is non-linear and is described by eqs 1.5, coupled with the *radiative transfer* equation

$$\frac{dI_\nu(s)}{ds} = j_\nu(s) - \kappa_\nu(s) I_\nu(s) \tag{1.6}$$

(see Mihalas, 1978, for a complete discussion of radiative transfer theory and Carlsson, 1997, for an eloquent summary of the same.) Here $I_\nu(s)$ is the monochromatic specific intensity (normally called the intensity), $j_\nu(s)$ is the emissivity or emission coefficient, $\kappa_\nu(s)$ is the opacity or absorption coefficient and s is the geometric distance along the ray. These quantities will be defined in more detail in chapter 2. This equation describes the propagation of photons along a ray and must in principle be solved simultaneously with eqs 1.5 if the population structure and/or the emergent intensities along the ray are to be known. The radiation term in eqs 1.5 is $u(\nu)$ which is related to $I_\nu(s)$ as follows:

$$u(\nu) = \frac{h\nu}{c} \int I_\nu(\theta, \phi) d\Omega \tag{1.7}$$

where $d\Omega$ is an element of solid angle. Thus the population structure is no longer dependent merely on local plasma conditions but is coupled into the dynamics and structure of the whole plasma. Consequently radiation transfer plays an important role in determining the structure and energy balance of the solar chromosphere and TR.

Eq. 1.6 implies that the number of photons escaping along the ray is proportional to the opacity and also to the intensity itself. The directional dependence of the intensity follows from the dependence of ds on direction. In the presence of fields (eg. electric, magnetic or velocity), $j_\nu(s)$ and $\kappa_\nu(s)$ may also be directionally dependent.

In a plane-parallel atmosphere the geometrical height, z, which increases outward along the normal of the atmosphere, may be defined. If then the angle between the ray and the normal of the atmosphere is labelled θ and the directional cosine, $\mu = \cos\theta$,

the radiative transfer equation becomes

$$\mu \frac{dI_{\nu\mu}(z)}{dz} = j_\nu(z) - \kappa_\nu(z) I_{\nu\mu}(z) \tag{1.8}$$

It is useful to write this equation in terms of the ratio of the emissivity to the opacity, namely the *source function*, $S_\nu \equiv j_\nu/\kappa_\nu$. Furthermore it is useful to make use of the *optical depth*, τ_ν, which is defined via

$$d\tau_\nu = -\kappa_\nu dz \tag{1.9}$$

With this the radiative transfer equation becomes

$$\mu \frac{dI_{\nu\mu}}{d\tau_\nu} = I_{\nu\mu} - S_\nu \tag{1.10}$$

This is a first order differential equation and thus one boundary condition is required for its solution. In a plane parallel atmosphere there are two boundaries and photons escape through one boundary for negative values of μ and the other boundary for positive values of μ. The conditions for each are $I_\nu^-(0) = 0$ and $I_\nu^+(\tau_{max}) = S_\nu(\tau_{max})$, where the superscripts denote the sign of μ. It follows that the solution of eq. 1.10 is

$$I_{\nu\mu}(\tau_\nu) = \begin{cases} \frac{1}{\mu} \int_{\tau_\nu}^{\infty} S_\nu(t) e^{-(t-\tau_\nu)/\mu} dt & \text{if } \mu > 0 \\ \frac{1}{-\mu} \int_0^{\tau_\nu} S_\nu(t) e^{-(\tau_\nu - t)/(-\mu)} dt & \text{if } \mu < 0 \end{cases} \tag{1.11}$$

This is the *formal* solution of the radiative transfer equation and can only be evaluated if the source function and opacity are known. The source function is dependent on space, frequency and, in essence, upon intensity. The latter dependence follows from that of the emissivity on the upper level population density and will be clarified in chapter 2.

It is useful to define the *contribution function to the intensity*, C_I, which has the defining property

$$I_{\nu\mu}(\tau_\nu) = \int C_I(z) dz \tag{1.12}$$

It follows from eq. 1.11 that

$$C_I(z) = \frac{1}{\mu} S_\nu(\tau_\nu) e^{-\tau_\nu/\mu} \kappa_\nu \tag{1.13}$$

It is important also to consider the difference between *pure absorption* of a photon and *scattering* of a photon. Both are significant in the radiative transfer problem. In pure absorption a photon is absorbed leading to the excitation of an electron which subsequently de-excites via a collisional process. Consequently pure absorption leads to thermal coupling between the point of emission of the photon and that of absorption. In the scattering process a photon is absorbed leading again to the excitation of an electron which this time de-excites via a radiative process. Thus the scattering process does not lead to thermal coupling but, unlike the case of pure absorption, results in a distortion of the emission profile since the photon may be scattered in any direction. Scattering leads to diffusion of photons from the Doppler core where the probability of absorption (i.e. the opacity) is greatest. This in turn leads to the distortion and/or *self-reversal* of emission lines (see fig. 1.8). This effect is termed *partial frequency redistribution* within radiative transfer theory (see sec. 1.3.2). If this is neglected then *complete frequency redistribution* is assumed. This assumption is valid if there are sufficient randomising/redistributive collisions between photo-absorption and re-emission to ensure that there is no dependence of the emission profile on the absorption profile.

1.3.2 Solving the radiative transfer problem

The coupled equations of statistical balance and radiative transfer are currently impossible to solve completely given that in principle their solution involves plasma geometry, flow and even electric and magnetic fields. Advances in computer technology have led to more and more complex treatments of this problem but each solution invokes approximations of either a physical or mathematical nature. These relate to all aspects of the problem, from atomic physics considerations (eg. 2-level atoms – Auer & Paletou, 1994) to the plasma geometries and dynamics (eg. one dimensional static slabs – Carlsson, 1986; Anzer & Heinzel, 1999, 2000). Methods of solution may be grouped into three categories: firstly the methods of *radiative transfer*, secondly *Monte Carlo* computations and thirdly *escape probability* techniques.

Methods of radiative transfer

Radiative transfer methods (see for example Carlsson, 1986; Olson et al., 1986) solve the radiative transfer and statistical balance equations iteratively using a Newton-Raphson technique. The equations are linearised using the Feautrier method (Feautrier, 1964) and solved using *lambda iteration* or *Accelerated Lambda Iteration* (ALI – see Rybicki & Hummer, 1991). Detailed one-dimensional (1D) numerical modelling began with Poland et al. (1971) and Ishizawa (1971). Since then techniques have been extensively developed to include many (i.e. more than two) atomic levels plus continuum states (Heasley & Mihalas, 1976), PRD (eg. Heinzel et al., 1987) and more than one spatial dimension (eg. Paletou et al., 1993). Codes such as MULTI (Carlsson, 1986) and MALI (Rybicki & Hummer, 1991, 1992) have been used by many authors to consider solar and stellar atmospheres as well as solar structures such as prominences and spicules.

Prominences represent a classic radiative transfer problem. Their temperature, density, turbulence and magnetic field are now relatively well known but critical to this understanding was the realisation that observed high excitation temperatures do not reflect the actual electron temperature and density but are the result of non-LTE effects. That is, the incident UV radiation from the chromosphere below has key importance in the ionisation within the prominence. Photo-absorption is thus critical to the energy balance of prominences from the standpoint of ionisation, particularly of hydrogen, and of radiative power loss, particularly from the Lyα and Lyβ lines which are optically thick and strongly self reversed (see fig. 1.8).

The radiative transfer calculations of MULTI and MALI each depend upon an atomic and an atmosphere model. The atomic model contains information on collisional and radiative excitation, de-excitation, ionisation and re-combination processes for all the species to be considered. The atmosphere model contains information on electron temperature and density and elemental abundances. On this basis the calculation consists of iterating back-and-forth between an estimate of the source function and the computation of the associated radiation field until some convergence criterion is reached. This yields key properties for each line including the source function, contribution function, opacity, optical depth and emergent intensity as well as the

excited state population structures for each species considered.

Models such as these are necessary for considering the energy balance in and radiative power loss from optically thick and photo-ionised plasmas. This follows the large oscillator strengths of Lyα and Lyβ, coupled with the abundance of neutral hydrogen in the TR, which lead to these lines being dominant and optically thick radiators. Radiative transfer models are also necessary for the computation of absolute intensities, intensity ratios of lines of different species and emergent line profiles.

The problem with these methods however, is that they are computationally intensive, time-consuming and also usually limited in applicability to particular source configurations which places a limitation on their validity for inhomogeneous plasmas. Plasma geometries considered in this model are usually 1D plane parallel, semi-infinite slabs (eg. Carlsson, 1986; Heinzel et al., 1987; Lanzafame, 1994; Hubeny & Lites, 1995; Goutikakis et al., 1997; Anzer & Heinzel, 1999, 2000) that are stratified with electron temperature and density based on hydrostatic equilibrium (eg. Vernazza et al., 1981, henceforth referred to as VAL), or 1D slabs that are vertically (Heinzel, 1995) or horizontally (Mein et al., 1996) oriented and illuminated, perhaps, by an external source such as the underlying chromosphere and transition region. Two dimensional (2D) models have been developed which allow for transport in two directions but source geometries in such calculations remain simplistic – 2D slabs (Paletou et al., 1993; Auer & Paletou, 1994; Paletou 1996) or isolated prominence threads (Fontenla et al., 1996) for example. In these thread models individual threads are modelled as plane-parallel slabs immersed in a radiation field due to the other slabs.

The problem is that the solar atmosphere has a complex structure and the results from radiative transfer computations may only be interpreted within the simple geometries for which they apply. For example, to approximate the solar transition region as a plane parallel, semi-infinite slab, with electron temperature and density following that of the VAL model, leads to emission at the limb (i.e. looking along the infinite dimension) which is impossible to predict, and zero emission above it. Such a model fails to account for the extension of the transition region into the corona due to the spicule-like structures described in sec. 1.1.1. Moreover, these techniques provide no way to extract information directly from observations about optical depths

or plasma structure. This is not to say that radiative transfer based diagnostics of plasmas are not made. Heinzel et al. (1996) performed a complex diagnostic of prominences using 140 models computed by Gouttebroze et al. (1993). However, plasma parameters deduced from such diagnostics can only be interpreted with reference to a preconceived plasma configuration.

Monte Carlo methods

Monte Carlo techniques for radiative transfer have been used in astrophysics to model plasmas with random geometries such as the Lyα forest (Zheng et al., 1998) and optically thick *blobs* in stars and the interstellar medium (Code & Whitney, 1995). Such techniques have also been used to model solar phenomena such as coronal loops (Guttebroze et al., 1986; Wood & Raymond, 2000). The advantage of Monte Carlo radiation transfer simulations is that they naturally account for arbitrary illumination and multiple scattering in complex geometries.

In the Monte Carlo method photon scattering is described by using random numbers to sample from probabilistic interaction laws in order to follow photons as they scatter through a medium.

Again, however, approximations are necessary and in this case there is a trade off between geometric complexity and detail in the line formation process. More specifically, these calculations model random walks of photons and so purely describe the scattering process. Many subtleties arising from absorption such as the influence of opacity on the source and contribution functions and ionisation balance are not included. Consequently these methods are restricted to moderate optical depths. This is not a severe restriction since many astronomical lines have low but non-zero optical depths. However, Monte Carlo techniques are model based and so, as with the radiative transfer techniques, they provide no means by which plasma parameters may be extracted directly from observations independently of a geometric model.

Escape probability techniques

The escape probability was introduced by Holstein (1947) and associated expressions have since been developed by a number of authors (McWhirter, 1965; Irons, 1979; Hummer & Rybicki, 1982: Kastner & Kastner, 1990). The effects of opacity in solar spectral lines have been studied on a number of occasions using such methods (Jordan, 1967; Doschek et al., 1976; Doyle & McWhirter, 1980). Jordan established the technique of using branching ratios of lines arising from a common upper level to extract information on opacities directly from spectral observations. Doyle & McWhirter subsequently developed this same technique to study opacity at the solar limb and their work included a simple model of predicted line ratios from the region on-disk up to the limb. Many authors have constructed models of both laboratory and astrophysical plasmas using escape probability techniques (Doyle & McWhirter, 1980; Orrall & Schmahl, 1980; Keenan & Kingston ,1986; Brooks et al., 2000).

Escape probability methods, which will be discussed in detail in subsequent chapters, rely on assumptions that simplify the source function term in eqs 1.5 and 1.6. These assumptions naturally decouple and linearise the equations. Consequently these methods provide approximate solutions to eqs 1.5 and 1.6 in a moderate optical depth regime. This approach has the virtue of practicality. As stated above, escape probability expressions provide diagnostic tools to extract plasma parameters directly from observations. Furthermore they have the potential to be used in plasma models of arbitrary geometric complexity. For example, Orral & Schmahl (1980) used *attenuation factors* (identical in principle to escape probabilities) to account for opacity within prominence models. These models consisted of resolved slabs or unresolved threads. The radiative transfer computations (as stated above) consider individual threads in isolation and model them as plane parallel slabs.

1.4 Thesis overview

The techniques described above all rely on a set of assumptions which differ between and within the three approaches presented. The validity of any solution, assuming any

numerical schemes employed are effective (efficiently or otherwise), is entirely dependent on the prescribed problem – that is the nature of the assumptions made. It does not matter that a solution is numerically sophisticated if the underlying assumptions are invalid.

This work aims to investigate the relatively simple escape probability techniques for solving the coupled sets of equations of statistical balance and radiative transfer (eqs 1.5 and 1.6). The assumptions that underpin such techniques will be tested in order to asses the extent of their validity and the nature of their invalidity as the regime is entered within which they break down.

In chapter 2 an overview of the techniques will be given and their coupling to simple atmosphere models will be demonstrated in comparison with data from the SOHO-SUMER spectrometer. In chapter 3 these methods will be reviewed to consider inhomogeneous models in a consistent way and to assess the modification to the source function due to opacity. In chapter 4 the effects of line blending will be analysed and in chapter 5 the influence of structure and plasma flows will be examined. Then in chapter 6 the SUMER observations discussed in chapter 2 will be re-visited from a model and diagnostic perspective. The improved escape probability techniques will be used to re-assess simple empirical models and to extract information on optical depths and structure directly from observations in a manner that is model independent.

Chapter 2

The escape probability approach to opacity

It is clear that opacity as a phenomenon is at its most challenging in plasmas that exist between the two extreme regimes of thermodynamic equilibrium (eg. the photosphere) and optically thin plasma (eg. the corona). Between the photosphere and the corona the electron density varies from $\sim 10^{14}$ to $\sim 10^{9}$ cm^{-3} (see fig. 1.7) and conditions change from those of thermodynamic equilibrium to optically thin so that in between – i.e. in the chromospheric and the TR – there exists non-LTE plasma of significant opacity. Conditions and emission from such plasmas are complicated by long range coupling due to photo-absorption that may involve different electronic transitions and potentially a variety of atomic species. Consequently, a bound electron in a plasma, will potentially 'see' the rest of the plasma to some considerable distance or even in its entirety and conditions at this point are thus determined by those at all 'visible' positions. Each point in an optically thick plasma is therefore coupled in terms of energy and excitation to non-local regions with potentially different temperatures, densities, geometries and flows.

Opacity modifies the excited state population structure of an ion via the introduction of photo-excitation terms in the statistical balance equations. In turn, this modification influences spectral line emission. Additionally, the emission along a line-of-sight is affected by opacity due to a loss of photons along that line-of-sight either

by absorption or scattering. It follows that opacity influences radiative cooling (or heating) timescales which are relevant to radiative power loss. Even though the local radiative power loss coefficients in a dynamic plasma may not be sensitive to opacity, the time taken for photons to propagate through and escape from an emitting structure is sensitive. Therefore opacity must be significant from an energy transport perspective in at least some dynamic plasmas. Furthermore, photoionisation will alter the ionisation balance which in turn modifies spectral emission characteristics and the radiative power loss functions at a particular temperature.

A more subtle effect is that of partial frequency redistribution which relates to the ultimate fate of absorbed photons. The effect of this is to diffuse photons in frequency space toward the line wings thus altering (principally but not exclusively) emergent line profiles.

The emission from an optically thick plasma is characterised by two sets of coupled differential equations, namely those of radiative transfer and statistical balance – eqs 2.1 and 2.2 respectively.

$$\frac{dI_\nu(s)}{ds} = j_\nu(s) - \kappa_\nu(s) I_\nu(s) \tag{2.1}$$

$$\begin{aligned} \frac{dN_u(\mathbf{r})}{dt} &= -A_{u\to l} N_u(\mathbf{r}) + \frac{4\pi}{c} B_{l\to u} N_l(\mathbf{r}) \int \bar{I}_\nu(\mathbf{r}) \phi(\nu) d\nu \\ &+ \; other\ collisional\ and\ radiative\ terms \end{aligned} \tag{2.2}$$

These were discussed in some detail in secs. 1.2 and 1.3. Eq. 2.2 is written here for level u and differs from eq. 1.5 in that the photo-absorption process corresponding to the transition $l \to u$ has been included and the spatial dependence is made explicit. Statistical balance holds if all derivatives, $dN_u(\mathbf{r})/dt$, are zero. That is, it holds for ions whose atomic populations are in steady state. If this is so then the loss of electrons from a level due to excitation, de-excitation, ionisation and recombination is balanced, statistically speaking, by the reverse processes that serve to populate the level. This contrasts with thermodynamic equilibrium where each process is balanced by its inverse (detailed balance).

The radiative transfer equations describe the propagation of photons along a line-of-sight and so have obvious relevance to observed emission. In integrating eq. 2.1,

contributions to the intensity, both negative and positive, at each point, are summed. Coupling with eq. 2.2 is via the dependence on the population distribution terms implicit within the emission and the absorption coefficients which are proportional to the upper and lower level populations respectively. Coupling also acts in the reverse direction since the statistical balance equations require for their solution at any particular point, knowledge of the radiation field. This term involves an integration of the intensity along every line-of-sight that terminates at the point of interest and thus requires, in principle, the solution of eq. 2.1 along each of these lines of sight.

It is then clear that opacity presents a significant difficulty and, as discussed in sec. 1.3.2, a number of approaches exist to deal with it. In this work spectral emission in lines of moderate opacity is of interest with the focus being on emitting plasma structure. For such lines the relative simplicity of the escape probability approach is desirable since it allows complex emitting geometries to be considered. In this chapter the escape probability and associated quantities will be defined and evaluated and applied to data from the SOHO-SUMER spectrometer to extract optical depths of spectral lines of C II and C III. Escape probabilities will also be used in conjunction with some simple stratified atmosphere models to determine their effectiveness in describing the observed spectral emission characteristics on crossing the solar limb. In subsequent chapters the escape probability and absorption factor expressions will be analysed and developed for use within more detailed atmosphere models.

2.1 The effect of opacity on emergent intensities

The escape probability approach fits naturally within a collisional radiative framework allowing opacity to be included in the equations of statistical balance. The following definitions are made:

1. intensity, I_ν – the number of photons of frequency ν propagating in a given direction, crossing a unit area perpendicular to that direction, per unit volume, per unit time, per unit solid angle, with units $\mathrm{cm}^{-2}\mathrm{s}^{-1}\mathrm{st}^{-1}$.

2. emissivity, j_ν – the number of photons of frequency ν emitted at a point per

unit volume, per unit time, per unit solid angle, with units $\mathrm{cm}^{-3}\mathrm{s}^{-1}\mathrm{st}^{-1}$.

3. absorption coefficient, κ_ν – defined such that $\kappa_\nu I_\nu$ is the number of photons of frequency ν absorbed at a point per unit volume, per unit time per unit solid angle. κ_ν has units of cm^{-1}.

These definitions lead to the following:

$$j_\nu(\mathbf{r}) = \frac{1}{4\pi} A_{u\to l} N_u(\mathbf{r}) \phi_e(\nu) \tag{2.3}$$

$$\kappa_\nu(\mathbf{r}) = \frac{1}{c} N_l h\nu B_{l\to u} \phi_a(\nu) \tag{2.4}$$

where $\phi_e(\nu)$ and $\phi_a(\nu)$ are the emission and absorption profiles respectively. From these, eqs 2.1 and 2.2 may be rewritten as follows

$$\frac{dI(s)}{ds} = \frac{1}{4\pi} A_{u\to l} N_u(s) \left[1 - \frac{N_l(s)\omega_u}{N_u(s)\omega_l} \frac{c^2}{2\nu_0^2} \int I_\nu(s)\phi_e(\nu) d\nu\right] \tag{2.5}$$

$$\begin{aligned} \frac{dN_u(\mathbf{r})}{dt} &= -A_{u\to l} N_u(\mathbf{r}) \left[1 - \frac{N_l(\mathbf{r})\omega_u}{N_u(\mathbf{r})\omega_l} \frac{c^2}{2\nu_0^2} \int \bar{I}_\nu(\mathbf{r})\phi_a(\nu) d\nu\right] \\ &+ \textit{other collisional and radiative terms} \end{aligned} \tag{2.6}$$

Here ds is an element of distance along the line of sight, $A_{u\to l}$ is the Einstein A-coefficient, N_u and N_l are the upper and lower level population densities respectively and the ω's are statistical weights.

The terms in the brackets are markedly similar, the only difference being in the specification of the intensity terms. In the eq. 2.5 the intensity term $I_\nu(s)$ is the intensity at the point s along the path $0 \to s$ and so is related to the emissivity, $j_\nu(s)$, along that path. In eq. 2.6, however, $\bar{I}_\nu(\mathbf{r})$ is the radiation field at $\mathbf{r}$ due to surrounding plasma and so is related to the integral of $j_\nu(\mathbf{x})$, and thus also of $N_u(\mathbf{x})$ over all points $\mathbf{x}$.

The escape probability approach may be illustrated if eqs 2.5 and 2.6 are re-written as follows:

$$\frac{dI(s)}{ds} = \frac{1}{4\pi} A_{u\to l} N_u(s) g(s) \tag{2.7}$$

$$\frac{dN_u(\mathbf{r})}{dt} = -A_{u\rightarrow l}N_u(\mathbf{r})\Lambda(\mathbf{r}) + the\,other\,terms \quad (2.8)$$

$g(s)$ is the *escape probability*, representing the probability that a photon emitted at a point s in the direction of the line-of-sight will escape the plasma. $\Lambda(\mathbf{r})$ is the *Biberman-Holstein coefficient* or *net-radiative bracket* (Irons, 1979) and is called here the *absorption factor*. It relates to the probability that a photo-absorption will occur at the point $\mathbf{r}$. Both terms may be viewed as providing parametric adjustments to the Einstein A-coefficients in the equations of radiative transfer and statistical balance. Thus, providing the A-coefficients are modified appropriately, the optically thick population structure may be obtained in an identical manner as the optically thin one. This will be discussed in more detail later.

The escape probability was first introduced by Holstein (1947) and has subsequently been considered by many authors (e.g. McWhirter, 1965; Irons, 1979; Doyle & McWhirter, 1980). Holstein's work focused on the emission point of view but McWhirter (1965) considered the population structure and since then expressions have been used and developed in both contexts. More recent are works by Kastner & Bhatia (1989), Kastner & Kastner (1990) and Kastner & Bhatia (1992). These authors have extensively developed escape probability and absorption factor expressions and used them for predicting emergent intensities and optically thick population structures. A useful aspect to the escape probability approach is in diagnosing optical depths directly from observations – a method that was established by Jordan (1967). This technique (described in more detail below) makes use of observed branching ratios of spectral lines that share a common upper level and has been used by several authors (Doyle & McWhirter, 1980; Keenan & Kingston, 1986; Brooks et al., 2000) to extract optical depths from spectral observations of solar plasmas.

In first deriving an expression for the escape probability, Holstein, rather than evaluating the bracketed term in eq. 2.5, considered the definition of $g(s)$ as a probability of escape. If one considers the propagation of a photon by a distance d along a line of sight, the radiative transfer equation is

$$\frac{dI_\nu(s)}{ds} = -\kappa_{\nu,l\rightarrow u}I_\nu(s) \quad (2.9)$$

$$\Rightarrow I_\nu(d) = I_\nu(0)e^{-\kappa_{\nu,l\rightarrow u}d} \quad (2.10)$$

Holstein defined $T(\kappa_{\nu,l\to u}s,\nu) = exp(\kappa_{\nu,l\to u}s)$ as the *monochromatic transmission probability*. The escape probability is this quantity averaged over the emission profile, $\phi_e(\nu)$, i.e.

$$g(s) = \int \phi(\nu)_e T(\kappa_{\nu,l\to u}s,\nu)d\nu \tag{2.11}$$

$\kappa_{\nu,l\to u}$ is in general a function of space as well as frequency but if it is assumed to be constant with respect to space, and furthermore, if emission and absorption profiles are assumed to be purely Doppler broadened, i.e.

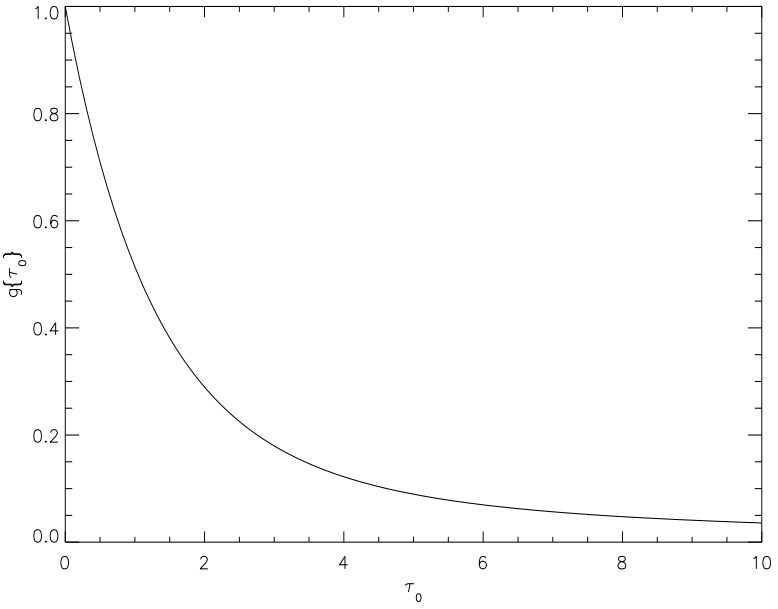

Figure 2.1: Plot of $g\{\tau_0\}$ versus τ_0.

$$\phi_e(\nu) \equiv \phi_a(\nu) \equiv \phi(\nu) = \frac{1}{\sqrt{\pi}\Delta\nu_D} exp\left\{-\left(\frac{\nu-\nu_0}{\Delta\nu_D}\right)^2\right\} \tag{2.12}$$

with $\Delta\nu_D$ the Doppler width, then if the line of sight is defined by $s: 0 \to L$,

$$g(s) = \frac{1}{\sqrt{\pi}} \int_{-\infty}^{\infty} e^{-u^2}\, exp\{-\tau_0(s)e^{-u^2}\}\, du \tag{2.13}$$

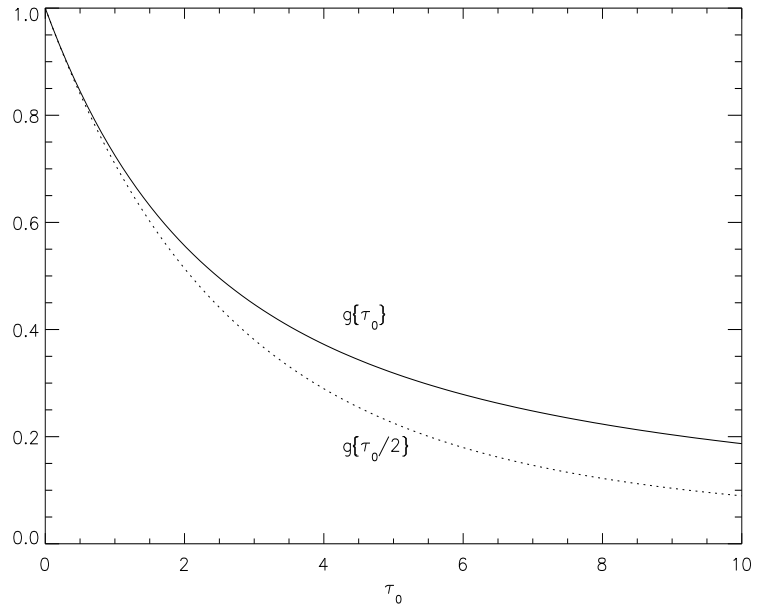

Figure 2.2: Solid line – $\bar{g}\{\tau_0\}$ versus τ_0; dotted line – $g\{\tau_0/2\}$ versus τ_0 (see sec. 2.6 for discussion).

where $u = (\nu - \nu_0)/\Delta\nu_D$ and $\tau_0 = \kappa_{0,l\to u}(L - s)$. It is convenient to write $g(s)$ in terms of optical depth, i.e. as $g\{\tau_0(s)\}$. Following Mitchell & Zemansky (1961),

$$\tau_0(s) = 1.16^{-6}\sqrt{M/T_i}\lambda_0 N_l f_{l\to u}(L - s) \tag{2.14}$$

where T_i is the ion temperature (K), M is the atomic mass number, λ_0 is the central wavelength (cm), N_l is the number density of the lower level of the transition (cm^{-3}), $f_{l\to u}$ is the absorption oscillator strength and L is the physical thickness of the plasma along the line of sight (cm). A plot of $g\{\tau_0\}$ versus τ_0 is shown in fig. 2.1.

Integrating eq. 2.7 yields

$$I = \frac{1}{4\pi}A_{u\to l}N_u\bar{g}\{\tau_0\}L \tag{2.15}$$

where $\bar{g}\{\tau_0\}$ is the *line-of-sight averaged escape probability* and τ_0 is the total optical depth along the line-of-sight, i.e.

$$\tau_0 = 1.16^{-6}\sqrt{M/T_i}\lambda_0 N_l f_{l\to u}L \equiv \tau_0(0) \tag{2.16}$$

Since the density is assumed constant, $\bar{g}\{\tau_0\}$ is given by

$$\bar{g}\{\tau_0\} = \frac{1}{\sqrt{\pi}} \int_{-\infty}^{\infty} \left[\frac{1 - exp\{-\tau_0 e^{-u^2}\}}{\tau_0} \right] du \tag{2.17}$$

$\bar{g}\{\tau_0\}$ is compared to $g\{\tau_0/2\}$ in fig. 2.2.

Although $g\{\tau_0(s)\}$ is the probability of escape, it is identical to what Irons (1979) called the *transmission factor*, $T(\tau_0)$, which is a more appropriate label for a general picture. The former is a probability of escape since it relates to the likelihood of a photon propagating from its point of origin to a second point that is located *outwith* the plasma. If, however, that point is within the plasma then, though the probability is purely that of propagation from one point to another and not specifically of escape, the expression is identical. In this case *transmission factor* is the appropriate label. Kastner & Kastner (1990) describe $g\{\tau_0\}$, which they denote by $p_f(\hat{\nu}, \vec{k}, \tau : 0)$, as corresponding to the case of isolated emitters and absorbers (denoted '0') as it does not include the effect of emission at other optical depths along the line-of-sight. Averaging this expression along the line-of-sight leads to what Kastner & Kastner describe as being the *proper* escape probability for emergent intensities, given by $p_f(\hat{\nu}, \vec{k}, \tau : 1) \equiv \bar{g}\{\tau_0\}$. This represents the *mean* probability that a photon, emitted from some point along a line-of-sight of depth τ_0, in the direction of the line-of-sight, will escape from the plasma, as described above.

This expression assumes that the only effect of opacity is to scatter photons out of the line-of-sight. This is not true as photons may also be scattered *into* the line-of-sight. This was recognised by Jordan (1967) who wrote

$$E_i \sim N_u W_i = \frac{N_u b_i q_i}{1 - \sum_n (b_n [1 - q_n])} \tag{2.18}$$

where E_i is the energy intensity ($E_i = h\nu I_i$), W_i is the fraction of photons created, escaping in line i; q_i is equivalent in principle to $\bar{g}\{\tau_0\}$ and the denominator accounts for the scattering into the line-of-sight. This was subsequently re-written by Kastner & Bhatia (1992) as the correct line-of-sight escape probability, p_e, which is given by

$$p_{e,j} = \frac{\vec{p}_{f,j}}{1 - \sum_i b_i (1 - p_{d,i})(1 - \bar{p}_{f,i})(1 - \vec{p}_{f,i})} \tag{2.19}$$

where $p_{d,i}$ is the photon loss probability (defined as the ratio of collisional de-excitation to total de-excitation – Kastner, 1981), $\vec{p}_{f,j} = p_f(\hat{\nu}, \vec{k}, \tau : 1) \equiv \bar{g}\{\tau_0\}$, and $\bar{p}_{f,i} = p_f(\hat{\nu}, \hat{\vec{k}}, \tau : 0)$. $\bar{p}_{f,i}$ is the mean probability that a photon emitted anywhere in the layer will travel to the surface and escape. This latter term is equivalent to Irons' *escape factor*, θ (Irons, 1979).

2.1.1 Deduction of opacity from observations

It was pointed out by Jordan (1967) that for intensity ratios of lines arising from a common upper level the denominator of $p_{e,j}$ cancels out leaving just $\vec{p}_{f,j} \equiv \bar{g}\{\tau_0\}$ as the appropriate escape probability for this ratio analysis.

Jordan introduced the idea that such a quantity could be used to diagnose optical depths from observations of such ratios. She wrote the energy intensity ratio of two lines, 1 and 2, arising from a common upper level as

$$\frac{E_1}{E_2} = \frac{b_1 q_1}{\lambda_1} \frac{\lambda_2}{b_2 q_2} \tag{2.20}$$

where q_1 and q_2 are the escape probabilities for lines 1 and 2 respectively (equivalent in principle to $\bar{g}\{\tau_0^{(1)}\}$ and $\bar{g}\{\tau_0^{(2)}\}$) and b_1 and b_2 are the probabilities that photons will be emitted in lines 1 and 2 respectively, i.e.

$$b_i = \frac{A_i}{\sum\limits_n (A_n + C_n N_e) + \sum\limits_m (u_\nu B_m + C_m N_e)} \tag{2.21}$$

where the sum over n refers to processes below the excited level and the sum over m refers to processes above the excited level. $C_n N_e$ is the collisional de-excitation rate, $C_m N_e$ is the collisional excitation rate and $u_\nu B_m$ is the photo-excitation rate. Although her escape probability expression was much simpler than those considered here and was derived by assuming that all photons emitted in the line wings where $\tau < 1$ escape whereas all those emitted near line centre where $\tau > 1$ do not, the idea is effective. In the present notation, equation 2.20 is

$$\frac{I_{u \to l_1}}{I_{u \to l_2}} = \frac{A_{u \to l_1}}{A_{u \to l_2}} \frac{\bar{g}\{\tau_{0, l_1 \to u}\}}{\bar{g}\{\tau_{0, l_2 \to u}\}} \tag{2.22}$$

$$\Rightarrow \frac{\bar{g}\{\tau_{0, l_1 \to u}\}}{\bar{g}\{\tau_{0, l_2 \to u}\}} = \frac{I_{u \to l_1}}{I_{u \to l_2}} \frac{A_{u \to l_2}}{A_{u \to l_1}} \tag{2.23}$$

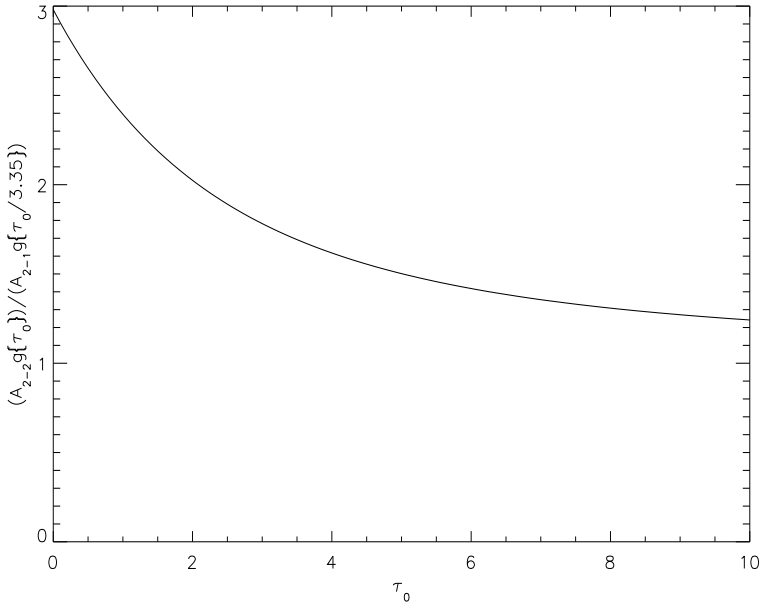

Figure 2.3: Plot of $A_{2-2}\bar{g}\{\tau_0\}/A_{2-1}\bar{g}\{\tau_0/3.35\}$ versus τ_0. This ratio is equal to the intensity ratio of the C III $2s2p^3P$ - $2p^2\,^3P$ 2–2 line over the 1–2 line. Optical depths versus position may be determined by comparison of the observed ratios shown in fig. 2.10a.

Photo-absorption is most likely to occur when the lower level populations are large and long lived – i.e. metastable. Such populations, however, are collisionally controlled and so the relative populations of two metastable levels of an ion are insensitive to opacity and may be determined in an optically thin model, i.e.

$$\tau_{0,l_1\rightarrow u} = const \times \tau_{0,l_2\rightarrow u} \tag{2.24}$$

$$\Rightarrow \tau_{0,l_2\rightarrow u} = \tau_{0,l_1\rightarrow u}/const \tag{2.25}$$

$$\Rightarrow \tau_{0,l_1\rightarrow u} = R^{-1}\left(\frac{\bar{g}\{\tau_{0,l_1\rightarrow u}\}}{\bar{g}\{\tau_{0,l_1\rightarrow u}/const\}}\right) \tag{2.26}$$

where

$$R(\tau_0) = \bar{g}\{\tau_{0,l_1\rightarrow u}\}/\bar{g}\{\tau_{0,l_1\rightarrow u}/const\} \tag{2.27}$$

Thus optical depth may be deduced directly from observations of spectral line intensities. For example, fig. 2.3 shows $A_{2-2}\bar{g}\{\tau_0\}/A_{2-1}\bar{g}\{\tau_0/3.35\}$ versus τ_0. Comparison

between this curve and observed values of the I(2–2)/I(1–2) ratio of the C III $2s2p^3P$ – $2p^2{}^3P$ multiplet (1175 Å) yields values for $\tau_{0,2-2}$. This is demonstrated in sec. 2.3.

2.2 The effect of opacity on the population structure

It is demonstrated above that in the ratio of lines arising from a common upper level, the term that accounts for the effect of scattering into the line-of-sight disappears. Equivalently, it can be said that this ratio does not depend on the population structure. However, there is an effect on the population structure due to opacity. McWhirter (1965) introduced an escape factor type approach to this problem as follows. The intensity term, $\bar{I}_\nu$ in eq. 2.6 for some point in a layer is

$$\bar{I}_\nu = \frac{1}{4\pi}\int_0^{4\pi} I_\nu(\theta,\phi)d\Omega \tag{2.28}$$

where $I_\nu(\theta,\phi)$ is the intensity along a path in the direction (θ,ϕ) and $d\Omega$ is an element of solid angle. $I_\nu(\theta,\phi)$ may be obtained for the constant density case via the solution of the radiative transfer equation, i.e.

$$\begin{aligned}
\frac{dI_\nu}{dx} + \kappa_\nu I_\nu &= j_\nu \\
\Rightarrow \frac{d}{dx}(e^{\kappa_\nu} I_\nu) &= e^{\kappa_\nu} j_\nu \\
\Rightarrow I_\nu(x) &= \frac{\kappa_\nu}{j_\nu}\left[e^{\kappa_\nu(L-x)} - e^{-\kappa_\nu x}\right] \\
\Rightarrow I_\nu = I_\nu(L) &= \frac{\kappa_\nu}{j_\nu}\left[1 - e^{-\kappa_\nu L}\right] = \frac{\kappa_\nu}{j_\nu}\left[1 - e^{-\tau_\nu(\theta,\phi)}\right]
\end{aligned} \tag{2.29}$$

where L is the path length in direction (θ,ϕ) and $\tau_\nu(\theta,\phi) = \kappa_\nu L$. Thus

$$\begin{aligned}
\bar{I}_\nu &= \frac{1}{4\pi}\int_0^{4\pi} \frac{\kappa_\nu}{j_\nu}\left[1 - e^{-\tau_\nu(\theta,\phi)}\right] d\omega \\
&= \frac{\kappa_\nu}{j_\nu}\left[\overline{1 - e^{-\tau_\nu(\theta,\phi)}}\right]
\end{aligned} \tag{2.30}$$

where $\overline{1 - e^{-\tau_\nu(\theta,\phi)}}$ is the average of $1 - e^{-\tau_\nu(\theta,\phi)}$ over direction. $\bar{I}_\nu$ may be written as

$$\bar{I}_\nu = \frac{\kappa_\nu}{j_\nu}\left[1 - e^{-\bar{\tau}_\nu(\theta,\phi)}\right] \tag{2.31}$$

for $\overline{\tau}_\nu = \kappa_\nu \bar{L}$ where $\bar{L}$ is *some representative length.* If it is further assumed, as it was earlier, that the emission and absorption profiles are identical and are purely Doppler broadened, then

$$\frac{\kappa_\nu}{j_\nu} = \frac{N_l}{N_u}\frac{\omega_u}{\omega_l}\frac{2\nu_0^2}{c^2} \tag{2.32}$$

From eq. 2.6

$$\Lambda(\mathbf{r}) = 1 - \frac{N_l(\mathbf{r})\omega_u}{N_u(\mathbf{r})\omega_l}\frac{c^2}{2\nu_0^2}\int \bar{I}_\nu(\mathbf{r})\phi(\nu)d\nu \tag{2.33}$$

and thus it follows that

$$\Lambda(\mathbf{r}) = 1 - \frac{1}{\sqrt{\pi}}\int_{-\infty}^{\infty}\left[1 - exp\{-\bar{\tau}_0 e^{-u^2}\}\right]e^{-u^2}du \equiv g\{\bar{\tau}_0\} \tag{2.34}$$

This is a useful result except for the fact that the precise meaning of $\bar{\tau}_0$ is not clear (this is discussed more in sec. 2.6.)

A less ambiguous result may be obtained as follows: consider a plane parallel, semi-infinite layer of constant density and thickness D, and consider a point, $\mathbf{0}$, at its centre. Now consider the intensity, dI_ν at $\mathbf{0}$ due to a volume element, dV, located at the point $\mathbf{r}$. This may be written as

$$dI_\nu = \frac{j_\nu e^{-\kappa_\nu r}}{r^2}dV \tag{2.35}$$

The intensity, $\bar{I}_\nu$, is then

$$\begin{aligned} I_\nu &= \frac{1}{4\pi}\int\int\int_V \frac{j_\nu e^{-\kappa_\nu r}}{r^2}dV \\ &= \frac{2}{4\pi}\int_0^\pi 2\int_0^{D/2}\int_x^\infty \frac{j_\nu e^{-\kappa_\nu r}}{r^2}r\,dr\,dx\,d\theta \end{aligned} \tag{2.36}$$

Changing the order of integration yields

$$\begin{aligned} I_\nu &= \int_0^{D/2}\int_0^r \frac{j_\nu e^{-\kappa_\nu r}}{r}dx\,dr + \int_{D/2}^\infty\int_0^{D/2}\frac{j_\nu e^{-\kappa_\nu r}}{r}dx\,dr \\ &= \int_0^{D/2} j_\nu e^{-\kappa_\nu r}dr + \frac{d}{2}\int_{D/2}^\infty \frac{j_\nu e^{-\kappa_\nu r}}{r} \\ &= \frac{j_\nu}{\kappa_\nu}\left[1 - e^{-\kappa_\nu D/2} + \frac{\kappa_\nu D}{2}E_1\left(\frac{\kappa_\nu D}{2}\right)\right] \end{aligned} \tag{2.37}$$

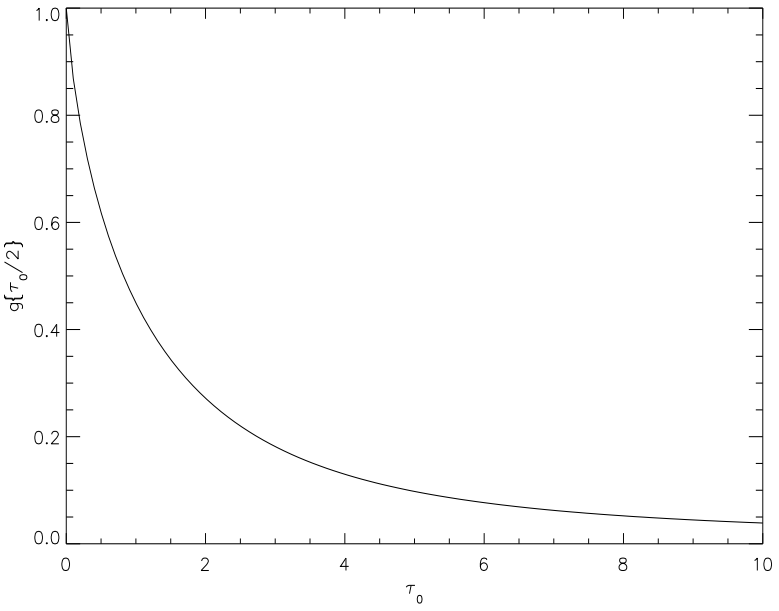

Figure 2.4: Plot of $\bar{\bar{g}}\{\tau_0/2\}$ versus τ_0.

where E_1 is the first exponential integral. It follows that

$$\begin{aligned}\Lambda(\mathbf{r}) &= 1 - \frac{1}{\sqrt{\pi}} \int_{-\infty}^{\infty} e^{-u^2} \left[1 - e^{-\kappa_\nu D/2} + \frac{\kappa_\nu D}{2} E_1\left(\frac{\kappa_\nu D}{2}\right)\right] du \\ &= \frac{1}{\sqrt{\pi}} \int_{-\infty}^{\infty} e^{-u^2} \left[exp\left\{\frac{-\kappa_0 e^{-u^2} D}{2}\right\} - \left\{\frac{\kappa_0 e^{-u^2} D}{2}\right\} E_1\left\{\frac{\kappa_0 e^{-u^2} D}{2}\right\}\right] du \end{aligned} \tag{2.38}$$

i.e.

$$\Lambda(\mathbf{r}) = \frac{1}{\sqrt{\pi}} \int_{-\infty}^{\infty} e^{-u^2} \left[exp\left\{\frac{-\tau_0 e^{-u^2}}{2}\right\} - \left\{\frac{\tau_0 e^{-u^2}}{2}\right\} E_1\left\{\frac{\tau_0 e^{-u^2}}{2}\right\}\right] du \tag{2.39}$$

Thus the absorption factor for a plane parallel slab of constant density may be written purely as a function of the *perpendicular* optical depth and so it is called here $\bar{\bar{g}}\{\tau_0/2\}$ (Brooks et al., 2000). This expression is the same as that denoted by Bhatia & Kastner (1997) as $SEFD(C,T)$ (which stands for *slab escape factor, Doppler* which

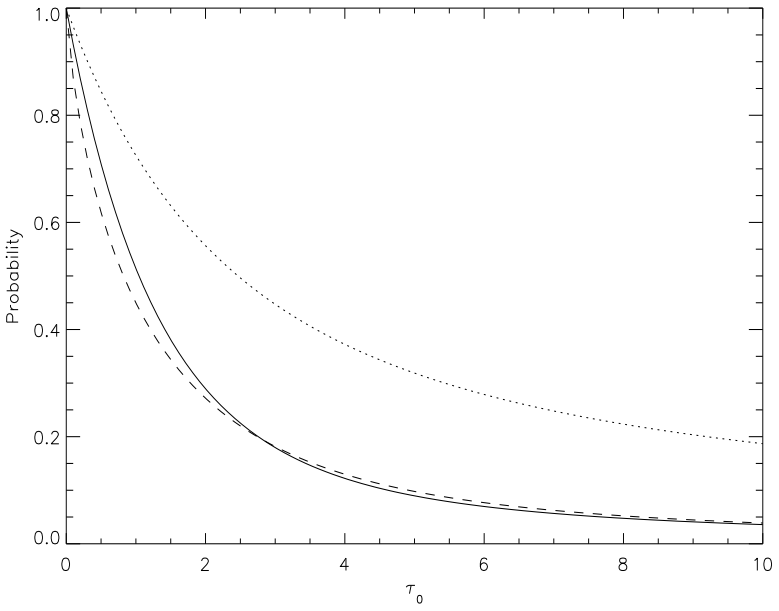

Figure 2.5: Solid line – $g\{\tau_0\}$; dotted line – $\bar{g}\{\tau_0\}$; dashed line – $\bar{\bar{g}}\{\tau_0/2\}$ versus τ_0.

is a function of position, C, in the layer and optical depth, T – Bhatia & Kastner's notation). $\bar{\bar{g}}\{\tau_0/2\}$ is plotted versus optical depth in fig. 2.4. In fig. 2.5 it is shown in comparison with $g\{\tau_0\}$ and $\bar{g}\{\tau_0\}$ where it can be seen that it is close to $g\{\tau_0\}$. Figs 2.6 and 2.7 show the C III $2p^{2\,3}P_2/2p^{2\,3}P_1$ and $2p^{2\,3}P_2/2s2p^3P_2$ population density ratios respectively, versus optical depth. Both are calculated by including appropriate $\bar{\bar{g}}\{\tau_0/2\}$ values in the statistical balance equations. The former ratio varies markedly for small values of optical depth but levels off with large values. This is due to the sensitivity of the corresponding $\bar{\bar{g}}\{\tau_0/2\}$ ratio which is high for small optical depth values and low for large values. Fig. 2.7 illustrates the dependence of the source function of the C III $2s2p^3P_2 - 2p^{2\,3}P_2$ line on optical depth based again on $\bar{\bar{g}}\{\tau_0/2\}$.

2.2.1 Extrapolation to all transitions of an ion

Since optical depth may be extracted from observation as described above, if this is done for a spectral line at disk centre then the absorption factor is also known for

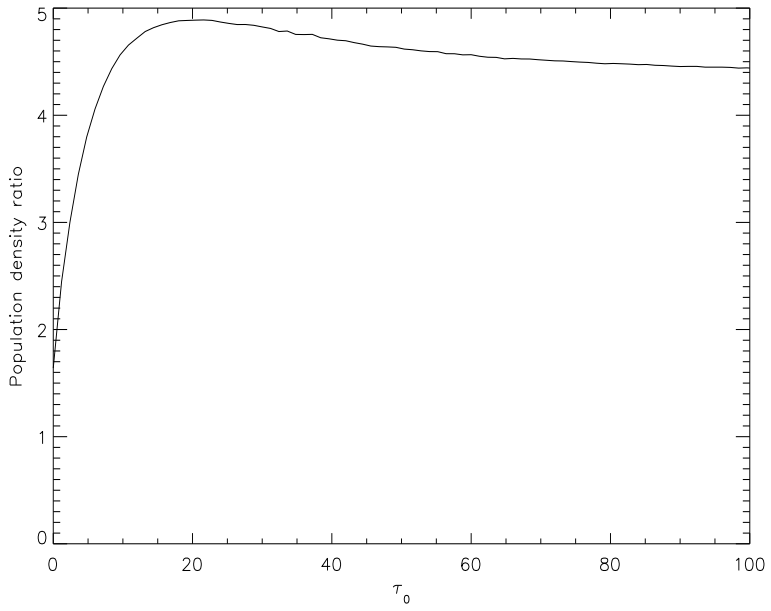

Figure 2.6: Plot of C III $2p^2\,^3P_2/2p^2\,^3P_1$ population density ratio versus τ_0 based on $\bar{g}\{\tau_0/2\}$.

that line. As stated earlier in sec. 2.1.1, the spectral lines that are most significantly modified by opacity are those whose lower levels are metastable. These levels are not significantly altered due to their large population densities and are collisionally controlled. Thus the relative population of metastable components is negligibly affected by opacity and may be calculated by solving eq. 2.6 in the optically thin approximation. It follows that optical depths for all lines of an ion whose lower levels are metastable may be deduced via eq. 2.24 from a single optical depth value. If it is assumed that all other optical depths are negligible then all are known for the ion.

2.3 Opacity deduction at the limb of the sun

In September 1996 an observing sequence was run using the SUMER spectrometer on board the SOHO spacecraft. SUMER is a normal incidence extreme ultraviolet (EUV) spectrometer (Wilhelm et al., 1995) with a spatial resolution of $\sim$ 1 arc sec

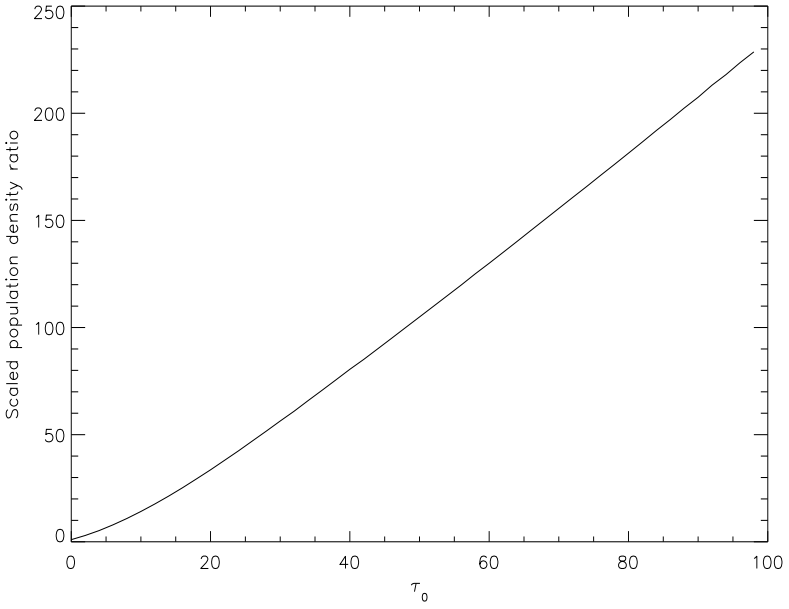

Figure 2.7: Plot of C III $2p^2\,{}^3P_2/2s2p^3P_2$ population density ratio versus τ_0 based on $\bar{\bar{g}}\{\tau_0/2\}$. This ratio is scaled so that it is unity for an optical depth of 0. This ratio illustrates the dependence of the source function of the C III $2s2p^3P_2 - 2p^2\,{}^3P_2$ line on optical depth.

which corresponds to a distance a little less than 1000 km on the sun. The sequence comprised of east-west scans in 18 spatial steps over the west (receding) limb of the sun. Surface plots of the cross-limb data are shown for the C II 904 Å and C III 1175 Å multiples in fig. 2.8. The limb region was chosen for its great variation in optical depth. It can be seen from eq. 2.16 that the optical depth of a spectral line is proportional to both the lower level population density and the thickness along the line-of-sight of the emitting layer. Thus, thinking of the layer as a spherical shell above the sun's surface, on approaching the limb from the disk the optical depth increases as the line-of-sight thickness increases. On crossing the limb the optical thickness doubles as the portion of the emitting layer on the far side of the sun can be viewed, reaching a maximum when the edge of the emitting layer is reached. After this point, in a stratified atmosphere picture the optical depth decreases rapidly due to the fall off of density with height above the surface.

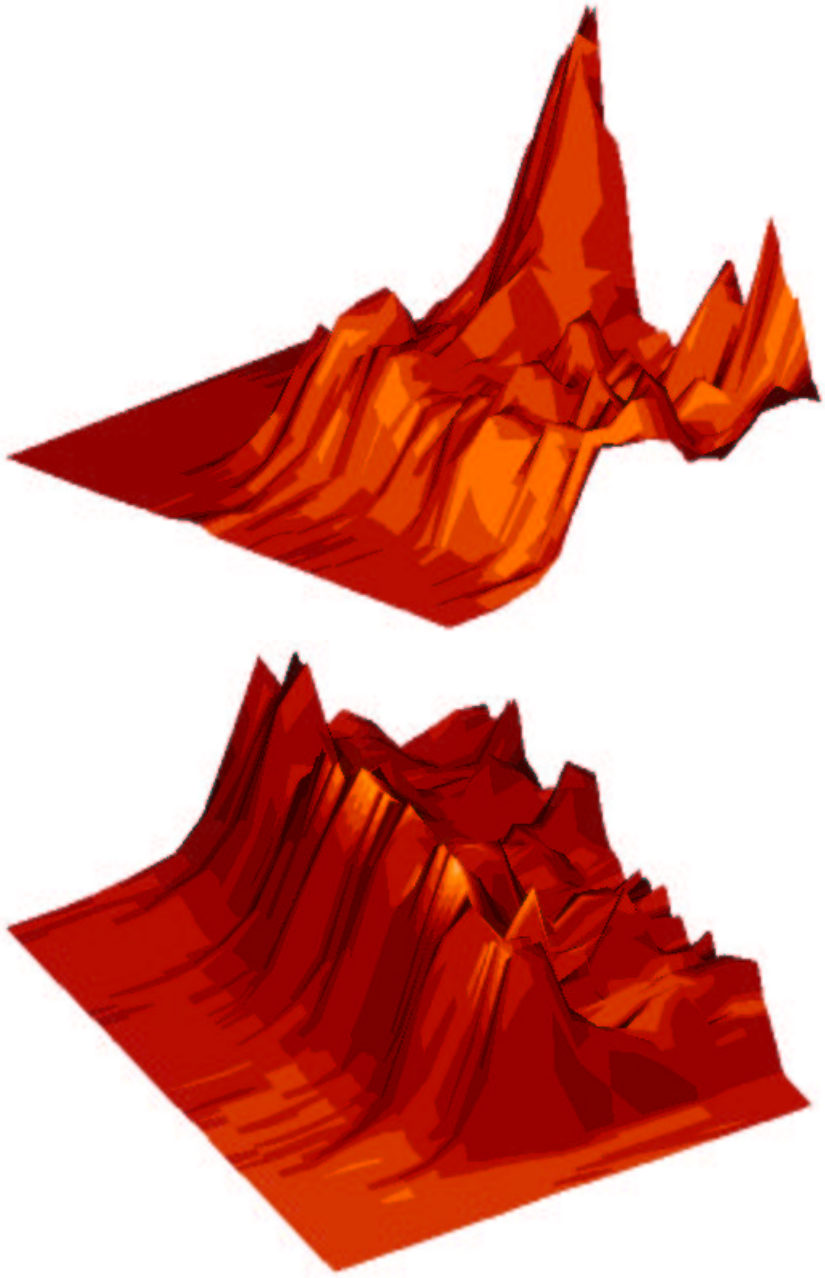

Figure 2.8: Surface plots of total flux in the slit/raster plane for the C II 904 Å (top) and C III 1175 Å (bottom) multiplets. Note that the slit dimension is up and to the left and the raster dimension is down and to the left. The low counts to the extreme left correspond to the off-limb data. The low counts at the top left in the C II case and the bottom right in the C III case are due to un-exposed regions of the detector.

The observed SUMER spectral line fluxes (proportional to intensity) were analysed in the escape probability model described to obtain optical depths for all the spectral lines of C II and C III. The results of this analysis are shown in tables 2.1 $\rightarrow$ 2.5.

Table 2.1: Summary of data for the C III $2s2p\ ^3P_2 - 2p^2\ ^3P_2$ transition for each raster scan position. $\tau_{0,2-2}/\tau_{0,1-2} = 3.204$

Pos.(")	$\tau_{0,2-2}$	$\bar{g}\{\tau_{0,2-2}\}$	$\bar{\tau}_{0,2-2}$	$g\{\tau_{0,2-2}\}$
943.06	0.74	0.78	0.35	0.79
944.94	0.94	0.74	0.43	0.75
946.81	1.09	0.71	0.49	0.72
948.69	1.27	0.67	0.56	0.67
950.56	1.05	0.71	0.47	0.73
952.44	1.18	0.69	0.53	0.70
954.31	1.86	0.58	0.78	0.60
956.19	3.42	0.41	1.23	0.45
958.06	-	-	3.12	0.17
959.94	-	-	4.24	0.11
961.88	8.64	0.21	2.00	0.29
963.75	1.68	0.60	0.71	0.62
965.63	1.27	0.67	0.56	0.69
967.50	1.42	0.64	0.62	0.66
969.38	1.81	0.58	0.76	0.60
971.25	1.67	0.60	0.71	0.62
973.13	2.24	0.53	0.90	0.55
975.00	2.13	0.54	0.87	0.56

2.4 Atmosphere Modelling

Spectral intervals spanning the C II $2s^2p^2P$ – $2s2p^2\,^2S$ multiplet at $\sim$ 1036 Å and the C III $2s2p^3P$ – $2p^2\,^3P$ multiplet at $\sim$ 1175 Å are shown in figs 2.9a and 2.10a respectively. The multiplet components are labelled according to their J quantum numbers. Observed flux ratios for the C II I(3/2–1/2)/I(1/2–1/2) ratio and the C III I(2–2)/I(1–2) ratio are shown in figs 2.9b and 2.10b. As stated earlier, in both cases the lines

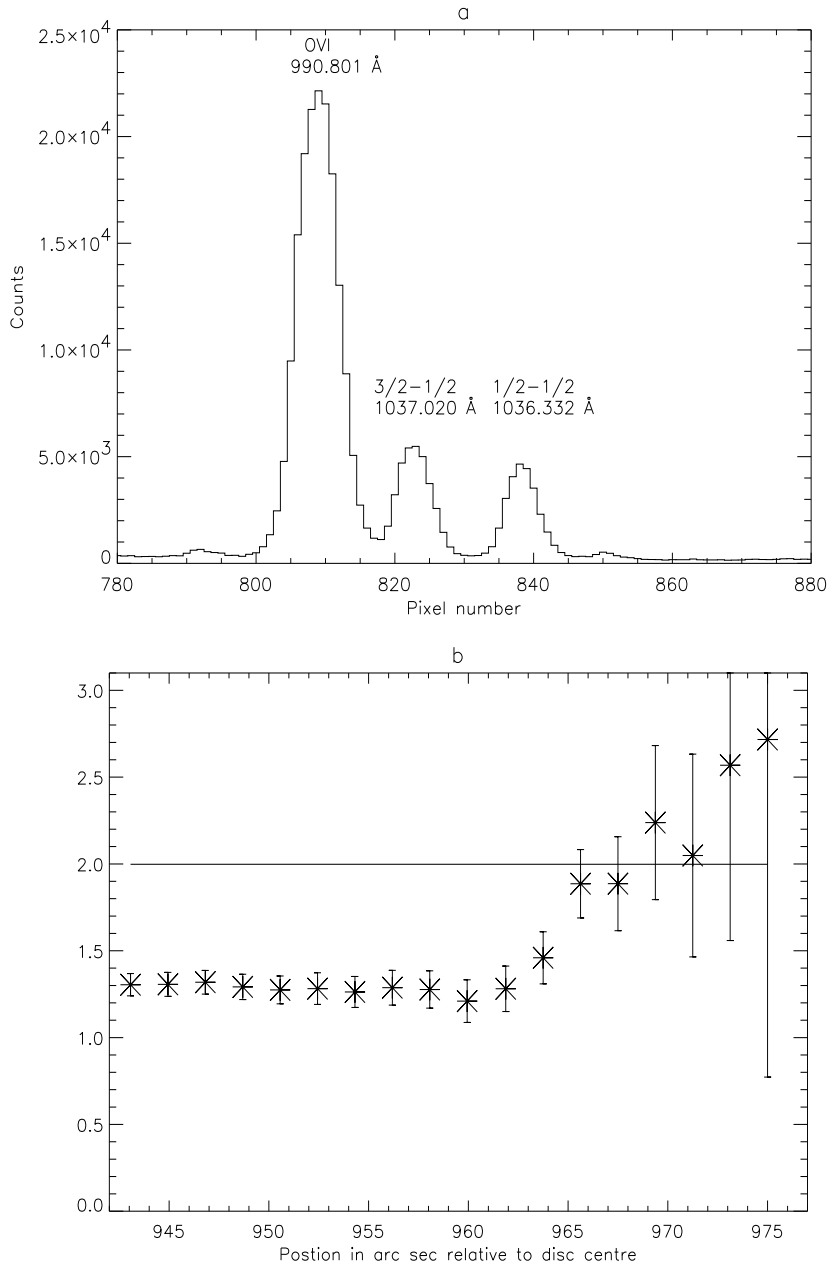

Figure 2.9: (a) Spectral interval spanning the C II $2s^2p^2P$ – $2s2p^2{}^2S$ (1036 Å) multiplet with component identification. The ordinate scale records the number of counts integrated along the line-of-sight and for each pixel along the wavelength scale measured in the 100 sec. of exposure time. (b) Branching line intensity ratios versus raster position in arc sec relative to the disk centre. The set of values correspond to the I(3/2-1/2)/I(1/2-1/2) ratio. The solid line shows the corresponding A-value ratio.

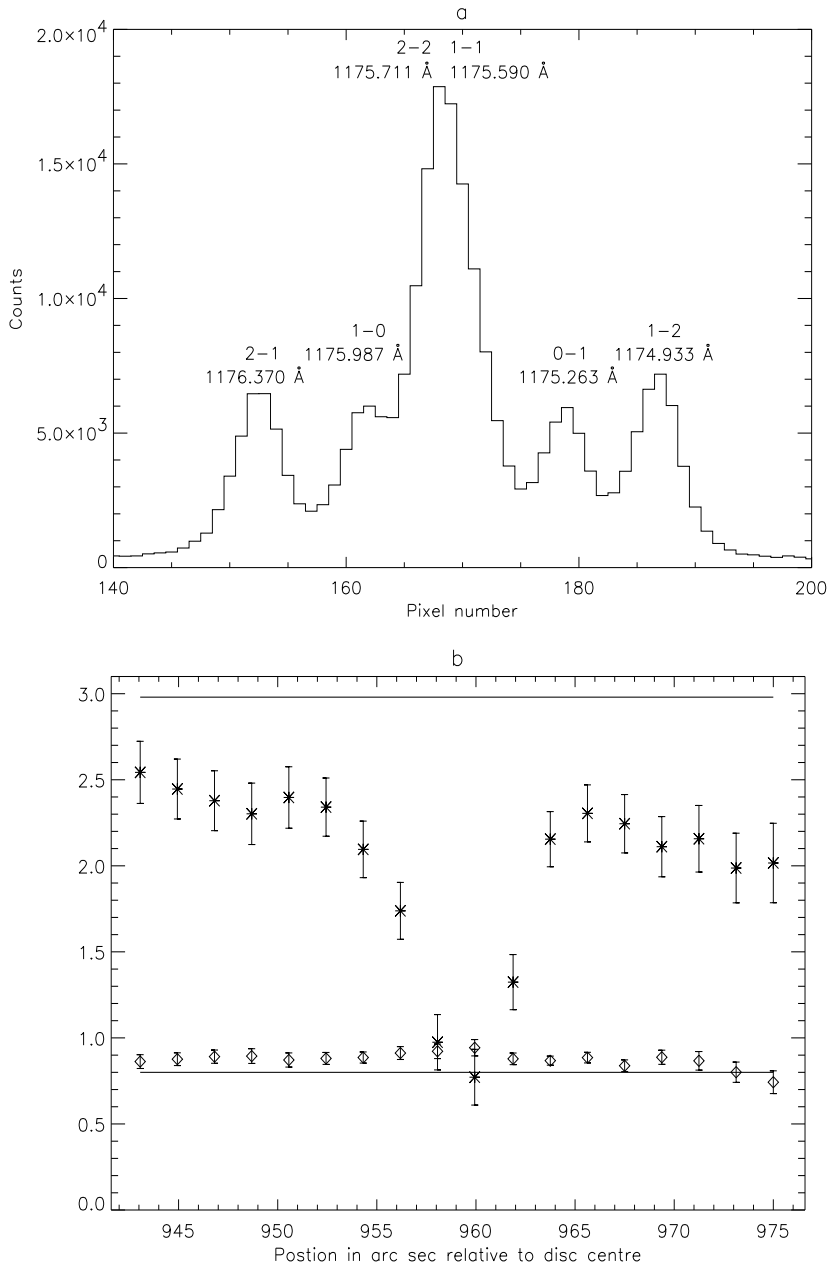

Figure 2.10: a) Spectral interval spanning the C III $2s2p^3P$ – $2p^2\,^3P$ (1175 Å) multiplet with component identification. Ordinate scale as in fig. 2.9a. (b) Branching line intensity ratios versus raster position in arc sec relative to the disk centre. The upper set of values ($*$'s) correspond to the I(2–2)/I(1–2) ratio and the lower set ($\diamond$'s) correspond to the I(0–1)/I(2–1). The solid lines show the corresponding A-value ratios.

Table 2.2: Summary of data for the C III $2s2p\ ^3P_0 - 2p^2\ ^3P_1$ transition for each raster scan position. $\tau_{0,0-1}/\tau_{0,2-1} = 0.779$. Since the optical depth ratio is fairly close to unity, the absolute optical depths inferred here are expected to have large associated errors and would be more reliably obtained from the 2–2 values shown in table 2.1.

Pos.(")	$\tau_{0,0-1}$	$\bar{g}\{\tau_{0,0-1}\}$	$\bar{\tau}_{0,0-1}$	$g\{\tau_{0,0-1}\}$
943.06	0.91	0.77	0.39	0.77
944.94	1.16	0.71	0.48	0.72
946.81	1.47	0.65	0.58	0.68
948.69	1.55	0.64	0.60	0.67
950.56	1.07	0.73	0.45	0.74
952.44	1.25	0.69	0.51	0.71
954.31	1.36	0.67	0.55	0.69
956.19	2.02	0.57	0.72	0.62
958.06	2.34	0.52	0.79	0.59
959.94	3.26	0.44	0.94	0.54
961.88	1.20	0.70	0.50	0.72
963.75	1.00	0.75	0.43	0.75
965.63	1.35	0.66	0.54	0.70
967.50	0.51	0.87	0.24	0.85
969.38	1.39	0.67	0.56	0.69
971.25	0.98	0.75	0.42	0.75
973.13	0.01	1.00	0.00	1.00
975.00	0.00	1.00	0.00	1.00

involved arise from common upper levels and so the ratios do not depend upon the population structure. Thus the ratios are only modified from their optically thin values (shown in each case by a solid horizontal line) due to the scattering of photons out of the line-of-sight. Variations in the ratios therefore reflect variations in optical depth which is, simplistically speaking, linearly dependent on the length of the line-of-sight and on the lower level population density (see eq. 2.16).

Consider first the C III ratio plot (fig. 2.10b). The optical depth ratio of the 0–1 component to the 2–1 component ($\tau_{0,0-1}/\tau_{0,2-1}$) is close to unity. Consequently the escape probability ratio of these two lines is also close to unity for all optical depths. It follows that the corresponding intensity ratio does not deviate significantly from

Table 2.3: Summary of data for the C II $2s^2 2p\ ^2P_{3/2} - 2s2p^2\ ^2S_{1/2}$ transition for each raster scan position. $\tau_{0,3/2-1/2}/\tau_{0,1/2-1/2} = 1.97$.

Pos.(")	$\tau_{0,3/2-1/2}$	$\bar{g}\{\tau_{0,3/2-1/2}\}$	$\bar{\tau}_{0,3/2-1/2}$	$g\{\tau_{0,3/2-1/2}\}$
943.06	5.30	0.31	1.47	0.39
944.94	5.25	0.31	1.46	0.39
946.81	4.95	0.32	1.42	0.40
948.69	5.70	0.29	1.51	0.38
950.56	6.23	0.27	1.56	0.37
952.44	6.00	0.28	1.54	0.37
954.31	6.70	0.26	1.60	0.36
956.19	5.80	0.29	1.52	0.38
958.06	6.20	0.27	1.56	0.37
959.94	10.2	0.18	1.80	0.32
961.88	6.00	0.28	1.54	0.37
963.75	2.82	0.46	1.03	0.50
965.63	0.36	0.88	0.17	0.89
967.50	0.36	0.88	0.17	0.89
969.38	-	-	-	-
971.25	-	-	-	-
973.13	-	-	-	-
975.00	-	-	-	-

the optically thin value on crossing the limb. However, the $\tau_{0,2-2}/\tau_{0,1-2}$ ratio is ~ 3 and so the intensity ratio I(2–2)/I(1–2) is opacity sensitive. On disk the emitting layer is only moderately thick and so the observed flux ratios are close to their optically thin value. As the limb is approached the ratios deviate markedly from their thin value due to the variation of optical depth with line-of-sight thickness, as discussed in sec. 2.3. This deviation is most pronounced at the position of the visible limb ($\sim$ 959.6 arc sec) where the line-of-sight doubles in length. The ratio continues to drop until the inner edge of the emitting layer is reached ($\sim$ 964 arc sec) whereafter it rises again toward the thin value. In a stratified atmosphere picture, this rise is due to the fall off of density with height above the solar surface. The ratios do not return to their optically thin value as might be expected but rather level off at a value similar to

Table 2.4: Summary of data for the C II $2s^2 2p\ ^2P_{3/2} - 2s2p^2\ ^2P_{1/2}$ transition for each raster scan position. $\tau_{0,3/2-1/2}/\tau_{0,1/2-1/2} = 0.507$. The opacity ratio is again fairly close to unity and the comments on table 2.2 apply.

Pos.(")	$\tau_{0,3/2-1/2}$	$\bar{g}\{\tau_{0,3/2-1/2}\}$	$\bar{\tau}_{0,3/2-1/2}$	$g\{\tau_{0,3/2-1/2}\}$
943.06	0.66	0.80	0.29	0.83
944.94	0.47	0.85	0.21	0.87
946.81	0.31	0.90	0.14	0.91
948.69	0.12	0.96	0.06	0.97
950.56	0.33	0.89	0.15	0.91
952.44	0.49	0.85	0.22	0.87
954.31	0.47	0.85	0.21	0.87
956.19	0.19	0.94	0.09	0.95
958.06	0.43	0.86	0.20	0.88
959.94	0.33	0.89	0.15	0.91
961.88	0.39	0.87	0.18	0.89
963.75	0.12	0.96	0.06	0.97
965.63	0.14	0.95	0.07	0.97
967.50	0.10	0.97	0.05	0.98
969.38	1.50	0.63	0.54	0.70
971.25	1.47	0.64	0.53	0.70
973.13	8.46	0.21	0.99	0.52
975.00	-	-	1.41	0.40

that on disk. A plot of observed flux of the C III $2s2p^3P_2 - 2p^2\,^3P_2$ line at 1175.711 Å versus position is shown in fig. 2.11. It is clear that at the heights above 967 arc sec where the ratios indicate that the lines are thick, the fluxes are very small and so it is possible that the observed signal is dominated by instrumentally scattered light – light that reflects off the interior of the telescope prior to passing through the entrance slit. Instrumentally scattered light originates from points on the solar disk and thus it would be reasonable to expect such light to imply opacities associated with the disk. This idea is supported by the fitted centroid positions of the C III 1175 Å multiplet components which are shown in fig. 2.12. The overlapped 2–2 and 1–1 components are awkward to fit, especially at the limb where the optical depths are greatest and thus the deviation due to opacity of line-shapes from Gaussian is most significant.

Table 2.5: Summary of data for the C II $2s^2 2p\ ^2P_{3/2} - 2s2p^2\ ^2P_{3/2}$ transition for each raster scan position. $\tau_{0,3/2-3/2}/\tau_{0,the1/2-3/2} = 5.05$.

Pos.(")	$\tau_{0,3/2-3/2}$	$\bar{g}\{\tau_{0,3/2-3/2}\}$	$\bar{\tau}_{0,3/2-3/2}$	$g\{\tau_{0,3/2-3/2}\}$
943.06	4.95	0.32	1.64	0.36
944.94	5.01	0.32	1.65	0.35
946.81	4.13	0.36	1.46	0.39
948.69	4.37	0.35	1.51	0.38
950.56	5.15	0.31	1.68	0.35
952.44	4.81	0.33	1.61	0.36
954.31	4.56	0.34	1.55	0.37
956.19	5.23	0.31	1.69	0.34
958.06	5.10	0.31	1.67	0.35
959.94	4.69	0.33	1.58	0.37
961.88	4.84	0.33	1.61	0.36
963.75	4.40	0.35	1.52	0.38
965.63	2.88	0.46	1.13	0.48
967.50	2.36	0.51	0.96	0.53
969.38	1.07	0.71	0.49	0.72
971.25	1.40	0.65	0.62	0.66
973.13	1.63	0.61	0.71	0.62
975.00	1.29	0.67	0.58	0.68

As such, a wavelength direction pixel shift vector was imposed, determined from the centroid positions of the well separated 2–1 and 1–2 multiplet components. It can be seen from fig. 2.12 that beyond the limb, at a height of around 967.50 arc sec, the centroids are shifted to the blue indicative of upflows along the line-of-sight of $\sim$ 20 km/s. The onset of this shift is beyond the visible limb (959.6 arc sec) and the inner edge of the C III emitting layer ($\sim$ 962 arc sec) and coincides with the point at which the model ratios (fig. 2.16b – see sec. 2.4.1) begin to deviate from the observed ones. If this is the case then the scattered light – which is a whole disk integrated effect – has a blue shift relative to the limb observations of $\sim$ 20 km/s. This is in contrast to observations of emission at TR temperatures which show that downflows with similar speeds are dominant on the disk (Athay and Holzer, 1982; Brekke et al.,

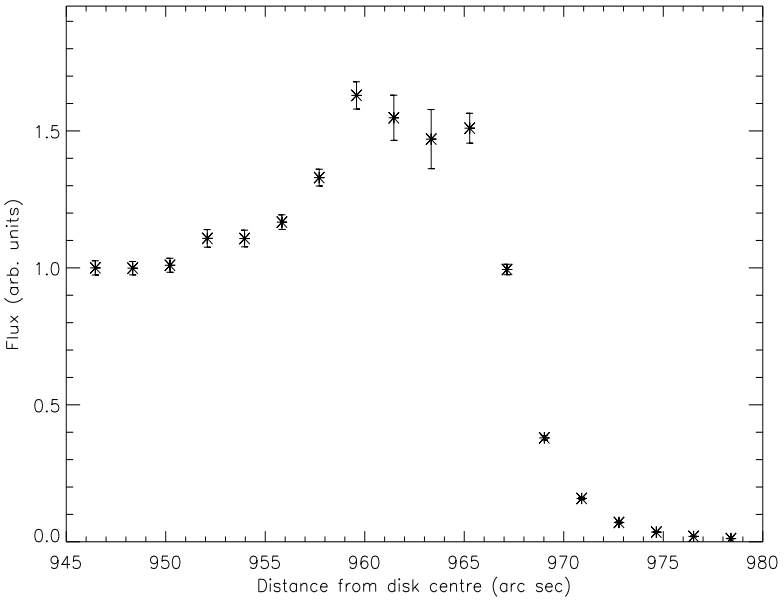

Figure 2.11: Integrated line fluxes for the C III $2s2p^3P_2$ – $2p^{2\,3}P_2$ line at 1175.711 Å. Ordinate scale as in fig. 2.9a.

1997; Chae et al., 1998).

An alternative explanation follows if the signals at such heights are in fact true. At heights above 967 arc sec the fluxes imply smaller column densities than those on disk since the intensity is proportional to the upper level column density (see eq. 2.15). However, the ratios suggest that the column densities at such heights are comparable with those on disk, since the ratios follow the optical depth variation which is determined by that of the lower level column density (see eq. 2.16). These seemingly contradictory implications are reconciled if the *filling factor* changes with height. That is, if there are structures above 964 arc sec which are unresolved in observations. In order to settle this issue the expected contribution of scattered light must be carefully considered (see chap 6).

The C II ratios (fig. 2.9b) differ from those of C III. On disk their value is markedly different to the optically thin value and on approaching and crossing the limb the ratio changes little. The reason for this is that the C II line optical depths are greater than 1

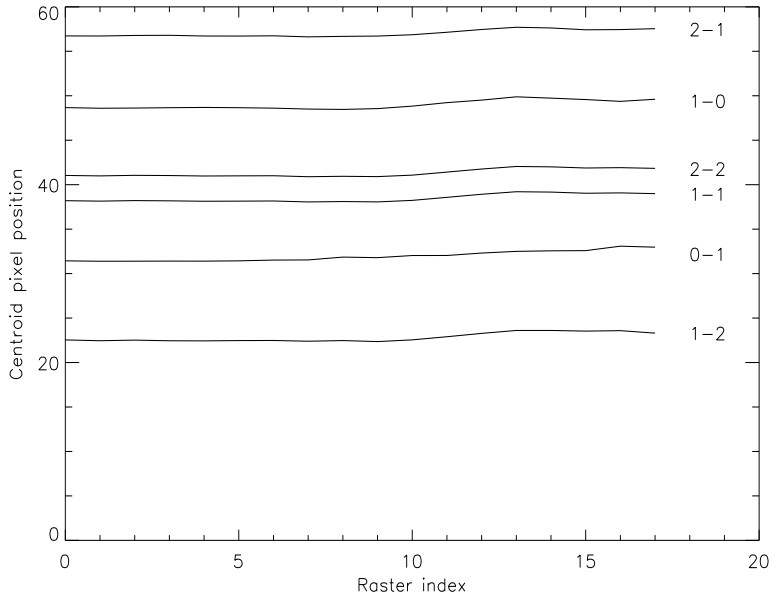

Figure 2.12: Centroid pixel positions for the C III $2s2p^3P - 2p^2\,^3P$ multiplet components.

prior to the limb and so light emitted at the inner edge of the layer does not have a significant probability of escaping the layer along the line-of-sight. In other words, the layer can only partially be 'seen'. Thus as the layer thickens with height the visible portion does not change and so the thickening of the line-of-sight makes little difference. Upon crossing the inner edge of the emitting layer (at $\sim$ 961 arc sec), as in the C III case, the ratio rises toward the optically thin value. No comment can be made here on the issue of scattered light due to the large error bars.

2.4.1 Modelling flux ratios on disk

In this chapter stratified atmosphere models are considered. Consequently two distinct regimes exist, one where the opacity variation is principally determined by the geometric extension of the line-of-sight and another where the density fall off with height is determinate. Two models are constructed: the first describes the former

regime and thus deals purely with the observations up to the inner edge of the emitting layer situated a few arc sec above the limb and is termed the *inner* model; the second describes the latter regime and thus regions above the emitting layer edge and is termed the *outer* model.

Following Doyle & McWhirter (1980 – hereafter referred to as DM), the inner model is made up of a spherical shell of constant density. In this picture the optical depth is proportional to $1/cos\theta$ where θ is 0 at disk centre and $\pi/2$ at the inner edge of the emitting layer. Specifically $\tau_0 = \tau_{0,dc} \times \delta/cos\theta$ where $\tau_{0,dc}$ is the optical depth at disk centre. $\delta = 1$ before the visible limb and 2 beyond it, and accounts for the doubling in length of the line-of-sight at the limb since the emitting layer on the far side of the sun may be viewed beyond this point.

Using this expression for optical depth, models of the flux ratios for the C II and C III ratios shown in figs 2.9b and 2.10b, were calculated using equation 2.22. The fit to the C III ratios, shown in fig. 2.13(a), reveals a pointing error of $\sim$ 3.4 arc sec. This is consistent with the positional error in SUMER which is $\sim$ 10 arc sec. The fit to the C II fit is shown in fig. 2.14. Also shown are the results obtained using $g\{\tau_0\}$ rather than $\bar{g}\{\tau_0\}$. The former quantity was used by DM and its use is discussed in sec. 2.6.

2.4.2 Modelling flux ratios beyond the limb

It is expected that beyond the limb the opacity variation will be determined by the fall off of density. The model thus far is of a static stratified atmosphere. In such an atmosphere there is both energy and pressure balance and through consideration of these, the temperature and electron density versus height may be determined. Therefore emission following the $G(T_e)$ function[1] with a TR layer as described above is considered. T_e and N_e follow the VAL quiet sun atmosphere model. The optical depth for a given height, h, above the surface, is then

[1] The $G(T_e)$ function describes the emission from a particular transition as a function of electron temperature.

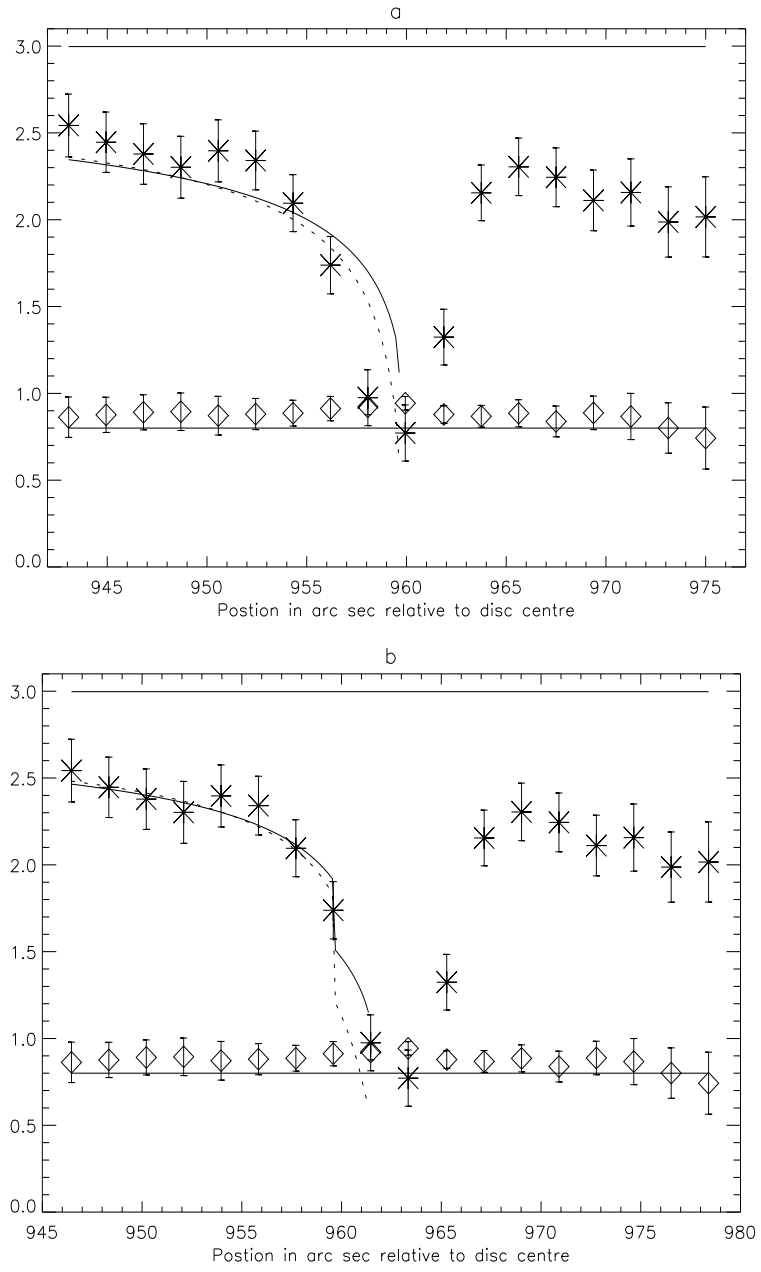

Figure 2.13: Observed branching line intensity ratios versus raster position in arc sec relative to the disk centre for the C III $2s2p\ ^3P$ - $2p^2\ ^3P$ (1175 Å) multiplet component ratios I(2–2)/I(1–2) and I(0–1)/I(2–1) as in fig. 2.10b. Inner model values using $\bar{g}\{\tau_0\}$ (solid line) and $g\{\tau_0\}$ (dashed line) are overlaid. The x-axis uses the position for the visible limb (a) from the telemetry and (b) from an optimised fit of the model to the observed I(2–2)/I(1–2) ratio values.

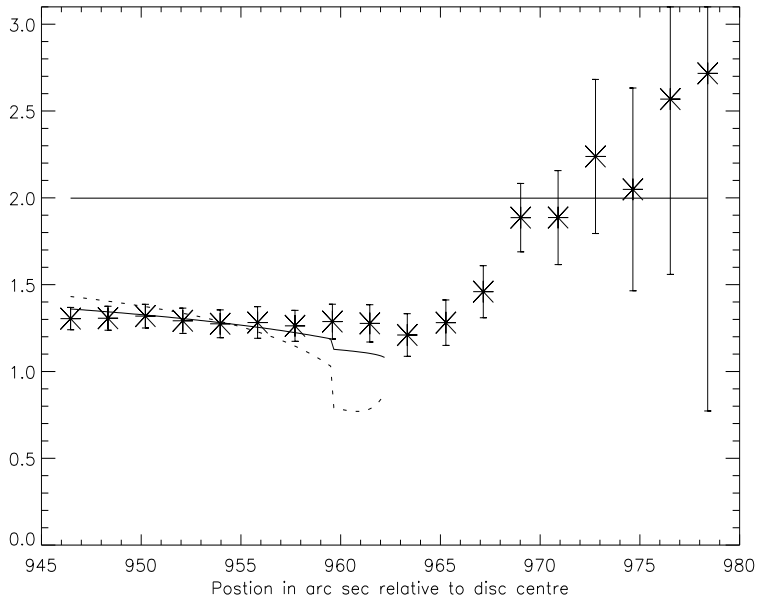

Figure 2.14: (a) Calculated intensity ratios for the C II $2s^2p^2P$ – $2s2p^2{}^2S$ (1036 Å) multiplet component ratios I(3/2–1/2)/I(1/2–1/2) versus raster position in arc sec relative to the disc centre compared with the observed ratios. Solid and dashed lines are as in fig. 2.13.

$$\begin{aligned} \tau(h) &= a\int_{l.o.s.} N_l(h)ds \\ &= b\int_{l.o.s.} N_e(h)\bar{G}_{u\to l}(h)ds \end{aligned} \tag{2.40}$$

where $\bar{G}_{u\to l}(h) \equiv G_{u\to l}(T_e(h))$, a and b are constants and *l.o.s.* stands for *line-of-sight*. Using this and eq. 2.22, the ratio variations for C II and C III may be modelled. The results of this model can be seen in figs 2.15a and b which clearly demonstrate that the model fails completely. The results of the model follow intuitively from consideration of fig. 1.7 which predicts a very narrow TR of only a few hundred kilometres width. Thus the ratios, in such a picture, move from thick to thin in less that 1 arc sec. This failure of the VAL model is not surprising when one considers images such as figs 2.8a and b which demonstrate that the TR is far from homogeneous.

The failure here does not invalidate the VAL model as such, but, rather, implies

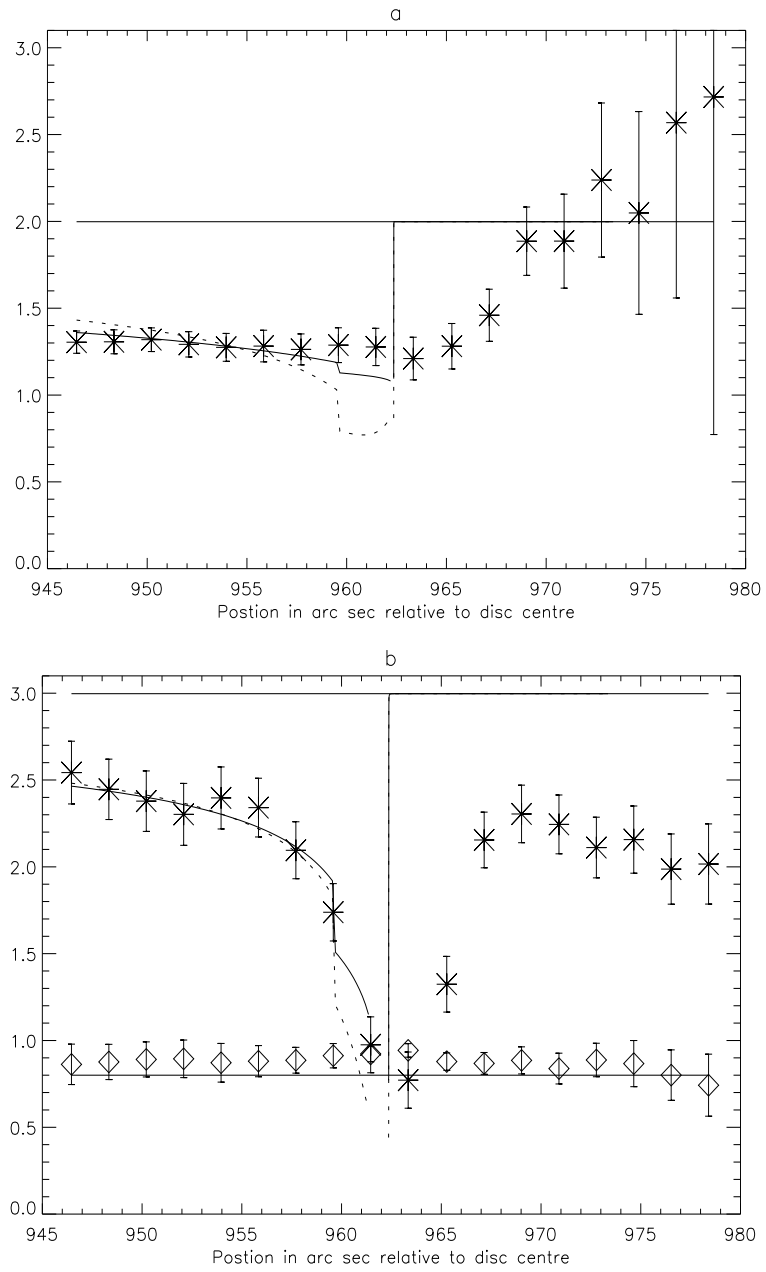

Figure 2.15: Observed branching line intensity ratios versus raster position in arc sec relative to the disk centre for the (a) C II I(3/2–1/2)/I(1/2–1/2) ratio as in fig. 2.9 and (b) C III I(2–2)/I(1–2) ratio as in figs 2.10 and 2.13. The results of the VAL based model are overlaid. The solid line curves show the $\bar{g}\{\tau_0\}$ based results and the dashed line shows the $g\{\tau_0\}$ based results.

that the assumption of stratification is ineffective beyond the limb. It is useful to take account of the extension of the TR into the corona due to structures such as spicules within retaining the stratified atmosphere picture.

Although in a stratified atmosphere the variation of opacity above the limb is not principally determined by the geometric variation in the line-of-sight, its length features significantly in the determination of the optical depth by way of the variation with height of what is called here the *line-of-sight filling factor*. The latter is the number of structures intersected by the line-of-sight. It is possible to handle this within a stratified model via an appropriate choice of density profile. Two further models are therefore considered: firstly, following the approach of Kastner and Bhatia (1992), an emission layer of constant (adjustable) thickness and density is envisaged. This model is a simple parametric adjustment which does not attempt to capture anything of the nature of the spicule structures. Nevertheless, it is useful to consider such a model in order to put the success of any other simple model in context. Secondly, a layer of density which falls off exponentially with adjustable scale height is envisaged. That is, the density falls off as $Be^{-x/H}$ for some constants H and B. This is motivated by the findings of Mariska et al. (1978) who considered models where the dominant contribution to the EUV signal was due to TR sheaths around isolated cylindrical Hα spicules. They showed that 'above the emission peak the amount of emitting material in the line-of-sight for any spectral line must decrease exponentially with height with a scale height that depends on temperature' . This is identical, in essence if not in approach, to the model of Withbroe & Mariska (1976). In summary the models considered are

1. Thin TR based on the VAL atmosphere model
2. Spherical shell of constant density
3. Layer of density that falls off exponentially with height

The results of these models are shown in figs 2.16a and b from which it is clear that both models 2 and 3 are much more effective than the VAL model. Both capture qualitatively the ratio variation as it increases toward the optically thin limit, with

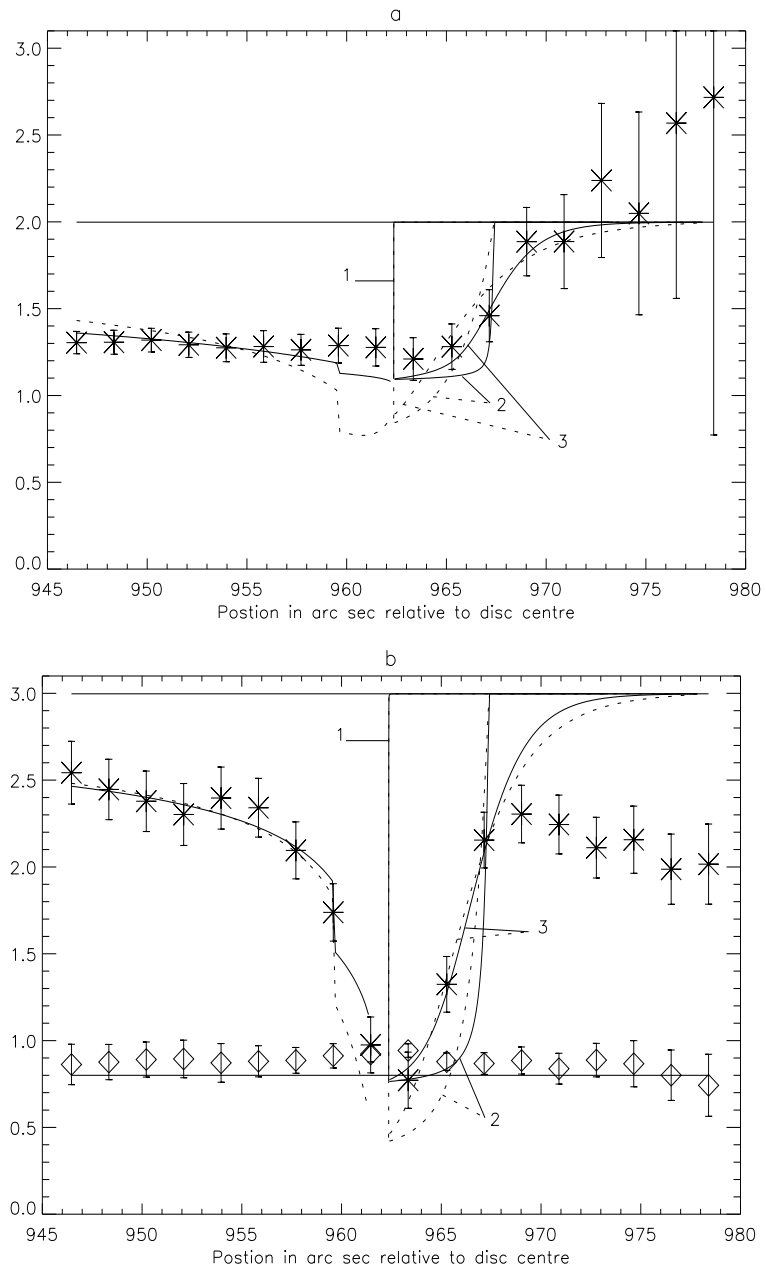

Figure 2.16: Observed branching line intensity ratios versus raster position in arc sec relative to the disk centre for the (a) C II I(3/2–1/2)/I(1/2–1/2) ratio as in fig. 2.15a and (b) C III I(2–2)/I(1–2) ratio as in fig. 2.15b. The results of all three models are overlaid. The solid line curves show the $\bar{g}\{\tau_0\}$ based results and the dashed line shows the $g\{\tau_0\}$ based results. The off-limb models are numbered corresponding to the specification in sec. 2.4.2. The best fit in each case is achieved with the exponential density model and using $\bar{g}\{\tau_0\}$.

the latter model being the most effective in this regard. Both verify the intuitive expectation that the ratio should return to the optically thin value at large heights.

The inner model was optimised for both the optical depth at disk centre and the position of the visible limb. The outer models were optimised for the layer thickness in the constant density case and scale height in the exponential case. The models begin at the inner edge of the emitting layer which is estimated from the height corresponding to the temperature of the peak of the $G(T_e)$ function, obtained from the VAL model. The optical depth at this height is chosen to be consistent with the inner model. The optimised disk centre optical depths were 0.643 for the C II 3/2–1/2 line and 0.156 for the C III 2–2 line respectively. The optimised thickness in model 2 was 5 arc sec for both C II and C III and the scale heights obtained for model 3 were 1.3 arc sec and 1.4 arc sec respectively, equivalent to 942 km and 1015 km. These are smaller than, but comparable to, those suggested by Mariska et al. (1978) ($\sim$ 1.5 arc sec) and decrease with decreasing temperature of line formation. These deduced disk centre optical depths allow the spectral lines of C II and C III to be classified according to their optical thickness at disk centre and at the limb. Since it is the disk centre (perpendicular) optical depth that is used within $\bar{\bar{g}}\{\tau_0/2\}$, this classification includes the effect of opacity upon the population structure.

It is interesting to note that the optimised disk centre optical depth for the C III 2–2 line using $g\{\tau_0\}$ is 0.069 which compares with a value of 0.068 obtained by DM using the same method applied to *Skylab* data.

2.5 Spectral line classification

It is useful to classify spectral lines according to the influence of opacity on both emergent fluxes and on level populations. Such a classification will in general be dependent upon position and time but in the first instance it is useful to consider the quiet sun at disk centre as representative. This classification is pertinent to *differential emission measure* (DEM) studies which allow the *amount of plasma* as a function of electron temperature to be deduced directly from measurements of spectral intensities (Craig & Brown, 1973). Such studies assume optically thin conditions and so using

the escape probability tools described, opacity modified spectral lines may be rejected or intensity adjusted for use in DEM studies.

The modification to emergent fluxes is line-of-sight dependent and so the classification is made according to modifications both at disk centre and at the limb. In contrast, the effects on the population structure are specified by disk centre (perpendicular) optical depths only. The upper level population density of a spectral line may be modified *directly* due to absorption in that same line or *indirectly* due to absorption in another line. As such the spectral lines of an ion may grouped into the following categories:

1. optically thin (t) – emergent fluxes unmodified on-disk and at the limb; populations unmodified

2. modified thin (mt) – emergent fluxes unmodified on-disk and at the limb; populations indirectly modified

3. weakly thin (wt) – emergent fluxes unmodified on-disk but modified at the limb; populations unmodified

4. modified weakly thin (mwt) – emergent fluxes unmodified on-disk but modified at the limb; populations indirectly modified

5. modified (m) – emergent fluxes modified on-disk and at the limb; populations modified

To do this, for each line two numbers are required: the optical depth at disk centre, $\tau_{0,dc}$, and the optical depth at the limb, $\tau_{0,l}$. These may be deduced for every transition of an ion from just two values, as described in sec. 2.2.1. Consequently only two numbers are required from which a classification may be obtained for every line.

This was done for lines of C II and C III using the optical depths extracted from the OPAC data. A 10% alteration to the Einstein A-coefficient was chosen as the modification criterion. Since $\bar{g}\{\tau_0\} < 0.9$ for $\tau_0 > 0.307$ and $\bar{\bar{g}}\{\tau_0/2\} < 0.9$ for $\tau_0 > 0.072$ the classification becomes

1. optically thin (t) – $\tau_0 < 0.307$ at the limb, populations unmodified

2. modified thin (mt) – $\tau_0 < 0.307$ at the limb, populations indirectly modified

3. weakly thin (wt) – $\tau_0 < 0.072$ on disk, $\tau_0 > 0.307$ at the limb, populations unmodified

4. modified weakly thin (mwt) – $\tau_0 < 0.072$ on disk, $\tau_0 > 0.307$ at the limb, populations indirectly modified

5. modified (m) – $\tau_0 > 0.072$ on disk

Direct population modification is evident immediately from the optical depth – $\tau_0 > 0.072$ on disk. Indirect population modification, however, is only evident from an optically thick population calculation. In this case a 10% modification in the population was taken as the criterion for modification.

The results for some of the lines of C II and C III are shown in tables 2.6 and 2.7.

2.6 The use of $g\{\tau_0\}$ versus $\bar{g}\{\tau_0\}$

Also featuring in figs 2.16a and b are the results based on $g\{\tau_0\}$ rather than $\bar{g}\{\tau_0\}$. To see how they compare, recall eq. 2.7 and use the intermediate value theorem so that

$$\bar{I} \;=\; (1/4\pi)A_{u\rightarrow l}N_u g\{\bar{\tau}_0\}L \tag{2.41}$$

where $\bar{\tau}_0$ is some value of τ_0 such that $0 \leq \bar{\tau}_0 < \tau_0$. This approach mimics that of McWhirter (1965) in the consideration of the absorption factor, described in sec. 2.2. From this it is evident that the DM analysis requires that $\bar{\tau}_0$ replaces $\tau_0$and $g\{\bar{\tau}_0\}$ replaces $\bar{g}\{\tau_0\}$. However, a question arises as to the definition of $\bar{\tau}_0$. It can be written that $\bar{\tau}_0 = \Delta(\tau_0)\tau_0$. For $\tau_0 < 1$ it can be seen from fig. 2.2 that $\Delta \approx 1/2$ which is to say that the *mean* probability of escape from a layer of optical depth less than unity is equivalent to the probability of escape from the centre of the layer. However, it can also be seen from Fig. 2.2 that for optical depths larger than unity, $\Delta < 1/2$ as

Table 2.6: Characterisation and classification of some spectral lines of C II at disk centre.

Line	$\lambda(\AA)$	f	τ_0	$\bar{\bar{g}}(\tau_0/2)$	$\bar{g}(\tau_0)$	Class
$2s^2 2p\ ^2P - 2s2p^2\ ^2D$						
3/2-5/2	1335.709	0.115	0.628	0.638	0.812	m
1/2-3/2	1334.524	0.128	0.353	0.732	0.887	m
3/2-3/2	1335.665	0.027	0.147	0.842	0.950	m
$2s^2 2p\ ^2P - 2s2p^2\ ^2S$						
3/2-1/2	1037.012	0.129	0.643	0.634	0.808	m
1/2-1/2	1036.332	0.131	0.330	0.742	0.893	m
$2s^2 2p\ ^2P - 2s2p^2\ ^2P$						
3/2-3/2	904.143	0.405	1.760	0.433	0.590	m
1/2-1/2	903.958	0.331	0.727	0.611	0.787	m
3/2-1/2	904.481	0.0798	0.347	0.734	0.888	m
1/2-3/2	903.620	0.163	0.358	0.730	0.885	m
$2s^2 2p\ ^2P - 2s^2 3s\ ^2S$						
3/2-1/2	858.560	0.00615	0.0254	0.956	0.991	mwt
1/2-1/2	858.089	0.00404	0.00843	0.982	0.997	t
$2s^2 2p\ ^2P - 2s^2 3d\ ^2D$						
3/2-5/2	687.346	0.282	0.932	0.565	0.740	m
1/2-3/2	687.051	0.270	0.451	0.694	0.859	m
3/2-3/2	687.353	0.025	0.0826	0.893	0.972	m

Table 2.7: Characterisation and classification of some spectral lines of C III at disk centre.

Line	$\lambda(\AA)$	f	τ_0	$\bar{\bar{g}}\{\tau_0/2\}$	$\bar{g}\{\tau_0\}$	Class
$2s2p\ ^3P - 2p^2\ ^3P$						
2-2	1175.711	0.221	0.156	0.836	0.947	m
1-1	1175.590	0.0713	0.0286	0.9521	0.990	mwt
2-1	1176.370	0.0715	0.0505	0.925	0.983	mwt
1-0	1175.987	0.0913	0.0366	0.942	0.987	wt
1-2	1174.933	0.1176	0.0471	0.929	0.984	mwt
0-1	1175.263	0.2792	0.0393	0.938	0.987	mwt
$2s2p\ ^3P - 2s3s\ ^3S$						
2-1	538.312	0.031	0.0100	0.979	0.997	wt
1-1	538.149	0.031	0.00569	0.987	0.998	t
0-1	538.075	0.031	0.00200	0.995	1.000	t
$2s2p\ ^3P - 2s3d\ ^3D$						
2-3	459.627	0.434	0.120	0.862	0.959	m
1-2	459.514	0.394	0.0617	0.914	0.979	wt
0-1	459.466	0.525	0.0289	0.951	0.990	wt
2-2	459.633	0.063	0.0174	0.968	0.994	wt
1-1	459.516	0.100	0.0157	0.970	0.995	wt
2-1	459.635	0.0042	0.00116	0.997	1.000	wt
$2s^2\ ^1S - 2s2p\ ^1P$						
0-1	977.020	0.746	0.665	0.628	0.802	m
$2s^2\ ^1S - 2s3p\ ^1P$						
0-1	386.203	0.220	0.0775	0.898	0.973	m
$2s^2\ ^1S - 2s4p\ ^1P$						
0-1	310.170	0.016	0.00453	0.989	0.999	t

expected since for layers of optical depth greater than 1 not all of the layer is 'seen'. The implication for the optical depth deduction from this is that

$$\frac{\bar{\tau}_{0,l_1-u}}{\bar{\tau}_{0,l_2-u}} = \frac{\tau_{0,l_1-u}}{\tau_{0,l_2-u}} \frac{\Delta(\tau_{0,l_1-u})}{\Delta(\tau_{0,l_2-u})} \neq constant \tag{2.42}$$

and the use of $g\{\tau_0\}$ instead of $\bar{g}\{\tau_0\}$ is inappropriate for optical depths greater than 1.

2.7 Concluding remarks

Opacity presents a sizeable problem in modelling and understanding spectral emission from optically thick plasmas. In principle the problem demands the full solution of the coupled non-linear sets of equations of radiative transfer and statistical balance (eqs 2.1 and 2.2). The escape probability quantities, $\bar{g}\{\tau_0\}$ (eq. 2.17) and $\bar{\bar{g}}\{\tau_0/2\}$ (eq. 2.39) – both purely functions of single optical depths – provide a simple route to linearising and decoupling the equations based on a number of assumptions. These assumptions are that the density is constant in space and that the source function (j_ν/κ_ν) is constant with respect to both space and frequency. Implicit within the latter assumption is that spectral line profiles are Gaussian, that frequency redistribution is complete and there is no line blending. The validity of $\bar{\bar{g}}\{\tau_0/2\}$ also requires the plasma geometry to be that of a semi-infinite plane parallel slab. The simplicity of this approach allows for the deduction of spectral line optical depths directly from observations of branching line ratios and the extrapolation to all other lines of the ion in question. In addition, when coupled with simple atmosphere models it is possible to extract plasma parameters such as density scale heights and disk centre optical depths. The latter are required to assess the influence of opacity upon the population structure and thus lines have been classified according to line-of-sight attenuation and the modification to the population densities of the levels from which they stem.

It is clear that the escape probability techniques, coupled with the exponential density model, are effective in modelling the observed branching ratio variations in the lines of both C II and C III. However, consideration of the observed fluxes of the C III $2s2p^3P_2$ – $2p^{2\,3}P_2$ line at 1175.711 Å paints a different picture. These are shown in fig. 2.17 with the predicted fluxes for the exponential density model overlaid. The

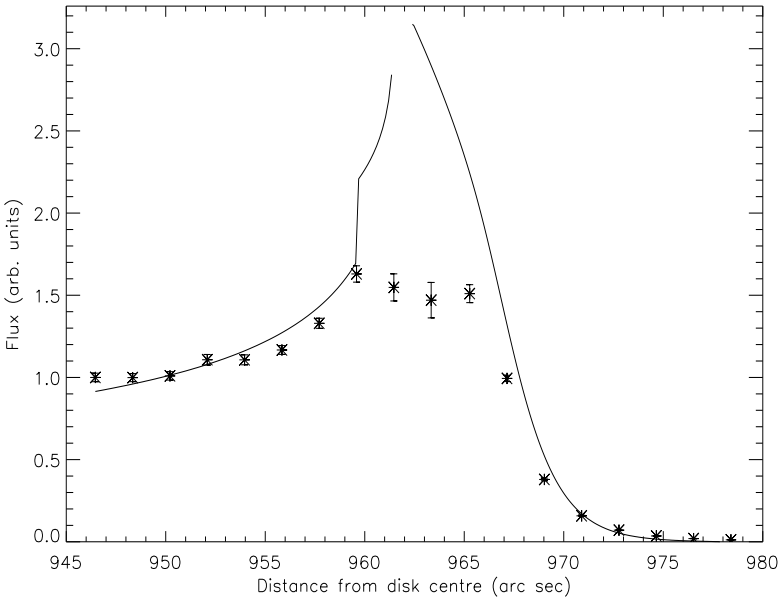

Figure 2.17: Observed fluxes for the C III $2s2p^3P_2$ – $2p^2\,^3P_2$ line (1175.711 Å) line with model fluxes for the exponential density model (model 3) overlaid. The latter were calculated via eq. 2.43 and were scaled to match the observed points at 950.212 arc sec.

model fluxes were calculated using

$$I \sim \tau_0 \bar{g}\{\tau_0\} \tag{2.43}$$

Eq. 2.43 follows immediately from eq. 2.15 in the constant density case since $(N_u \Delta x)/\tau_0$ = *const*. It will be shown in chapter 3 that this also holds for the variable density case. It can be seen from fig. 2.17 that the model deviates markedly from the observed fluxes at the limb. This implies an overestimate in column density in the vicinity of the limb whereas fit to the ratios (fig. 2.16b) suggest that the model column densities are accurate in this region. In contrast, the fit to the fluxes at heights above $\sim$ 970 arc sec is good whereas the fit to the ratios at these heights implies again an overestimation of column density.

Evidently there is a breakdown in the assumptions mentioned above in these regions. This can also be seen in table 2.1 where there are no optical depths extracted at heights 958.06 and 959.94 arc sec.

The good comparison to the ratios and fluxes on disk and in regions beyond the limb inspires confidence in the techniques but the real implications of making the assumptions listed above are unclear and consequently such techniques have so far only been considered as a useful approximation. In the subsequent chapters each of the assumptions listed will be considered and the discrepancies in the model will be addressed.

Chapter 3

The extended escape probability approach: the effect of a variable source function

Escape probability techniques for modelling and interpreting spectral emission from optically thick plasmas are potentially very useful. If they can be shown to be valid for a particular set of circumstances then the equations of radiative transfer and statistical balance are naturally linearised and decoupled. This comparative simplicity that escape probability methods introduce is desirable if they are to be used for studying such complex plasmas as those in the chromosphere and TR where there is much detailed structure and flow.

It is clear, however, that the expressions and methods presented thus far are insufficient to completely describe the SOHO-SUMER limb observations discussed in sec 2.3 and 2.4. When coupled with simple atmosphere models the line-of-sight averaged escape probability ($\bar{g}\{\tau_0\}$) is effective in modelling the opacity sensitive C II and C III branching ratios but is ineffective in regard to the observed fluxes. Departures of modelled from observed values occurred at and beyond the limb. These discrepancies must be due to the assumptions within the escape probability expressions and/or the atmosphere model. These assumptions relate to

1. variation of the source function

2. atmospheric structure

3. instrumental effects

In order to develop the escape probability methods it is important to consider each of the underlying assumptions to detect sources of error and to determine regimes of validity. Item 1 above incorporates variations of the source function with respect to both space and frequency due to absorption, scattering, line blending and flow. In this chapter, the variation of the source function with respect to space only is considered. In the subsequent chapters the frequency dependence of the source function will be addressed as well as items 2 and 3 above.

3.1 The source function

The source function, $S_\nu(\mathbf{x})$, is the ratio at $\mathbf{x}$ of the emissivity (emission coefficient) to the opacity (absorption coefficient) and is therefore given by

$$S_\nu(\mathbf{x}) = \frac{j_\nu(\mathbf{x})}{\kappa_\nu(\mathbf{x})} \tag{3.1}$$

$$= \frac{\omega_l}{\omega_u}\frac{2\nu^2}{c^2}\frac{\phi_e(\nu)}{\phi_a(\nu)}\frac{N_u(\mathbf{x})}{N_l(\mathbf{x})} \tag{3.2}$$

The variation of $S_\nu(\mathbf{x})$ in space follows that of $N_u(\mathbf{x})/N_l(\mathbf{x})$. In optically thin conditions this ratio is dependent on electron temperature and density but in thick conditions it is also influenced by opacity since photo-absorption will generally enhance N_u and deplete N_l.

Following the implications of fig. 2.15, the VAL atmosphere is not considered to be an appropriate model in regard to the C II and C III emission. However, envisaged here are C II and C III emission layers that comprise of TR sheaths around spicule-like structures and the VAL atmosphere model is adopted to represent each sheath. In optically thin conditions, the emission in a line versus temperature is described by the $G(T_e)$ function (see sec. 2.4.2). $G(T_e)$ functions versus T_e are shown in fig. 3.1 for the C II $2s^2 2p\,^2P_{3/2} - 2s2p^2\,^2P_{3/2}$ line at 904.143 Å and the C III $2s2p^3P_2$ - $2p^2\,^3P_2$ line at 1175.711 Å. The temperature range where these functions

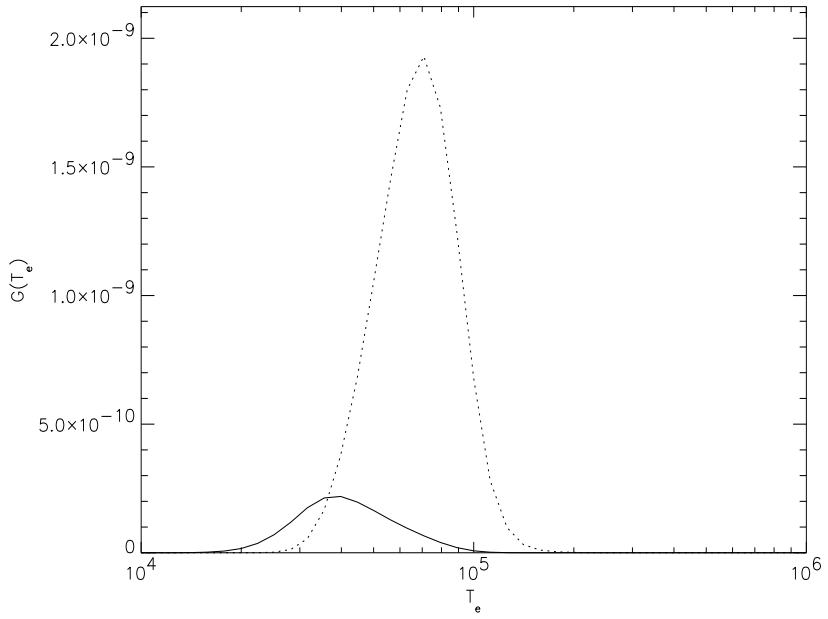

Figure 3.1: $G(T_e)$ functions for the C II $2s^2 2p^2\,{}^1P_{3/2} - 2s2p^2\,{}^2P_{3/2}$ line at 904.143 Å (solid line) and the C III $2s2p^3\,{}^2P_2$ - $2p^2\,{}^3P_2$ line at 1175.711 Å (dotted line).

are non-negligible corresponds to a very narrow region in the VAL model and thus the sheaths predicted by this model are very thin. However, the electron density also varies rapidly over such regions and so even though the spatial extent of each sheath is small, the variation of electron density within them is significant. This is illustrated in figs 3.2a and b which show $G(T_e(N_e)) \times N_e$ versus N_e for both C II and C III. These functions are related to the *optically thin contribution functions* and are indicative of the degree of spectral emission as a function of electron density. It is evident from these that the electron density varies significantly over the region of line formation. Figs 3.3a and b show optically thin population density ratios versus electron density for C II $2s2p^2\,{}^2P_{3/2}/2s^2 2p^2\,{}^1P_{3/2}$ and C III $2p^2\,{}^3P_2/2s2p^3\,{}^3P_2$ with the $G(T_e(N_e)) \times N_e$ functions of figs 3.2a and b overlaid. From these it is clear that the ratios (and thus also the source function in each case) vary by several orders of magnitude over the region of line formation.

Consider a point in the emitting layer for either C II and C III and consider a

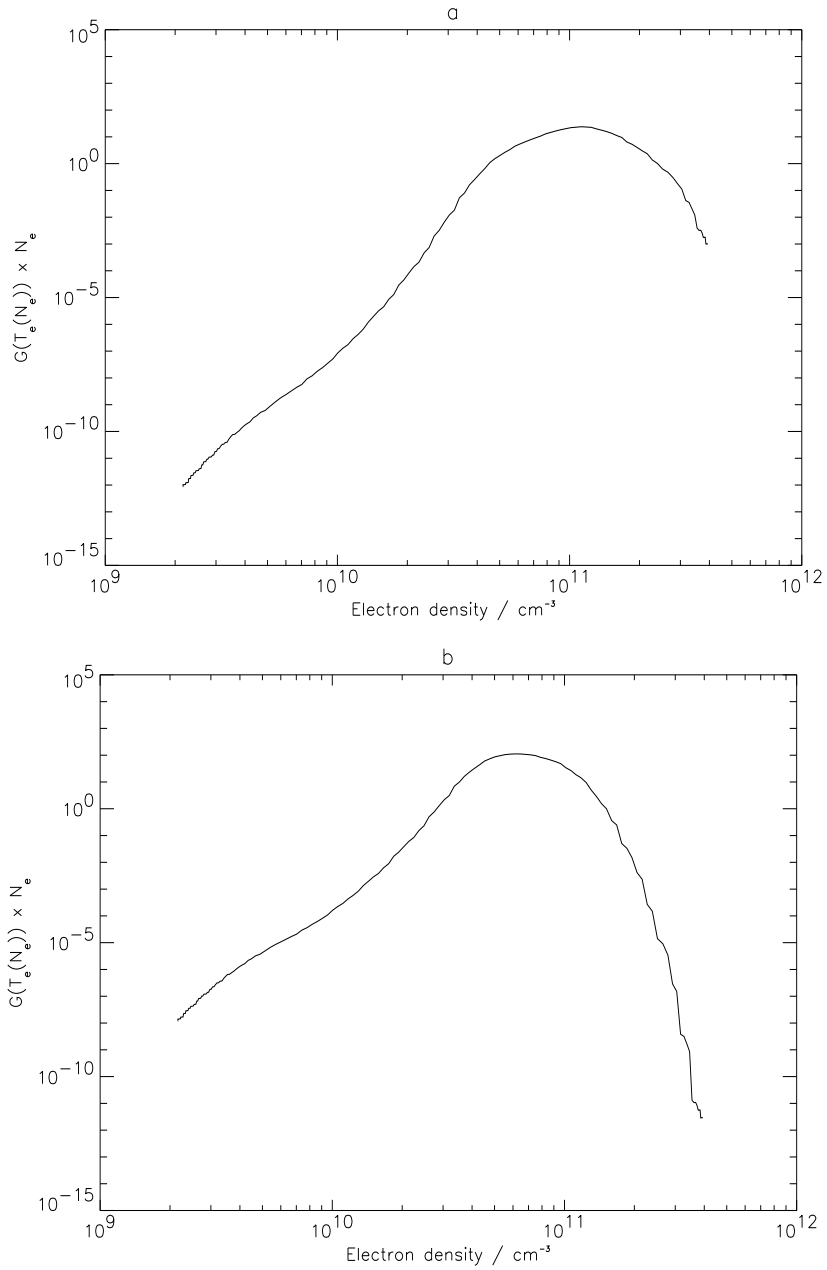

Figure 3.2: $G(T_e(N_e)) \times N_e$ versus N_e on a log-log scale for (a) the C II $2s^2 2p\,^2P_{3/2} - 2s2p^2\,^2P_{3/2}$ line at 904.143 Å and (b) the C III $2s2p^3P_2$ - $2p^2\,^3P_2$ line at 1175.711 Å. $T_e(N_e)$ follows from the VAL atmosphere model. These functions are related to the optically thin contribution functions.

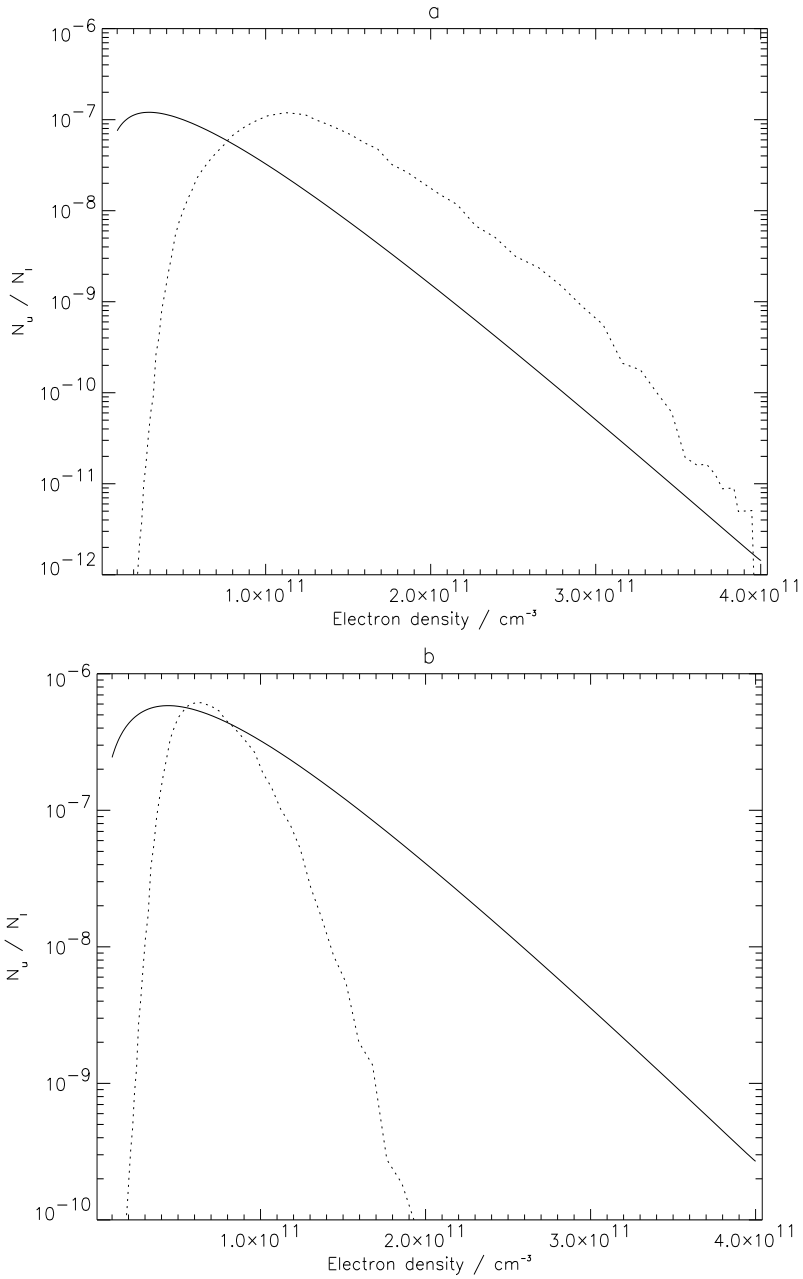

Figure 3.3: Optically thin population density ratios versus electron density on a log-log scale for (a) C II $2s2p^2\,^2P_{3/2}/2s^22p^2P_{3/2}$ and (b) C III $2p^2\,^3P_2/2s2p^3P_2$. These ratios are indicative of the dependence of the corresponding source functions upon electron density. The dotted lines correspond to $G(T_e(N_e)) \times N_e$ as in figs 3.2a and b, scaled to fit the plot in order to indicate the optically thin region of line formation. In both the C II and C III cases the population ratios vary several orders of magnitude over the region of line formation.

ray from that point leading out of the plasma. This ray will in general intersect many structures with sheaths as described. Consequently the source function will oscillate with respect to position along the ray. However, it will not, in optically thin circumstances, vary with position along the length of the spicule-like structures. Since the length of these structures is in general much larger than the thickness of the surrounding sheaths, the dependence of the source function on electron density is ignored here. Rather it is assumed that the population structure throughout the sheath is represented by one (T_e, N_e) pair, namely the temperature corresponding to the peak of the $G(T_e)$ function and the density at this temperature implied by the VAL model. This assumption seems severe but will be justified from observations in chapter 6.

Making this assumption enables the examination, within an escape probability picture, of the variation of the source function due to photo-absorption. In other words, this assumption allows focus to be made on the effect of scattering *into* the line-of-sight. For this eqs 2.7 and 2.8 must be revisited.

3.2 The spatially resolved absorption factor

3.2.1 $\bar{\bar{g}}\{\tau_0\}$ as a function of space

The picture considered here in regard to the effect of opacity upon the populations structure, is that of a semi-infinite plane-parallel slab. Within such a plasma the population structure will in general be dependent on height within the layer. The absorption factor expression developed in chapter 2, namely $\bar{\bar{g}}\{\tau_0\}$, predicts this even though this quantity itself was derived assuming that both the upper and lower level population densities are constant – i.e. that the population structure is independent of spatial position. By symmetry $\bar{\bar{g}}\{\tau_0\}$ may be written as a function of space. Consider absorption at the point x_0 in a slab of thickness D, due to the portion of the emitting layer defined by $0 \leq x \leq x_0$. The corresponding absorption factor is

$$\begin{aligned}\bar{\bar{g}}^{-}\{\tau_0^{-}(x_0)\} &= \frac{1}{2}\frac{1}{\sqrt{\pi}}\int_{-\infty}^{\infty} e^{-u^2}\Big[exp\left\{-\tau_0^{-}(x_0)e^{-u^2}\right\} - \\ &\quad \left\{\tau_0^{-}(x_0)e^{-u^2}\right\} E_1\left\{\tau_0^{-}(x_0)e^{-u^2}\right\}\Big]du \\ &= \frac{1}{2}\bar{\bar{g}}\{\tau_0^{-}(x_0)\} \end{aligned} \tag{3.3}$$

where

$$\tau_0^{-}(x_0) = \kappa_0 x_0 \tag{3.4}$$

A similar result follows for the portion of the emitting layer defined by $x_0 \leq x \leq D$ giving

$$\bar{\bar{g}}\{\tau_0/2\} = \frac{1}{2}\left(\bar{\bar{g}}\{\tau_0^{+}(x_0)\} + \bar{\bar{g}}\{\tau_0^{-}(x_0)\}\right) \tag{3.5}$$

where

$$\tau_0^{+}(x_0) = \kappa_0(D - x_0) \tag{3.6}$$

It follows therefore that a spatially dependent absorption factor, $\mathcal{G}(\tau_0, x)$, may be defined as

$$\mathcal{G}(\tau_0, x) = \frac{1}{2}\left(\bar{\bar{g}}\{\tau_0^{+}(x)\} + \bar{\bar{g}}\{\tau_0^{-}(x)\}\right) \tag{3.7}$$

Fig. 3.4 shows $\mathcal{G}(\tau_0, x)$ versus τ_0 for $x = 0$ and $x = D/2$ from which it is clear that $\mathcal{G}(\tau_0, x)$ is indeed spatially dependent. This illustrates that for $\tau_0 \neq 0$ the population structure differs at layer edge compared to layer centre and thus the ratio of upper to lower level population density varies throughout the layer. This in turn violates the constant density assumption that underpins the $\mathcal{G}(\tau_0, x)$ expression.

3.2.2 Inclusion of variable density in the absorption factor expression

For $\mathcal{G}(\tau_0, x)$ to be valid both the upper and lower level population densities must be constant. If this assumption is not made then the *spatially resolved* absorption factor is obtained.

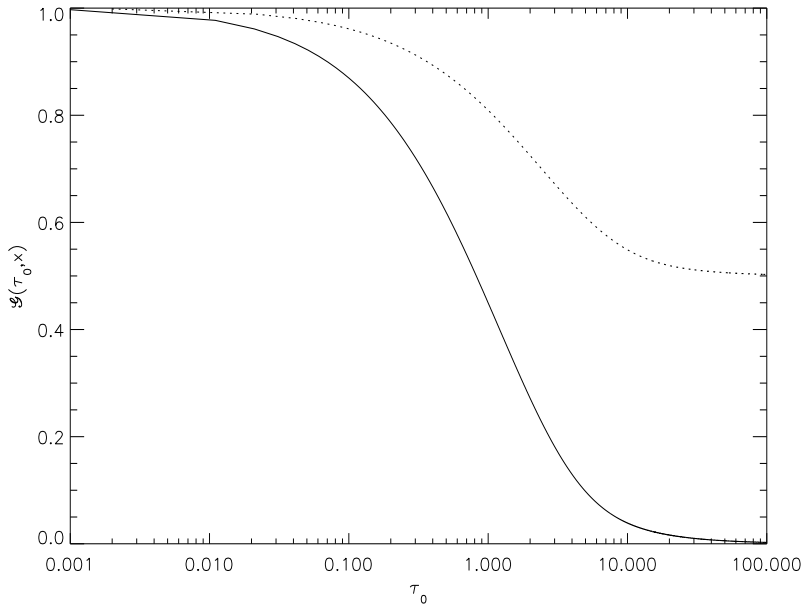

Figure 3.4: $\mathcal{G}(\tau_0, x)$ versus τ_0 for $x = 0$ (solid line) and $x = D/2$ (dotted line).

For a stratified atmosphere it may be written that $N_l \equiv N_l(x)$. The probability, dT_ν, that a photon of frequency ν emitted at point x in the layer will propagate a distance dl at an angle θ to the x-axis is

$$dT_\nu(x, \theta, dl) = exp(-\kappa_\nu(x) dl) \tag{3.8}$$

$$= exp(-\kappa_\nu(x) dx/cos\theta) \tag{3.9}$$

The probability that the photon will propagate a further distance dl is

$$dT_\nu(x, \theta, 2dx/cos\theta) = exp(-\kappa_\nu(x) dx/cos\theta) \times exp(-\kappa_\nu(x + dx) dx/cos\theta) \tag{3.10}$$

$$= exp(-[\kappa_\nu(x) + \kappa_\nu(x + dx)] dx/cos\theta) \tag{3.11}$$

Following this, the probability, T_ν, that a photon of frequency ν emitted at the point x in the layer will propagate a distance l at an angle θ to the x-axis is

$$T_\nu(x, \theta, l) = exp\left(-\frac{1}{cos\theta} \int_x^{x_1} \kappa_\nu(x') dx'\right) \tag{3.12}$$

where $x_1 = x + lcos\theta$.

The intensity, dI_ν at $\mathbf{x} = (x_0, 0)$ due to the volume element dV is

$$\begin{aligned}
dI_\nu(\mathbf{x}) &= \frac{j_\nu(\mathbf{r})}{|\mathbf{r}-\mathbf{x}|^2} exp\left\{-\int_{\mathbf{r}\to\mathbf{x}} \kappa_\nu(\mathbf{r})dl\right\} dV \\
\Rightarrow I_\nu(\mathbf{x_0}) &= \frac{1}{4\pi}\int\int_V\int \frac{j_\nu(x)}{l^2} exp\left\{-\frac{l}{x}\int_x^{x_0}\kappa_\nu(x')dx'\right\} dV \\
&= \frac{1}{4\pi}\int_0^{2\pi}\left[\int_0^{x_0}\int_x^\infty \frac{j_\nu(x)}{l^2} exp\left\{-\frac{l}{x}\int_x^{x_0}\kappa_\nu(x')dx'\right\} ldldx\right. \\
&\quad \left. + \int_{x_0}^{D}\int_x^\infty \frac{j_\nu(x)}{l^2} exp\left\{-\frac{l}{x}\int_{x_0}^{x}\kappa_\nu(x')dx'\right\} ldldx\right] d\theta \\
&= \frac{1}{2}\left[\int_0^{x_0} j_\nu(x) E_1\left\{\int_x^{x_0}\kappa_\nu(x')dx'\right\} dx\right. \\
&\quad \left. + \int_{x_0}^{D} j_\nu(x) E_1\left\{\int_{x_0}^{x}\kappa_\nu(x')dx'\right\} dx\right] \qquad (3.13)
\end{aligned}$$

Thus, from eq. 2.6,

$$\begin{aligned}
\Lambda(\tau_0, x_0) = 1 &- \frac{1}{2}\frac{N_l(x_0)}{N_u(x_0)}\frac{\omega_u}{\omega_l}\frac{c^2}{2\nu_0^2}\int\phi(\nu)\left[\int_0^{x_0} j_\nu(x)E_1\left\{\int_x^{x_0}\kappa_\nu(x')dx'\right\}dx\right. \\
&+ \left.\int_{x_0}^{D} j_\nu(x)E_1\left\{\int_{x_0}^{x}\kappa_\nu(x')dx'\right\}dx\right]d\nu \qquad (3.14)
\end{aligned}$$

Using the relation between $j_\nu(x)$ and $\kappa_\nu(x)$ specified in eq. 2.32, and considering purely Doppler broadened profiles, this becomes

$$\begin{aligned}
\Lambda(\tau_0, x_0) = 1 &- \frac{1}{2\sqrt{\pi}}\frac{N_l(x_0)}{N_u(x_0)}\int e^{-2u^2}\left[\int_0^{x_0} N_u(x)\kappa_0 E_1\left\{e^{u^2}\tau_0(x, x_0)\right\}dx\right. \\
&+ \left.\int_{x_0}^{D} N_u(x)\kappa_0 E_1\left\{e^{u^2}\tau_0(x_0, x)\right\}dx\right]d\nu \qquad (3.15)
\end{aligned}$$

Eq. 3.15 is the absorption factor at the point x_0 in a semi-infinite plane-parallel slab. No assumption is made here about the density, nor the variation of the source function with respect to space. This expression reintroduces nonlinearity and coupling to the radiative transfer equations. Therefore it must be solved iteratively.

The absorption factor has a functional dependence on the optical depth quantities $\tau_0(x_1, x_2)$ defined as

$$\tau_0(x_1, x_2) = \kappa_0\int_{x_1}^{x_2} N_l(x)dx \qquad (3.16)$$

However, for a particular lower level population density distribution, the absorption factor at the point x_0 is prescribed by the total optical depth, $\tau_0 \equiv \tau_0(0, D)$, and so is denoted $\Lambda(\tau_0, x_0)$.

3.2.3 Verification of the Λ result

Eq. 3.15 may be checked by considering the case where both N_u and N_l are constant in space. In this case, $\Lambda(\tau_0, D/2) \equiv \bar{\bar{g}}\{\tau_0/2\}$, viz.

$$\begin{aligned}
\Lambda(\tau_0, D/2) &= 1 - \frac{2}{2\sqrt{\pi}} \frac{N_l}{N_u} N_u \kappa_0 \int_{-\infty}^{\infty} e^{-2u^2} \int_0^{D/2} E_1 \left\{ \kappa_0 N_l (D/2 - x) e^{-u^2} \right\} dx du \\
&= 1 - \frac{N_l \kappa_0}{\sqrt{\pi}} \int_{-\infty}^{\infty} e^{-2u^2} \int_0^{D/2} \int_x^{\infty} \frac{e^{l \kappa_0 N_l e^{-u^2}}}{l} dl dx du \\
&= 1 - \frac{N_l \kappa_0}{\sqrt{\pi}} \int_{-\infty}^{\infty} e^{-2u^2} \left[\int_0^{D/2} \int_0^{l} \frac{e^{l \kappa_0 N_l e^{-u^2}}}{l} dx dl + \int_{D/2}^{\infty} \int_0^{D/2} \frac{e^{l \kappa_0 N_l e^{-u^2}}}{l} dx dl \right] du \\
&= 1 - \frac{N_l \kappa_0}{\sqrt{\pi}} \int_{-\infty}^{\infty} e^{-2u^2} \left[\int_0^{D/2} e^{l \kappa_0 N_l e^{-u^2}} dl + \int_{D/2}^{\infty} \frac{D}{2} \frac{e^{l \kappa_0 N_l e^{-u^2}}}{l} dl \right] du \\
&= 1 - \frac{N_l \kappa_0}{\sqrt{\pi}} \int_{-\infty}^{\infty} e^{-2u^2} \left[-\frac{e^{D \kappa_0 N_l e^{-u^2}/2}}{\kappa_0 N_l e^{-u^2}} + \frac{1}{\kappa_0 N_l e^{-u^2}} + \frac{D}{2} E_1 \left\{ \kappa_0 N_l e^{-u^2} \right\} \right] du \\
&= \frac{1}{\sqrt{\pi}} \int_{-\infty}^{\infty} e^{-u^2} \left[exp \left\{ -\frac{\tau_0}{2} e_{-u^2} \right\} - \frac{\tau_0}{2} e^{-u^2} E_1 \left\{ \frac{\tau_0}{2} e^{-u^2} \right\} \right] du \\
&\equiv \bar{\bar{g}}\{\tau_0/2\}
\end{aligned} \tag{3.17}$$

3.3 The assumption of constant source function

The results discussed above provide a route to obtaining an optically thick upper level population distribution via calculation of the spatially resolved absorption factor, $\Lambda(\tau_0, x_0)$ (eq. 3.15). Using this upper level population distribution, optically thick emergent fluxes may then be calculated via

$$I = \frac{1}{4\pi} A_{u \to l} \int_{l.o.s} N_u(s) g\{\tau_0(s)\} ds \tag{3.18}$$

Thus it is possibly to assess directly the implications of assuming that the source function is constant in space.

The impact of this assumption is profound. If it is made, then eqs 2.17 and 2.38 (i.e. $\bar{g}\{\tau_0\}$ and $\bar{\bar{g}}\{\tau_0/2\}$) may be extended into the variable density case as follows: consider emission along a line-of-sight of length L. If an element of distance along this line-of-sight is denoted ds then eq. 3.18 may be written as

$$I \sim \int_0^L N_u(s) g\{\tau_0(s)\} ds \tag{3.19}$$

with

$$\tau_0(s) = \kappa_0 \int_0^s N_l(s') ds' \tag{3.20}$$

Since it is assumed that the source function is constant, it may be written that

$$\frac{N_u(s)}{N_l(s)} = R = const \tag{3.21}$$

If $\bar{N}_u$ and $\bar{N}_l$ are defined as

$$\begin{aligned} \bar{N}_u &= \frac{\int_0^L N_u(s) ds}{L} \\ \bar{N}_l &= \frac{\int_0^L N_l(s) ds}{L} \end{aligned} \tag{3.22}$$

then it follows that

$$\Rightarrow \frac{\bar{N}_u}{\bar{N}_l} = \frac{N_u(s)}{N_l(s)} = R \tag{3.23}$$

It is useful to define $\eta(s)$ as follows:

$$\begin{aligned} \eta(s) &= \frac{\int_0^s N_l(s') ds'}{\bar{N}_l} \\ \Rightarrow \frac{d\eta}{ds} &= \frac{N_l(s)}{\bar{N}_l} \\ \Rightarrow N_u(s) ds &= \bar{N}_u \frac{N_l(s)}{\bar{N}_l} ds = \bar{N}_u \frac{d\eta}{ds} ds \end{aligned} \tag{3.24}$$

Therefore

$$\begin{aligned} I &\sim \int_0^L \bar{N}_u g\{\kappa_0 \bar{N}_l \eta\} d\eta \\ &\sim \bar{N}_u \bar{g}\{\tau_0\} \end{aligned} \tag{3.25}$$

It may also be shown that $\bar{\bar{g}}\{\tau_0\}$ is valid if the source function is constant with respect to space. As before

$$dI_\nu = \frac{j_\nu(\mathbf{x})}{l^2} exp\left\{-\int_{\mathbf{x}\to\mathbf{0}} \kappa_\nu(\mathbf{x}')d\mathbf{x}'\right\} dV \tag{3.26}$$

and

$$\bar{I}_\nu = \frac{1}{4\pi}\int\int_V\int dI_\nu \tag{3.27}$$

Consider the intensity, $\bar{I}_\nu^-$, due to the portion of the emitting layer defined by $0 \le x \le x_0$. This is given by

$$\bar{I}_\nu^- = \frac{1}{4\pi}\int_0^\pi\int_0^{x_0}\int_{x_0}^\infty \frac{j_\nu(\mathbf{x})}{l^2} exp\left\{-\int_0^{x_0}\kappa_\nu(\mathbf{x}')d\mathbf{x}'\frac{l}{x}\right\} l dl dx d\theta \tag{3.28}$$

It is convenient to re-write this in spherical polar coordinates:

$$\begin{aligned}
\bar{I}_\nu^- &= \frac{1}{4\pi}\int_0^\pi 2\int_0^{\pi/2}\int_0^{x_0/cos\theta} \frac{j_\nu(r\,cos\theta)}{r^2} exp\left\{-\frac{1}{cos\theta}\int_0^{r\,cos\theta}\kappa_\nu(x)dx\right\} r^2 sin\theta dr d\theta d\phi \\
&= \frac{1}{2}\int_0^{\pi/2}\int_0^{x_0/cos\theta} \sigma\kappa_0 e^{-u^2}\frac{\bar{N}_u}{\bar{N}_l}N_l(r\,cos\theta) exp\left\{-\frac{1}{cos\theta}\int_0^{r\,cos\theta}\kappa_\nu(x)dx\right\} sin\theta dr d\theta
\end{aligned} \tag{3.29}$$

where

$$\sigma = \frac{\omega_l}{\omega_u}\frac{2\nu_0^2}{c^2} \tag{3.30}$$

Defining s as

$$s(r\,cos\theta) = \frac{\int_0^{x_0} N_l(x)dx}{x_0} \tag{3.31}$$

it then follows that

$$\begin{aligned}
\bar{I}_\nu^- &= \frac{1}{2}\int_0^{\pi/2}\int_0^{x_0}\sigma\kappa_0 e^{-u^2}\bar{N}_u exp\left\{-\frac{\kappa_0\bar{N}_l e^{-u^2}}{cos\theta}s\right\}\frac{sin\theta}{cos\theta}ds d\theta \\
&= \frac{1}{2}\frac{\bar{N}_u}{\bar{N}_l}\sigma\int_0^{\pi/2} sin\theta\left[1 - exp\left\{-\frac{\kappa_0\bar{N}_l x_0 e^{-u^2}}{cos\theta}\right\}\right] d\theta \\
&= \frac{1}{2}\frac{\bar{N}_u}{\bar{N}_l}\sigma\left[-cos\theta\Big|_0^{\pi/2} - \int_0^{\pi/2} sin\theta\, exp\left\{-\frac{\kappa_0\bar{N}_l x_0 e^{-u^2}}{cos\theta}\right\}\right] d\theta
\end{aligned}$$

$$
\begin{aligned}
&= \frac{1}{2}\frac{\bar{N}_u}{\bar{N}_l}\sigma\left[1-\int_1^\infty \frac{1}{t^2} exp\left\{-\kappa_0 \bar{N}_l x_0 e^{-u^2} t\right\} dt\right] \\
&= \frac{1}{2}\frac{\bar{N}_u}{\bar{N}_l}\sigma\left[1-E_2\kappa_0 \bar{N}_l x_0 e^{-u^2}\right] \\
&= \frac{1}{2}\frac{\bar{N}_u}{\bar{N}_l}\sigma\left[1+\frac{exp\left\{\kappa_0 \bar{N}_l x_0 e^{-u^2} t\right\}}{t}\Big|_1^\infty + \kappa_0 \bar{N}_l x_0 e^{-u^2}\int_1^\infty \frac{1}{t} exp\left\{\kappa_0 \bar{N}_l x_0 e^{-u^2} t\right\} dt\right] \\
&= \frac{1}{2}\frac{\bar{N}_u}{\bar{N}_l}\sigma\left[1-exp\{-\tau_0^- e^{-u^2}\}+\tau_0^- e^{-u^2} E_1\{\tau_0^- e^{-u^2}\}\right] \qquad (3.32)
\end{aligned}
$$

where

$$\tau_0^- = \kappa_0 \int_0^{x_0} N_l(x)dx$$
$$\tau_0^+ = \kappa_0 \int_{x_0}^{D} N_l(x)dx$$

Therefore,

$$\bar{\bar{g}}^-\{\tau_0^-\} = \frac{1}{2}-\frac{1}{2\sqrt{\pi}}\int_{-\infty}^{\infty} e^{-u^2}\left[exp\{-\tau_0^- e^{-u^2}\}-\tau_0^- e^{-u^2} E_1\{\tau_0^- e^{-u^2}\}\right] \qquad (3.33)$$

An analogous result exists for $\bar{\bar{g}}^+\{\tau_0^-\}$ and thus

$$\Lambda(\tau_0, x_0) = \left(\bar{\bar{g}}\{\tau_0^-\}+\bar{\bar{g}}\{\tau_0^+\}\right)/2 \equiv \mathcal{G}(\tau_0, x_0) \qquad (3.34)$$

3.4 The spatially resolved population calculation

Shown in figs 3.5 and 3.6 are absorption factors versus position for a selection of spectral lines of C II corresponding to three sets of optical depths. Since the absorption factors depend upon the optical depth rather than the geometrical thickness of the model plasma, and since plots are shown for three sets of optical depths, the x-axis is labelled *position index*. This relates to the computational grid and is equivalent to the geometric position in arbitrary units. The first step in their calculation is choosing a lower level population density distribution. This distribution describes the spatial variation of the lower level population densities of the optically thick lines. As discussed earlier, only lines whose lower levels are metastable are considered to be potentially thick and these levels are negligibly affected by opacity for the moderate optical depths considered here. Consequently the lower level population density

distributions remain constant throughout the calculation. From these, the optical depths, $\tau_0(x_1, x_2)$ may be calculated for each (x_1, x_2) pair, and these also remain constant throughout the calculation. An initial guess for $N_u(x)$ is then required. This is taken to be either the optically thin value – simply a multiple of $N_l(x)$ for each line – or the output of a previous iteration. However, any initial guess is valid (in principle) providing that convergence is subsequently achieved from it. From these $\Lambda(\tau_0, x)$ may be calculated for every line at each x via eq. 3.15. Then at each point the Λ's may be used to modify the Einstein A-coefficients in the statistical balance equations to obtain the optically thick population structure at each point in the layer. From this the optically thick upper level population distributions may be assembled via the lower level distributions which, as stated above, are unchanged.

3.5 The effect of an opacity modified source function upon the absorption factor

Inspection of eq. 3.15 reveals that it is not so much the value of the source function at a particular point that is important but rather the variation of the source function throughout the emitting layer. This can be seen by consideration of the $N_l(x_0)N_u(x)/N_u(x_0)$ term. It is not the value of $N_u(x)$ that matters, nor the ratio $N_u(x)/N_l(x)$ but rather the ratio $N_u(x)/N_u(x_0)$. The calculation is sensitive to this ratio – a fact that impinges upon its convergence (or otherwise).

Presented below is a brief summary of the characteristics of the absorption factors of lines of each of the C II multiplets containing optically thick lines.

The 1335 Å multiplet

The absorption factors of all three of these lines follow the $\mathcal{G}(\tau_0, x)$ trend broadly speaking. The most notable deviation is in the $2s^2 2p\,^2P_{3/2} - 2s2p^2\,^2D_{3/2}$ line at 1335.665 Å. This line shares its upper level with the $2s^2 2p\,^2P_{1/2} - 2s2p^2\,^2D_{3/2}$ line at 1334.524 Å but is less optically thick.

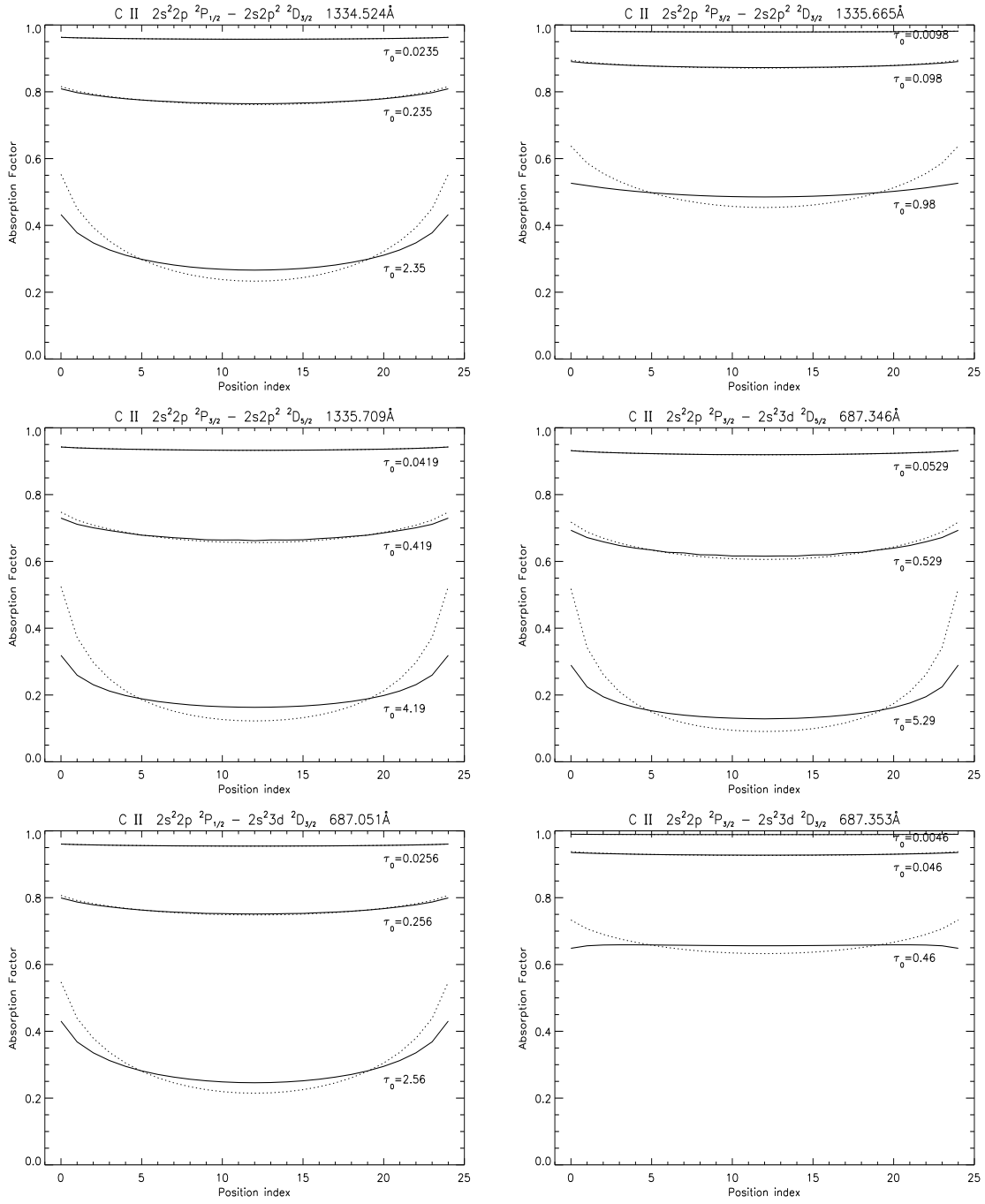

Figure 3.5: Absorption factors versus position for selected lines of C II corresponding to three sets of optical depths. Absorption factors are calculated iteratively via eqs 3.15 and 2.8. The solid lines are $\Lambda(\tau_0, x)$ and the dotted lines are $\mathcal{G}\{\tau_0, x\}$.

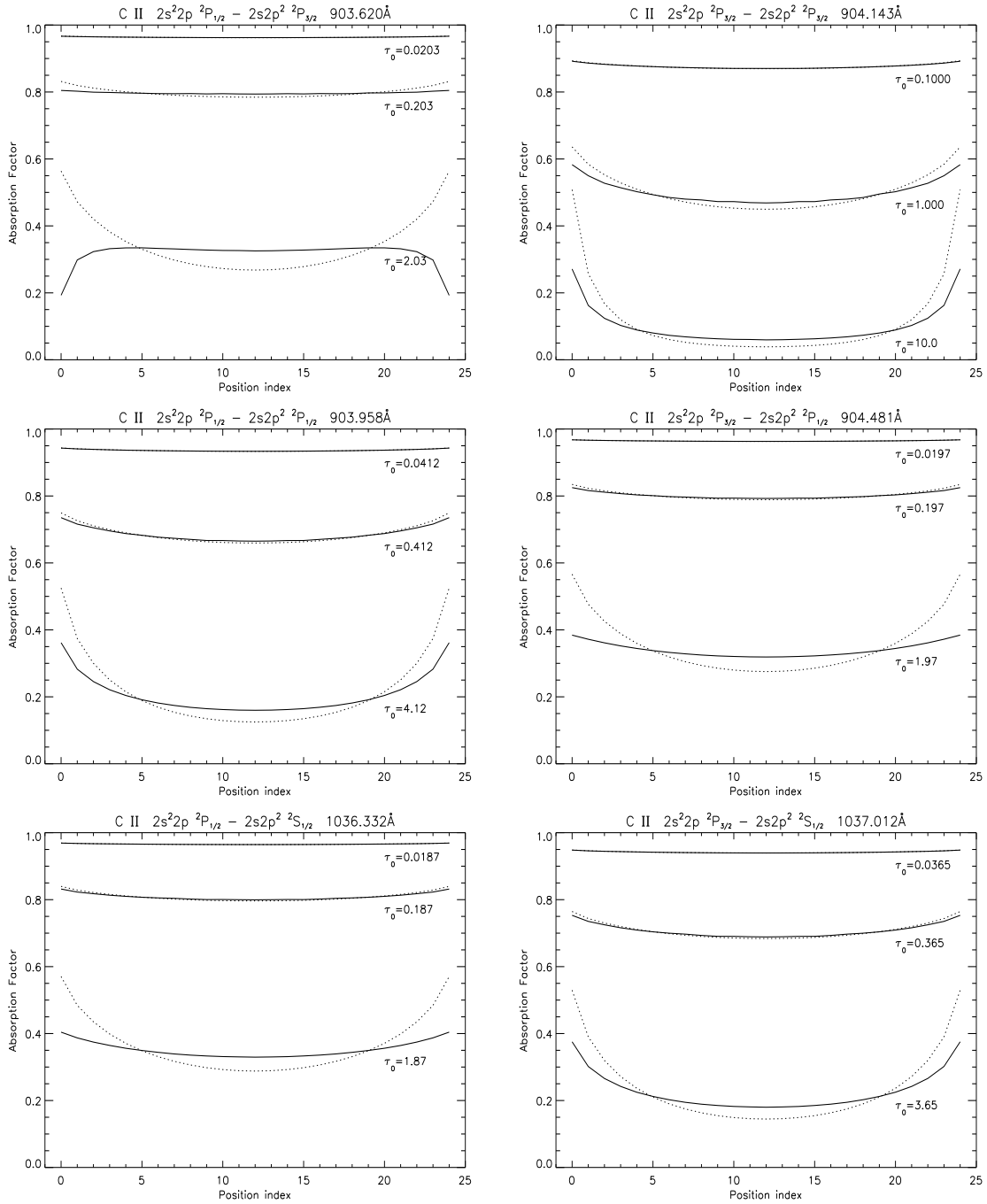

Figure 3.6: Absorption factors versus position for selected lines of C II as in fig 3.5.

The 687 Å multiplet

In this case the absorption factors of both the $2s^2 2p\,^2P_{3/2} - 2s^2 3d\,^2D_{5/2}$ line at 687.346 Å and the $2s^2 2p\,^2P_{1/2} - 2s^2 3d\,^2D_{3/2}$ line at 687.051 Å follow the $\mathcal{G}(\tau_0, x)$ trend. At an optical depth of 10 in the *control line* (the $2s^2 2p\,^2P_{3/2} - 2s2p^2\,^2P_{3/2}$ line at 904.143 Å) the $2s^2 2p\,^2P_{3/2} - 2s^2 3d\,^2D_{3/2}$ line at 687.353 Å deviates from the $\mathcal{G}(\tau_0, x)$ trend. Again, this line shares its upper level with another (the 687.346 Å line) which is more optically thick.

The 904 Å multiplet

In this multiplet the absorption factors of two of the lines follow the $\mathcal{G}(\tau_0, x)$ trend and two deviate. The $2s^2 2p\,^2P_{3/2} - 2s2p^2\,^2P_{3/2}$ line at 904.143 Å and the $2s^2 2p\,^2P_{3/2} - 2s2p^2\,^2P_{1/2}$ line at 903.958 Å are the followers and they are also the most optically thick of the four lines. The $2s^2 2p\,^2P_{1/2} - 2s2p^2\,^2P_{3/2}$ line at 903.620 Å and the $2s^2 2p\,^2P_{3/2} - 2s2p^2\,^2P_{1/2}$ line at 904.481 Å are thinner and share upper levels with the 904.143 Å and 903.958 Å lines respectively.

The 1036 Å multiplet

Both the lines of the 1036 Å multiplet share an upper level and both follow the $\mathcal{G}(\tau_0, x)$ trend broadly speaking, one slightly more than the other. The one that deviates most markedly, namely the $2s^2 2p\,^2P_{1/2} - 2s2p^2\,^2S_{1/2}$ line at 1036.332 Å, is, once again, the thinner of the two.

Discussion

In all the C II multiplets listed above there is a deviation in $\Lambda(\tau_0, x)$ from $\mathcal{G}(\tau_0, x)$ and in each this deviation is due to the distortion of $N_u(x)$ with respect to space (see figs 3.8 $\rightarrow$ 3.11). $\Lambda(\tau_0, x_0)$ depends on the integral of $N_u(x)/N_u(x_0)$ over x. Consequently $\Lambda(\tau_0, x_0) > \mathcal{G}(\tau_0, x_0)$ at layer centre since the population is most enhanced at this point – i.e. $N_u(x)/N_u(D/2) < 1$ for all $x \neq D/2$. Conversely, $\Lambda(\tau_0, x_0) < \mathcal{G}(\tau_0, x_0)$ at the edges since the population is least enhanced at these points – i.e. $N_u(x)/N_u(0) > 1$ and $N_u(x)/N_u(D) > 1$ for all $x \neq 0, D$. Thus there

is always a difference between the $\Lambda(\tau_0, x)$ and $\mathcal{G}(\tau_0, x)$ results since there is always at least *some* distortion of the upper level population distribution. Furthermore, this difference increases with optical depth since the distortion also increases with optical depth.

In each multiplet there are examples where the deviation of $\Lambda(\tau_0, x)$ from $\mathcal{G}(\tau_0, x)$ is particularly marked, in some instances reversing the $\mathcal{G}(\tau_0, x)$ versus x trend (e.g. the 903.620 Å line in fig. 3.6). In each of these cases the line in question shares its upper level with another, more optically thick line in the multiplet. In such circumstances both lines contribute to the deviation in the upper level density distribution due to reabsorption but more so the thicker line. Thus the upper level distribution is more significantly enhanced than it would be if just one of the lines were thick. It follows that for each line the population distribution is more distorted than it would be if that line were the only thick one and so the $\Lambda(\tau_0, x)$'s move further away from the corresponding $\mathcal{G}(\tau_0, x)$'s. This is true for all the lines stemming from the upper level in question but the effect is observed mostly in the thinner lines. This is because it is the thicker lines that make the most significant contribution to the upper level distortion and so the distortion itself is more consistent with the opacity in the thicker line than in the thinner ones.

3.6 The validity of $\mathcal{G}(\tau_0, x)$

The validity of $\mathcal{G}(\tau_0, x)$ can be found directly by looking for the region where the $\Lambda(\tau_0, x)$ results agree. This validity is evidently not a simple function of optical depth unless the line in question makes the dominant contribution to the upper level population enhancement with respect to all the other lines stemming from that same upper level.

Fig. 3.7 shows plots of $\Lambda(\tau_0, x)$ versus optical depth at layer centre and layer edge compared with $\mathcal{G}(\tau_0, x)$. For the C II spectral line classification (see table 2.6) the greatest optical depth was 1.76 for the $2s^2 2p\ ^2P_{3/2} - 2s2p^2\ ^2P_{3/2}$ line at 904.143 Å. This is in the regime where the deviation of $\Lambda(\tau_0, D/2)$ from $\mathcal{G}(\tau_0, D/2)$ ($\equiv \bar{\bar{g}}\{\tau_0/2\}$) is minimal. At layer centre $\Lambda(\tau_0, D/2)$ is close to being monotonic and is close to

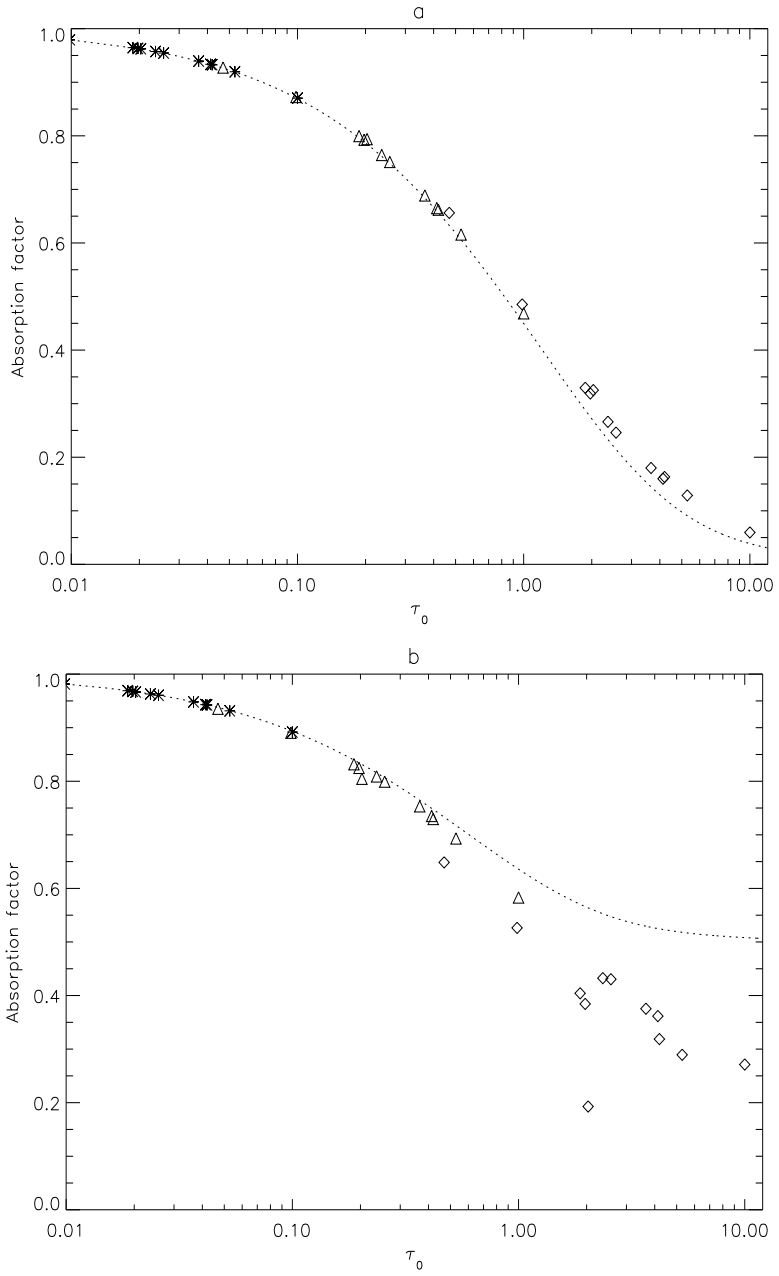

Figure 3.7: Absorption factors at (a) layer centre ($x = D/2$) and (b) layer edge ($x = 0$) versus optical depth for the constant lower level density model, taken from the plots in figs 3.5 and 3.6. The *'s, $\triangle$'s and $\diamond$'s are the absorption factors, $\Lambda(\tau_0, x)$, corresponding to the same three sets of optical depths as in figs 3.5 and 3.6. The dotted lines correspond to $\mathcal{G}(\tau_0, x)$.

$\mathcal{G}(\tau_0, D/2)$. At the edge, however, the variation of the source function becomes significant and $\mathcal{G}(\tau_0, 0)$ merely provides an upper limit to $\Lambda(\tau_0, 0)$. This figure shows $\mathcal{G}(\tau_0, x)$ to be a good approximation to $\Lambda(\tau_0, x)$ up to optical depths of around 0.5.

3.7 The effect upon the density distributions

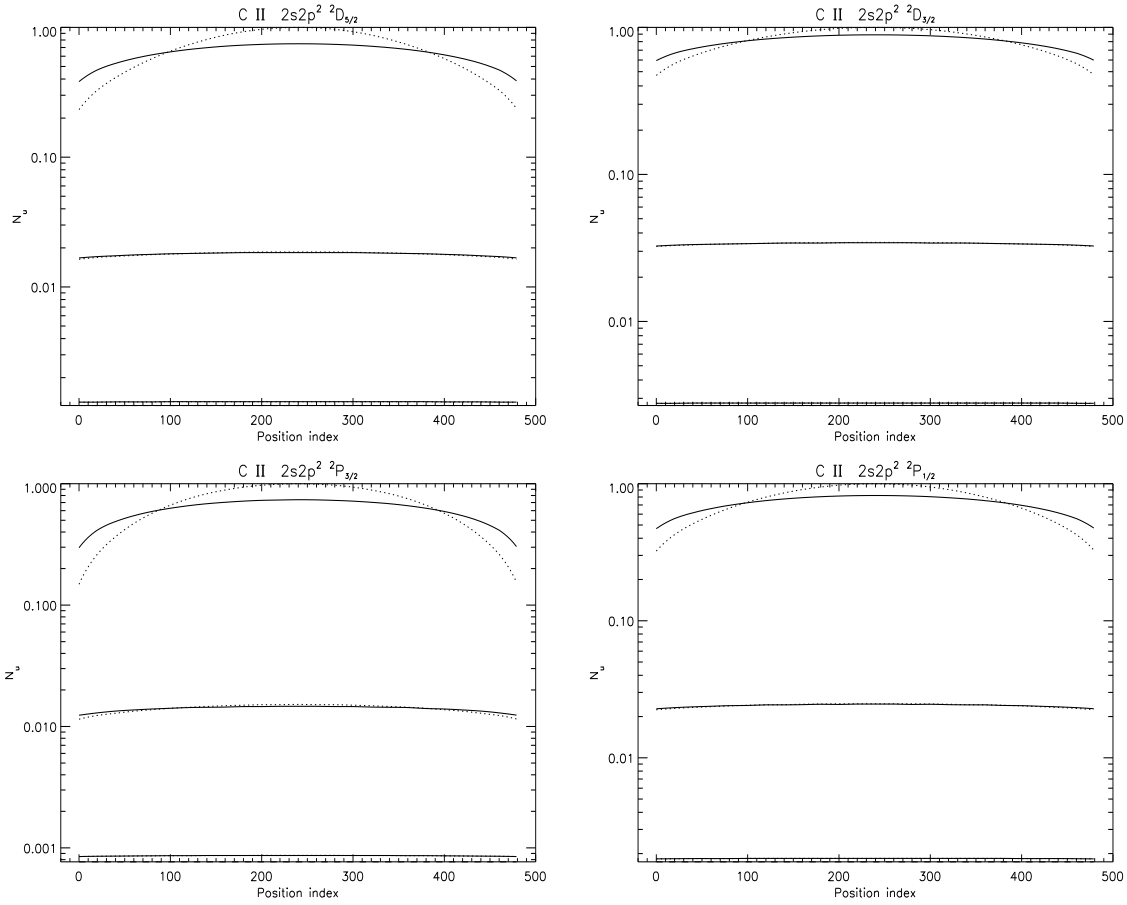

Figure 3.8: Upper level population densities versus spatial position for selected levels of C II. The solid lines correspond to calculations based on $\Lambda(\tau_0, x)$ for the same three sets of optical depths as in figs 3.5 and 3.6. The dotted lines represent the $\mathcal{G}(\tau_0, x)$ based calculations. Values are not absolute but are scaled so that the maximum population density value is unity.

From the above it is clear that the assumption that the source function is constant in space does not lead to an accurate calculation of the absorption factor, particularly

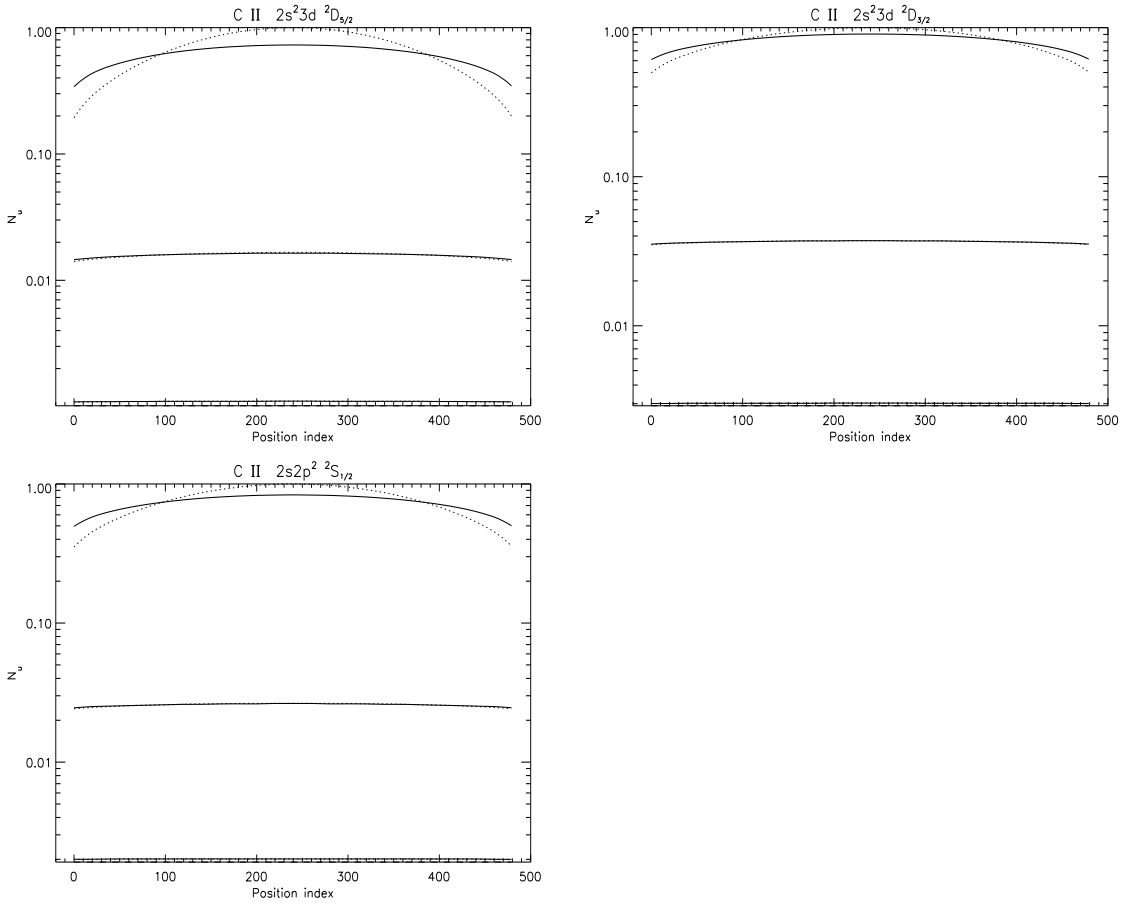

Figure 3.9: Upper level population densities versus spatial position for selected lines of C II. The solid and dotted lines are as in fig. 3.8. Values are not absolute but are scaled so that the maximum population density value is unity.

at the edge of the emitting layer. More important, however, is the validity of $\mathcal{G}(\tau_0, x)$ in predicting the population distributions. Figs 3.8 and 3.9 show the upper level population distributions for C II for the three optical depths regimes considered in figs 3.5 and 3.6. In these figures the logarithmic scale hides somewhat the extent of the difference in the populations calculated using $\Lambda(\tau_0, x)$ as compared with those using $\mathcal{G}(\tau_0, x)$. Figs 3.10 and 3.11 shows this difference on a linear scale for the most optically thick case. It is evident that in these figures there is a difference in the two and that $\mathcal{G}(\tau_0, x)$ is largely ineffective. However, the effect of using $\Lambda(\tau_0, x)$, and thus including the variation of the source function due to opacity, is to decrease the

degree of distortion of the upper level. The *absolute* value of the average population modification is not distinctly different between the two calculations but the variation in space is visibly less in the $\Lambda(\tau_0, x)$ case.

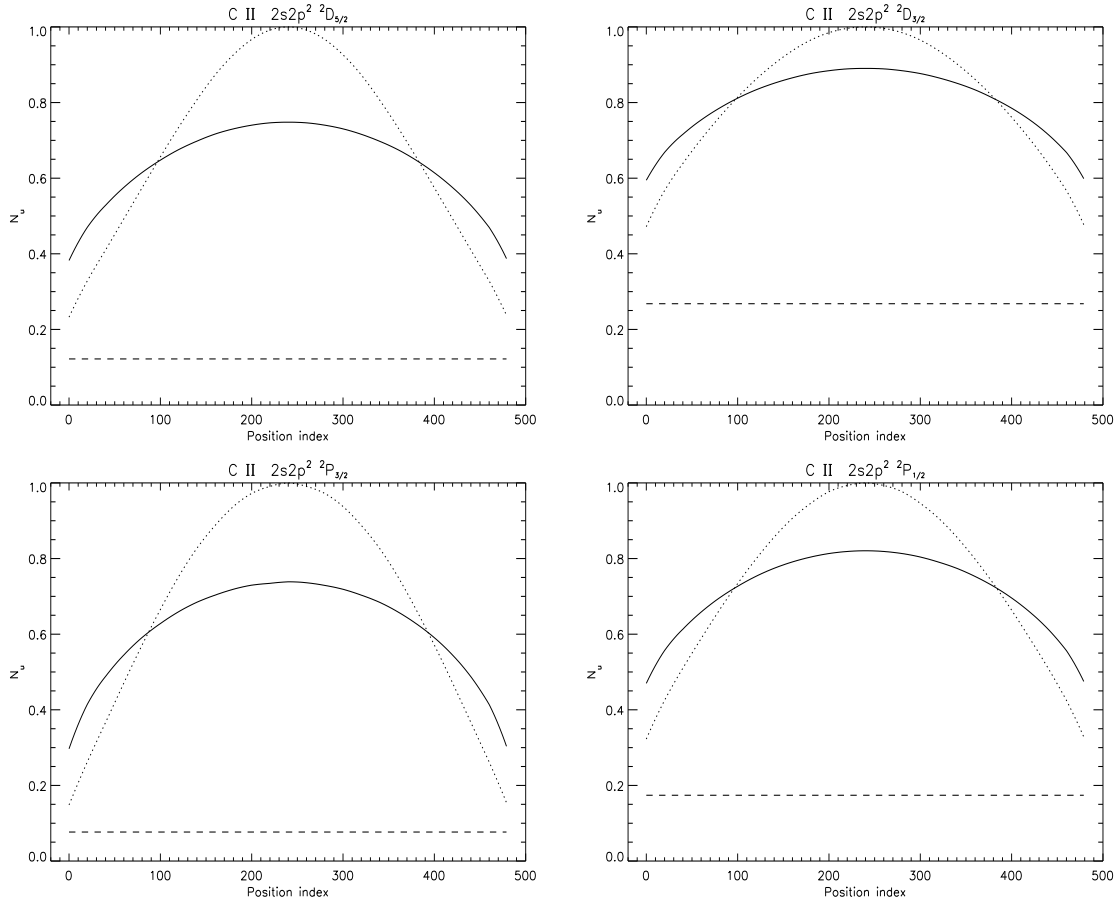

Figure 3.10: Upper level population densities versus spatial position for selected lines of C II as in figs 3.8 and 3.9 but just in the most optically thick case. The linear-linear scale reveals the degree of distortion of the upper level population density distribution for an optical depth of 10 in the control line (the C II $2s^2 2p^2 P_{3/2} - 2s2p^2\,^2P_{3/2}$ line at 904.143 Å). The solid and dotted lines are as in figs 3.8 and 3.9.

The subtle, indirect effects that influence lines such as the $2s^2 2p^2 P_{1/2} - 2s2p^2\,^2P_{3/2}$ line at 903.620 Å, evident in the absorption factors shown in figs 3.5 and 3.6, do not appear in the population distributions. This is because these indirect effects influence lines that share an upper level with lines that are thicker than themselves. These thicker partners, by virtue of their opacity, have $\Lambda(\tau_0, x)$ distributions that follow

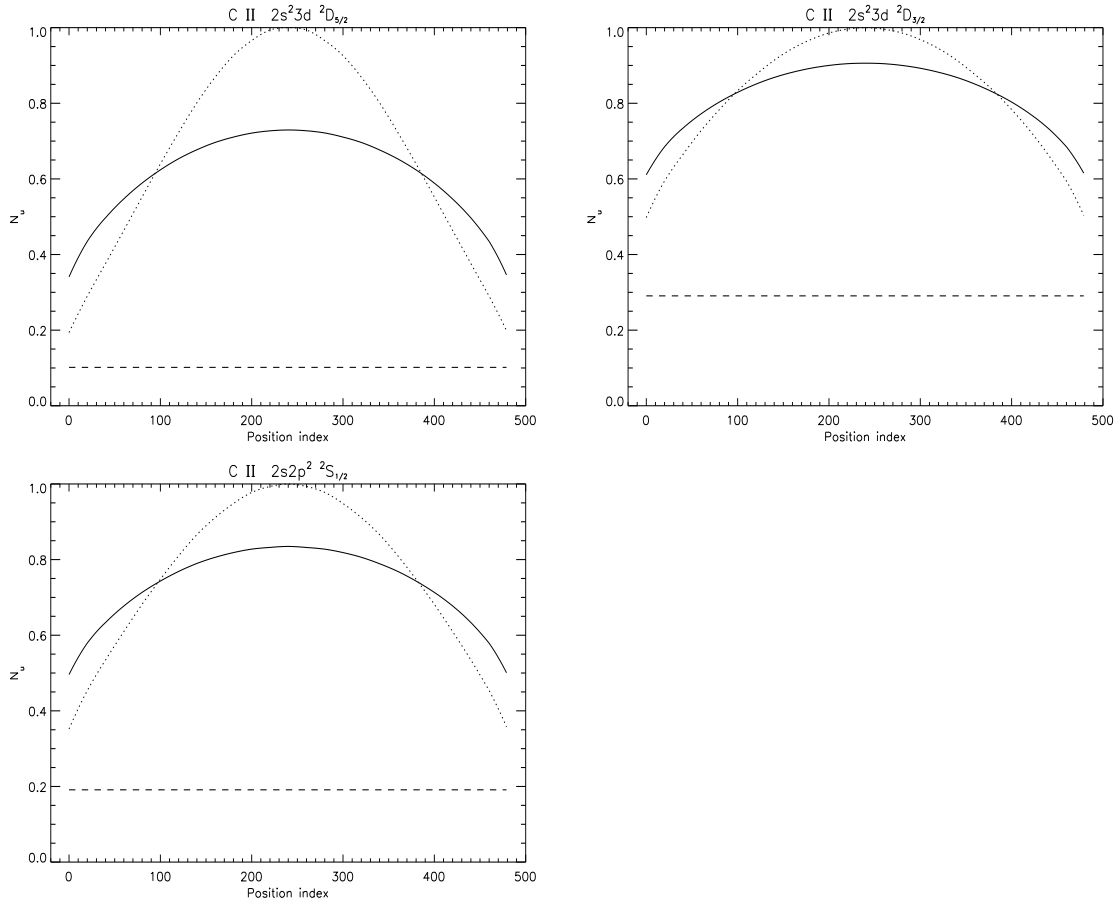

Figure 3.11: Upper level population densities versus spatial position for selected lines of C II as in fig. 3.10.

more closely the $\mathcal{G}(\tau_0, x)$ based distribution. These thicker lines, by virtue of their larger oscillator strengths (see eq. 2.14), have a more dominant role in the population calculation and so the indirect effects upon the absorption factors are minimised.

3.8 The exponential density case

The discussion so far has been restricted to the constant density case. Figures are shown in appendix A for the exponential density case. For this model the same conclusions follow.

3.9 Modelling emergent intensities

With opacity modified upper level population distributions calculated, emergent intensities may be obtained using eq. 3.18. Figs 3.12a and b show limb-brightening curves for the C II $2s^2 2p\,^2P_{3/2} - 2s2p^2\,^2P_{3/2}$ line at 904.143 Å calculated using eqs 3.18 and 3.25. For both atmosphere models considered in these figures it is clear that even with a disk centre optical depth of 10 the modified population makes little difference. Figs 3.13a and b show the same but for the C II $2s^2 2p\,^2P_{1/2} - 2s2p^2\,^2P_{3/2}$ line at 903.620 Å. This line shares its upper level with the 904.143 Å line and is considerably thinner than the latter. Thus its upper level is modified to a greater extent than its own optical depth would imply. It would be expected that for this line the population modification to the intensities would be more severe. However, as with the 904.143 Å line, there is only modest difference even in the most optically thick case. Indeed the difference is less than that for the 904.143 Å line.

Given the degree of distortion of the upper level population distribution evident in figs 3.10 and 3.11, the similarity between the $g\{\tau_0(x)\}$ based and $\bar{g}\{\tau_0\}$ based calculations is surprising. This is especially so given that the curves in figs 3.12 and 3.13 are scaled to match at disk centre. It is in moving away from disk centre toward the limb that the two results would be expected to deviate from one another the most since it is here that the geometric extension of the line-of-sight is minimal. In the vicinity of the limb the line-of-sight is extended, hence the total population modification is stretched and thus minimised with respect to the total line-of-sight optical depth.

To gain insight into this it is useful to generalise $\bar{g}\{\tau_0\}$ so that it may be expressed in the case where the source function is not constant.

3.9.1 The modified $\bar{g}\{\tau_0\}$

Following Behringer (1997) the line-of-sight averaged escape probability may be more generally defined as

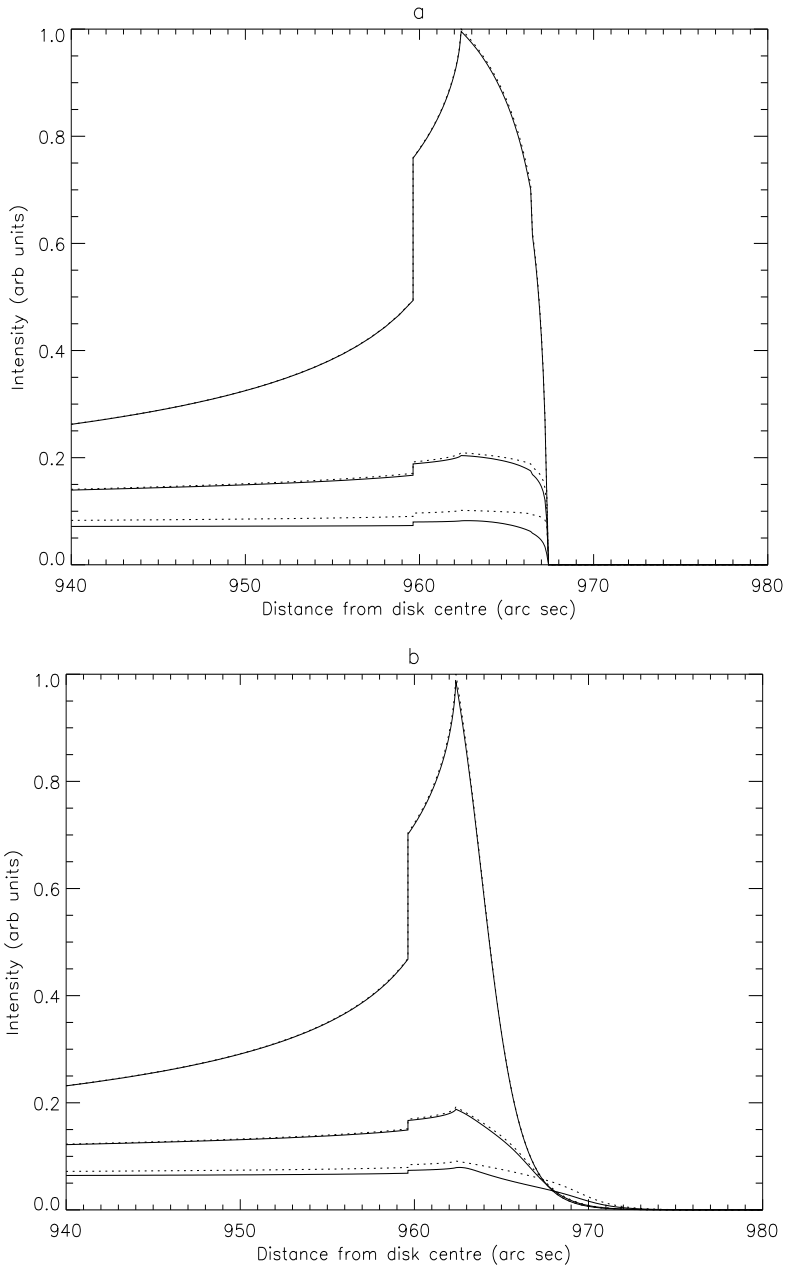

Figure 3.12: Predicted limb-brightening curves for the C II $2s^2 2p\,^2P_{3/2} - 2s2p^2\,^2P_{3/2}$ line at 904.143 Å calculated using $g\{\tau_0(x)\}$ with an opacity modified upper level population density distribution (solid lines) and using $\bar{g}\{\tau_0\}$ assuming constant source function (dotted lines) via eqs 3.18 and 3.25 respectively. Intensities are calculated in (a) a constant density model and (b) a model with density that decreases exponentially with height. Each contain three sets of curves corresponding to disk centre optical depths of 0.1, 1 and 10. The curves are scaled to match at disk centre.

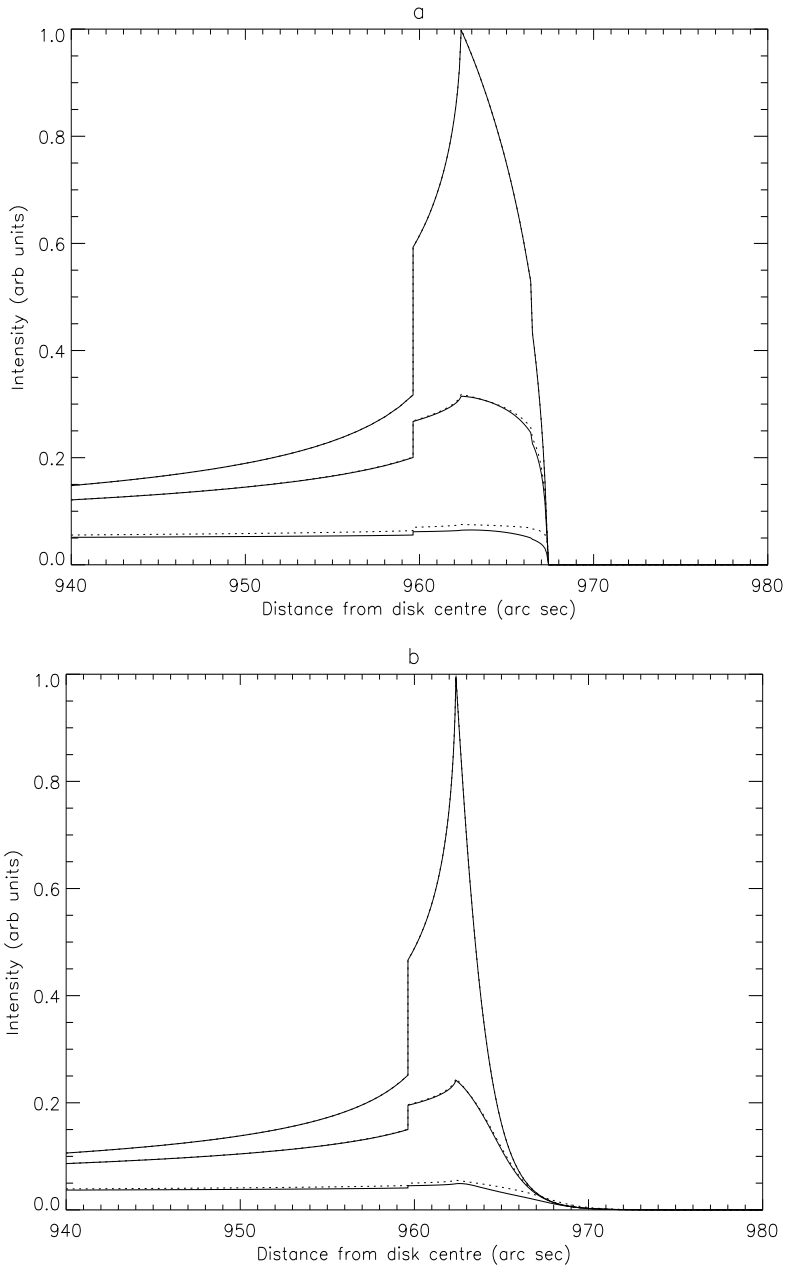

Figure 3.13: Predicted limb-brightening curves for the C II $2s^2 2p\,^2P_{1/2} - 2s2p^2\,^2P_{3/2}$ line at 903.620 Å calculated using $g\{\tau_0(x)\}$ with an opacity modified upper level population density distribution (solid lines) and using $\bar{g}\{\tau_0\}$ assuming constant source function (dotted lines) via eqs 3.18 and 3.25 respectively. (a) a constant density model and (b) a model with density that decreases exponentially with height. Each contain three sets of curves corresponding to disk centre optical depths of 0.02, 0.2 and 2. The curves are scaled to match at disk centre.

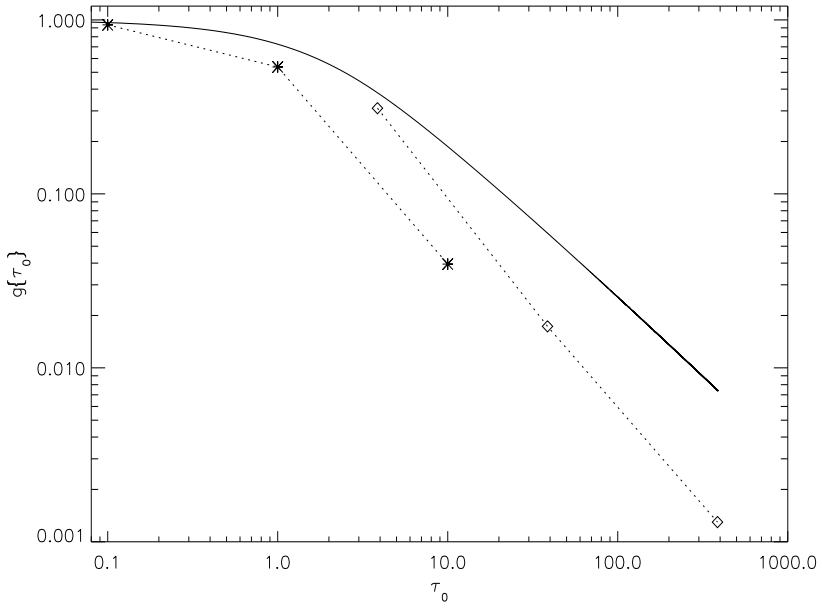

Figure 3.14: $\bar{g}\{\tau_0\}$ and $\bar{g}_r\{\tau_0\}$ versus τ_0 at disk centre and the limb shown on a log-log scale. The solid line shows $\bar{g}\{\tau_0\}$. The *'s correspond to $\bar{g}_r\{\tau_0\}$ at disk centre and the $\diamond$'s correspond to $\bar{g}_r\{\tau_0\}$ at the limb. The limb values are closer than the disk centre ones to the $\bar{g}\{\tau_0\}$ values. This is because the distortion of the upper level population density along the line-of-sight is less severe at the limb than at disk centre since the line-of-sight itself is geometrically extended.

$$\begin{aligned} \bar{g}_r[N_u(s), N_l(s), \tau_\nu] &\equiv \frac{I^{o.thick}}{I^{o.thin}} \\ &= \frac{\int_\nu \int_{l.o.s} N_u(s)\phi(\nu) exp\{-\tau_\nu\} ds d\nu}{\int_\nu \int_{l.o.s} N_u(s)\phi(\nu) ds d\nu} \end{aligned} \tag{3.35}$$

In general $\bar{g}_r[N_u(s), N_l(s), \tau_\nu]$ has a functional dependence upon the spatially resolved upper and lower level population densities, $N_u(s)$ and $N_l(s)$ but for particular choices of these, $\bar{g}_r[N_u(s), N_l(s), \tau_\nu]$ may be characterised purely as a function of optical depth, τ_0. Consequently $\bar{g}_r[N_u(s), N_l(s), \tau_\nu]$ may be written as $\bar{g}_r\{\tau_0\}$.

Since the optically thick emission must first be calculated for $\bar{g}_r\{\tau_0\}$ to be known, it is not a useful quantity for calculating optically thick emission. However, the comparison between $\bar{g}\{\tau_0\}$ and $\bar{g}_r\{\tau_0\}$ is insightful and is shown in fig. 3.14. The two are compared at disk centre and at the limb. As discussed above the difference

between $\bar{g}\{\tau_0\}$ and $\bar{g}_r\{\tau_0\}$ is less at the limb than at disk centre. This is because at the limb the population modification along the line-of-sight is minimised with respect to its optical depth due to the geometric extension of the line-of-sight in comparison with that at disk centre. For example, a disk centre optical depth of 1 translates, in the constant density model, to a limb optical depth of ~ 40. Yet the population modification along the line-of-sight at both disk centre and the limb is characterised by the smaller optical depth of 1.

There is an apparent discrepancy between figs 3.12 and 3.13 and fig. 3.14 as there is a more marked difference between $\bar{g}\{\tau_0\}$ and $\bar{g}_r\{\tau_0\}$ than there is between the intensity calculations based on $\bar{g}\{\tau_0\}$ and $g\{\tau_0(s)\}$. That is, it appears from figs 3.12 and 3.13 that the emergent fluxes are insensitive to the distortion of the source function due to opacity, yet fig. 3.14 indicates that the escape probability is sensitive.

The answer to this lies in the denominator of eq. 3.35, namely $I^{o.thin}$. This quantity, given by

$$I^{o.thin} = \int_{\nu} \int_{l.o.s} N_u(l)\phi(\nu) dl d\nu \tag{3.36}$$

is greater in the case in the case where the population modification is included because the population modification is an enhancement. The optically thick intensity is given by

$$I^{o.thick} = I^{o.thin} \times \frac{I^{o.thick}}{I^{o.thin}} = I^{o.thin}\bar{g}_r\{\tau_0\} \tag{3.37}$$

If the optically thin emission in the population modified case is labelled $I_r^{o.thin}$ and in the unmodified case it is labelled $I_u^{o.thin}$, and similarly for the optically thick emission, then

$$I_r^{o.thin} > I_u^{o.thin} \text{ and } \bar{g}_r\{\tau_0\} < \bar{g}\{\tau_0\} \Rightarrow I_r^{o.thick} \approx I_u^{o.thick} \tag{3.38}$$

which is true for optical depths even up to ~ 10.

3.9.2 The perspective of scattering into the line-of-sight

The effect of the enhancement of the upper level – or, in other words, the modification to the source function – due to opacity may be viewed from the perspective of

scattering *into* as well as out of the line-of-sight. In radiative transfer theory the term *scattering* has a very specific meaning. Specifically, a scattering event is one in which a photon is absorbed and re-emitted before the absorbing atom or ion suffers any collisions leading to excitation, de-excitation or ionisation. If collisions do occur after the photon is captured and before another photon is emitted then the captured photon is said to be *absorbed*. The distinction between these two events is significant when considering frequency redistribution since scattering leads to a relationship between the emission and absorption profiles. This was discussed in sec. 1.3.1. Within escape probability theory such subtleties are not considered since the techniques are invalid within the optical depth regime where partial frequency redistribution becomes an important issue (see chapter 6). In the context of escape probability theory, scattering into the line-of-sight refers to any absorption of a photon that leads to emission in a line somewhere along a line-of-sight in the direction of that line-of-sight.

Kastner & Bhatia (1992), following the work of Jordan (1967), wrote that the fraction of photons created, escaping in line i is

$$b_i p_{e,j} = \frac{b_i \ \vec{p}_{f,j}}{1 - \sum_i b_i (1 - p_{d,i})(1 - \bar{p}_{f,i})(1 - \vec{p}_{f,i})} \tag{3.39}$$

where $p_{d,i}$ is the photon loss probability (Kastner, 1981), $\vec{p}_{f,j} = p_f(\hat{\nu}, \vec{k}, \tau : 1) \equiv \bar{g}\{\tau_0\}$, and $\bar{p}_{f,i} = p_f(\hat{\nu}, \vec{k}, \tau : 0)$. $\bar{p}_{f,i}$ is the mean probability that a photon emitted anywhere in the layer will travel to the surface and escape. This was described in chapter 2. This approach assumes that the emission at a point is characterised by an optically thin (unmodified) population structure but includes contributions at each point due to light scattered into the line-of-sight from all other points. Thus

$$I^{(o.thick)} \sim \int_{l.o.s.} N_u^{(o.thin)}(s) A_{u\to l}^{(o.thick)} g\{\tau_0(s)\} ds \tag{3.40}$$

where $A_{u\to l}^{(o.thick)}$ is $A_{u\to l}$ divided by the denominator of eq. 3.39.

In the work presented in sec. 3.9 eq. 3.40 is written differently. Specifically, if at each point along a line-of-sight an optically thick population structure is obtained via the solution of eq. 2.6, then the intensity is

$$I \sim \int_{l.o.s.} N_u^{(o.thick)}(s) A_{u\to l}^{(o.thin)} g\{\tau_0(s)\} ds \tag{3.41}$$

In this picture emission at a point is characterised by an optically thick population structure and the only effect of opacity thereafter (excluding, that is, partial frequency redistribution) is due to scattering out of the line-of-sight. There is no scattering into the line-of-sight in this picture as the enhancement due to photons absorbed and re-emitted in line i is taken into account in the $\bar{I}_\nu$ term in eq. 2.6.

Bhatia & Kastner (1999) calculated optically thick populations iteratively starting from an optically thin solution and assuming that the source function is constant throughout the emitting layer. Here a similar approach is taken but for each iteration the populations are calculated at every point throughout the layer using the resolved absorption factor – the absorption factor as a function of space – to obtain an optically thick upper level population distribution. Thus in this work the spatial variation of the source function is included within the iterative process.

3.10 The implications of a spatially varying source function upon escape probability techniques

It has been shown above that the modification to the source function due to photo-absorption has a minimal effect upon the validity of $\bar{g}\{\tau_0\}$ (via eq. 3.25) in describing optically thick spectral emission for disk centre optical depths up to (and perhaps beyond) ~ 10. The viewpoint of scattering into the line-of-sight has been introduced to separate out the spatial variation of the source function, $S_\nu(\mathbf{x})$, due to opacity from that due to the more general variation due to the changes in (T_e, N_e) throughout the region of line formation. It was shown in sec. 3.1 that this variation is likely to be severe in the C II and C III emitting layers. The assumption that a single (T_e, N_e) pair is sufficient to describe the C II and C III emitting layers has thus far not been justified and will be addressed later in chapter 6. However, consider for the moment the intensity from a layer of variable source function. Such emission is given by

$$I \sim \int_0^L S(s) g(\kappa_0 \int_0^s N_l(s') ds') ds \tag{3.42}$$

Here it is assumed that the source function, $S(s)$, is independent of frequency. Putting

$$\begin{aligned} t(s) &= \kappa_0 \int_0^s N_l(s')ds' \\ \Rightarrow \frac{dt}{ds} &= \kappa_0 N_l(s) \end{aligned} \tag{3.43}$$

leads to

$$\begin{aligned} I &\sim \int_0^L S(s(t))g(t)dt \\ \Rightarrow I &\sim \bar{N}_l \bar{g}\{\tau_0\} L f_{los}\{\tau_0\} \end{aligned} \tag{3.44}$$

where

$$f_{los}\{\tau_0\} = \int_0^L \frac{\tilde{N}_u(t)}{\tilde{N}_l(t)} \frac{g(t)}{\bar{g}\{\tau_0\}} dt \tag{3.45}$$

$f_{los}\{\tau_0\}$ is in general line-of-sight and optical depth dependent. The validity of modelling branching ratios and limb-brightening curves using eq. 3.25 hinges upon the nature of the dependence of $f_{los}\{\tau_0\}$ on τ_0 and line-of-sight.

Eq. 3.44 may be written as

$$I \sim \tilde{N}_l \bar{g}\{\tau_0\} L \tag{3.46}$$

where $\tilde{N}_l = \bar{N}_l f_{los}\{\tau_0\}$ is some representative upper level population density and is a function of optical depth and line of sight. The optical depth diagnostic described in sec. 2.1.1 depends upon the cancellation of the density terms in eq. 3.25. The fact that two lines in an intensity ratio arise from a common upper level is no longer guarantee that this cancellation occurs. However, since the diagnostic applies to one line-of-sight at a time, the dependence of $f_{los}\{\tau_0\}$ on line-of-sight is irrelevant.

For the time being it is assumed that $f_{los}\{\tau_0\} = const.$ This will be justified in chapter 6.

3.11 Concluding remarks

The spatially resolved absorption factor, $\Lambda(\tau_0, x)$, that has been develop here for a plane parallel stratified atmosphere, provides a route to examining the implications of

the assumption of constant source function on the validity of the escape probability technique. In particular, it enables the effect of scattering into the line-of-sight to be examined in a consistent manner. It is found that the $\mathcal{G}(\tau_0, x)$ quantity is generally ineffective for describing the spatial variation of absorption characteristics in spectral lines. This deficiency is due to coupling of lines that share a common upper level. Absorption of photons in an optically thick line will lead to a distortion of the upper level population distribution of that line. This will in turn influence the emission and thus also the absorption in that same line and also in other lines stemming from that same upper level. This coupling influences most markedly lines that share an upper level with a line that is more optically thick.

This deficiency in the $\mathcal{G}(\tau_0, x)$ quantity is minimised at layer centre. At an optical depth of 10 in the control line (the C II $2s^2 2p\,^2P_{3/2} - 2s2p^2\,^2P_{3/2}$ line at 904.143 Å), $\mathcal{G}(\tau_0, D/2)$ and $\Lambda(\tau_0, D/2)$ differ by $\sim 30\%$. However, at an optical depth of 1 in the control line the difference is only a few percent and the two quantities both vary monotonically with optical depth (see fig. 3.7a). Thus $\bar{\bar{g}}\{\tau_0/2\}$ is appropriate for describing the modification to the population structure due to opacity for a range of optical depths. Furthermore only modest scaling of this quantity would extend its range of validity up to an optical depth of 10 or more. The value for optical depth at disk centre of the control line deduced in chapter 2 was 1.76. This was the largest of all the C II lines and thus the $\bar{\bar{g}}\{\tau_0/2\}$ is appropriate for the classification of the C II spectral lines. The maximum optical depth in the C III lines was 0.156 which is well within the regime where $\bar{\bar{g}}\{\tau_0/2\}$ is valid.

The modified population density distributions do not display such sensitivity to the coupling effects described above since they are controlled by the strongest, and thus thickest lines which are the least influenced by these indirect effects. Moreover the predicted limb brightening curves show less sensitivity. These curves indicate that for $\tau_0 \sim 10$ in the control line, scattering into the line-of-sight is non-negligible. At optical depths less than this the modification to the source function due to opacity is not manifested in the emergent intensities. This implies an upper limit to the line-of-sight averaged escape probability, $\bar{g}\{\tau_0\}$, of $\sim \tau_0 = 10$. This is identical to the upper limit found by Kastner (1999) based on an intensity/linewidth method to

deduce optical depths from spectral observations using escape probabilities.

Chapter 4

The effects of spectral line blending on photo-absorption

In chapter 3 the variation of the source function with respect to space was considered but in general it is also dependent on frequency. This dependence arises from any phenomenon that causes the emission and absorption profiles to be shifted and/or distorted with respect to one another. For example, photon scattering can lead to distorted emission profiles in the case of partial frequency redistribution. The probability of absorption (i.e. the opacity) is greatest at line centre but since there may be a change in direction of propagation in the scattering process, Doppler shifts can lead to a diffusion of photons toward the line wings. Also if a plasma is exposed to a radiation field which arises from a region that is moving relative to it, the resultant emission profiles will be distorted and asymmetric.

Another contributer to frequency dependence is spectral line blending. When two spectral lines overlap in frequency space, photons from one line may be absorbed by the other. This leads to an enhancement or deficit in the emergent line intensities depending on the nature of the overlap. For instance, if one line is thick and the other thin, then the thin one will be attenuated due to absorption of its photons by the thick line. Such absorption, however, will enhance the upper level of the thick transition and thus result in a relative enhancement of the thick line emission. Hence, in this instance, blending thickens the thin line and thins the thick one. Line shapes are also

influenced by the fact that photo-absorption will no longer be symmetric about line centre (the term $\bar{I}_\nu \phi(\nu)$ is not symmetric about ν_0 when there is line blending).

Fig. 2.10a shows an example of line blending in an opacity modified multiplet. Blending influences both the emission and absorption and so if escape probability techniques are to be used then account must be taken of blending within the escape probability and absorption factor expressions.

In this chapter line blending is considered within the escape probability framework. Spatially resolved quantities are derived as in chapter 3 and are used to calculate optically thick population distributions and limb-brightening curves in order to assess the validity of the line-of-sight averaged escape probability in the case of blended spectral lines.

4.1 Blended escape probabilities

Blending influences the probability of escape in that it increases the number of potential absorbers. Consider the case of M lines blended together. The monochromatic transmission factor of a line in the blend is

$$T_\nu(s_1, s_2) = exp\left\{-\sum_n \tau_\nu^{(n)}(s_1, s_2)\right\} \tag{4.1}$$

where $\tau_\nu^{(n)}(s_1, s_2)$ is the optical depth at frequency ν between two points s_1 and s_2 of the n^{th} line in the blend, i.e.

$$\tau_0^{(n)}(s_1, s_2) = \int_{s_1}^{s_2} \kappa_0^{(n)}(s) ds \tag{4.2}$$

Thus the escape probability is no longer purely a function of the optical depth of one line. Rather, it is dependent on a set of M optical depths, $\{\tau_0^{(n)}\}$. If it is assumed that all the lines in the blend have the same width (a reasonable assumption they are all of the same ion) and define υ_{in} as

$$\upsilon_{in} = \frac{\nu_0^{(i)} - \nu_0^{(n)}}{\Delta\nu_D} \tag{4.3}$$

then the mean escape probability of a photon emitted in line i at a point s along some line-of-sight is

$$g^{(i)}[\{\tau_0^{(n)}\},\{\upsilon_{in}\}] = \frac{1}{\sqrt{\pi}}\int_{-\infty}^{\infty} e^{-u^2} exp\left\{-\sum_n \tau_0^{(n)}(s)e^{-(u+\upsilon_{in})^2}\right\} du \qquad (4.4)$$

From this the blended line-of-sight averaged escape probability (formerly $\bar{g}\{\tau_0\}$) follows immediately as

$$\bar{g}^{(i)}[\{\tau_0^{(n)}\},\{\upsilon_{in}\}] = \frac{1}{\sqrt{\pi}}\int_{-\infty}^{\infty} e^{-u^2}\left[\frac{1-exp\left\{-\sum_n \tau_0^{(n)}e^{-(u+\upsilon_{in})^2}\right\}}{\sum_n \tau_0^{(n)}e^{-(u+\upsilon_{in})^2}}\right] du \qquad (4.5)$$

Both $g^{(i)}[\{\tau_0^{(n)}\},\{\upsilon_{in}\}]$ and $\bar{g}^{(i)}[\{\tau_0^{(n)}\},\{\upsilon_{in}\}]$ are prescribed by a set of optical depths,

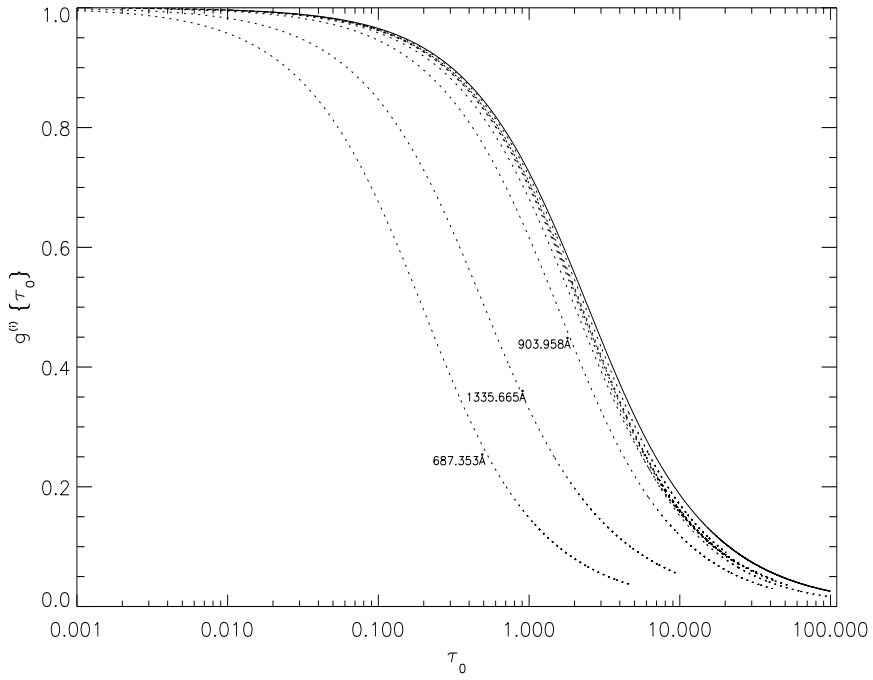

Figure 4.1: Line-of-sight averaged escape probabilities versus optical depth excluding line blending ($\bar{g}\{\tau_0\}$ – solid line) and including line blending for a selection of spectral lines of C II ($\bar{g}^{(i)}\{\tau_0\}$ – dotted lines). The three cases which deviate most markedly from the unblended result are labelled.

$\{\tau_0^{(n)}\}$ and a set of *overlap parameters* $\{\upsilon_{in}\}$. The latter are constants, though they

may act as variable parameters in an emission model or diagnostic. Furthermore, the set of optical depths may be related via eq. 2.24 and so the escape probabilities become prescribed by a single optical depth and a set of optical depth ratios, $\{\tau_0^{(n)}/\tau_0^i\}$. Thus $g^{(i)}[\{\tau_0^{(n)}\},\{\upsilon_{in}\}]$ and $\bar{g}^{(i)}[\{\tau_0^{(n)}\},\{\upsilon_{in}\}]$ become $g^{(i)}\{\tau_0\}$ and $\bar{g}^{(i)}\{\tau_0\}$ and may be plotted as functions of optical depth. Fig. 4.1 shows $\bar{g}^{(i)}\{\tau_0\}$ versus optical depth for a selection of C II spectral lines. It is evident from this graph that, as expected, the unblended result represents an upper limit since blending leads to additional attenuation due to overlapped components.

This does not negate the statement made above that blending can lead to an enhancement of a spectral line. Blending will always decrease the probability of escape but it will also lead to an enhancement of the upper levels of optically thick lines and thus to an enhancement in emission. The combined effect can be to enhance or deplete the emergent intensity. Which will be the case may be determined using a blended absorption factor.

4.2 The blended absorption factor

Photo-absorption at a point in a plasma is influenced by blending in two ways. Firstly, photons of more than one line may be absorbed. Secondly, those photons may be absorbed by a number of lines en-route. The blended absorption factor quantities may be derived following the same reasoning as before but with $j_\nu^{(tot)}$ and $\kappa_\nu^{(tot)}$ replacing j_ν and κ_ν where

$$j_\nu^{(tot)} = \sum_n j_\nu^{(n)} = \sum_n \frac{\omega_l^{(n)}}{\omega_u^{(n)}} \frac{2\nu_0^2}{c^2} \frac{N_u^{(n)}}{N_l^{(n)}} \kappa_\nu^{(n)} \tag{4.6}$$

with

$$\kappa_\nu^{(n)} = \kappa_0^{(n)} N_l^{(n)} e^{-(u+\upsilon_{in})^2} \tag{4.7}$$

$$\Rightarrow j_\nu^{(tot)} = \sum_n \frac{\omega_l^{(n)}}{\omega_u^{(n)}} \frac{2\nu_0^2}{c^2} N_u^{(n)} \kappa_0^{(n)} e^{-(u+\upsilon_{in})^2} \tag{4.8}$$

and

$$\kappa_\nu^{(tot)} = \sum_n \kappa_\nu^{(n)} = \sum_n \kappa_0^{(n)} N_l^{(n)} e^{-(u+\upsilon_{in})^2} \tag{4.9}$$

These give

$$\bar{\bar{g}}^{(i)}\{\tau_0/2\} = 1 - \frac{\omega_u^{(i)}}{\omega_l^{(i)}} \frac{N_l^{(i)}}{N_u^{(i)}} \int_{-\infty}^{\infty} \frac{c^2}{2\nu^2} \bar{I}_\nu \phi_\nu d\nu \tag{4.10}$$

with

$$\bar{I}_\nu = \frac{j_\nu^{(tot)}}{\kappa_\nu^{(tot)}} \left[1 - e^{-\kappa_\nu^{(tot)} x_1} + \kappa_\nu^{(tot)} x_1 E_1 \left\{\kappa_\nu^{(tot)} x_1\right\}\right] \tag{4.11}$$

Now

$$\begin{aligned} \frac{j_\nu^{(tot)}}{\kappa_\nu^{(tot)}} &= \frac{\sum_n \frac{\omega_l^{(n)}}{\omega_u^{(n)}} \frac{2\nu_0^2}{c^2} \frac{N_u^{(n)}}{N_l^{(n)}} \kappa_\nu^{(n)}}{\sum_n \kappa_0^{(n)} N_l^{(n)} e^{-(u+v_{in})^2}} \\ &= \frac{2\nu_0^2}{c^2} \frac{N_u^{(i)}}{N_l^{(i)}} \frac{\sum_n \frac{\omega_l^{(n)}}{\omega_u^{(n)}} \frac{N_u^{(n)}}{N_u^{(i)}} \frac{\kappa_0^{(n)}}{\kappa_0^{(i)}} e^{-(u+v_{in})^2}}{\sum_n \frac{\tau_0^{(n)}}{\tau_0^{(i)}} e^{-(u+v_{in})^2}} \end{aligned} \tag{4.12}$$

Therefore

$$\begin{aligned} \bar{\bar{g}}^{(i)}\{\tau_0/2\} = \; 1 - \; & \frac{\omega_u^{(i)}}{\omega_l^{(i)}} \frac{1}{\sqrt{\pi}} \int_{-\infty}^{\infty} e^{-u^2} \frac{\sum_n \frac{\omega_l^{(n)}}{\omega_u^{(n)}} \frac{N_u^{(n)}}{N_u^{(i)}} \frac{\kappa_0^{(n)}}{\kappa_0^{(i)}} e^{(u+v_{in})^2}}{\sum_n \frac{\tau_0^{(n)}}{\tau_0^{(i)}} e^{-(u+v_{in})^2}} \Bigg[1 - \\ & exp\left\{-\frac{1}{2} \sum_n \tau_0^{(n)} e^{-(u+v_{in})^2}\right\} + \\ & \frac{1}{2} \sum_n \tau_0^{(n)} e^{-(u+v_{in})^2} E_1 \left\{\frac{1}{2} \sum_n \tau_0^{(n)} e^{-(u+v_{in})^2}\right\}\Bigg] du \end{aligned} \tag{4.13}$$

$$\tag{4.14}$$

From this $\mathcal{G}^{(i)}(\tau_0, x)$ follows as

$$\mathcal{G}^{(i)}(\tau_0, x) = \frac{1}{2}\left(\bar{\bar{g}}^{(i)}\{\tau_0^+\} + \bar{\bar{g}}^{(i)}\{\tau_0^-\}\right) \tag{4.15}$$

Similarly

$$\Lambda^{(i)}(\tau_0, x_0) = 1 - \frac{\omega_u^{(i)}}{\omega_l^{(i)}} \frac{N_l^{(i)}(x_0)}{N_u^{(i)}(x_0)} \int \frac{c^2}{2\nu^2} \bar{I}_\nu \phi_\nu d\nu \tag{4.16}$$

with

$$\begin{aligned}\bar{I}_\nu &= \frac{1}{2}\left[\int_0^{x_0} j_\nu^{(tot)}(x)E_1\left\{\int_x^{x_0}\kappa_\nu^{(tot)}(x')dx'\right\}dx + \int_{x_0}^{\Delta x} \mathrm{J}_\nu^{(tot)}(x)E_1\left\{\int_{x_0}^{x}\kappa_\nu^{(tot)}(x')dx'\right\}\right] \\ &= \frac{2\nu_0^2}{c^2}\left[\int_0^{x_0}\sum_n \frac{\omega_l^{(n)}}{\omega_u^{(n)}}N_u^{(n)}\kappa_0^{(n)}e^{-(u+v_{in})^2}E_1\left\{\sum_n \tau_0^{(n)}(x,x_0)e^{-(u+v_{in})^2}\right\}dx + \right. \\ &\quad \left.\int_{x_0}^{\Delta x}\sum_n \frac{\omega_l^{(n)}}{\omega_u^{(n)}}N_u^{(n)}\kappa_0^{(n)}e^{-(u+v_{in})^2}E_1\left\{\sum_n \tau_0^{(n)}(x_0,x)e^{-(u+v_{in})^2}\right\}dx\right] \qquad (4.17)\end{aligned}$$

and thus

$$\begin{aligned}\Lambda^{(i)}(\tau_0,x_0) = 1- &\frac{1}{2\sqrt{\pi}}\frac{\omega_u^{(i)}}{\omega_l^{(i)}}\frac{N_l^{(i)}(x_0)}{N_u^{(i)}(x_0)}\int_{-\infty}^{\infty}e^{-u^2}\left[\int_0^{x_0}\sum_n\frac{\omega_l^{(n)}}{\omega_u^{(n)}}N_u^{(n)}(x)\kappa_0^{(n)}e^{-(u+v_{in})^2}\times\right. \\ &E_1\left\{\sum_n\tau_0^{(n)}(x,x_0)e^{-(u+v_{in})^2}\right\}dx + \\ &\int_{x_0}^{\Delta x}\sum_n\frac{\omega_l^{(n)}}{\omega_u^{(n)}}N_u^{(n)}(x)\kappa_0^{(n)}e^{-(u+v_{in})^2}\times \\ &\left.E_1\left\{\sum_n\tau_0^{(n)}(x_0,x)e^{-(u+v_{in})^2}\right\}dx\right]du \qquad (4.18)\end{aligned}$$

As in the unblended case, the absorption factor, $\Lambda^{(i)}(\tau_0,x_0)$, depends on the upper level population distribution via the $N_u^{(i)}(x)/N_u^{(i)}(x_0)$ term. In this way the absorption factor is sensitive to the distortion of the upper level population density distribution relative to the optically thin one which places a constraint on the effectiveness of the first order iterative scheme employed here. However, unlike in the emergent flux case ($\bar{g}^{(i)}\{\tau_0\}$), there is also an explicit dependence here upon upper level population densities, $N_u^{(n)}$, in both eqs 4.13 and 4.18. The ratios $N_u^{(n)}/N_u^{(i)}$ are sensitive to opacity and thus further restricts the range of optical depths for which eq. 4.18 may be calculated using the method described in chapter 3. Furthermore, eq. 4.13 must now also be calculated iteratively. However, the purpose of this work is not to develop effective techniques for solving the equations of radiative transfer and statistical balance *simultaneously*, but rather to examine the optical depth regime within which these equations may be *naturally* linearised and de-coupled thus avoiding the need for their simultaneous solution. Eqs 4.13 and 4.18 are calculable using first order techniques

to optical depths beyond the point where the simple escape probability expressions break down. Thus more sophisticated schemes are not necessary here.

Fig. 4.2a shows the C II $2s2p^2\,{}^2D_{5/2}/2s^22p\,{}^2P_{1/2}$ population density ratio versus optical depth, in the blended and unblended cases. These are calculated using eqs 4.13 and 2.39. For this ratio it is clear that the variation with optical depth is more rapid in the blended case than in the unblended case and this is true for all the C II levels. This is not surprising since, as stated above, blending increases the effect of opacity in a line due to absorptions by other lines. Fig. 4.2b shows the C II $2s2p^2\,{}^2D_{3/2}/2s2p^2\,{}^2D_{5/2}$ population density ratio versus τ_0. This curve also demonstrates the dependence of upper level populations upon line blending and illustrates the difficulty in calculating $\bar{\bar{g}}^{(i)}\{\tau_0/2\}$ which depend on such density ratios. These ratios determine the extent to which absorption in a line is influenced by overlapped components and since they depend on both optical depth and linewidth, eq. 4.13 must be calculated iteratively.

In fig. 4.3 $\bar{\bar{g}}^{(i)}\{\tau_0/2\}$ is plotted versus *degree of overlap* (model line width/observed line width) for a selection of spectral lines of C II. This plot corresponds to a single set of optical depths such that the optical depth in the $2s^22p\,{}^2P_{3/2} - 2s2p^2\,{}^2P_{3/2}$ line at 904.143 Å is 3. It is evident from this that blending always leads to a net decreases in the absorption factor – i.e. it increases the effect of opacity upon the population structure. However, it is interesting to note that in the $2s^22p\,{}^2P_{3/2} - 2s^23d\,{}^2D_{3/2}$ line at 687.353 Å, blending initially leads to a decrease in $\bar{\bar{g}}^{(i)}\{\tau_0/2\}$ but this ultimately reverses as the degree of overlap increases. The initial decrease in the absorption factor is due to the increase in absorption of 687.353 Å photons by the $2s^22p\,{}^2P_{3/2} - 2s^23d\,{}^2D_{5/2}$ line at 687.346 Å. The influence of the 687.346 Å component on the 687.353 Å one through blending is determined by the relative strength of the two lines which is determined by the $N_{5/2}/N_{3/2}$ ratio of the C II $2s^23d\,{}^2D$ term. This ratio is also dependent on the degree of blending. The upturn in the $\bar{\bar{g}}^{(i)}\{\tau_0/2\}$ versus degree of overlap trend for the 687.353 Å line corresponds to the increase of emission in the 687.353 Å line due to the enhancement of the $2s^23d\,{}^2D_{5/2}$ level 'winning' over the absorption of photons by the 687.346 Å component.

It can be seen in fig. 4.3 that, as expected, the absorption factor only varies in the cases where there is blending. The indirect effects described above do not influence the

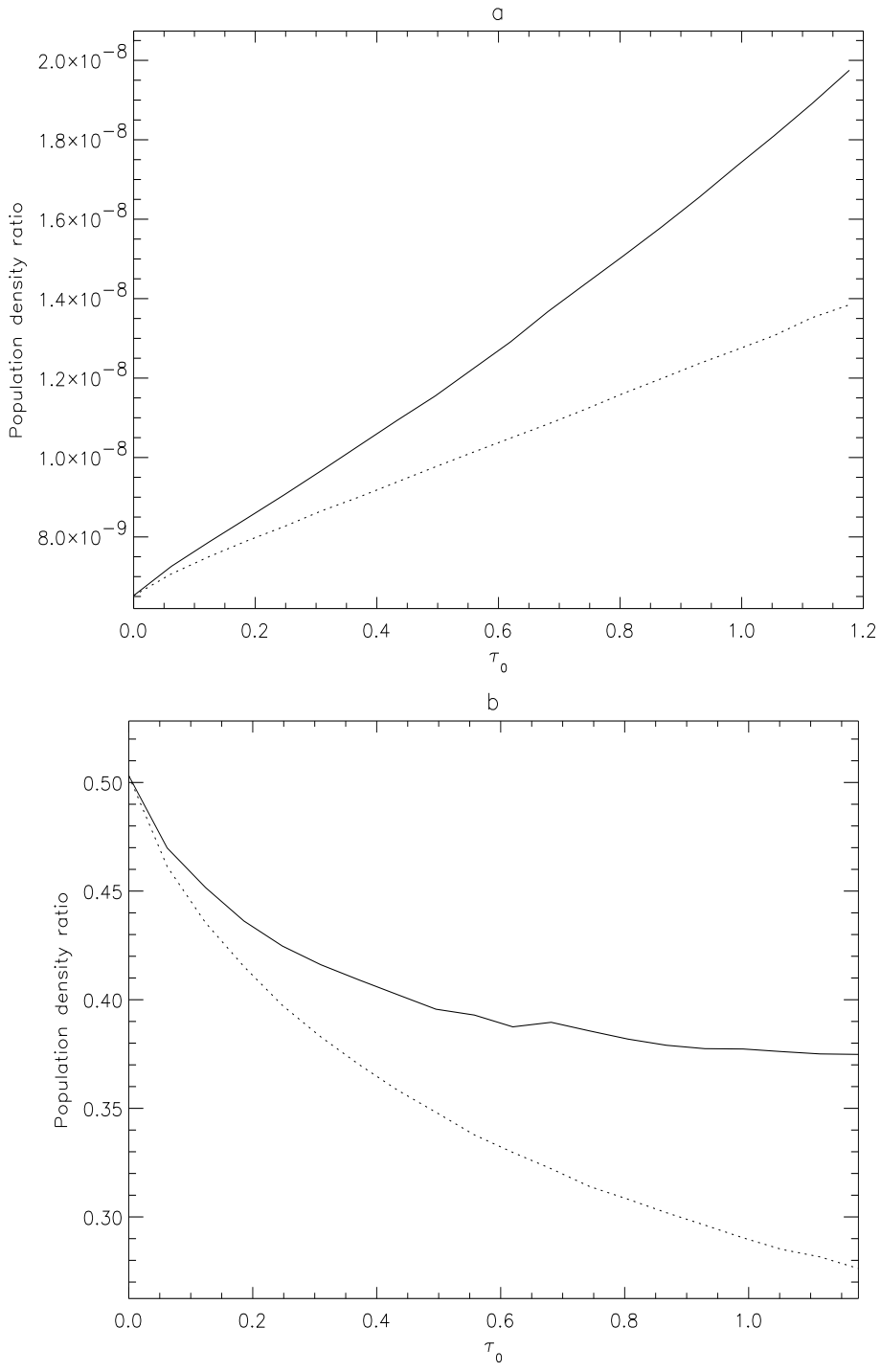

Figure 4.2: Plots of (a) C II $2s2p^2\,{}^2D_{5/2}/2s^22p\,{}^2P_{1/2}$ and (b) C II $2s2p^2\,{}^2D_{3/2}/2s2p^2\,{}^2D_{5/2}$ population density ratios versus τ_0. The solid line corresponds to the blended calculation and the dotted line to the unblended calculation.

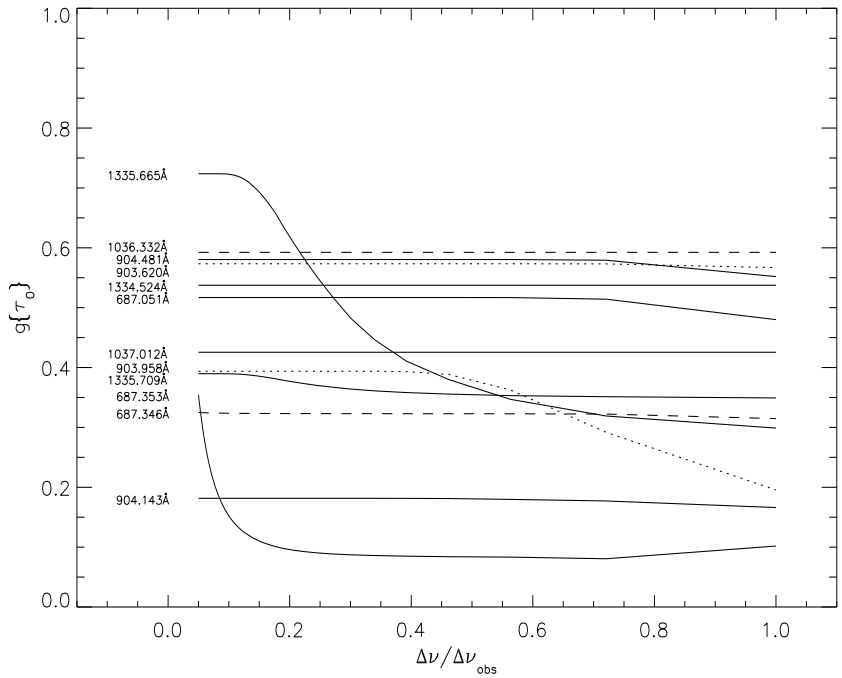

Figure 4.3: $\bar{\bar{g}}^{(i)}\{\tau_0/2\}$ versus *degree of overlap* (model line width/observed line width) for a selection of spectral lines of C II. This plot corresponds to a single set of optical depths such that the optical depth in the $2s^2 2p\,^2P_{3/2} - 2s2p^2\,^2P_{3/2}$ line at 904.143 Å is 3. The variety of line-styles used are to clarify the distinctions between lines.

unblended lines. This is because $\bar{\bar{g}}\{\tau_0/2\}$ (the unblended quantity) is only dependent on optical depth. Consequently the indirect influence of blending on the upper level population densities of *unblended* lines does not manifest itself. Such indirect effects are expected to be present when the spatial dependence of the absorption factor is considered (see sec. 4.4).

4.3 Modelling emergent intensities with blending included

If it is assumed that the source function is constant, or if an optically thick upper level population distribution has been obtained using eq. 4.18, emergent intensities may be calculated in the same way as in sec. 3.9. Blending does not increase the computational complexity of this calculation since neither $g^{(i)}\{\tau_0\}$ nor $\bar{g}^{(i)}\{\tau_0\}$ depend upon upper level population density ratios. Rather they depend on lower level ones which are not sensitive to optical depth.

Fig. 4.4 shows limb brightening curves for the C II $2s^2 2p\,^2P_{3/2} - 2s2p^2\,^2P_{3/2}$ line at 904.143 Å and the C II $2s^2 2p\,^2P_{1/2} - 2s2p^2\,^2P_{3/2}$ line at 903.958 Å. These curves are based on eq. 3.25 in both the unblended and blended cases using $\bar{g}\{\tau_0\}$ (eq. 2.17) and $\bar{g}^{(i)}\{\tau_0\}$ (eq. 4.5) respectively. Though there is still a significant issue of the variation of the source function to address, it is clear that even for a disk centre optical depth of ~ 0.1 blending plays a significant role. Given that the indirect population modification effects seen in chapter 3 influenced the weaker line (the 903.958 Å line) more than the stronger one (the 904.143 Å line), the influence of blending might also be expected to affect the weaker line more. Fig. 4.4b shows, however, that this is not so. Evidently the low optical depth minimises the effect of blending, since the blended and unblended escape probabilities converge as $\tau_0 \to 0$.

A further effect of line blending is to produce an asymmetry in the emergent spectral line profiles. This occurs since overlapped lines are generally displaced in frequency space from one another. The emergent line profiles may be examined from eq. 4.5 since

$$I_\nu \sim \bar{N}_u \frac{1}{\sqrt{\pi}} e^{-u^2} \left[\frac{1 - exp\left\{ -\sum_n \tau_0^{(n)} e^{-(u+v_{in})^2} \right\}}{\sum_n \tau_0^{(n)} e^{-(u+v_{in})^2}} \right] \tag{4.19}$$

If blending is neglected eq. 4.19 is the same as that used by Doyle et al. (2000) to study the effects of line broadening due to opacity in spectral lines from the solar TR. Fig. 4.5a shows the C II $2s^2 2p\,^2P - 2s2p^2\,^2P$ multiplet at ~ 904 Å for a disk centre optical depth of 1, and a line-of-sight optical depth of 10. The calculation uses eq. 4.19

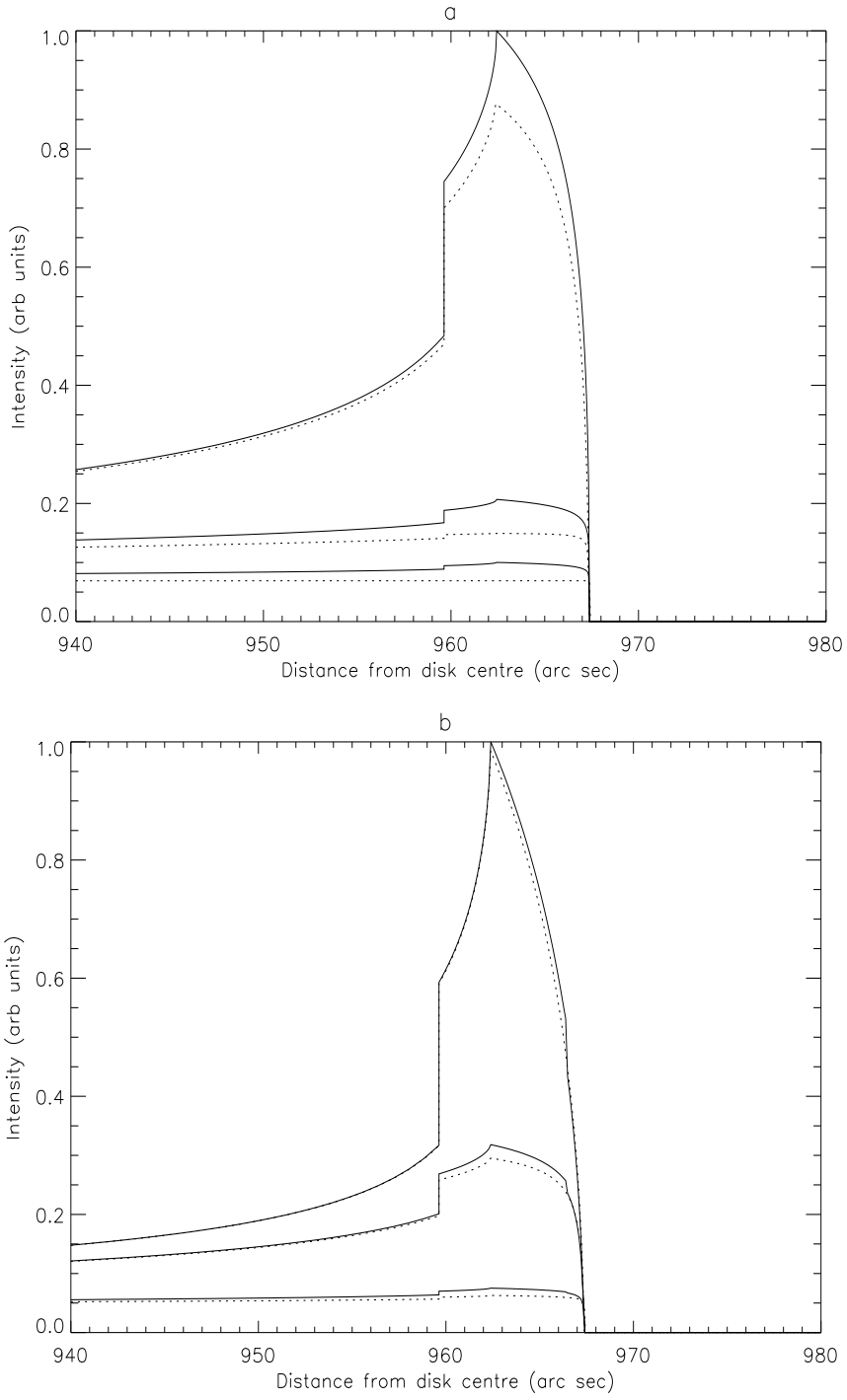

Figure 4.4: Predicted limb-brightening curves for (a) the C II $2s^2 2p^2 P_{3/2} - 2s2p^2\,{}^2P_{3/2}$ line at 904.143 Å and (b) the C II $2s^2 2p^2 P_{1/2} - 2s2p^2\,{}^2P_{3/2}$ line at 903.958 Å, calculated using eq. 3.25 excluding line blending (solid lines) and including line blending (dotted lines). Intensities are calculated in a constant density model. Each graph contains three sets of curves corresponding to disk centre optical depths of 0.1, 1 and 4. The curves are scaled to match at disk centre.

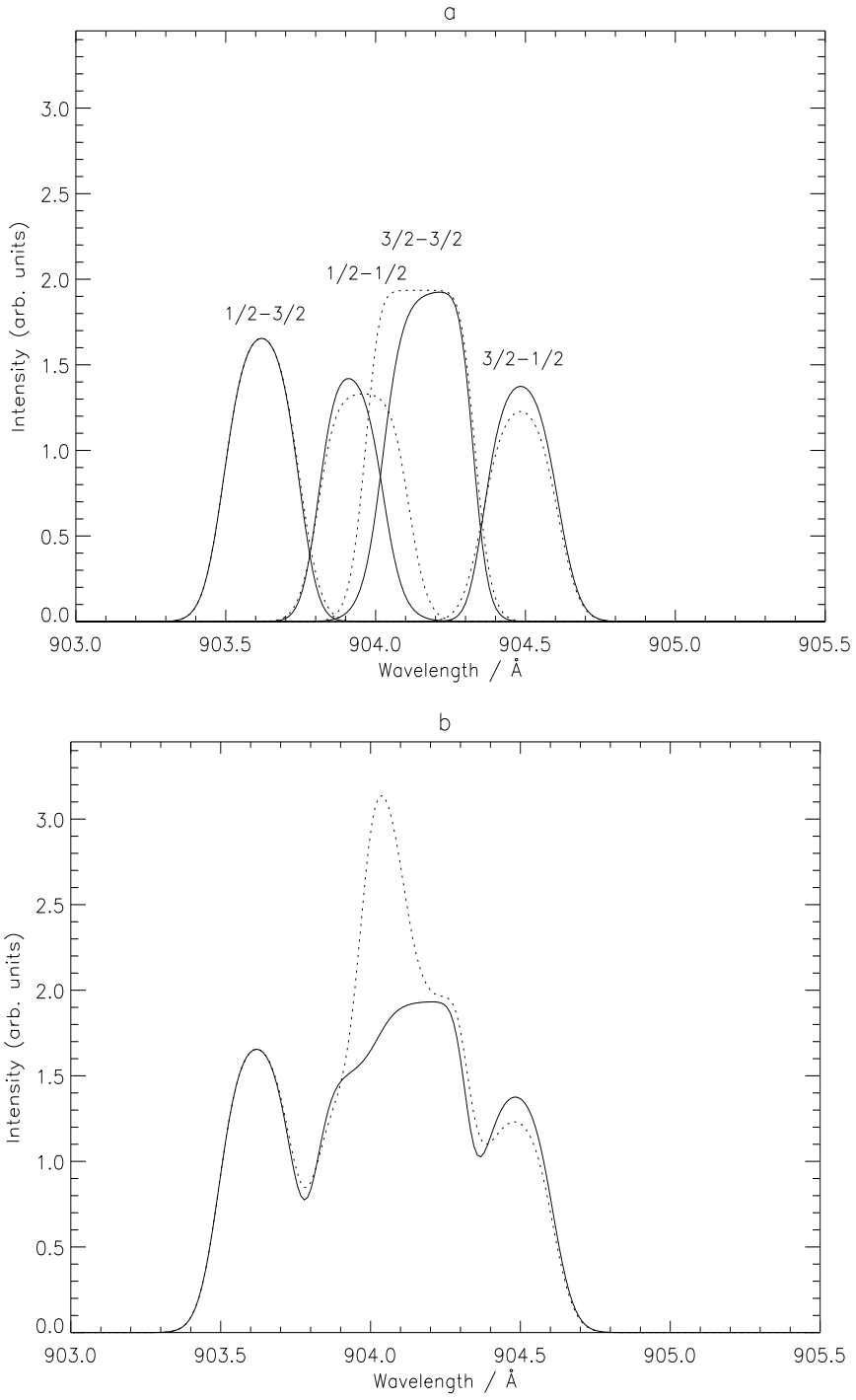

Figure 4.5: (a) Predicted spectral line profiles of the C II $2s^2 2p\,^2P - 2s2p^2\,^2P$ multiplet at ~ 904 Å for a disk centre optical depth of 1, and a line-of-sight optical depth of 10 with blending included (solid line) and blending excluded (dotted line). (b) C II 904 Å multiplet emission summed over each of the lines. Solid and dotted lines as in (a).

and is contrasted with the unblended case. Fig. 4.5b shows the multiplet envelope in each case and illustrates a significant difference to the shape of the multiplet as a whole, especially in the vicinity of the blend. Fig. 4.6 shows in more detail the blended 1/2–1/2 and 3/2–3/2 components. The distortion of the lineshapes is clearly present.

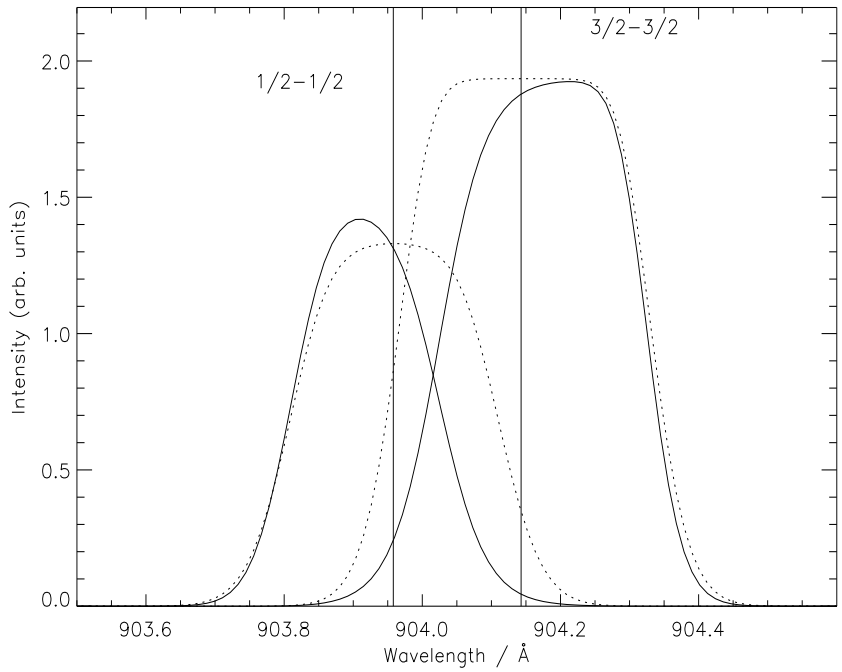

Figure 4.6: Predicted spectral line profiles of the C II $2s^2 2p\,^2P - 2s2p^2\,^2P$ 1/2–1/2 and 3/2–3/2 lines at 903.958 Å and 904.143 Å respectively, with blending included (solid line) and blending excluded (dotted line). The vertical lines indicate the rest wavelengths. Note that blending makes the 1/2–1/2 and 3/2–3/2 components look shifted to the left and right respectively.

Also evident is the further attenuation of the intensity of the 3/2–3/2 component in the blended case as compared with the unblended calculation. This is due to 3/2–3/2 photons being absorbed by the 1/2–1/2 line. In the 1/2–1/2 case, however, the peak intensity is greater when blending is included than when it is not. This seems to be in contradiction to fig. 4.1 which demonstrates that $\bar{g}^{(i)}\{\tau_0\}$ is maximal when there is no blending. That is, the attenuation is minimal in the unblended case. This is true for although the attenuation in the 1/2–1/2 line is increased due to blending with the

3/2–3/2 line, the upper level population density of the $2s2p^2\,{}^2P_{1/2}$ level is enhanced due to absorption of 3/2–3/2 photons in the 1/2–1/2 line. This illustrates the point made at the beginning of the chapter that under certain circumstances blending can lead to an increase in emission. Another interesting feature is that the distortion of the profiles leads to apparent centroid shifts to the blue in the 1/2–1/2 case and to the red in the 3/2–3/2 case.

4.4 The effect of a variable source function on absorption

Shown in figs 4.7 and 4.8 are plots of absorption factors versus position for a selection of spectral lines of C II and for three sets of optical depths. These figures are similar to figs 3.5 and 3.6 but with line blending included. A further difference is that the sets of optical depths correspond to values in the control line (the $2s^22p\,{}^2P_{3/2} - 2s2p^2\,{}^2P_{3/2}$ line at 904.143 Å as before) of 0.1, 1 and 4 as opposed to 0.1, 1, and 10 in the figures of chapter 3. As in figs 3.5 and 3.6 the absorption factor calculations are computed within a constant density atmosphere model. The main features of these graphs may be summarised as follows:

The 1335 Å multiplet

The $2s^22p\,{}^2P_{3/2} - 2s2p^2\,{}^2D_{5/2}$ line at 1335.709 Å shows a slight deviation due to blending with the $2s^22p\,{}^2P_{3/2} - 2s2p^2\,{}^2D_{3/2}$ line at 1335.665 Å which is more optically thin. The 1335.665 Å line itself displays a significant deviation due to blending with the 1335.709 Å component. The 1335.665 Å line is also indirectly modified due to the $2s^22p\,{}^2P_{1/2} - 2s2p^2\,{}^2D_{3/2}$ line at 1334.524 Å (see sec. 3.5). The 1334.524 Å line is as before (sec. 3.5) with a slight modification due to indirect effects caused by the line at 1335.665 Å.

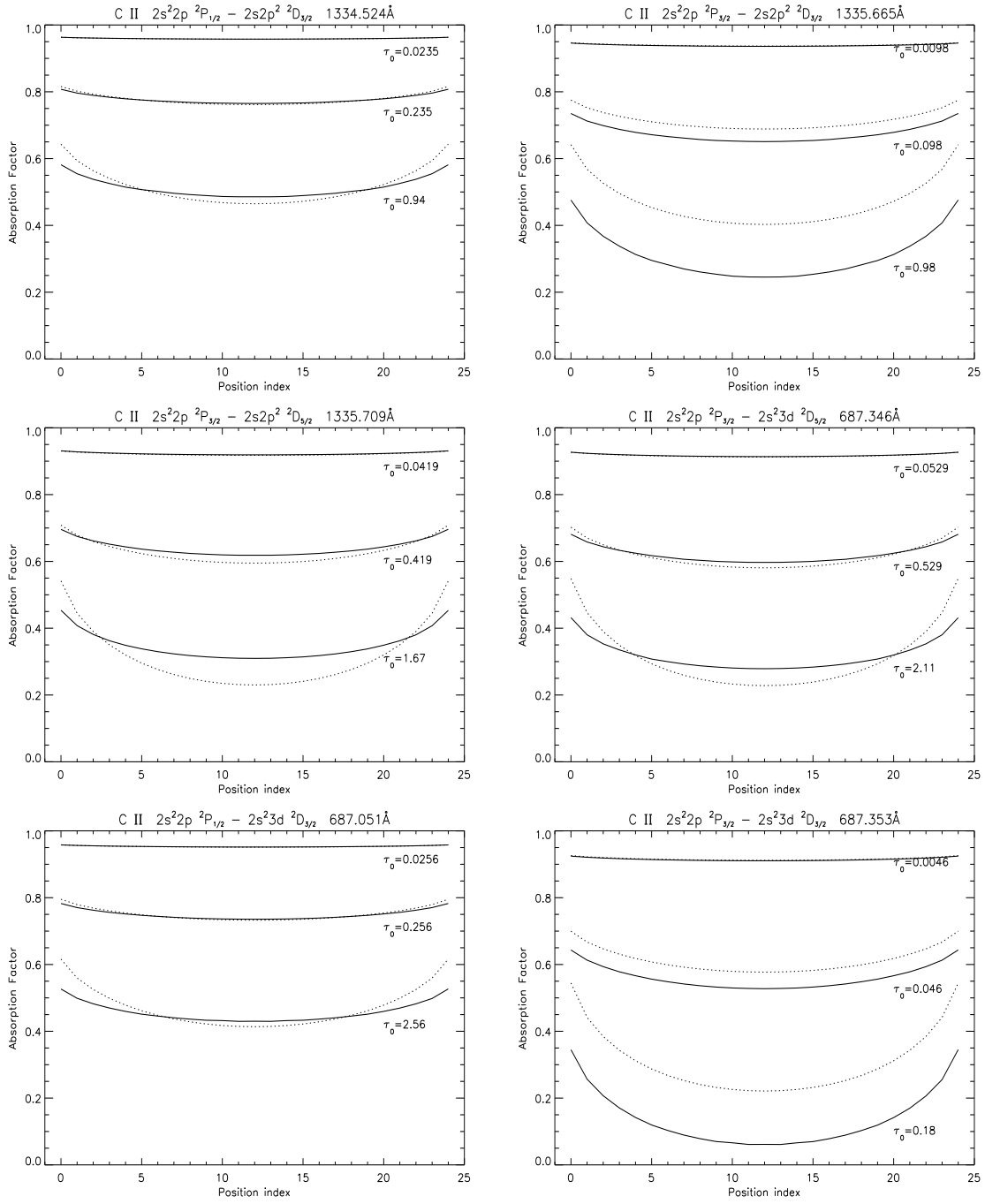

Figure 4.7: Absorption factors with blending included versus position for selected lines of C II corresponding to three sets of optical depths. Absorption factors are calculated iteratively via eqs 4.18 and 2.8. The solid lines are $\Lambda^{(i)}(\tau_0, x)$ and the dotted lines are $\mathcal{G}^{(i)}\{\tau_0, x\}$.

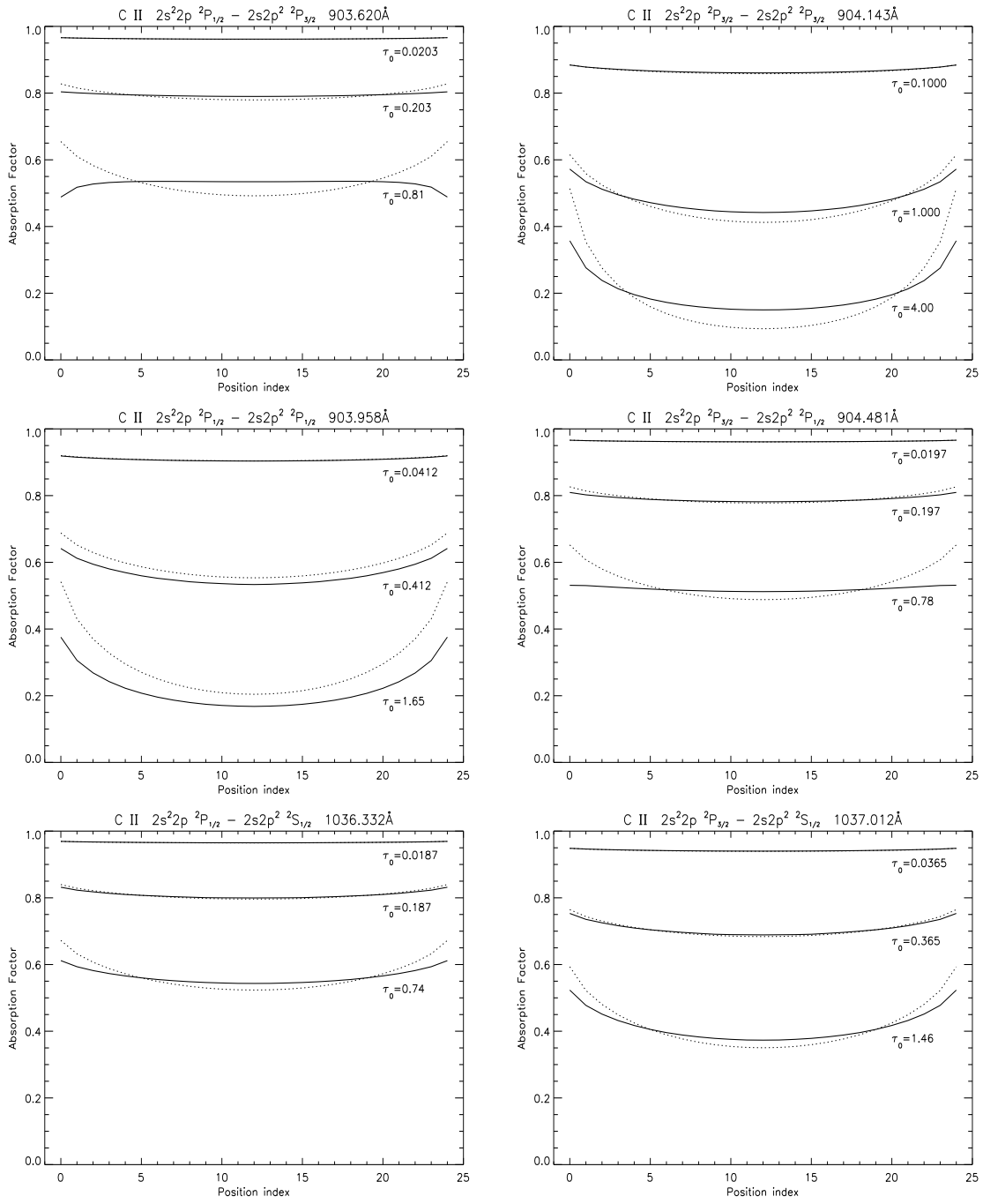

Figure 4.8: Absorption factors with blending included versus position for selected lines of C II as in fig 4.7.

The 687 Å multiplet

The $2s^2 2p\,^2P_{3/2} - 2s^2 3d\,^2D_{5/2}$ line at 687.346 Å shows a slight deviation due to blending with the $2s^2 2p\,^2P_{3/2} - 2s^2 3d\,^2D_{3/2}$ line at 687.353 Å. The $2s^2 2p\,^2P_{1/2} - 2s^2 3d\,^2D_{3/2}$ line at 687.051 Å shows minor modification due to blending with the 687.346 Å line and also moderate modification from indirect effects again due to the 687.346 Å component. The line at 687.353 Å displays significant deviation due to blending with the 687.346 Å component which is more optically thick. There is also indirect modification due to the 687.051 Å line.

The 904 Å multiplet

The $2s^2 2p\,^2P_{1/2} - 2s2p^2\,^2P_{3/2}$ line at 903.620 Å is, as before (see sec. 3.5), indirectly modified due to the $2s^2 2p\,^2P_{3/2} - 2s2p^2\,^2P_{3/2}$ line at 904.143 Å. The 904.143 Å line shows slight modification due to blending with the $2s^2 2p\,^2P_{3/2} - 2s2p^2\,^2P_{1/2}$ and $2s^2 2p\,^2P_{3/2} - 2s2p^2\,^2P_{1/2}$ lines at 903.958 Å and 904.481 Å respectively. The 904.481 Å component displays slight deviation due to blending with the 904.143 Å line and there is indirect modification due to the 903.958 Å component.

The 1036 Å multiplet

These lines are not blended together and they do not share upper levels with any of the above lines. Thus their absorption factors are as before (see sec. 3.5).

Discussion

As in the unblended case, the source function variation manifests itself in eq. 4.18 via the $N_u(x)/N_u(x_0)$ term. Thus it is the shape of the $N_u(x)$ versus x curve that comes into play and not the absolute value of $N_u(x)$. Blending, however, introduces a dependence of the integrand of this equation on $N_u^{(i)}(x)/N_u^{(j)}(x)$ where i and j indicate separate lines in a blend. The effect of this is to decrease the absorption factors everywhere as compared with $\mathcal{G}^{(i)}(\tau_0, x)$. This decrease acts to shift the absorption factor curves downward rather than to distort them further. It is not sufficient,

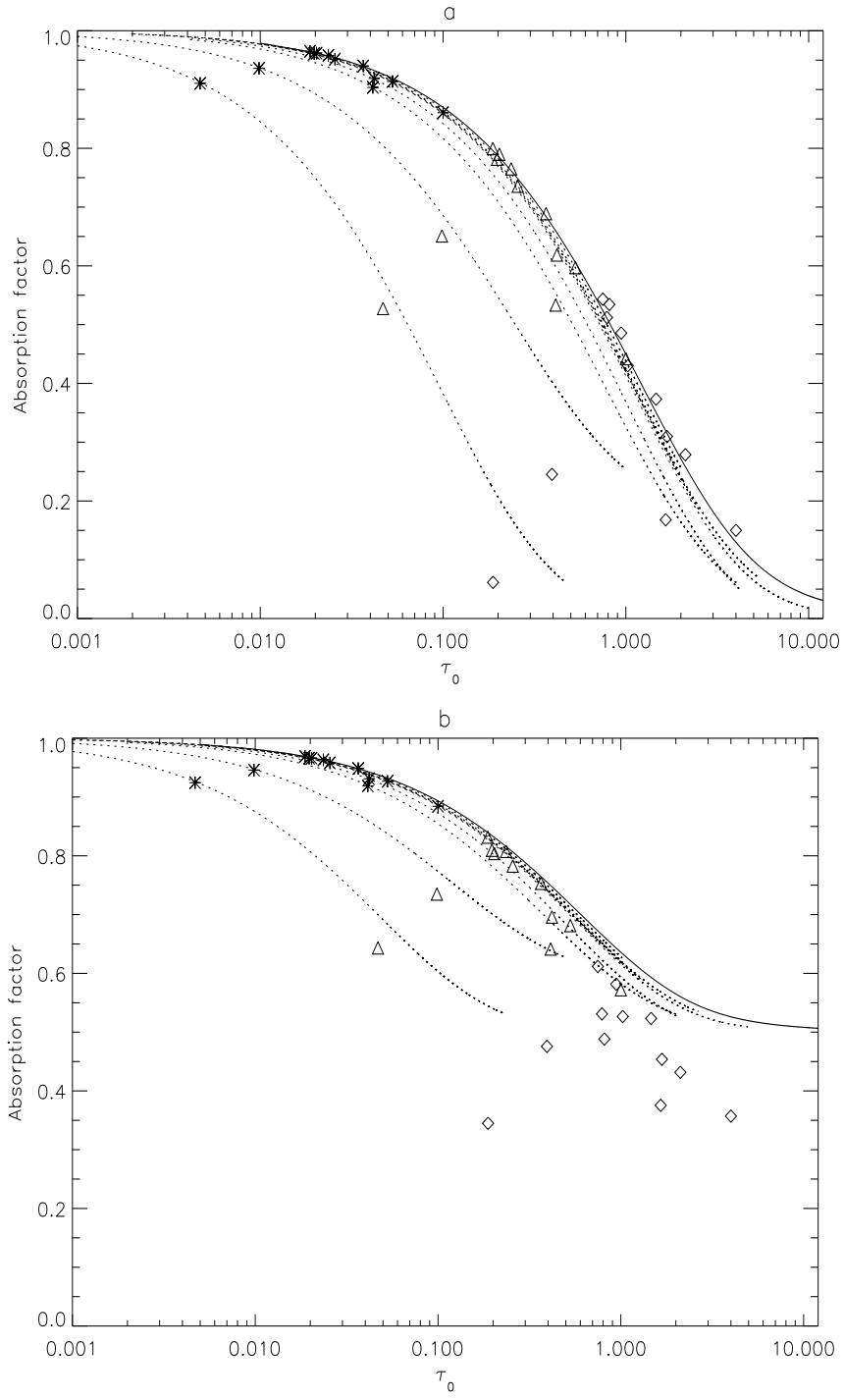

Figure 4.9: Absorption factors including line blending at (a) layer centre ($x = D/2$) and (b) layer edge ($x = 0$) versus optical depth for the constant lower level density model, taken from the plots in figs 4.7 and 4.8. The *'s, $\triangle$'s and $\diamond$'s are the absorption factors, $\Lambda^{(i)}(\tau_0, x)$ (eq. 4.18), corresponding to the three sets of optical depths. The solid line is $\mathcal{G}(\tau_0, x)$ and the dotted lines are $\mathcal{G}^{(i)}(\tau_0, x)$.

however, to say that blending effectively increases the optical depth, although this is certainly an effect (see the summation of optical depths in eq. 4.18).

It is clear that the effects of blending are more severe than the indirect effects on thin lines with thick partners, discussed in chapter 3. Furthermore, blending is more apt to affect lines that markedly influence the population distribution – i.e. the stronger (thicker) lines – unlike the indirect effects which mainly alter the absorption factors of the weaker (thinner) lines.

4.5 The validity of $\mathcal{G}^{(i)}(\tau_0, x)$ in the blended case

It is clear from figs 4.7 and 4.8 that blending decreases the range of optical depths for which $\mathcal{G}(\tau_0, x)$ is effective for describing self absorption in spectral lines. Previously the absorption factors of the strongest and most dominant lines – that is, those that most significantly influence the population structure calculation – broadly speaking followed the $\mathcal{G}(\tau_0, x)$ versus x trend. Moreover, they were in fairly close agreement at layer centre (see figs 3.5 and 3.6). With blending included, though the trends still follow those of $\mathcal{G}^{(i)}(\tau_0, x)$ (indirectly modified lines excepting), the layer centre values can be markedly different (see, for example, the $2s^2 2p\,^2P_{3/2} - 2s2p^2\,^2D_{3/2}$ line at 1335.665 Å shown in fig. 4.7). Significantly, it is not just the weaker, less important (with respect to the population calculation) lines that are so affected.

Figs 4.9a and b show the blended absorption factors at layer centre (a) and the layer edge (b). Unlike the unblended case (see fig. 3.7), at layer centre the absorption factor can not be considered a monotonic decreasing function of optical depth since it is line specific. As in the unblended case, at layer centre $\mathcal{G}^{(i)}(\tau_0, D/2)$ is effective for moderate optical depths. However, for significantly blended lines the optical depth regime where this is true is reduced as compared with the unblended case. At the layer edge indirect effects come into play and $\mathcal{G}^{(i)}(\tau_0, 0)$ (which is identical to $\mathcal{G}^{(i)}(\tau_0, D)$ in the constant density case) is less effective.

Fig. 4.9a displays a degree of agreement between $\mathcal{G}^{(i)}(\tau_0, D/2)$ (i.e. $\bar{\bar{g}}^{(i)}\{\tau_0/2\}$) and $\Lambda^{(i)}(\tau_0, D/2)$ that is greater than that implied by figs 4.7 and 4.8. In the latter two figures the $\mathcal{G}^{(i)}(\tau_0, x)$ values are calculated without iteration. That is, they represent

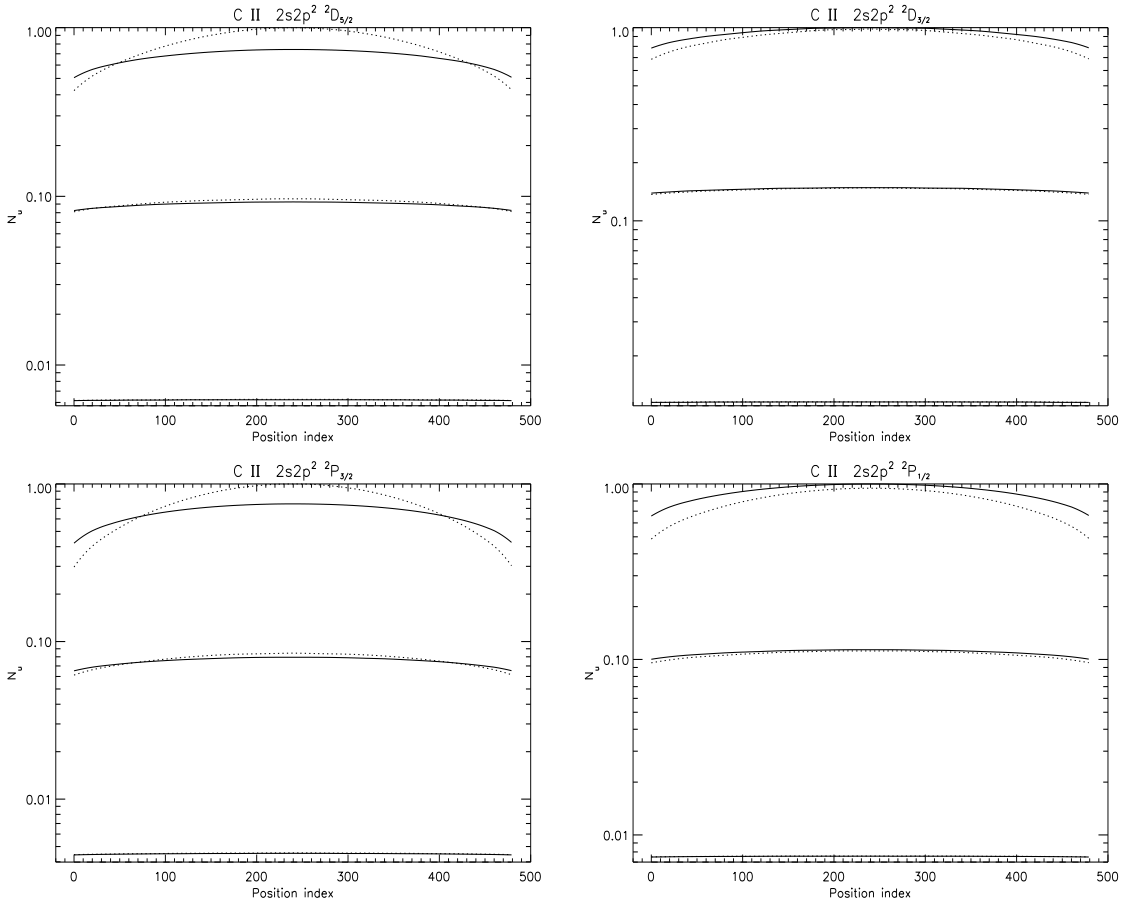

Figure 4.10: Upper level population densities versus spatial position for selected lines of C II. The solid lines correspond to calculations based on $\Lambda^{(i)}(\tau_0, x)$ for the same three sets of optical depths as in figs 4.7 and 4.8. The dotted lines represent the $\mathcal{G}^{(i)}(\tau_0, x)$ based calculations. Values are not absolute but are scaled so that the maximum population density value is unity.

the initial values of the absorption factor in the iterative process. In general, however, $\mathcal{G}^{(i)}(\tau_0, x)$ must be computed iteratively due to its explicit dependence on upper level population density ratios of overlapped lines. In figs 4.9a and b the $\mathcal{G}^{(i)}(\tau_0, x)$ values are computed iteratively and are thus closer to the $\Lambda^{(i)}(\tau_0, x)$ values. Figs 4.9a and b are therefore indicative of the influence of the modification of the source function due to opacity upon absorption factors in the case where blending is included.

The usefulness of the escape probability techniques is that they represent accurate solutions to the radiative transfer and statistical balance equations in a regime in which these equations naturally linearise and de-couple. Line blending re-introduces

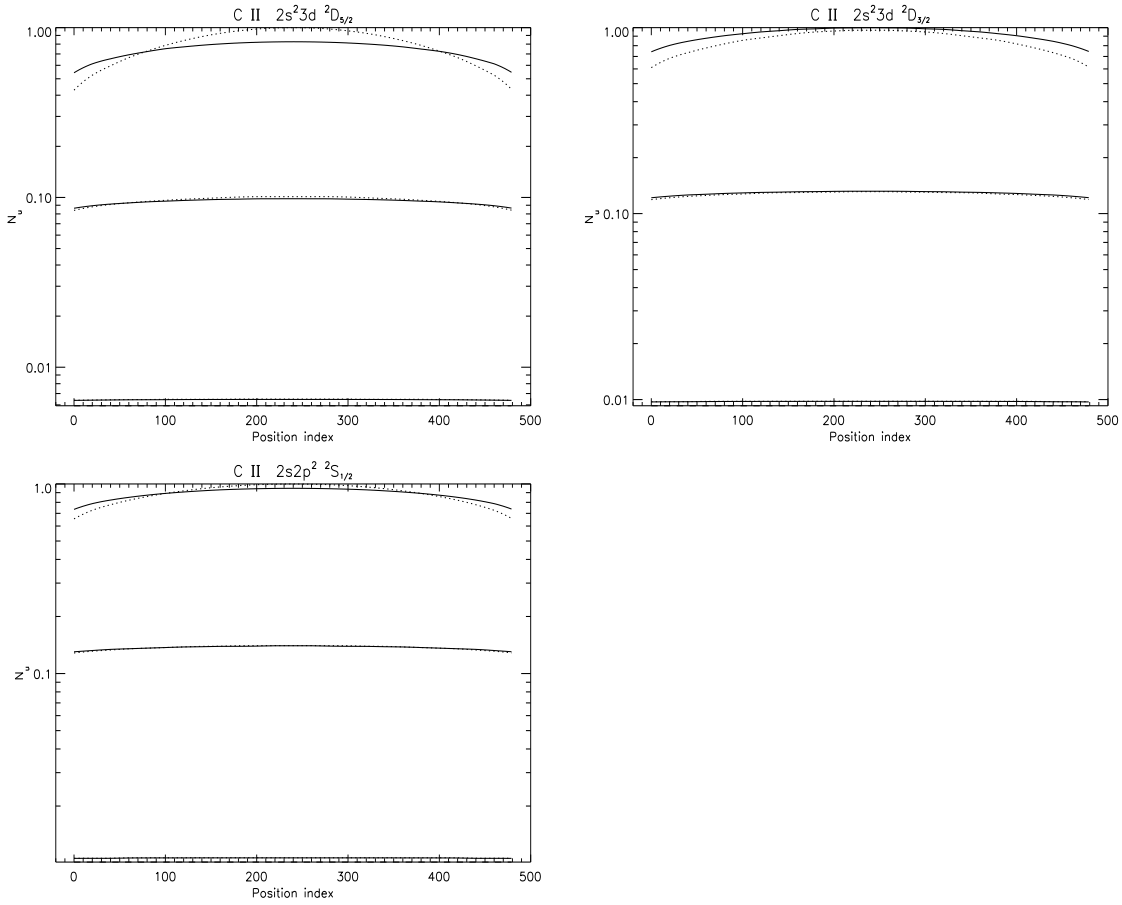

Figure 4.11: Upper level population densities versus spatial position for selected lines of C II. The solid and dotted lines are as in fig. 4.10.

non-linearity into the statistical balance equations via the dependence of the absorption factor on upper level population density ratios. To perform an iterative process to calculate $\mathcal{G}^{(i)}(\tau_0, x)$ therefore compromises the appeal of the absorption factor approach. Computational simplicity may be restored, however, by simply ignoring this non-linearity and utilising upper level population densities deduced from an optically thin calculation thus further restricting the optical depth regime within which $\mathcal{G}^{(i)}(\tau_0, x)$ is effective. In this respect figs 4.7 and 4.8 demonstrate the applicability, or otherwise, of $\mathcal{G}^{(i)}(\tau_0, x)$ for practical use. In these figures the $\Lambda^{(i)}(\tau_0, x)$ curves often seem to follow the $\mathcal{G}^{(i)}(\tau_0, x)$ trends but are shifted downward. If $\mathcal{G}^{(i)}(\tau_0, x)$ is

calculated iteratively then these downward shifts disappear and the results are similar to those of chapter 3, with the deviation of $\Lambda^{(i)}(\tau_0, x)$ from $\mathcal{G}^{(i)}(\tau_0, x)$ minimal at layer centre and significant at the edge, characterised by the degree of distortion of the upper level with respect to the lower. However, the fact that blending effectively increases the optical depth serves to restrict the region of validity of the $\mathcal{G}^{(i)}(\tau_0, x)$ quantity. Nevertheless a spectral line classification that includes the effects of line blending is possible using $\bar{\bar{g}}^{(i)}\{\tau_0/2\}$ providing an iteration process is performed. The validity of this classification is optical depth and line dependent. For most of the C II lines $\bar{\bar{g}}^{(i)}\{\tau_0/2\}$ is effective, as in the unblended case, for disk centre optical depths up to ~ 1. For the most severely blended lines, however, the restriction is more severe.

4.6 The effect of blending upon the density distributions

Upper level population densities for the C II lines in figs 4.7 and 4.8 for the same three sets of optical depths are shown in figs 4.10 and 4.11. These plots have a logarithmic scale that masks somewhat the true extent of the distortion of upper levels. Plots of the same for just the maximum optical depths are shown on a linear scale in figs 4.12 and 4.13.

Increased absorption in blended lines distorts the upper level population density distributions with respect to the lower ones in a manner that increases with optical depth. This effect was seen in the unblended case (see sec. 3.7) but is more severe here since blending serves to increase the radiation field in an overlapped line and also increases the effective optical depth. Moreover, the dependence upon upper level density ratios, discussed in sec. 4.4, has a marked effect upon the absorption factors but does not significantly alter the *shape* of the upper level population density distortion. That is, this secondary effect of blending leads to a population modification which is approximately constant in space. This is significant since it is the extent of the distortion rather than the absolute value of the modification that determines

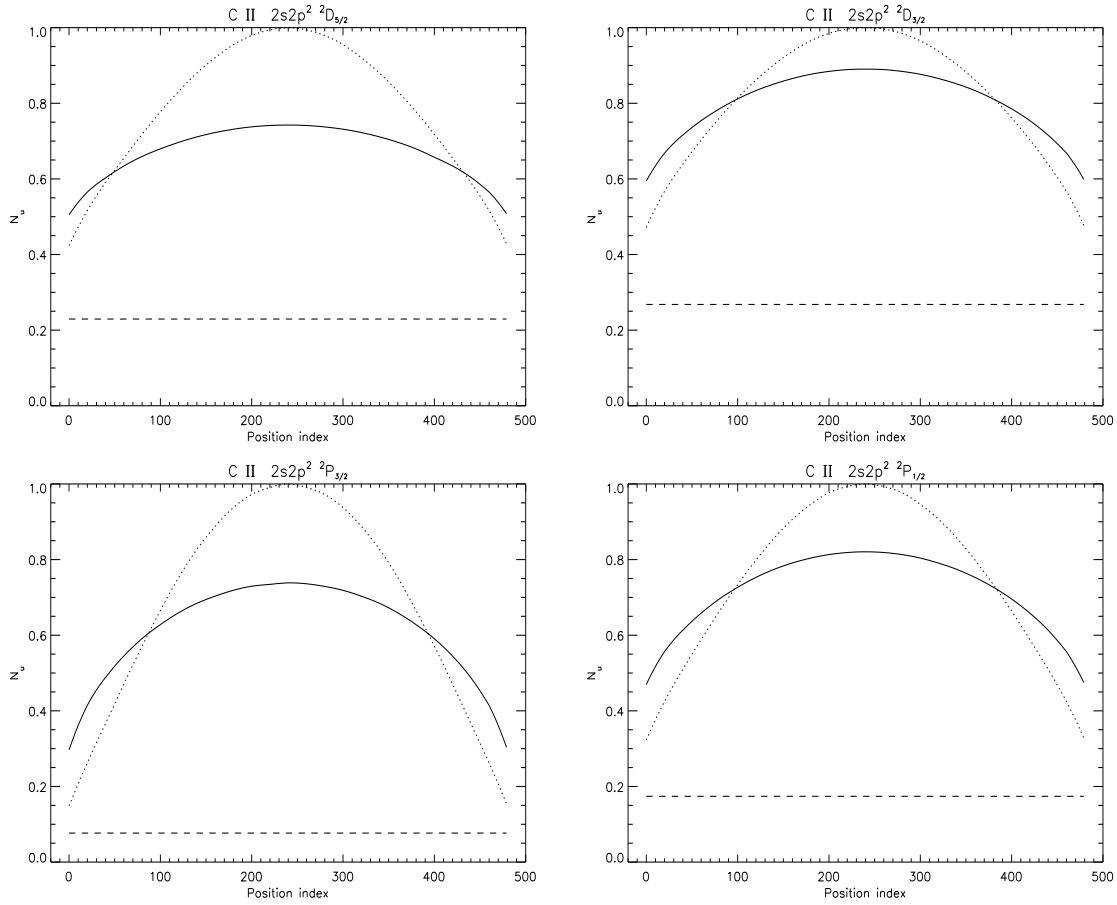

Figure 4.12: Upper level population densities versus spatial position including blending effects, for selected lines of C II as in figs 4.10 and 4.11 but just in the most optically thick case. The solid and dotted lines are as in figs 4.10 and 4.11. Values are not absolute but are scaled so that the maximum population density value is unity.

the validity, or otherwise, of the line-of-sight averaged escape probability. The absolute value of the absorption factor is dependent upon these ratios, hence the need to calculate $\mathcal{G}^{(i)}(\tau_0, x)$ iteratively. However, line blending only influences the validity of the line-of-sight averaged escape probability through the increase in effective optical depth.

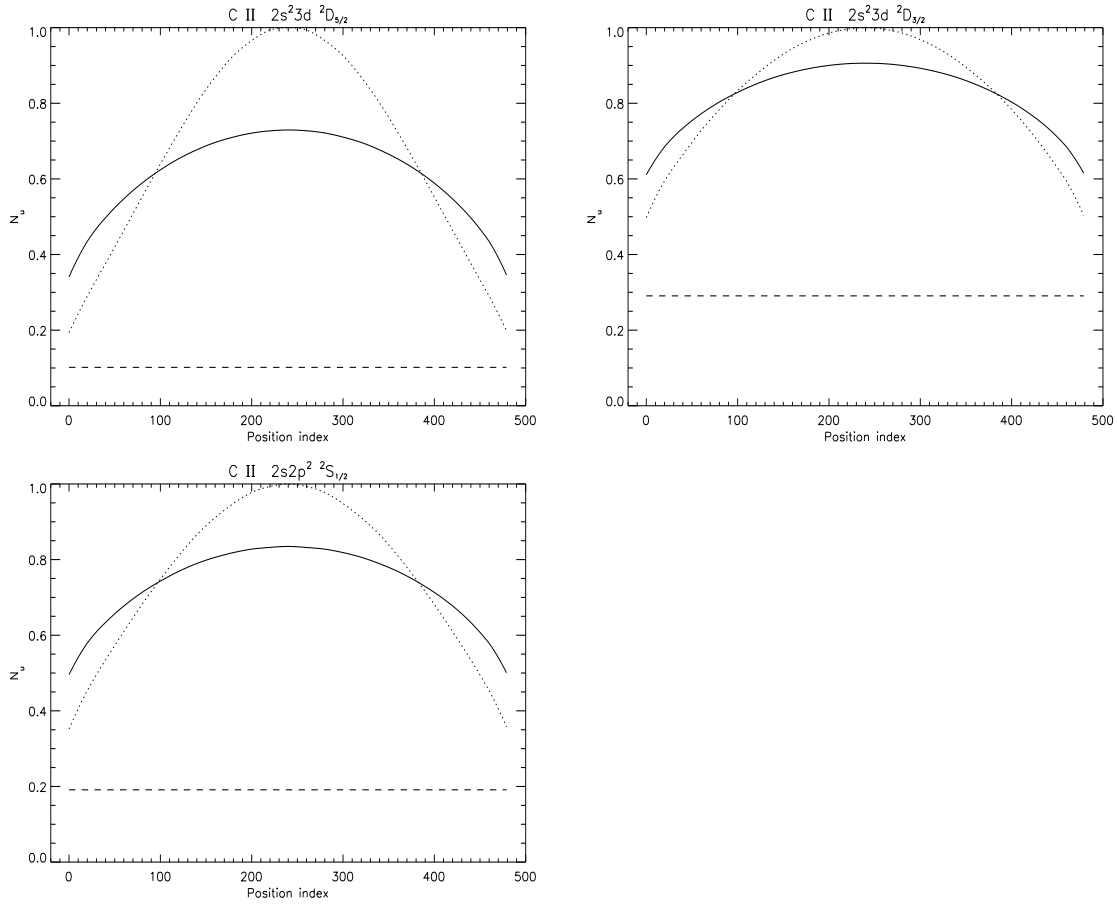

Figure 4.13: Upper level population densities versus spatial position including blending effects, for selected lines of C II as in fig. 4.12.

4.7 The effect of line blending on emergent fluxes

Figs 4.14a and b show predicted limb-brightening curves for the C II $2s^2 2p\,^2P_{3/2} - 2s2p^2\,^2P_{3/2}$ line at 904.143 Å, contrasting the *resolved* (population modification included) calculation with the *unresolved* (no population modification included) calculation. Line blending is included in both figures via eqs 4.4 and 4.5 respectively. These figures illustrate that for optical depths up to ~ 4 the modification to the population density distribution due to opacity, impinges minimally upon the limb-brightening curves. That is, it is sufficient to assume that the only effect of opacity is to scatter photons out of the line-of-sight, even when line blending is included, for

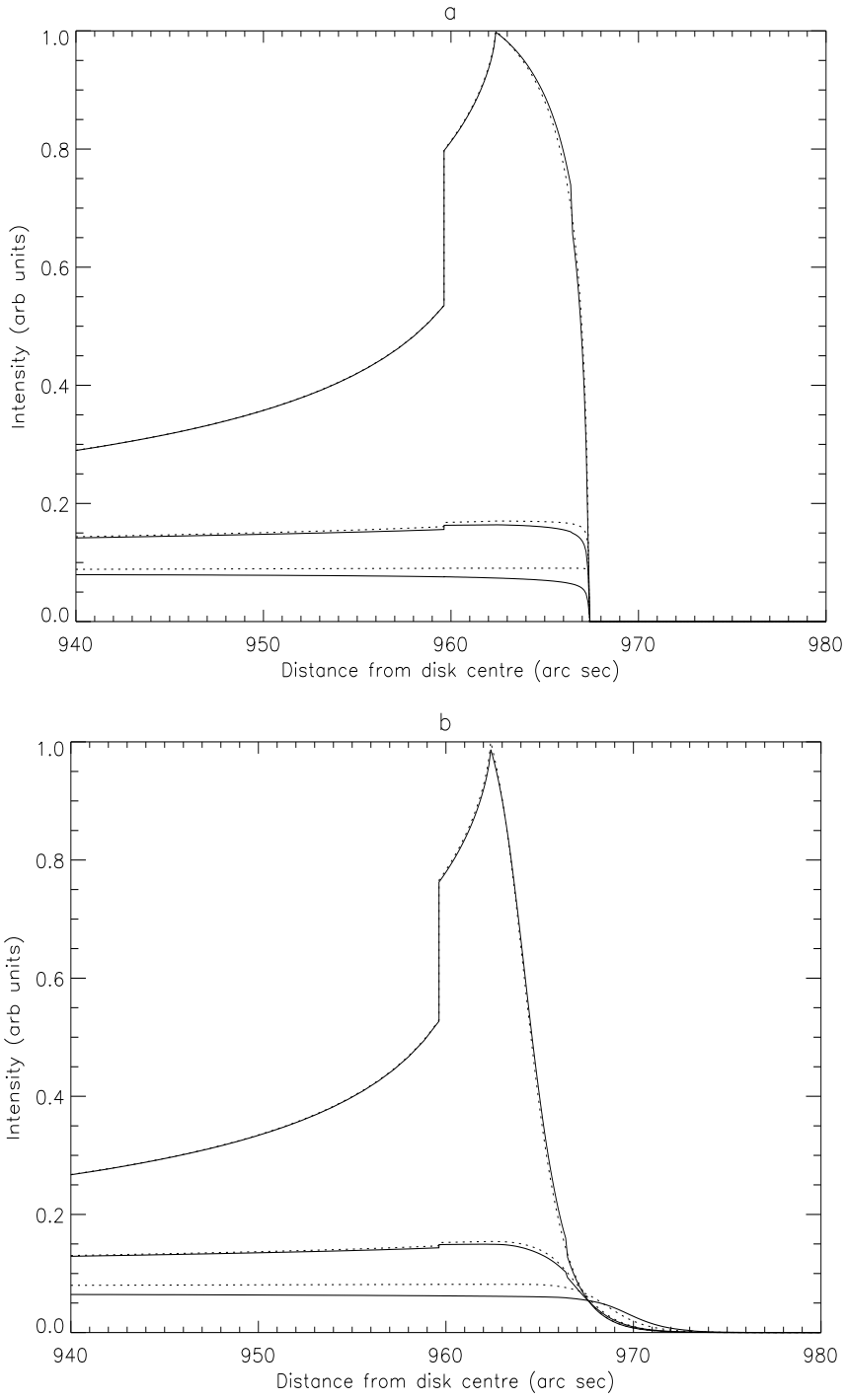

Figure 4.14: Predicted limb-brightening curves for the C II $2s^2 2p\,^2P_{3/2} - 2s2p^2\,^2P_{3/2}$ line at 904.143 Å. The solid lines correspond to calculations including line blending and the modification to the upper level population density distribution due to opacity using $g^{(i)}\{\tau_0\}$ and $\Lambda^{(i)}(\tau_0, x)$ (eqs 4.4 and 4.18 respectively). The dotted lines correspond to calculations including line blending and assuming constant source function using $\bar{g}^{(i)}\{\tau_0\}$ (eq. 4.5). Intensities are calculated in (a) a constant density model and (b) a model with density that decreases exponentially with height. Each plot contains three sets of curves corresponding to disk centre optical depths of 0.1, 1 and 4. The curves are scaled to match at disk centre.

optical depths in this range.

Figs 4.15a and b show the same as 4.14a and b but here the blended, resolved calculation is contrasted with the unresolved, unblended one. It is clear from these figures that blending has a more significant impact on the limb-brightening curves than the population modification.

4.8 Concluding remarks

From an algebraic perspective, the effects of spectral line blending may be incorporated easily within the escape probability and absorption factor expressions. However, blending re-introduces non-linearity into the optically thick statistical balance equation thus compromising the simplicity of the absorption factor approach. Blending leads to photons that are emitted in one line being absorbed by another which in turn leads to a sensitivity of the absorption factor to the ratio of upper level population densities of overlapped components. These ratios are themselves opacity sensitive. Consequently blending markedly influences the absorption factors. It does so in two ways. The first is due to the increase in effective optical depth which may in principle be characterised by an unblended calculation with a modified optical depth. This effective optical depth is always larger than the unblended one. The second way is due to the dependence of the absorption factor on upper level population density ratios and leads in general to a decrease in the absorption factor. It is, however, largely independent of spatial position and so does not further distort the resultant upper level population density distributions and therefore does not impinge on the validity of the line-of-sight averaged escape probability.

The validity of $\mathcal{G}^{(i)}(\tau_0, x)$ follows as in chapter 3, and is dominated by the indirect effects evident in lines that share an upper level with a more optically thick line. However, this is only true if $\mathcal{G}^{(i)}(\tau_0, x)$ is calculated iteratively. If iteration is not performed then $\mathcal{G}^{(i)}(\tau_0, x)$ is ineffective for blended lines even for small optical depths.

As in chapter 3, the $\bar{g}^{(i)}\{\tau_0\}$ quantity (eq. 4.5) is effective for optical depths up to some maximum. With blending included this cut-off is reduced from ~ 10 to ~ 4. It is clear from fig. 4.15 that the error introduced by the neglect of the modification to

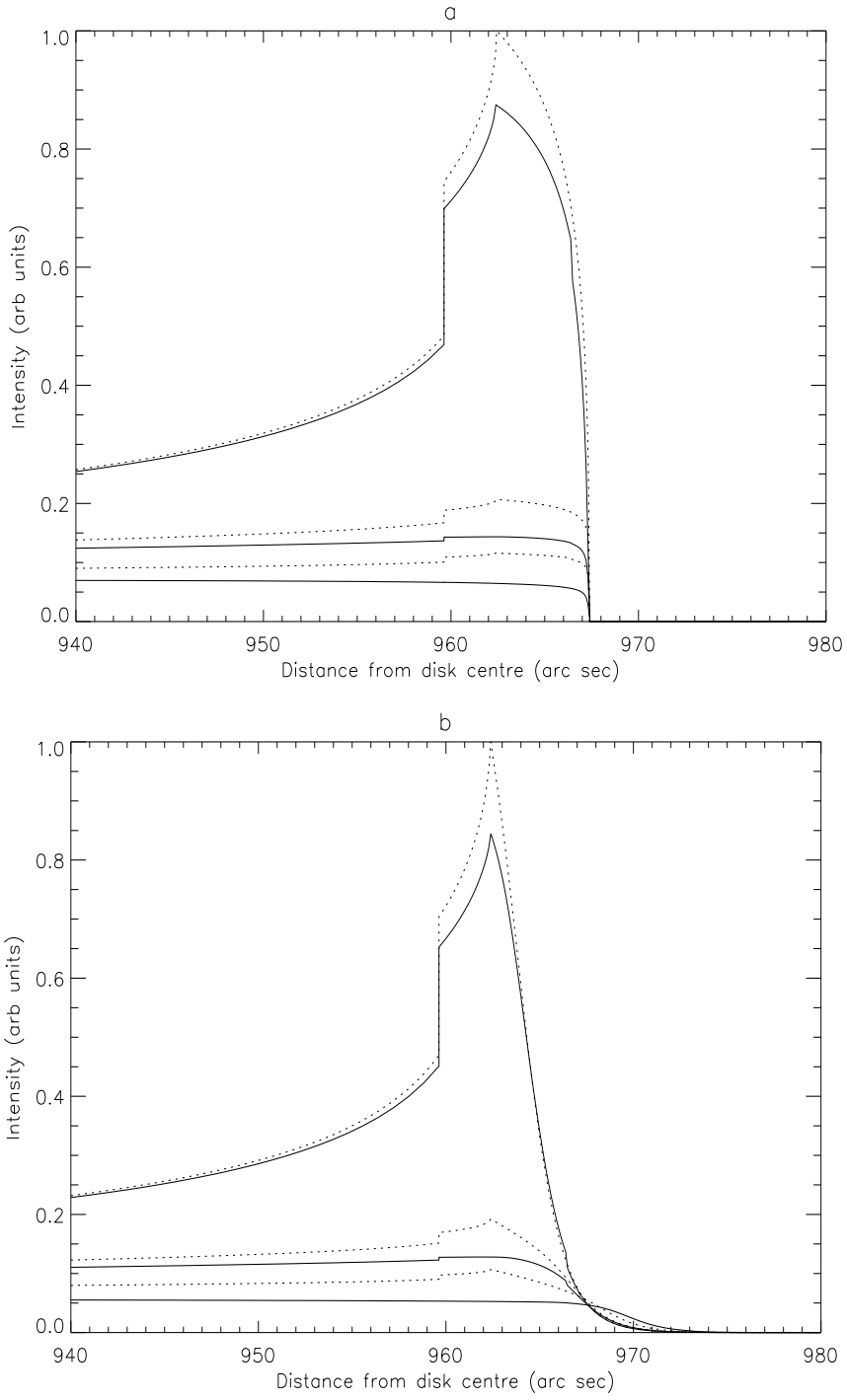

Figure 4.15: Predicted limb-brightening curves for the C II $2s^2 2p\,^2P_{3/2} - 2s2p^2\,^2P_{3/2}$ line at 904.143 Å as in fig. 4.14. The solid lines correspond to calculations including line blending and the modification to the upper level population density distribution due to opacity. The dotted lines correspond to calculations neglecting both line blending and the modification to the upper level population density distribution.

the source function due to opacity is negligible compared to that due to the neglect of line blending. Even at an optical depth of 0.1 blending significantly modifies the emergent fluxes. Thus a regime exists where opacity effects are significant and $\bar{g}^{(i)}\{\tau_0\}$ is effective. Moreover, both the C II and C III datasets discussed in chapter 2 fall within this regime.

Chapter 5

Comments on the effects of structure and flow

In chapter 2 escape probability and absorption factor techniques were introduced and applied to spectral data from the SOHO-SUMER spectrometer in both a diagnostic and modelling capacity. These analyses were effective in extracting optical depths of spectral lines of C II and C III and led to the classification of lines of these two ions based on the influence of opacity on both atomic population structures and emergent intensities. Also the techniques, when coupled with simple stratified atmosphere models were successful in describing observed C II and C III branching ratios of lines arising from common upper levels. However, inadequacies were found in the escape probability/absorption factor methods, such as their inability to extract optical depths from C III branching ratios in the vicinity of the limb and the failure to accurately predict emergent intensities. The relative simplicity of these methods, however, make them desirable and have prompted this study into their validity.

So far the influence of the spatial dependence of the source function due to opacity has been analysed as well as its frequency dependence through spectral line blending. These studies have led to the identification of an optical depth regime within which the line-of-sight averaged escape probability, $\bar{g}^{(i)}\{\tau_0\}$, is valid. However, some assumptions underpinning these expressions remain untested. Specifically the neglect

of the spatial dependence of the source function due to the variation of (T_e, N_e) remains unjustified as do the effects of plasma flow and partial frequency redistribution. The latter two, like line blending lead to a dependence of the source function on frequency. In addition, the roles played by solar atmospheric structure and instrumental effects in interpreting and modelling spectral emission are yet to be addressed.

In this chapter the influence of atmospheric structure and plasma flow upon the escape probability approach are considered. The remaining issues listed above will be addressed in chapter 6.

5.1 Non-stratified models

The atmosphere models examined thus far have been simple but the only structural restriction on them, as far as the escape probability and absorption factor expressions are concerned, is that they are static and stratified. Therefore it is necessary to find a stratified model that best captures the radiative characteristics of the real solar atmosphere. For example, the exponential model described in chapter 2 is more effective than the VAL model in describing cross-limb flux ratio variations despite its empirical nature. This is because it takes account of the extention of the TR into the corona due to spicule-like structures.

However, the solar atmosphere is not stratified, nor is it static. A question therefore presents itself as to how structure and flow affect absorption characteristics in a plasma and the quantities derived thus far.

Absorption at a point is dependent upon the radiation field at that point. This radiation field is determined by the number of emitters in the plasma and the probability that photons emitted from them will reach the point in question. This probability is dependent upon the number of absorbers along the line-of-sight from the emitter to the absorber. Consider two plasmas of the same total number of emitters and absorbers, one stratified and one non-stratified. Absorption will be greater in the stratified plasma than the non-stratified one since in the latter, the particles will appear more overlapped along each line-of-sight. This may be shown mathematically as follows: Consider the absorption factor at layer centre. If the layer extends from

$x = -D/2$ to $x = D/2$ then this is given by

$$\Lambda(\tau_0, 0) = 1 - \frac{N_l(0)}{N_u(0)} \frac{\omega_u}{\omega_l} \frac{c^2}{2\nu_0^2} \int I_\nu \phi_\nu d\nu \tag{5.1}$$

where

$$I_\nu = \frac{1}{4\pi} \int \int_V \int \frac{j_\nu(\mathbf{r})}{r^2} e^{-\tau_\nu(\mathbf{r})} dV \tag{5.2}$$

If it is written that

$$\tau_\nu(\mathbf{r}) = \alpha_\nu \int_{\mathbf{r}\to\mathbf{0}} N_l(\mathbf{r}') dr' \tag{5.3}$$

and

$$j_\nu(\mathbf{r}) = \beta_\nu N_u(\mathbf{r}) \tag{5.4}$$

where

$$\alpha_\nu = \frac{1}{c} h\nu B_{l\to u} \phi(\nu) \tag{5.5}$$

and

$$\beta_\nu = \frac{1}{4\pi} A_{u\to l} \phi(\nu) \tag{5.6}$$

then for a semi-infinite slab

$$I_\nu = \frac{\beta_\nu}{4\pi} \int_{-\pi}^{\pi} \int_{-\pi/2}^{\pi/2} \int_0^{R/\cos\theta} N_u(\mathbf{r}) exp\left\{ -\alpha_\nu \int_0^r N_l(\mathbf{r}') dr' \right\} |\sin\theta| dr d\theta d\phi \tag{5.7}$$

It is useful to define $\bar{N}_l(\theta, \phi)$ and $\bar{N}_u(\theta, \phi)$ as

$$\bar{N}_l(\theta, \phi) = \frac{\int_0^{R/\cos\theta} N_l(\mathbf{r}) dr}{R/\cos\theta} \tag{5.8}$$

$$\bar{N}_u(\theta, \phi) = \frac{\int_0^{R/\cos\theta} N_u(\mathbf{r}) dr}{R/\cos\theta} \tag{5.9}$$

and then to define s as

$$s = \frac{\int_0^r N_l(\mathbf{r}') dr'}{\bar{N}_l(\theta, \phi)} \tag{5.10}$$

$$\Rightarrow \frac{ds}{dr} = \frac{N_l(\mathbf{r})}{\bar{N}_l(\theta, \phi)} \tag{5.11}$$

$$\Rightarrow I_\nu = \frac{\beta_\nu}{4\pi} \int_{-\pi}^{\pi} \int_{-\pi/2}^{\pi/2} \int_0^{R/\cos\theta} \frac{N_u(\mathbf{r})}{N_l(\mathbf{r})} \bar{N}_l(\theta, \phi) e^{-\alpha_\nu \bar{N}_l(\theta,\phi) s} |\sin\theta| ds d\theta d\phi \tag{5.12}$$

Now consider the regime where the source function is approximately constant. Then

$$\frac{N_u(\mathbf{r})}{N_l(\mathbf{r})} = \frac{\bar{N}_u(\theta,\phi)}{\bar{N}_l(\theta,\phi)} \tag{5.13}$$

and so

$$\begin{aligned} I_\nu &= \frac{\beta_\nu}{4\pi}\int_{-\pi}^{\pi}\int_{-\pi/2}^{\pi/2}\int_0^{R/\cos\theta} \bar{N}_u(\theta,\phi)e^{-\alpha_\nu \bar{N}_l(\theta,\phi)s}|\sin\theta| ds d\theta d\phi \\ &= \frac{\beta_\nu}{4\pi}\int_{-\pi}^{\pi}\int_{-\pi/2}^{\pi/2}\frac{\bar{N}_u(\theta,\phi)}{\bar{N}_l(\theta,\phi)}\frac{1}{\alpha_\nu}\left[1-e^{-\alpha_\nu \bar{N}_l(\theta,\phi)R/\cos\theta}\right]|\sin\theta| d\theta d\phi \\ &= \frac{S_\nu}{4\pi}\int_{-\pi}^{\pi}\int_{-\pi/2}^{\pi/2}\left[1-e^{-\alpha_\nu \bar{N}_l(\theta,\phi)R/\cos\theta}\right]|\sin\theta| d\theta d\phi \end{aligned} \tag{5.14}$$

where S_ν is the source function. The question is now, how does structuring with respect to θ and ϕ influence the radiation field at a point? To answer this, consider the integral

$$\mathcal{I}_{\nu,\theta} = \int_{-\pi}^{\pi} e^{-\alpha_\nu \bar{N}_l(\theta,\phi)R/\cos\theta} d\phi \tag{5.15}$$

Intuitively, it is expected that structuring a plasma will lead to a reduction in the radiation field. This was discussed above. If this is so then introducing structure with respect to the angle ϕ in eq. 5.15 will lead to an increase in $\mathcal{I}_{\nu,\theta}$. This may be shown to be the case as follows: write

$$\mathcal{I}_{\nu,\theta} = \int_{-\pi}^{\pi} e^{-a_{\nu,\theta}\left(\bar{\bar{N}}_{l,\theta}+\varepsilon(\phi)\right)} d\phi \tag{5.16}$$

where

$$a_{\nu,\theta} = -\alpha_\nu \frac{R}{\cos\theta} \tag{5.17}$$

$$\bar{\bar{N}}_{l,\theta} = \frac{1}{2\pi}\int_{-\pi}^{\pi}\bar{N}_l(\theta,\phi)d\phi \tag{5.18}$$

$$\varepsilon(\phi) = \bar{N}_l(\theta,\phi) - \bar{\bar{N}}_{l,\theta} \tag{5.19}$$

Here $\bar{N}_l(\theta,\phi)$ is written as its average over ϕ – i.e. $\bar{\bar{N}}_{l,\theta}$ – plus a quantity, $\varepsilon(\phi)$, which describes the deviation of $\bar{N}_l(\theta,\phi)$ from the average. It follows that

$$\int_{-\pi}^{\pi}\varepsilon(\phi)d\phi = 0 \tag{5.20}$$

Euler's equation for eq. 5.16 subject to the condition specified in eq. 5.20 is then

$$\frac{\partial}{\partial \varepsilon}\left(e^{-a_{\nu,\theta}\left(\bar{\bar{N}}_{l,\theta}+\varepsilon(\phi)\right)}+\lambda\varepsilon(\phi)\right)=0 \tag{5.21}$$

where λ is a Lagrangian multiplier and is constant. This implies that

$$\begin{aligned} -a_{\nu,\theta}e^{-a_{\nu,\theta}\left(\bar{\bar{N}}_{l,\theta}+\varepsilon(\phi)\right)}+\lambda &= 0 \\ \Rightarrow \varepsilon(\phi) &= const=0 \end{aligned} \tag{5.22}$$

Thus with respect to ϕ, the stratified case is an extremal.

To determine whether or not is is a maximal or minimal solution, consider the following example:

$$\varepsilon(\phi)=\begin{cases} 1 \quad , & -\pi \le \phi < 0 \\ -1 \quad , & 0 \le \phi < \pi \end{cases} \tag{5.23}$$

Then

$$\begin{aligned} \mathcal{I}_{\nu,\theta} &= \pi e^{a(\bar{\bar{N}}_{l,\theta}+1)}+\pi e^{a(\bar{\bar{N}}_{l,\theta}+1)} \\ &= \pi e^{a\bar{\bar{N}}}\left(e^{-1}+e\right) > 2\pi e^{a\bar{\bar{N}}} \end{aligned} \tag{5.24}$$

Thus $\varepsilon(\phi)=0$ represents a minimal of eq. 5.15 and a maximal of eq. 5.14. Therefore, with respect to ϕ, the stratified case is a minimal of $\Lambda(\tau_0,0)$. That it is a minimal of $\Lambda(\tau_0,x)$ for all x follows from symmetry.

The dependence of $\Lambda(\tau_0,0)$ on structure with respect to θ does not follow easily in the plane-parallel case and so is demonstrated here for a spherical plasma.

For a spherical plasma the intensity at its centre is given by

$$\begin{aligned} I_\nu &= \frac{\beta_\nu}{4\pi}\int_{-\pi}^{\pi}\int_0^{\pi}\int_0^R N_u(\mathbf{r})exp\left\{-\alpha_\nu\int_0^r N_l(\mathbf{r}')dr'\right\}\sin\theta dr d\theta d\phi \\ &= \frac{S_\nu}{4\pi}\int_{-\pi}^{\pi}\int_0^{\pi}\left[1-e^{-\alpha_\nu R\bar{N}_l(\theta,\phi)}\right]\sin\theta d\theta \end{aligned} \tag{5.25}$$

Consider the integral

$$\begin{aligned} \mathcal{I}_{\nu,\phi} &= \int_0^{\pi} e^{-\alpha_\nu \bar{N}_l(\theta,\phi)R}\sin\theta d\theta \\ &= \int_0^{\pi} e^{-b_{\nu,\phi}\left(\bar{\bar{N}}_{l,\phi}+\eta(\theta)\right)}\sin\theta d\theta \end{aligned} \tag{5.26}$$

where

$$b_{\nu,\phi} = -\alpha_\nu R \tag{5.27}$$

$$\bar{\bar{N}}_{l,\phi} = \int_0^\pi \bar{N}_l(\theta,\phi)\sin\theta d\theta \tag{5.28}$$

$$\eta(\theta) = \bar{N}_l(\theta,\phi) - \bar{\bar{N}}_{l,\phi} \tag{5.29}$$

Hence

$$\int_0^\pi \eta(\theta)\sin\theta d\theta = 0 \tag{5.30}$$

Euler's equation for eq. 5.26 subject to the condition specified in eq. 5.30 is then

$$\begin{aligned} \frac{\partial}{\partial\eta}\left(e^{-b_{\nu,\phi}\left(\bar{\bar{N}}_{l,\phi}+\eta(\theta)\right)}\sin\theta + \lambda\eta(\theta)sin\theta\right) &= 0 \\ \Rightarrow -b_{\nu,\theta}e^{-b_{\nu,\theta}\left(\bar{\bar{N}}_{l,\phi}+\eta(\theta)\right)}\sin\theta + \lambda\sin\theta &= 0 \\ \Rightarrow \eta(\theta) &= const = 0 \end{aligned} \tag{5.31}$$

Thus with respect to θ, the stratified case is an extremal. Moreover, as before, with respect to θ, the stratified case represents a minimal of $\Lambda(\tau_0, 0)$.

Discussion

It follows from the above that it is possible to have two plasmas of the same apparent optical depth in terms of emission, but different optical depths from the perspective of absorption. This might be observable in disk centre spectra. Consider the intensity ratio of the 2–2 to the 1–2 component of the C III $2s2p\ ^3P$ – $2p^2\ ^3P$ multiplet ($\sim$ 1175 Å). Since these two lines arise from a common upper level, this ratio is proportional to that of their $\bar{g}\{\tau_0\}$ values which are determined by their line-of-sight optical depths. From an observation of this ratio at disk centre the optical depths of these lines may be deduced and from them the optical depths of all the other lines of C III may also be calculated. Thus all the C III optical depths may be known from a single $\bar{g}\{\tau_0\}$ ratio (see chapter 2). Now consider the intensity ratio of the 2–1 to the 1–2 component of the same C III multiplet. These lines do not share an upper level but have almost identical optical depths. Thus this ratio is proportional

to that of their upper level population densities which is determined by their $\bar{\bar{g}}\{\tau_0/2\}$ values. These in turn are dependent specifically upon optical depths at disk centre and thus the optical depths of all the C III may be deduced from the I(2–1)/I(1–2) intensity ratio. If the plasma is stratified then the two sets of optical depth should be in agreement. If it is not then those inferred from the latter ratio will be lower than those of the former.

This reasoning follows from consideration of two plasmas of the same total number of particles. If, on the other hand, a plasma is de-homogenised by the removal rather than re-organising or particles – that is, so that the two plasmas are not of the same total particle number – then the same conclusion results. Removing plasma so as to leave spicule like structures, for example, means that at disk centre the optical depths are the same but the degree of absorption is reduced.

The latter perspective is more useful when considering spicule-like structures (i.e. radial structures) at disk centre. The former perspective (re-organisation rather than removal) is more useful when considering such structures at the limb.

5.2 Models with flow

Flow introduces a dependence of the absorption and emission profiles on position. In the zero-flow case the absorption and emission profiles share the same centroid location and so when flow is introduced it can only act so as to displace one profile with respect to the other. Only moderate opacities, where the source function is close to constant, are considered here. In this regime, and in the absence of line blending, opacity serves at most to influence line profiles by way of flattening their peaks. In more severely thick circumstances partial frequency redistribution, which leads to a dependence of the source function upon frequency, can lead to self-reversal of spectral lines (see fig. 1.8). Thus for the optical depth regime considered here, if there is no line blending the only effect of this displacement is to reduce the degree of absorption. Thus the zero-flow, stratified case represents a minimal of $\Lambda(\tau_0, x)$. This may be illustrated as follows: consider the intensity, I_r, at the point 0 due to emission

along a ray path of length R. This is given by

$$I_r \sim \int_0^R \int_0^\infty \phi_a(\nu,0)\phi_e(\nu,r) exp\left\{-\int_0^r \kappa_0(r')\phi_e(\nu,r')dr'\right\} dudr \tag{5.32}$$

where $\phi_a(\nu,r)$ and $\phi_e(\nu,r)$ respectively denote the absorption and emission profiles at the point r. For Doppler broadened lines eq. 5.32 may be written as

$$I_r \sim \int_0^R \int_{-\infty}^\infty e^{u^2} e^{(u+\eta(r))^2} exp\left\{-\int_0^r \kappa_0(r') e^{(u+\eta(r'))^2} dr'\right\} dudr \tag{5.33}$$

where $\eta(r)$ is some function describing the Doppler shift of the line profile due to the flow velocity at the point r. If $f(\kappa_0,\eta,r)$ is defined such that

$$I_r \sim \int_0^R f(\kappa_0,\eta,r)dr \tag{5.34}$$

then for extremals with respect to η, Euler's equation is

$$\begin{aligned}
&\frac{\partial f}{\partial \eta} = 0 \\
\Rightarrow\ &\int_{-\infty}^\infty \left[e^{u^2} e^{(u+\eta(r))^2} (-2(u+\eta(r))) exp\left\{-\int_0^r \kappa_0(r') e^{(u+\eta(r'))^2} dr'\right\}\right. \\
&\quad + e^{u^2} e^{(u+\eta(r))^2} exp\left\{-\int_0^r \kappa_0(r') e^{(u+\eta(r'))^2} dr'\right\} \\
&\quad \left.\times \int_0^r \kappa_0(r') e^{(u+\eta(r'))^2} 2(u+\eta(r'))dr'\right] du = 0
\end{aligned} \tag{5.35}$$

This is satisfied if $\eta(r) = 0$ for all values of r and thus this condition specifies an extremal. To determine whether or not it is a maximal or minimal, consider the case where at all points along the ray the plasma is stationary except at the point of absorption ($r = 0$) where there is flow parallel to the ray. In this case the line profile due to emission along the ray is displaced in frequency space from the absorption profile at $r = 0$. The convolution of the two inevitably results in a decrease in absorption compared to the zero-flow case. Thus when there is no line blending the zero-flow case represents a minimal of the absorption factor.

In the case of line blending the situation becomes more complex. Blending itself leads to a decrease in the absorption factor and so since flow will contribute to the extent of blending, a *decrease* in the absorption factor results. Thus when there is blending, the zero-flow case does not necessarily represent a minimal.

In general flow and blending ought to be treated self-consistently but if the main influence of flow is to broaden emission profiles then flow may be accounted for within the blending formulation. In this event flow is included implicitly. This has in fact already been the case in the analyses presented so far since spectral lines emanating from the TR have Gaussian profiles broadened beyond their thermal widths due to non-thermal velocities (Spadaro et al., 1996).

5.3 Concluding remarks

The escape probability approach hinges on the separability of the effects of opacity upon the population structure and on emergent fluxes. This separability de-couples and linearises the equations of radiative transfer and statistical balance. In a stratified, stationary atmosphere an optical depth regime exists whereby this separability is possible and where opacity effects are significant and observable. This regime is defined according to the degree of absorption within the plasma and the extent of the modification to the upper level population density distribution due to opacity which are characterised by the absorption factor, $\Lambda(\tau_0, x)$. Following this the influence of structure and flow upon the extent of this optical depth regime must be addressed. Both structure and flow serve to diminish the degree of absorption as compared with the stratified, stationary case, except when there is blending where flow can enhance the blending effects and thus lead to an increase in the degree of absorption. Providing that plasma flow influences emission profiles by way of broadening and does not distort their shape then flow may be accounted for within blended lines as well as unblended ones. It is therefore appropriate to consider the stratified, stationary atmosphere in determining the region of validity of the $\bar{g}\{\tau_0\}$ quantity as structure and flow will not further restrict this region.

Chapter 6

Plasma diagnostics and models using the improved escape probability

In chapter 2 simple escape probability techniques were applied to C II and C III spectral measurements of the East solar limb using the SOHO-SUMER spectrometer. The line-of-sight averaged escape probability, $\bar{g}\{\tau_0\}$, was used to extract optical depths of certain C II and C III lines from observed branching ratios (see sec. 2.3), from which optical depths of all the lines of these ions can in principle be calculated. The $\bar{g}\{\tau_0\}$ quantity was then coupled with simple stratified atmosphere models to predict intensity ratio variations (figs 2.16a and b). These models were found to be effective from on the disk to beyond the limb at which point the model and observed values began to deviate, possibly indicating the dominance of instrumentally scattered light.

Based on the most effective fit to the observed branching ratios in the C III case, a model limb brightening curve was calculated for the C III $2s2p^3P_2$ – $2p^2\,^3P_2$ line at 1175.711 Å (see fig. 2.17). This model was successful on the disk, leading up to the limb but failed in the vicinity of the limb itself. In this region the model fluxes greatly exceeded the observed ones. This discrepancy was echoed in the failure of the escape probability technique to extract optical depth values for the C III lines just beyond the visible limb. The flux model was effective, however, at heights well above

the limb where the model ratios failed.

Fits to the ratios were optimised according to optical depth at disk centre, density scale height for the exponential density model, and layer thickness for the constant density model. From the disk centre optical depths obtained, along with those extracted at the limb, the spectral lines of C II and C III were classified according to the effects of opacity on both the population structure and emergent fluxes.

These results demonstrate that the escape probability and absorption factor techniques of chapter 2 provide useful and insightful solutions to the equations of radiative transfer and statistical balance. They also illustrate, however, that they are limited in applicability due to the underlying assumptions upon which they are based. These assumptions relate to variations in the line source functions, atmospheric structure and instrumental effects. Nevertheless, these methods are comparatively simple in comparison with the techniques of radiative transfer and Monte Carlo simulations, and they represent the only means by which optical depths may be extracted from observations in a manner that is model independent. Moreover, the line-of-sight averaged escape probability lends itself naturally to use within arbitrarily complex geometric models of the solar atmosphere.

These facts make the escape probability/absorption factor approach desirable and have prompted the study into their underlying assumptions that is presented here. So far in this study the variation of the source function due to opacity has been analysed and the effects of spectral line blending have been included within the escape probability/absorption factor framework. Furthermore, the influence of atmospheric structure and plasma flow have been considered. These investigations have shown that from consideration of an appropriate stratified, static, plane-parallel atmosphere, an optical depth regime may be identified within which the line-of-sight averaged escape probability, $\bar{g}^{(i)}\{\tau_0\}$, is sufficient to describe the effects of opacity on emergent intensities. It has also been shown that if $\bar{g}^{(i)}\{\tau_0\}$ is valid in the stratified, static case then it is also valid for an atmosphere with structure and non-zero flow providing that the latter does not lead to a deviation of emission profiles from Gaussian.

Figs 6.1a and b show observed line profiles for the C II $2s^2 2p\,^2P_{3/2} - 2s2p^2\,^2P_{1/2}$ line at 904.481 Å and the C III $2s2p^3P_2 - 2p^2\,^3P_1$ line at 1176.370 Å for every pointing

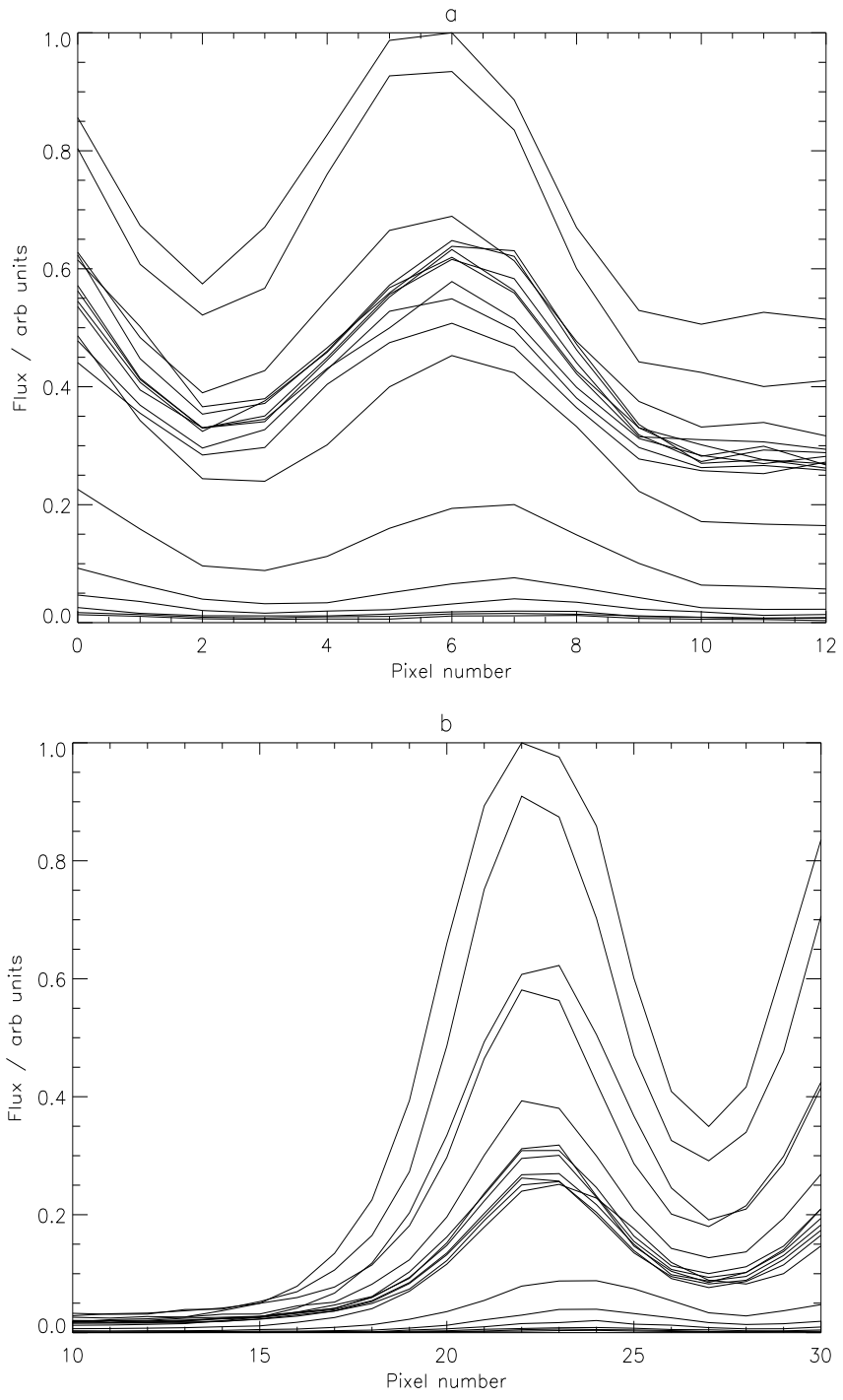

Figure 6.1: Observed line profiles for (a) the C II $2s^2 2p^2 P_{3/2} - 2s2p^2\,{}^2P_{1/2}$ line at 904.481 Å and (b) the C III $2s2p^3 P_2$ – $2p^2\,{}^3P_1$ line at 1176.370 Å. Profiles are shown for every pointing position.

position. These lines are unblended yet display no significant deviation from Gaussian at any point. It follows that for both the C II and C III datasets considered here, plasma flow may be included implicitly. Furthermore the disk centre optical depths deduced in chapter 2 imply that the $\bar{g}^{(i)}\{\tau_0\}$ expression is valid for the spectral lines of both these ions regardless of the structuring of the atmosphere.

In this chapter the SOHO-SUMER data discussed in chapter 2 is re-assessed using the blended escape probability from both a diagnostic and modelling perspective. The analyses so far, coupled with consistent treatment of the variation of optical depth with line-of-sight and the inclusion of instrumentally scattered light, allow the discrepancies found in chapter 2 between modelled and observed quantities to be resolved. In the process, the neglect of the spatial variation of the source function due to the variation of (T_e, N_e) will be justified. Additionally, spicule-like structures that are unresolved by the SUMER spectrometer will be identified.

6.1 The geometric extension of the line-of-sight

In chapter 2 the escape probabilities were derived within a constant density framework but were considered in variable density models. It has subsequently been shown that providing the source function is constant the $g^{(i)}\{\tau_0\}$ and $\bar{g}^{(i)}\{\tau_0\}$ expressions remain the same in the variable density case. However, the definition of τ_0 does change. In the constant density case the optical depth is given by

$$\tau_0 = \kappa_0 N_l \int_{l.o.s.} ds = \kappa_0 N_l L \tag{6.1}$$

where L is the length of the line-of-sight. In this case the geometric extension of the line-of-sight as a whole controls the variation of the optical depth with pointing position. In the variable density case, however, the optical depth is given instead by

$$\tau_0 = \kappa_0 \int_{l.o.s.} N_l(s) ds \tag{6.2}$$

For a stratified model it is again the geometric extension of the line-of-sight that controls the variation of optical depth, but due to the curvature of the atmosphere each *sub-layer* extends differently. Take, for example, the line-of-sight corresponding

to the inner edge of the emitting layer (approximately 962 arc sec). This line-of-sight intersects the inner edge of the emitting layer tangentially, but emerges from the layer at a sharper angle. Therefore the sub-layers near the inner edge of the emitting layer are extended to a greater extent in this region than those near the outer edge. This leads to a stronger disk-to-limb variation of optical depth in the models where the density of the emitting layer decreases with height.

Fig. 6.2a shows observed and model limb-brightening curves for the C III $2s2p^3P_2$ – $2p^2\,^3P_2$ line at 1175.711 Å. Model values are shown including and excluding line blending. The dotted line is directly comparable with fig. 2.17 from which it can be seen that the correct evaluation of optical depth has a marked influence upon the calculated fluxes. The fit is improved in the vicinity of the limb, although a discrepancy remains. Beyond the limb the fall-off of intensity is less well tracked than before.

Fig. 6.2b shows the corresponding branching ratios, I(2–2)/I(1–2), which are comparable with those of fig. 2.16b. Certain features are as expected: line blending leads to an increase in effective optical depth and improves the fit as compared with the unblended case and the optimal optical depth is less in the blended case. However, given, as stated above, that the optical depth variation in the variable density case is more marked than in the constant density case, it is somewhat surprising that the model curves to not track the observed ones so well as in fig. 2.16b. The reason for this is that the expression for optical depth used in chapter 2 ($\tau_0 = const \times \delta / \cos\theta$) is an approximation and breaks down, becoming infinite, at the inner edge of the emitting layer. Thus with this expression the optical depths are overestimated in the vicinity of the limb and this serves, ironically, to improve the fit to the ratios. It is also responsible, however, for the extent of the overestimate of the fluxes at the limb observable in fig. 2.11.

There remains a discrepancy between the observed and model fluxes and ratios in the region of and beyond the limb. The model overestimates both the fluxes and ratios in the vicinity of the limb, whereas beyond this region the fluxes are underestimated and the ratios are overestimated. The situation at the limb is interesting since if it is assumed that the ratio of upper to lower level population density is constant throughout the layer (i.e. that $\bar{g}^{(i)}\{\tau_0\}$ is valid) then fig. 6.2a implies that the column

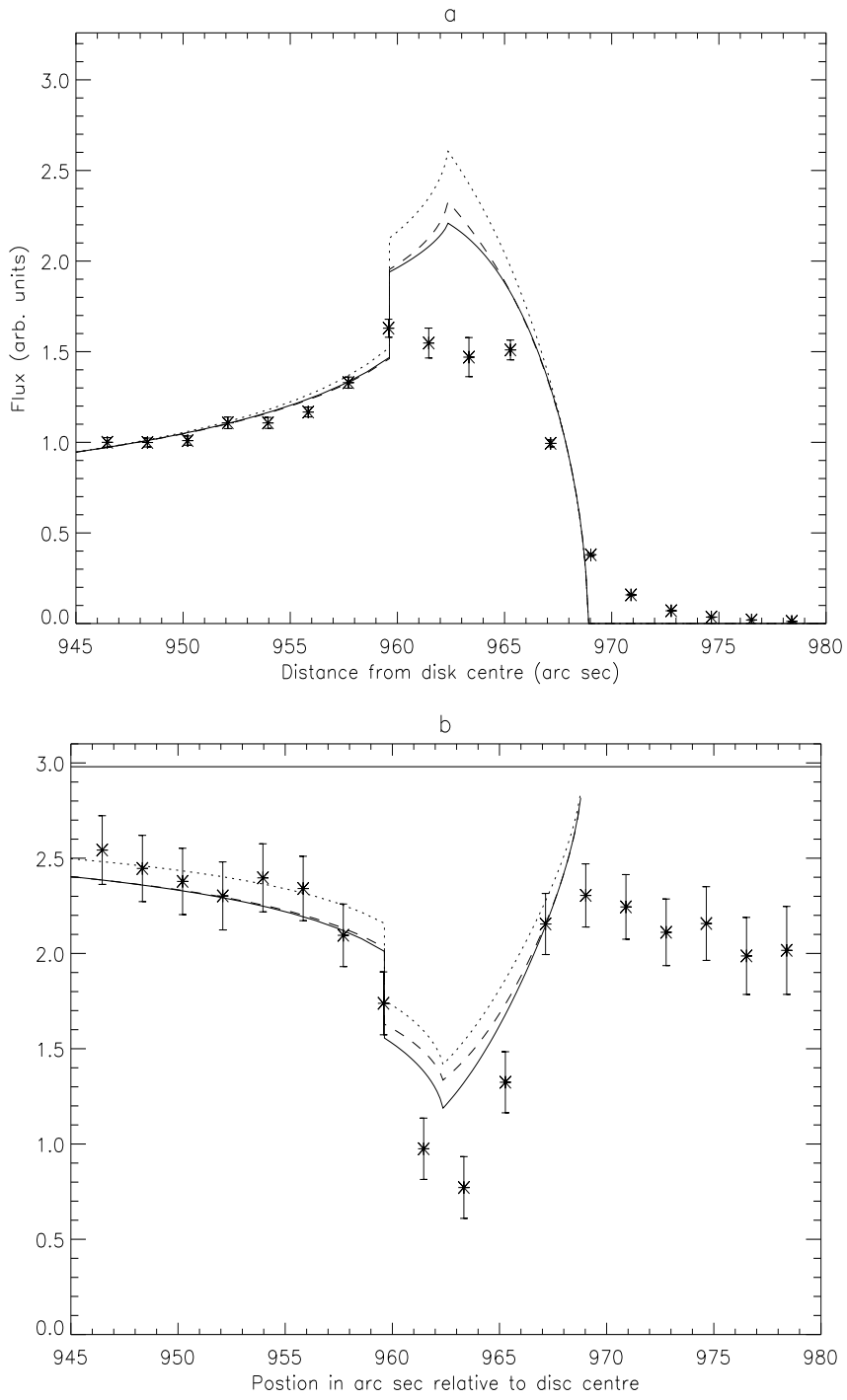

Figure 6.2: (a) Observed fluxes versus raster position for the C III $2s2p^3P_2$ – $2p^{2\,3}P_2$ line at 1175.711 Å. The solid line represents $\bar{g}^{(i)}\{\tau_0\}$ based model results with blending included (eq. 4.5) and with a disk centre optical depth of 0.16. The dotted line represents the same but with blending excluded (eq. 2.17). The dashed line represents the unblended calculation with an optical depth of 0.2. (b) Observed branching line intensity ratios versus raster position in arc sec relative to the disk centre for the C III I(2–2)/I(1–2) ratio as in fig. 2.15b. Solid, dotted and dashed lines are as in (a).

density is overestimated by the model, and fig. 6.2b implies the opposite. This paradox suggests the presence of structures that are observationally unresolved. This will be discussed later.

6.2 Instrumentally scattered light

In chapter 2 it was speculated that the off-limb discrepancy between the model and observed branching ratios indicated the dominance of instrumentally scattered light. If so then it is possible that scattered light will also account for the discrepancy in the fluxes at such heights. It is expected that the branching ratios should return to their optically thin values well above the limb as the (apparent) density of the atmosphere decreases. For C III this is not found. Rather the ratios in this case move closer to their on-disk values at heights above $\sim$ 970 arc sec. This is true even though the fluxes at these heights are very much smaller than those on disk. In addition, Doppler shifts of multiplet lines to the blue, seemingly indicative of tangential flows of the order of 20 km/s, are seen in the C III lines. The region of apparent onset of these shifts is the same as that where the branching ratios begin to deviate from the model values. These facts suggest that at heights above $\sim$ 970 arc sec instrumentally scattered light – that which originates from all locations on the sun and scatters off the interior of the telescope prior to passing through the entrance slit – dominates the observed signal. If this is so then the observed Doppler shifts indicated upflows on-disk and not beyond the limb.

The entire disk contributes to the scattered light signal with the contribution from each point being characterised by the instrument point spread function, *psf*, which represents the relative intensity of a point source as a function of lateral distance from the slit. This is shown in fig. 6.3. David et al. (1997) have shown that the pre-launch point spread function is still effective and so it may be used to complete the calculation. The emitted flux, $\mathcal{F}$, from position $\mathbf{h}$, which is related to the emitted intensity via $\mathcal{F}(\mathbf{h}) = const \times I(\mathbf{h})$, is given by

$$\mathcal{F}(\mathbf{h}) = \int\int_{disk} \mathcal{F}_t(\mathbf{x}) \times psf(|\mathbf{h} - \mathbf{x}|) d\mathbf{x} \tag{6.3}$$

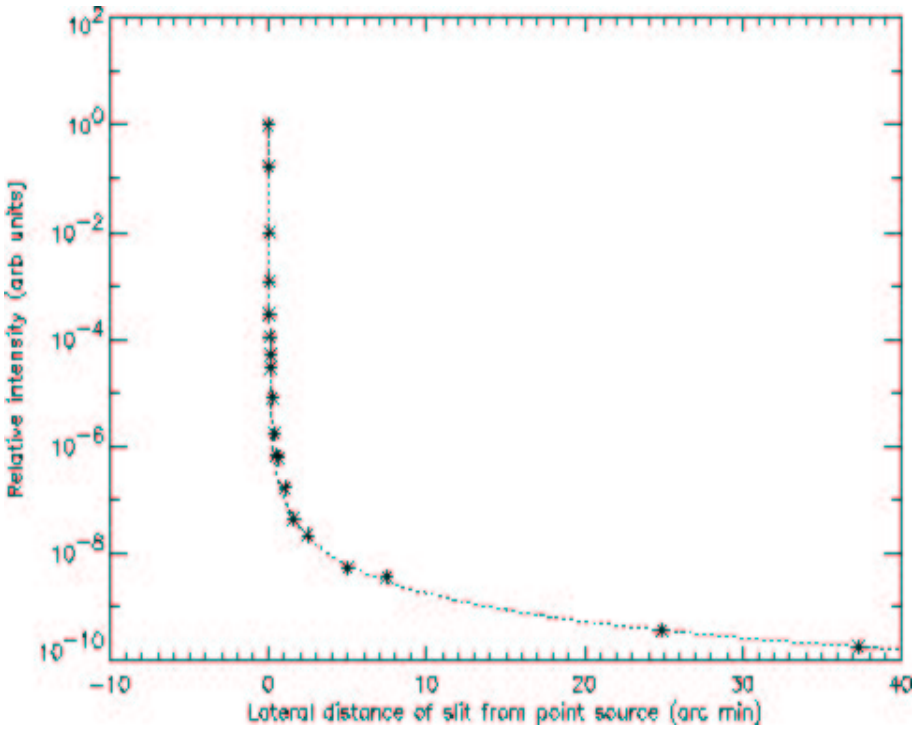

Figure 6.3: The SUMER pre-launch point spread function ($*$'s) (Lemaire, 1998) – relative intensity of a point source versus lateral distance from source to slit centre. The dotted line is a fit to the measured points used in the analysis described.

where $\mathcal{F}_t(\mathbf{x})$ is the true signal. Scattered light may be included within all the models presented so far using eq. 6.3. Model fluxes and ratios including the effects of instrumentally scattered light are presented below.

6.3 Model predictions

The three atmosphere models presented in chapter 2 are considered again. A fourth model is introduced that is a composite of models 1 and 3, comprising of a narrow TR shell with an exponential component to account for the extension of the TR into the corona due to spicule-like structures. Thus the models may be summarised as

1. Thin TR based on the VAL atmosphere model

2. Spherical shell of constant density

3. Layer of density that falls off exponentially with height

4. Composite of models 1 and 3

Each of these models includes the effects of line blending and scattered light. Using these stratified atmosphere models, limb-brightening curves and branching ratios versus pointing position may be calculated using eqs 3.25 and 4.5. Since it is assumed that the source function is constant in space, eq. 3.25 is equivalent to eq. 2.43, which was used in chapter 2 to model limb-brightening curves.

6.3.1 Fluxes

The observed spectral line fluxes for the C II $2s^2 2p\ ^2P_{3/2}$ – $2s2p^2\ ^2S_{1/2}$ line at 1037.020 Å and the C III $2s2p\ ^3P_2$ – $2p^2\ ^3P_2$ line at 1175.711 Å are shown in figs 6.4a and b respectively with the predicted fluxes (calculated via eq. 3.25) overlaid. Model 1 fails completely for both C II and C III as expected since it does not recognise the extension of the TR into the corona due to spicules and other structures. For this model, all the emission above 962 arc sec is due to scattered light. Also the point of peak emission in this model is shifted back from 962 arc sec to $\sim$ 960.5 arc sec since at this height there is a scattered light contribution from positions closer to and further from the solar disk. In contrast, at 962 arc sec there are only contributions to the scattered light component are from positions nearer to disk centre. Models 2, 3 and 4 track the trend in both cases in broad terms but not in detail, failing most markedly at the limb and well off limb. On disk, despite the averaging over the slit, the fluxes display a sensitivity to the structural detail. This detail is evident in the surface plots in figs 2.8a and b. The sensitivity of the emergent flux to column density is implied by eq. 3.25 since $\bar{g}\{\tau_0\}$ is insensitive to optical depth for values greater than $\sim$ 1 (see fig. 2.2).

At heights of $\sim$ 970 arc sec and above, despite the inclusion of scattered light, the fluxes are not tracked well by the models. Rather, the models predict intensities significantly smaller than those observed.

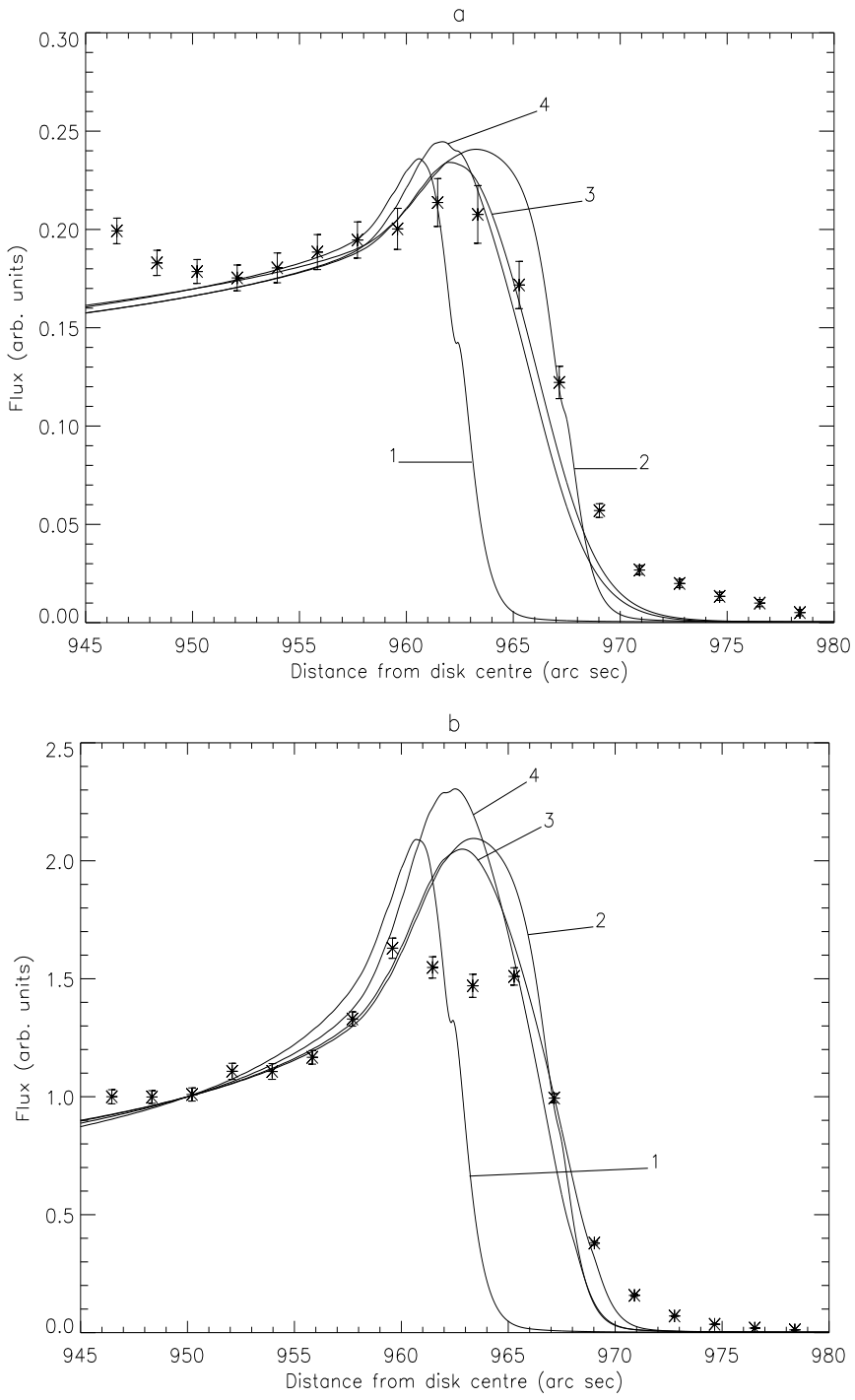

Figure 6.4: Observed and model fluxes for the (a) C II $2s^2 2p\ ^2P_{3/2} - 2s2p^2\ ^2S_{1/2}$ line at 1037.020 Å and (b) the C III $2s2p\ ^3P_2 - 2p^2\ ^3P_2$ line at 1175.711 Å. The $*$'s correspond to the observed fluxes and the solid lines are the model predictions numbered as in the text. Note that the visible limb is at 959.6 arc sec.

The inclusion of line blending, scattered light and the improved calculation of optical depth for each line-of-sight has a marked influence on the predicted fluxes. This difference is evident in the comparison of fig. 6.4b with fig. 2.17. It can be seen that these advancements to the models improve the fit to the fluxes at the limb but at heights beyond the limb the fit is less effective than before. Furthermore, while the fit is improved at the limb, the fluxes are still significantly overestimated by the models.

6.3.2 Ratios

The observed and model flux ratios of the (3/2–1/2)/(1/2–1/2) components of the C II $2s^2 2p\ ^2P - 2s2p^2\ ^2S$ multiplet and the (2–2)/(1–2) components of the C III $2s2p\ ^3P - 2p^2\ ^3P$ multiplet are shown in fig 6.5a and b respectively. The models here are much more effective than in the case of emergent fluxes since the linear dependence of the intensity on column density (eq. 3.25) is factored out (eq. 2.22). In the C III case the dip in the ratios at the limb is underestimated yet optical depths at this point are such that the $\bar{g}^{(i)}\{\tau_0\}$ ratio, in the absence of blending, is insensitive to optical depth (see fig. 6.6). When blending is included, absorption of 2–2 line photons by the 1–1 line leads to a decrease in the ratio. The underestimation of the observed values by the model at the limb suggests an underestimate in lower level population density of either the 2–2 line or the 1–1 line yet at this point the emergent intensities are overestimated suggesting an overestimate in the upper level column densities. This discrepancy is possibly due to a structure, not along the line-of-sight but along the slit. This will be discussed further in sec. 6.7.

For the model branching ratios the inclusions of scattered light is sufficient to ensure agreement within the error bars to the observed values at heights of ~ 970 arc sec and above. Comparison of figs 6.5a and b with figs 2.16a and b shows that the more advanced methods used here lead to an improvement to the fit to the ratios beyond the limb but a worse fit at the limb. Curiously the improvement in the fit to the ratios occurs where the fit to the fluxes reduces in quality, and vice versa.

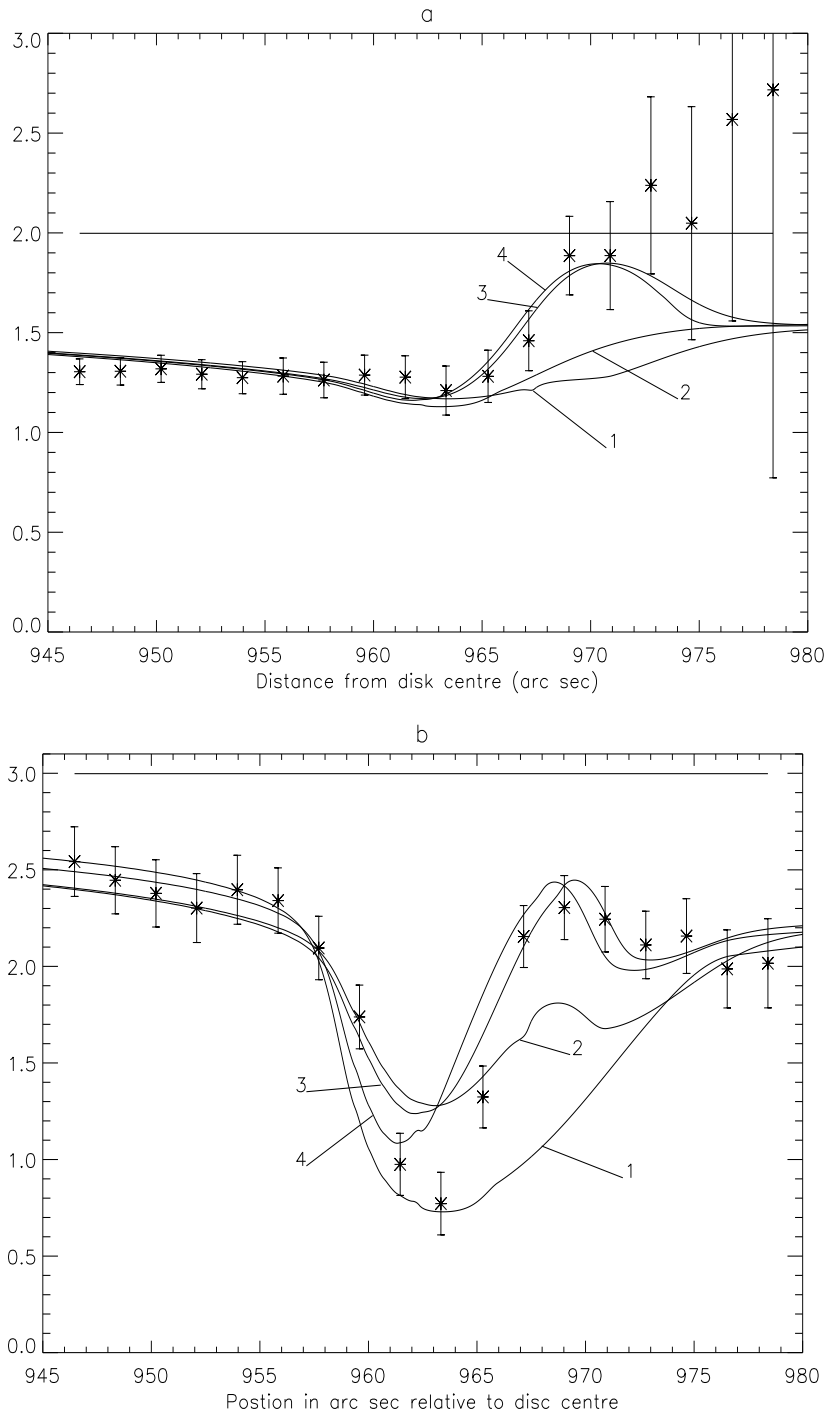

Figure 6.5: Observed and model branching ratios of the (a) (3/2–1/2)/(1/2–1/2) components of the C II $2s^2 2p\ ^2P - 2s2p^2\ ^2S$ multiplet and (b) the (2–2)/(1–2) components of the C III $2s2p\ ^3P - 2p^2\ ^3P$ multiplet.

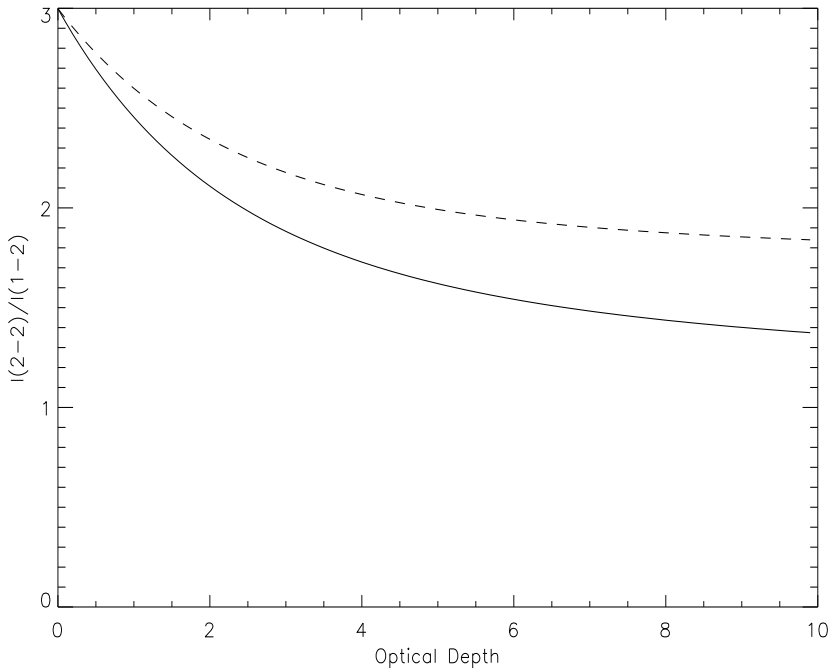

Figure 6.6: Intensity ratio of C III (2–2)/(1–2) versus optical depth for the unblended (dashed) and blended (solid) cases, calculated using eqs 2.17 and 4.5 respectively.

6.3.3 Discussion

The best fit to the observed ratios for each model yields optimal parameters for each of the two ions. The two most effective models in each case are models 3 and 4 for which the most significant parameters are optical depth at disk centre and density scale height. The disk centre optical depths returned were 0.7 and 0.15 for the C II $2s^2 2p\,^2P_{3/2} - 2s2p^2\,^2S_{1/2}$ line at 1037.012 Å and the C III $2s2p\,^3P_2 - 2p^2\,^3P_2$ line at 1175.711 Å respectively. These compare with values obtained in chapter 2 of 0.6 and 0.16 respectively. The difference in the C II case is due to the improved calculation of optical depth whereas the difference in the C III case is principally due to the inclusion of line blending.

Optimisation of density scale height yields values of 1.2 and 2.5 arc sec for both

models 3 and 4 for C II and C III respectively. The scattered light signal becomes significant at heights beyond the inner edge of the emitting layer – i.e. as the (apparent) density falls off to zero. As a consequence the optimised scale height is dependent upon the inclusion of scattered light. Specifically, it is less when scattered light is included. When it is excluded the optimal scale height for C III is 4 arc sec. These compare with values obtained in chapter 2 of 1.3 and 1.4 arc sec respectively. The difference in the C II values is due to the inclusion of scattered light. The difference in the C III case is due to the inaccurate fit to the observed ratios at the limb.

Fig. 6.5b shows that model 4 is slightly more effective than model 3 in describing the C III ratio variation across the limb. However, the relative magnitude of model 1 to model 3 in the composite case was treated as an adjustable parameter and while a large value (~ 100) is optimal in the C III case, a low value, namely 0, is the optimal value for C II. As a consequence model 4 is considered in this study to be largely redundant. The scale heights in both cases are similar to the ~ 1.5 arc sec findings of Mariska et al. (1978) and to those found in chapter 2 – noting that the C III scale height is likely to be an over estimate as the slope of the ratios in the region from $964 \rightarrow 970$ arc sec is not matched. They also agree with both in terms of the decrease with decreasing temperature of line formation.

In order for the scattered light to dominate at the appropriate point in the C III data, a departure from the exponential fall off of density is required. A cut-off is introduced in the model for this purpose, the position of which may be optimised for agreement with the observed ratios. This cut-off is found to be at ~ 969 arc sec. This value is influenced by the fact that the scale height is optimised as described above and is thus overestimated. Consequently in the absence of a cut-off the predicted onset of scattered light occurs later than observed.

A possible interpretation for this departure from an exponential fall off, or at least a change or even discontinuity in scale height, follows from the model considered by Mariska et al. (1978) who, as stated in chapter 2, envisaged cylindrical spicules. The exponential fall off of density in this picture reflects the change in filling factor as the number of spicules intersected by the line-of-sight decreases with distance beyond the limb. Ultimately, however, the density variation will reflect the genuine density

variation at the top of a spicule. However, the introduction of this parameter is introduced so that the off-limb discrepancy between observed and model branching ratios (seen in figs 2.16 and 6.2b) might be resolved by the inclusion of scattered light. This it does, but it does not account for the emergent fluxes observed at such heights. It is therefore likely that this parameter is a numerical fudge.

As predicted in chapter 2, the inclusion of scattered light is sufficient to match the off-limb model C III branching ratios to the observed ones within the error bars. However, the discrepancy between the model and observed fluxes at heights beyond $\sim$ 970 arc sec is non-trivial. This suggests that the signals at such heights are true and not dominated by instrumentally scattered light. If so, then the branching ratios indicate that the optical depths at heights beyond $\sim$ 970 arc sec are comparable with those on disk which in turn imply comparable column densities. The fluxes at such heights, however, are significantly smaller than those on disk which indicate that the column densities are significantly smaller than the ones on the disk. This is a paradox which may be resolved if the emitting structures at heights beyond $\sim$ 970 arc sec are unresolved (see sec. 6.7).

6.4 Comments on the effectiveness of stratified models

It is clear that stratified models are sufficient to track the branching ratio variations well, failing only in the C III case in the vicinity of the inner edge of the emitting layer. Furthermore, the inclusion of scattered light leads to an effective fit to the ratios above heights of $\sim$ 970 arc sec where previously there was a discrepancy between the model (and intuitive expectations) and the observations. The fit to the emergent fluxes, on the other hand, is improved compared to that in sec. 2.7, but, nevertheless, still not modelled well. Moreover, in the case of the fluxes, scattered light is not sufficient to explain the signals off limb. It is natural to conclude that this is due to the failure of the stratified model at heights lower than the region of scattered light dominance. But even if the observed signal is used to calculate the scattered contribution, the

predicted signal at heights above $\sim$ 970 arc sec is still much lower than that observed.

If the signal in these regions is predominantly a true signal, the issue of the mismatch between the column densities at such heights implied by the branching ratios, and those implied by fluxes resurfaces. In addition, the interpretation of the Doppler shifts discussed in sec 2.4 is again in doubt. The signals, being true, imply that these shifts indicate either 20 km/s upflows beyond the limb or 20 km/s downflows on disk, and at the limb. As discussed in chapter 1, although both upflows and downflows are evident in TR spectral lines, spectral emission from downflowing plasma is dominant. Typical velocities are $\sim 5 \rightarrow 16$ km/s (Brekke et al., 1997) which are less than those found here. They are, however, consistent in magnitude with velocities associated with rising spicule structures (Lorrain & Koutchmy, 1996). If the shifts are to the red, then they persist up until the limb. This is inconsistent with the analyses of Athay & Dere (1989) and Henze & Engvold (1992) who found that the shifts vanished at the limb. Feldman et al. (1982), however, suggest that the redshifts do not disappear at the limb though they do decrease. Following this, the findings here would suggest downflows of velocity greater than 20 km/s on disk.

As discussed earlier, the relative effectiveness of the fit to the ratios as compared with the fluxes is due to the fact that the linear dependence of the fluxes on column density is factored out in the ratios. This dependence is present in the fluxes themselves. Thus the ratios are relatively insensitive to structure. Since the ratios are indicators of absorption which is characterised by the absorption factor, this insensitivity to structure illustrates the appropriateness of the stratified model in the calculation of the absorption factor. This also follows intuitively from eq. 2.33 in which the intensity term is integrated over volume, thus averaging over the structural detail.

The fits to the fluxes, however, demonstrate a sensitivity to structure. The stratified models are able to describe the emission in broad terms but not in detail. For a more accurate fit, the fine structure must be included in the emergent flux model.

Table 6.1: Summary of data for the C III $2s2p\ ^3P_2 - 2p^2\ ^3P_2$ transition for each raster scan position. $\tau_{0,2-2}/\tau_{0,1-2} = 3.204$

Pos.(")	$\tau_{0,2-2}$	$\bar{g}\{\tau_{0,2-2}\}$	Pos.(")	$\tau_{0,2-2}$	$\bar{g}\{\tau_{0,2-2}\}$
943.06	0.61 (0.74)	0.80 (0.78)	959.94	54.0 (-)	0.03 (-)
944.94	0.80 (0.94)	0.75 (0.74)	961.88	5.40 (8.64)	0.27 (0.21)
946.81	0.90 (1.09)	0.73 (0.71)	963.75	1.40 (1.68)	0.62 (0.60)
948.69	1.05 (1.27)	0.69 (0.67)	965.63	1.04 (1.27)	0.70 (0.67)
950.56	0.86 (1.05)	0.74 (0.71)	967.50	1.20 (1.42)	0.66 (0.64)
952.44	1.00 (1.18)	0.71 (0.69)	969.38	1.50 (1.81)	0.61 (0.58)
954.31	1.51 (1.86)	0.60 (0.58)	971.25	1.40 (1.67)	0.62 (0.60)
956.19	2.70 (3.42)	0.45 (0.41)	973.13	1.81 (2.24)	0.56 (0.53)
958.06	15.0 (-)	0.11 (-)	975.00	1.72 (2.13)	0.57 (0.54)

6.5 Extraction of optical depth from observations and the validity of the escape probability approach

Optical depths may be deduced from the branching ratios with blending included following the approach described in sec. 2.3. Results corresponding to those of tables 2.1, 2.3 and 2.5 are shown in tables 6.1 $\rightarrow$ 6.3. The values in brackets are those deduced without blending (i.e. those of tables 2.1, 2.3 and 2.5). It can be seen that in each case the optical depths deduced when blending is included are smaller than those obtained when it is not.

It is interesting to note that for the C III $2s2p\ ^3P_2$ – $2p^2\ ^3P_2$ transition (table 6.1) the blended $\bar{g}^{(i)}\{\tau_0\}$ is effective in extracting optical depth values at 958.06 and 959.94 arc sec. With and without blending the $\bar{g}\{\tau_0^{(1)}\}/\bar{g}\{\tau_0^{(2)}\}$ curves decrease monotonically with a gradient that also decreases with optical depth (see fig. 6.6). Furthermore the gradient is greater when blending is included. Consequently, while without blending the $\bar{g}\{\tau_0\}$ quantity yields unphysical optical depths at 958.06 and 959.94 arc sec the values are meaningful when blending is included.

Table 6.2: Summary of data for the C II $2s^2 2p\ ^2P_{3/2} - 2s2p^2\ ^2S_{1/2}$ transition for each raster scan position. $\tau_{0,3/2-1/2}/\tau_{0,1/2-1/2} = 1.97$. These values are the same as in table 2.3 since there is no line blending here.

Pos.(")	$\tau_{0,3/2-1/2}$	$\bar{g}\{\tau_{0,3/2-1/2}\}$	Pos.(")	$\tau_{0,3/2-1/2}$	$\bar{g}\{\tau_{0,3/2-1/2}\}$
943.06	5.30 (5.30)	0.31 (0.31)	959.94	10.2 (10.2)	0.18 (0.18)
944.94	5.25 (5.25)	0.31 (0.31)	961.88	6.00 (6.00)	0.28 (0.28)
946.81	4.95 (4.95)	0.32 (0.32)	963.75	2.82 (2.82)	0.46 (0.46)
948.69	5.70 (5.70)	0.29 (0.29)	965.63	0.36 (0.36)	0.88 (0.88)
950.56	6.23 (6.23)	0.27 (0.27)	967.50	0.36 (0.36)	0.88 (0.88)
952.44	6.00 (6.00)	0.28 (0.28)	969.38	- (-)	- (-)
954.31	6.70 (6.70)	0.26 (0.26)	971.25	- (-)	- (-)
956.19	5.80 (5.80)	0.29 (0.29)	973.13	- (-)	- (-)
958.06	6.20 (6.20)	0.27 (0.27)	975.00	- (-)	- (-)

Table 6.3: Summary of data for the C II $2s^2 2p\ ^2P_{3/2} - 2s2p^2\ ^2P_{3/2}$ transition for each raster scan position. $\tau_{0,3/2-3/2}/\tau_{0,1/2-3/2} = 5.05$.

Pos.(")	$\tau_{0,3/2-3/2}$	$\bar{g}\{\tau_{0,3/2-3/2}\}$	Pos.(")	$\tau_{0,3/2-3/2}$	$\bar{g}\{\tau_{03/2-3/2}\}$
943.06	3.20 (4.95)	0.39 (0.32)	959.94	3.05 (4.69)	0.40 (0.33)
944.94	3.23 (5.01)	0.39 (0.32)	961.88	3.13 (4.84)	0.40 (0.33)
946.81	2.71 (4.13)	0.43 (0.36)	963.75	2.90 (4.40)	0.42 (0.35)
948.69	2.86 (4.37)	0.42 (0.35)	965.63	1.90 (2.88)	0.53 (0.46)
950.56	3.31 (5.15)	0.38 (0.31)	967.50	1.54 (2.36)	0.59 (0.51)
952.44	3.12 (4.81)	0.40 (0.33)	969.38	0.58 (1.07)	0.81 (0.71)
954.31	3.00 (4.56)	0.41 (0.34)	971.25	0.83 (1.40)	0.74 (0.65)
956.19	3.40 (5.23)	0.37 (0.31)	973.13	1.01 (1.63)	0.70 (0.61)
958.06	3.30 (5.10)	0.38 (0.31)	975.00	0.75 (1.29)	0.76 (0.67)

6.6 Removing the discrepancy between model and observed spectral data

It is clear that the stratified models presented, in conjunction with the blended, line-of-sight averaged escape probability, $\bar{g}^{(i)}\{\tau_0\}$, are unable to accurately describe the C II and C III spectral characteristics observed by SOHO-SUMER in the vicinity of the solar limb. Yet it has been asserted in this work that $\bar{g}^{(i)}\{\tau_0\}$ is appropriate and accurate in describing the effects of opacity in the spectral lines of these ions. If this is true then the failure of the models presented is in their treatment of structure, and thus the variations in column density, and *not* due to a dependence of the source function on space or frequency either due to photon scattering or plasma flow. To demonstrate that this is the case, consider fig. 6.7. This shows observed fluxes for the C III $2s2p\ ^3P_2 - 2p^2\ ^3P_2$ line at 1175.711 Å with the function $\tau_0\bar{g}^{(i)}\{\tau_0\}$ overlaid. Here the optical depth at each point is not based on any model, stratified or otherwise. Rather the optical depths are those extracted from the observed ratios and listed in table 6.1. The predicted fluxes are scaled to match the observed value at 943.06 arc sec. The discrepancy is marked and denotes a failure in the escape probability model. Clearly at least one assumption underpinning the theory is not valid.

It has been shown that the modification to the source function due to opacity is not significant for either the C II or C III. However, it was shown in chapter 3 that there is a spatial variation of the source function due to the variation of electron density and temperature through the emitting layer. This variation was overlooked and the assumption was made that each emitting layer may be represented by a single (T_e, N_e) pair. This assumption was motivated by the notion of an emitting layer comprising of thin TR sheaths surrounding spicule-like structures which extend into the corona with lengths greatly exceeding the thickness of each sheath. This assumption allowed the modification to the source function purely due to opacity – or alternatively, scattering into the line-of-sight – to be considered. It was not justified at the time and thus it is conceivable that this variation is partially or wholly responsible for the breakdown of the $\tau_0\bar{g}^{(i)}\{\tau_0\}$ expression evident in fig. 6.7.

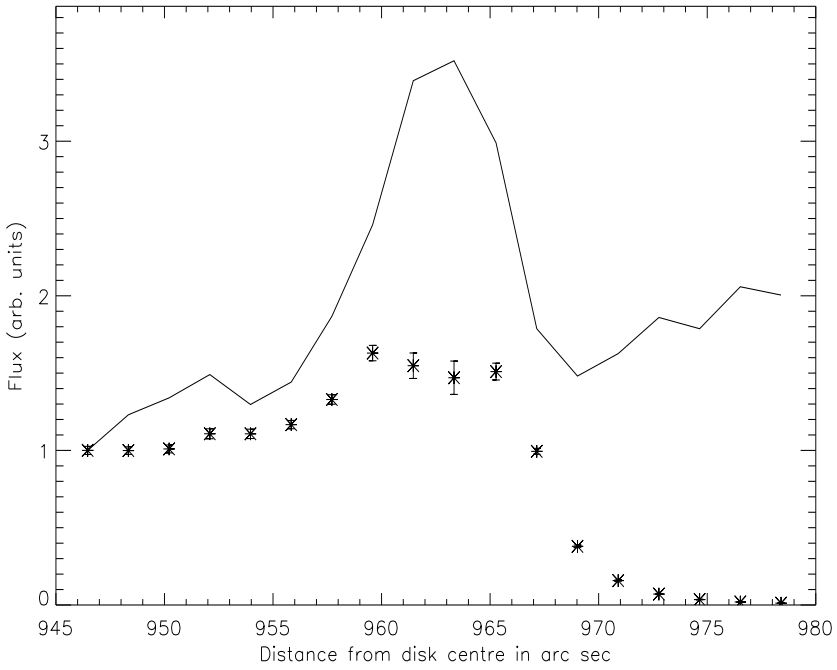

Figure 6.7: Observed fluxes for the C III $2s2p\ ^3P_2 - 2p^2\ ^3P_2$ line at 1175.711 Å. Overlaid is the function $\tau_0 \bar{g}^{(i)}\{\tau_0\}$ (solid line) where the optical depths, τ_0, for each position are taken from table 6.1.

It was shown in sec. 3.10 that the intensity of an unblended line may be written as

$$I \sim \bar{N}_l \bar{g}\{\tau_0\} L f_{los}\{\tau_0\} \tag{6.4}$$

where

$$f_{los}\{\tau_0\} = \int_0^L \frac{\tilde{N}_u(t)}{\tilde{N}_l(t)} \frac{g(t)}{\bar{g}\{\tau_0\}} dt \tag{6.5}$$

This extends to blended lines if $\bar{g}^{(i)}\{\tau_0\}$ replaces $\bar{g}\{\tau_0\}$ in eq. 6.4. There is therefore a key issue relating to the nature of the dependence of $f_{los}\{\tau_0\}$ on line-of-sight and optical depth.

Within the picture of thin sheaths around extended spicule-like structures, the

line-of-sight optical depth is principally determined by the number of structures intersected by that line-of-sight. Providing the conditions within each sheath are similar, the dependence of $f_{los}\{\tau_0\}$ on line-of-sight will be weak. The optical depth is smaller on-disk than at the limb – for example the model based optical depth at disk centre for the C III $2s2p\ ^3P_2 - 2p^2\ ^3P_2$ line at 1175.711 Å is 0.16 which compares with observationally deduced values of 0.61 and 1.40 at 943.06 and 963.75 arc sec respectively. Thus it may be deduced that for C II and C III optical depth of a single sheath is small and that the number of structures intersected by the each line-of-sight in the vicinity of the limb is large.

If the variation of the source function with respect to space is responsible for the deviation of observed and predicted fluxes in fig. 6.7, a correlation between this deviation and optical depth is expected. This would manifest itself at each raster position in a line to line variation of the deviation. An investigation into this is presented below but first, consider the dependence of the source function on frequency.

It has been shown in chapters 4 and 5 that the possible contributors to a dependence of the source function on frequency are either negligible or manageable within the escape probability framework. The relevant optical depths are sufficiently small that scattering into the line-of-sight is insignificant. Consequently the effects of blending may be included within the line-of-sight averaged escape probability, $\bar{g}^{(i)}\{\tau_0\}$. They are also sufficiently small to ensure complete frequency redistribution. This is confirmed by the observed line profiles which suffer minimal deviations from Gaussian profiles which may be described within the escape probability theory. Also confirmed by the observed profiles is the fact that plasma flow, though evident from the observed Doppler shifts (see sec. 2.4), presents no difficulty and may be accounted for within the blending formulation. Photon scattering can lead to a dependence of the source function on frequency through partial frequency redistribution. Multiple scattering in the wings of the Lα line of hydrogen can lead to significant changes in the flux of that line which in turn can affect the charge balance and gas pressure through modification of the ionisation balance of hydrogen. However, the effects of partial frequency redistribution on line fluxes of other lines are not typically very large and so complete frequency redistribution is usually a good approximation (Hubeny &

Lites, 1995). This is confirmed by fig. 6.1 which shows no significant deviation from Gaussian profiles.

The third potential source for the deviation of predicted from observed fluxes is atmospheric structure. In chapter 5 structure was discussed and it was demonstrated that it leads to a reduction in the degree of absorption within a plasma. Therefore, if the validity of $\bar{g}^{(i)}\{\tau_0\}$ is confirmed by consideration of the absorption factor within a stratified atmosphere model, then the presence of structure will strengthen rather than threaten this validity. Hence, from the perspective of the modification to the population structure (or scattering into the line-of-sight), structure does not influence the validity of the $\bar{g}^{(i)}\{\tau_0\}$ expression. Moreover, it was demonstrated in chapter 3 (see sec. 3.3) that if it is assumed that the source function is constant in space, then the $\bar{g}^{(i)}\{\tau_0\}$ expression is independent of the nature of the variation of density along the line-of-sight. So structure along the line-of-sight is not responsible for the discrepancy in fig. 6.7. However, structure will influence the fluxes if the observed structures are smaller in one or more dimension than the resolution limit of the instrument – i.e. if the observed structures are unresolved. If this is so then the term $f_{los}\{\tau_0\}$ may be interpreted as a *filling factor*. This is a purely geometric quantity and is therefore independent of optical depth.

If structure is responsible for the discrepancy in fig. 6.7, then in contrast to the case of the source function variation being responsible, a constancy of $f_{los}\{\tau_0\}$ with respect to τ_0 is expected.

Shown in fig. 6.8 are observed fluxes versus raster position for each component of the C III $2s2p\ ^3P - 2p^2\ ^3P$ multiplet with plots of $f_{los}\{\tau_0\}\tau_0\bar{g}^{(i)}\{\tau_0\}$ overlaid. As in fig. 6.7, the optical depths are those listed in table 6.1. The factors $f_{los}\{\tau_0\}$ are determined such that the observed and predicted fluxes in fig. 6.7 match exactly and so for each raster position there is only one scaling factor for all the lines of the multiplet. It can be seen from this figure that the single set of factors $f_{los}\{\tau_0\}$ is sufficient to match the predicted intensities to the observed ones almost exactly for each line with the exception of the 1–1 and 1–0 components. Both these are blended and the discrepancy between predicted and observed values is most significant in the vicinity of the limb which corresponds to the region of most significant optical thickness and

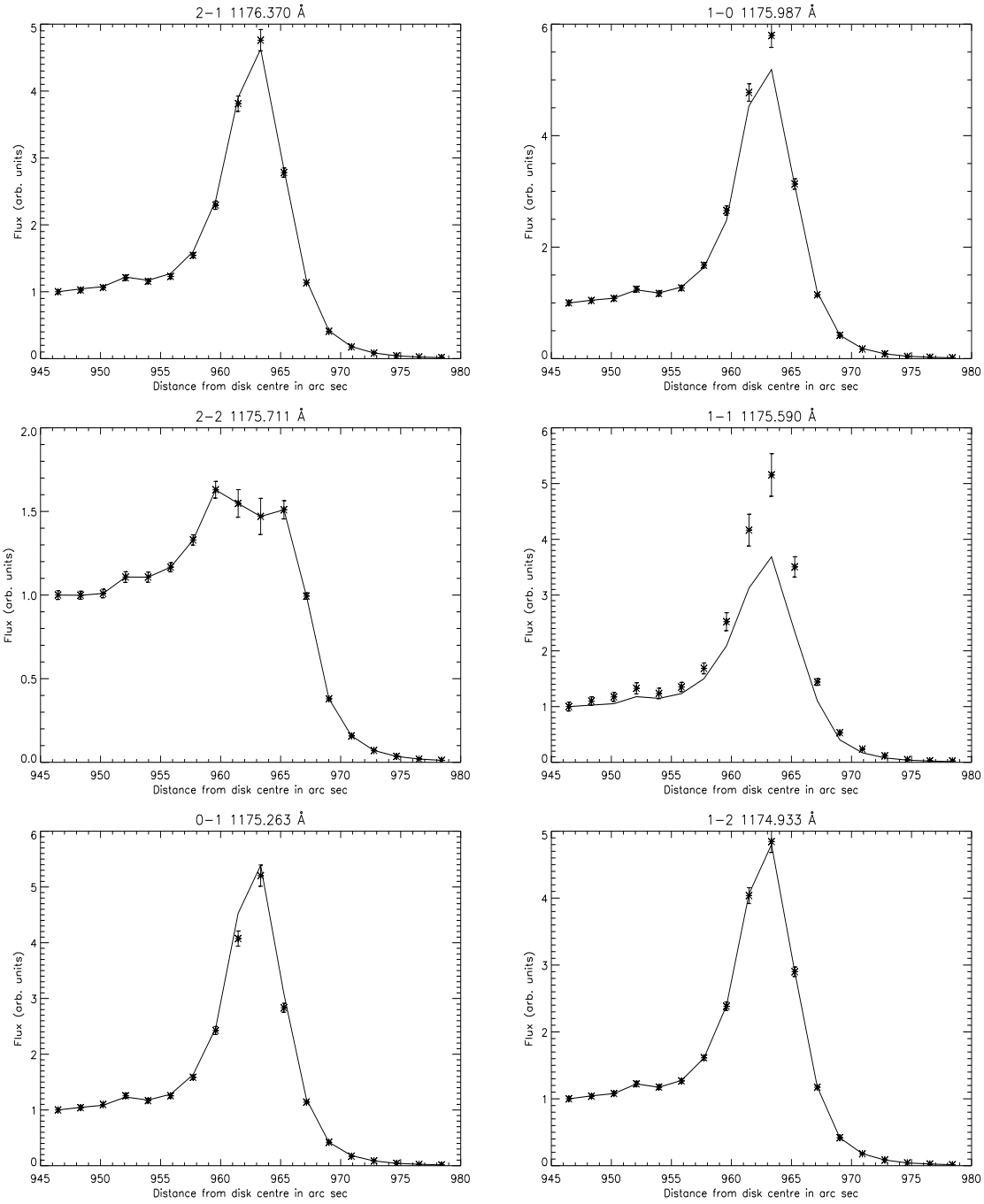

Figure 6.8: Observed fluxes versus raster position for each component of the C III $2s2p\,^3P - 2p^2\,^3P$ multiplet. Overlaid are plots of $f_{los}\{\tau_0\}\tau_0\bar{g}^{(i)}\{\tau_0\}$ where the optical depths are those deduced from the observed branching ratios which are listed for the 2–2 component in table 6.1. The factors $f_{los}\{\tau_0\}$ are determined such that the observed and predicted fluxes in fig. 6.7 match exactly.

thus also the greatest degree of blending. Furthermore the discrepancy is most marked for the 1–1 line which is in turn the most significantly blended of the two. These facts suggest that the discrepancies in the 1–1 and 1–0 components relate to the difficulty in resolving these lines and not due a weakness in the escape probability analysis. It is also true that the 1–1 and 1–0 components are the most optically thin of the multiplet (see table 2.7) which might suggest that the discrepancies in these lines are due to a dependence of $f_{los}\{\tau_0\}$ on optical depth. However, the 1–0 component has a comparable optical depth to that of the 0–1 component which shows good agreement between predicted and observed intensities.

Fig. 6.9 shows the same as fig. 6.8 but for the components of the C II $2s^2 2p\ ^2P$ – $2s2p^2\ ^2P$ multiplet. In these plots there is good agreement between model and observed fluxes for all the components with the only exception being the 1/2–1/2 component which is *not* the most optically thin. In fact it is the closest in optical depth to the *control* line (i.e. the one that determines the $f_{los}\{\tau_0\}$ values). It is, however, the most severely blended of all the lines of this multiplet.

Fig. 6.10 shows observed fluxes versus raster position for each component of the C II $2s^2 2p\ ^2P$ – $2s2p^2\ ^2P$ multiplet at $\sim$ 1036 Å again with plots of $f_{los}\{\tau_0\}\tau_0\bar{g}^{(i)}\{\tau_0\}$ overlaid. Here there is near perfect agreement between the two lines, neither of which are blended.

It follows then that $f_{los}\{\tau_0\}$ is independent of optical depth, τ_0, since the same set of factors, $f_{los}\{\tau_0\}$, are effective for each line even though the optical depth varies from line to line. Further confirmation of this follows from the findings of secs 6.3.1 and 6.3.2 in which it was found that at the limb the stratified models, coupled with the escape probability techniques, overestimate both the emergent fluxes and the C III branching ratios at the limb. Furthermore, at heights above $\sim$ 970 arc sec both the C II and C III emergent fluxes are underestimated whereas the branching ratios are overestimated if the effects of instrumentally scattered light are neglected. At the limb the stratified model predicts column densities too great to match the emergent fluxes but too small to match the ratios. This discrepancy is removed if the emitting structures in the vicinity of the limb are partially or wholly unresolved. Well beyond the limb the ratios indicate optical depths comparable with those on

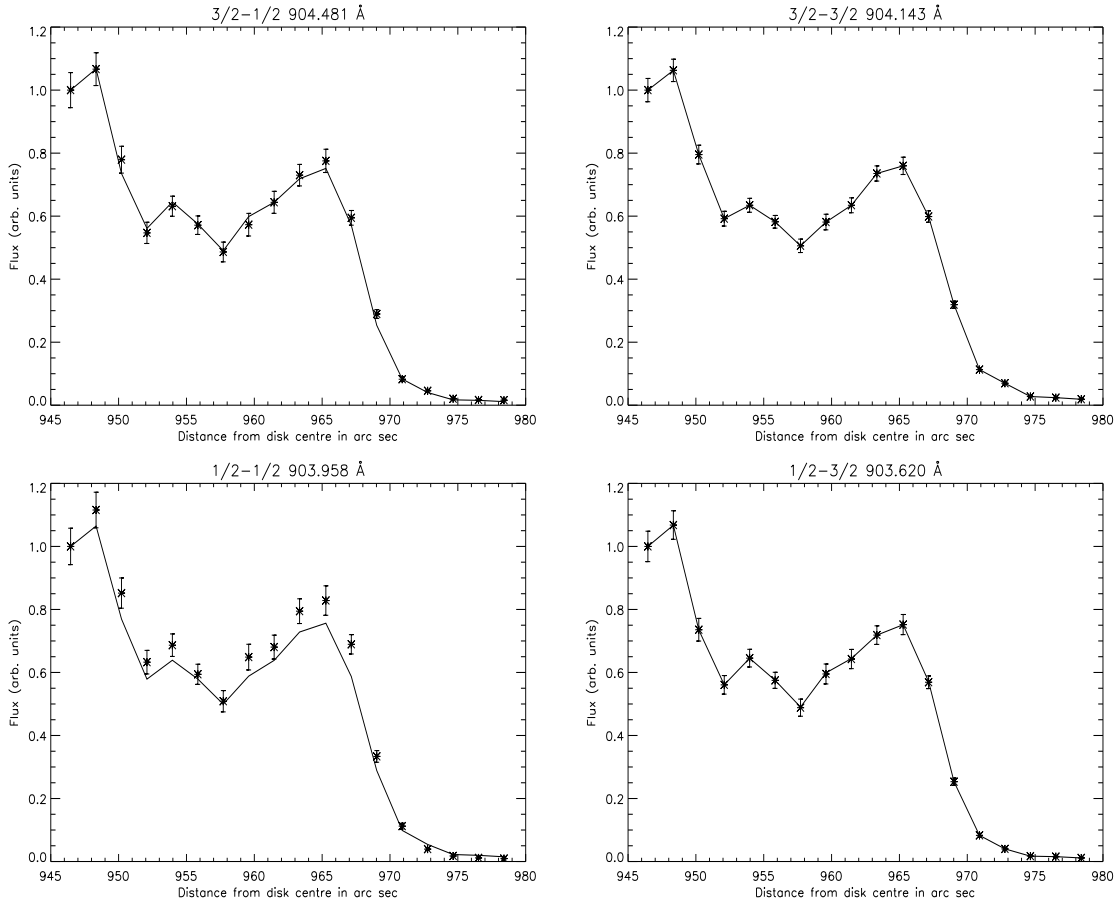

Figure 6.9: Observed fluxes versus raster position for each component of the C II $2s^2 2p\ ^2P$ – $2s2p^2\ ^2P$ multiplet. Overlaid are plots of $f_{los}\{\tau_0\}\tau_0\bar{g}^{(i)}\{\tau_0\}$ where the optical depths are those deduced from the observed branching ratios which are listed for the 3/2–3/2 in table 6.3. The factors $f_{los}\{\tau_0\}$ are determined such that the observed and predicted fluxes for the 3/2–3/2 component match exactly.

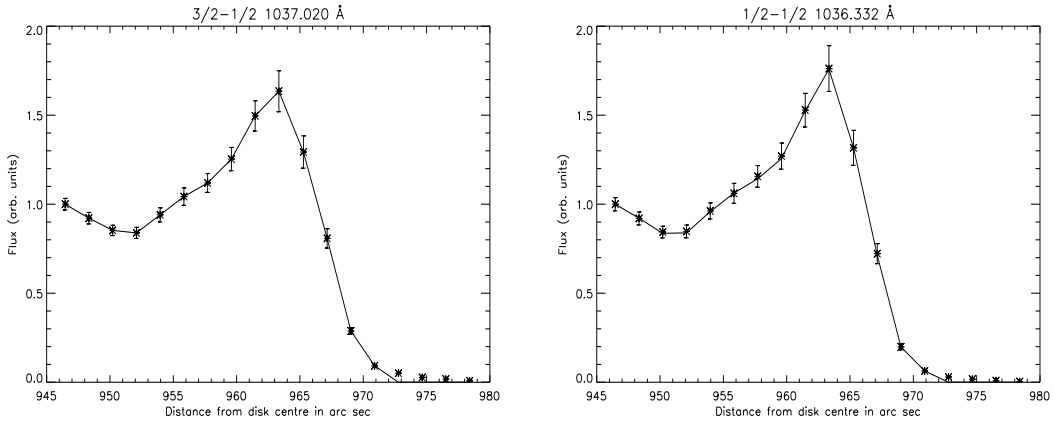

Figure 6.10: Observed fluxes versus raster position for each component of the C II $2s^2 2p\ ^2P$ – $2s2p^2\ ^2P$ multiplet. Overlaid are plots of $f_{los}\{\tau_0\}\tau_0\bar{g}^{(i)}\{\tau_0\}$ where the optical depths are those deduced from the observed branching ratios which are listed for the 3/2–1/2 in table 6.2. The factors $f_{los}\{\tau_0\}$ are determined such that the observed and predicted fluxes for the 3/2–1/2 component match exactly.

the disk despite the fact that the observed fluxes are significantly lower than those in this region. Moreover, the inclusion of instrumentally scattered light is insufficient to resolve this discrepancy. This signal, being true, again suggests the presence of unresolved structures.

This body of evidence demonstrates that the discrepancy in fig. 6.7 is not due to the spatial variation of the source function but is due to structure. It follows that the neglect of the dependence of the source function on space is appropriate and the line-of-sight averaged escape probability is effective.

6.7 Implications for transition region structure

It has been concluded that $f_{los}\{\tau_0\}$ may be interpreted as a filling factor, which represents the area of the slit occupied by emitting structures. Since it is independent of optical depth, it may be written as f_{los}. The deduced filling factors for the C II multiplets at 904 and 1036 Å are shown in figs 6.11a and b respectively and those of the C III multiplet at 1775 Å are shown in fig. 6.12. In each case the factors are

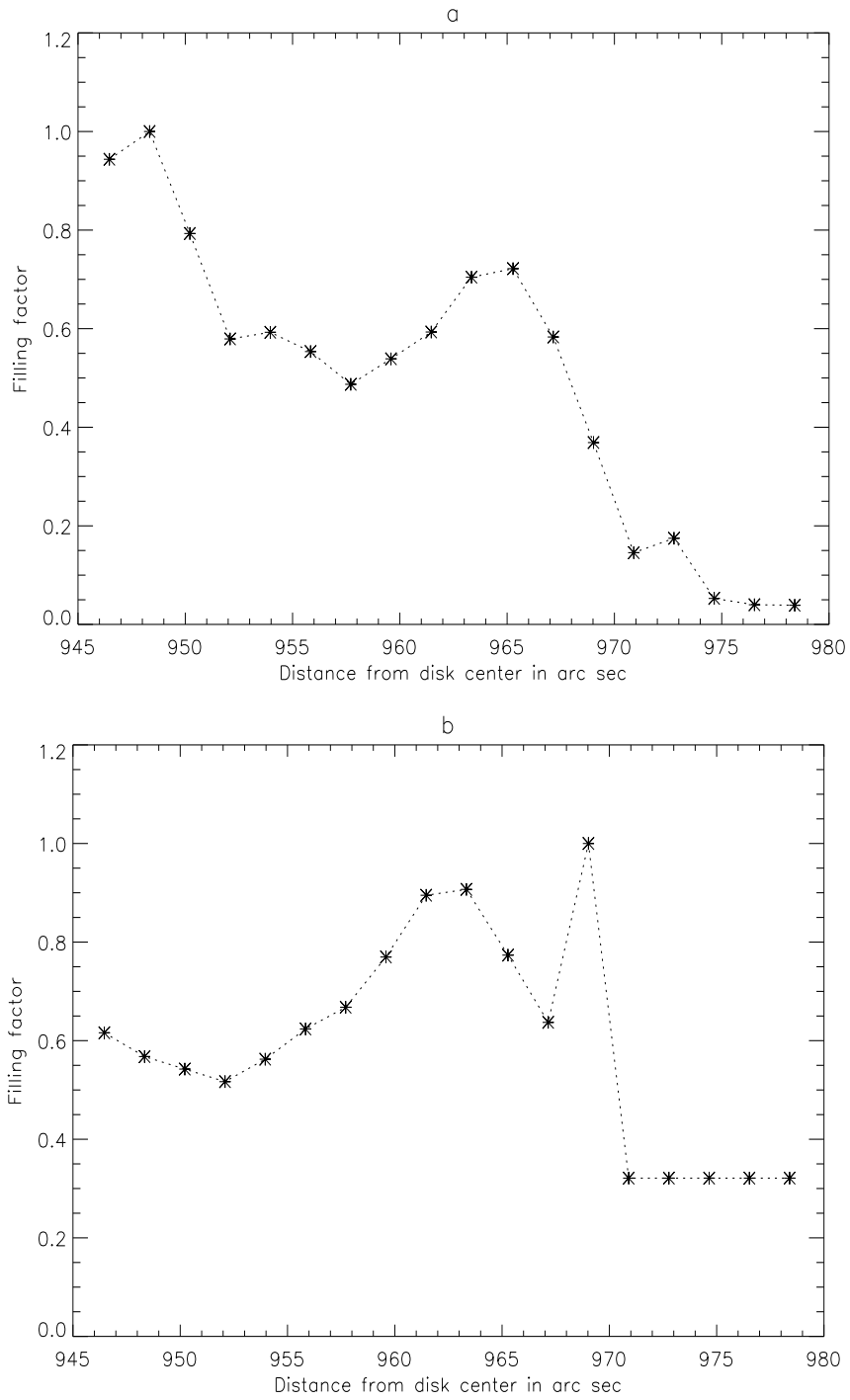

Figure 6.11: C II filling factors (f_{los}) versus pointing position for lines of (a) the 904 Å multiplet and (b) the 1036 Å multiplet. In (b) the filling factor values for the four highest pointing positions set to the value at 970.9 arc sec since no optical depths were deduced for these points (see table 6.2).

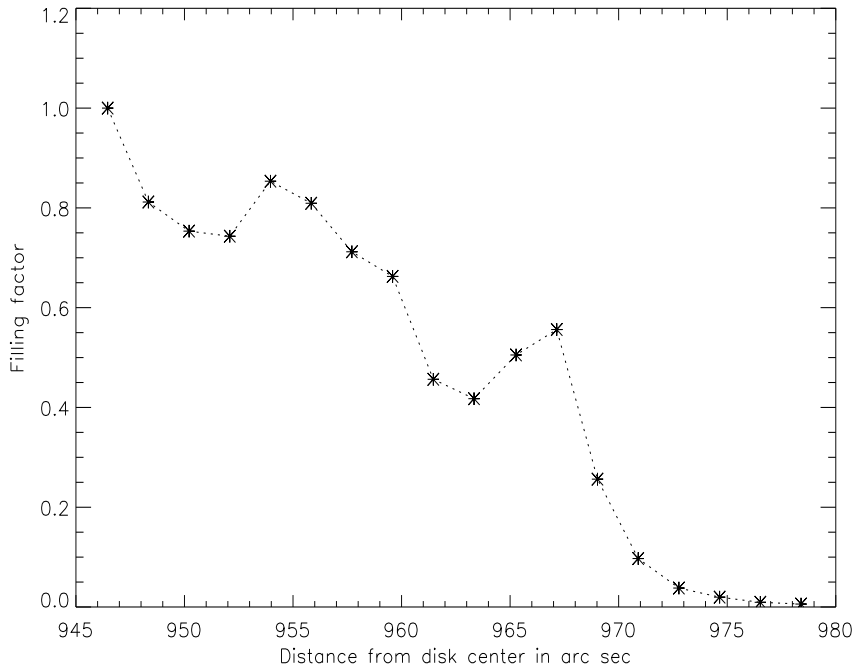

Figure 6.12: C III 1775 Å multiplet filling factors versus pointing position.

scaled to be unity at 946.462 arc sec. There is a general downward trend evident in figs 6.11a and 6.12 indicating a decrease in occupation of the slit by emitting structures with distance from disk centre. No such trend is evident in fig. 6.11b. In each figure, however, strong variations are evident. This variability implies that the absolute filling factors are unity at no more than one pointing position and are thus unlikely be unity anywhere. This implies the presence of unresolved structures at each pointing position – i.e. on the disk, at the limb and beyond.

Of course, the observed fluxes are summed over the slit which has a length of $\sim$ 60 arc sec. Thus the filling factors here correspond to the presence of spicule-like structures of diameter less than 60 arc sec. Such structures are evident in figs 2.8a and b. If at each pointing position the pixels are sorted according to their brightness, then the data may be split into regions associated with resolved structures and regions that are visibly in between the observable structures.

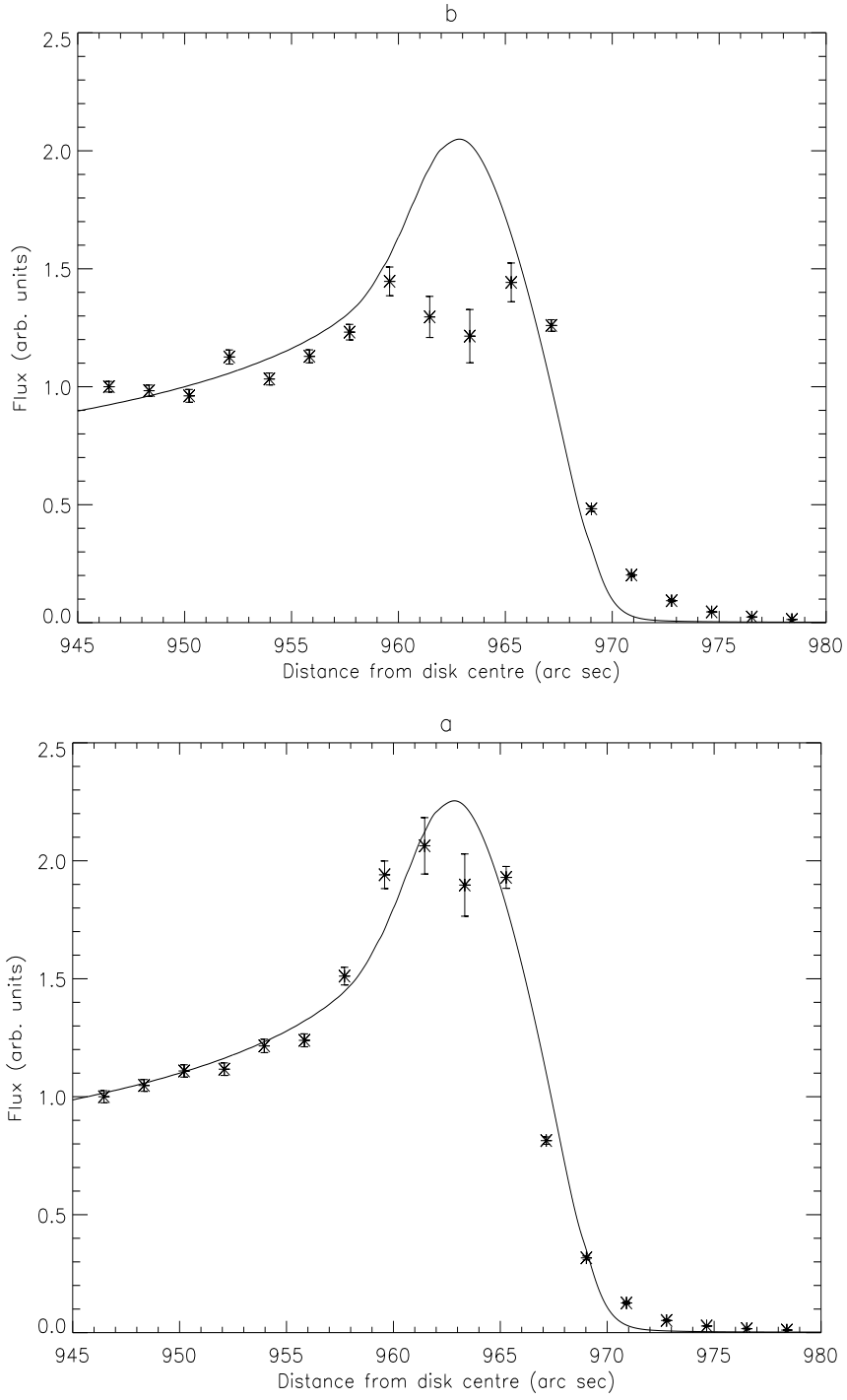

Figure 6.13: Observed fluxes of the C III $2s2p\ ^3P_2 - 2p^2\ ^3P_2$ line at 1175.711 Å compared with predicted values based on an exponential density model overlaid, for (a) regions associated with observable structure and (b) regions not associated with observable structure.

Figs 6.13a and b show observed and model fluxes of the C III $2s2p\ ^3P_2 - 2p^2\ ^3P_2$ line at 1175.711 Å for regions associated and not associated with observable structure. For regions associated with structure the stratified model clearly fails as before. For the *intra-structure* regions, however, the stratified model is much more effective. Figs 6.14a and b, on the other hand, show the same observed fluxes this time in comparison with $\tau_0 \bar{g}^{(i)}\{\tau_0\}$. In both cases there is a significant deviation indicating the presence of unresolved structures even in the *intra-structure* data.

6.8 Concluding remarks

In this chapter the C II and C III spectral data discussed in chapter 2 has been re-assessed both from a modelling and diagnostic perspective. The stratified models previously considered have been re-applied with an improved calculation of optical depth and with line blending and instrumentally scattered light included. The resultant fits to both observed fluxes and branching ratios are more effective at certain positions and less effective at others as compared with those of chapter 2. Optical depths at disk centre extracted from these models are comparable with those obtained in chapter 2. The deduced density scale height for C II is also comparable with that or chapter 2 but the C III value differs due to a poor fit to the branching ratios of this ion in the vicinity of the limb.

The inclusion of scattered light improves the fit to the branching ratios at positions above $\sim$ 970 arc sec but fails to account for the observed fluxes at such heights. This implies that the observed emission at such heights is not dominated by scattered light which in turn suggests that the emitting structures are observationally unresolved.

Consideration of observed fluxes in comparison with $\tau_0 \bar{g}^{(i)}\{\tau_0\}$ confirms the conclusion that the discrepancy between model and observed fluxes is due to the presence of unresolved emitting structures. This analysis serves also to validate the assumption asserted in chapter 3 that the spatial variation of the source function due to the variation of (T_e, N_e) is negligible in this context. This in turn confirms the effectiveness of the line-of-sight averaged escape probability, $\bar{g}^{(i)}\{\tau_0\}$, in a moderate disk centre optical depth regime.

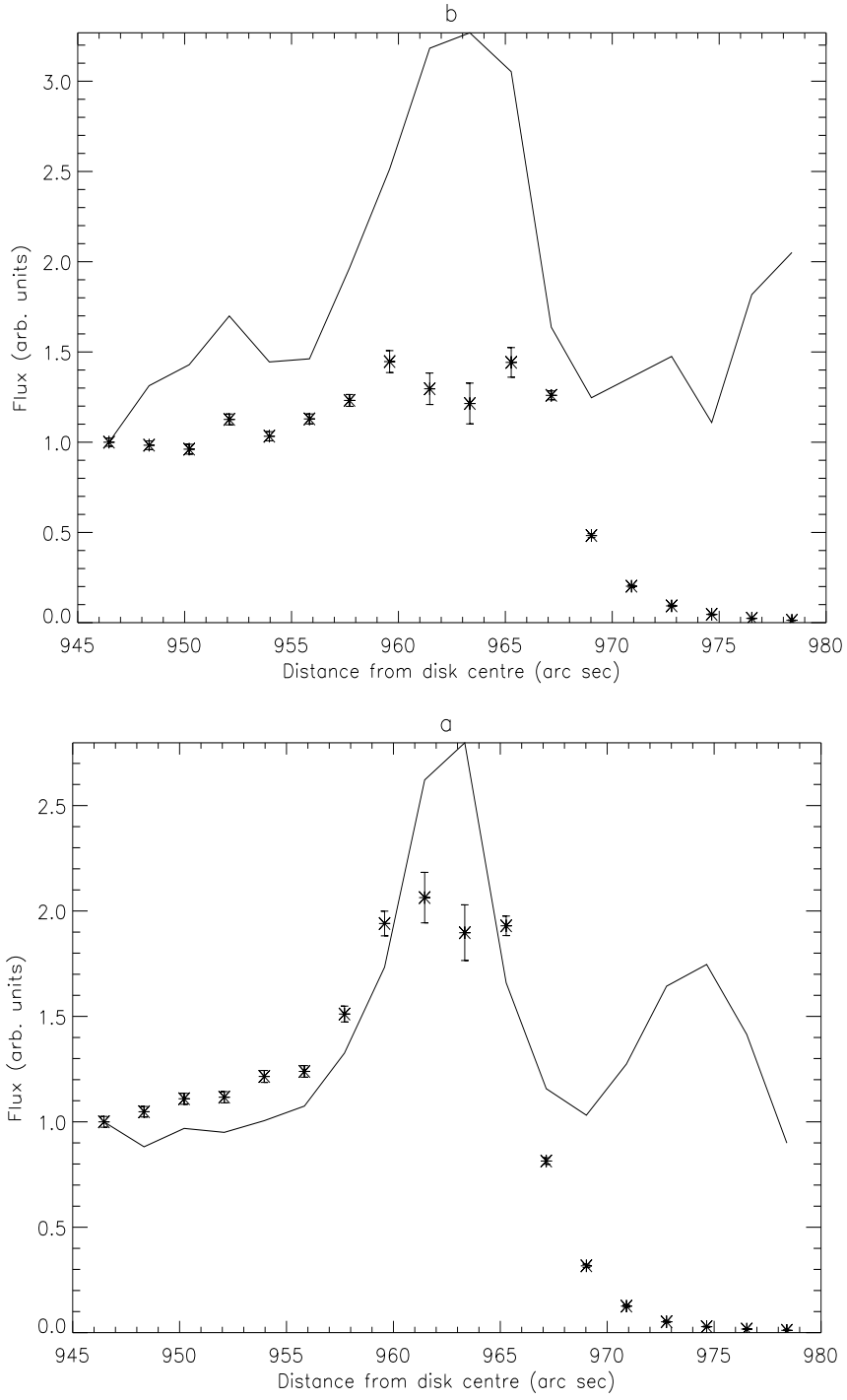

Figure 6.14: Observed fluxes of the C III $2s2p\ ^3P_2 - 2p^2\ ^3P_2$ line at 1175.711 Å with $\tau_0 \bar{g}^{(i)}\{\tau_0\}$ overlaid, for (a) regions associated with observable structure and (b) regions not associated with observable structure.

Scaled filling factors, which represent the portion of the slit occupied by emitting structures have been deduced for the 904 Å and 1036 Å multiplets of C II and the 1175.711 Å multiplet of C III. These demonstrate the presence of unresolved emitting structures at positions both on the disk and beyond the limb.

The spectral data has been split into regions visibly associated with and not associated with spicule-like structures. For the *intra-spicule* data the stratified model is effective in describing the observed C III $2s2p\ ^3P_2 - 2p^2\ ^3P_2$ line (1175.711 Å) fluxes. This is not the case for the *spicular* data. For both datasets, however, filling factors may be deduced indicating the presence of unresolved emitting structures within both the *intra-spicule* and *spicule* regions.

Chapter 7

Thesis summary

This thesis addresses the problem of diagnosing and modelling optically thick structures in the lower solar atmosphere – i.e. the chromosphere and transition region. Emission from such plasmas is described by the coupled, non-linear equations of radiative transfer and statistical balance. The solution of these equations is complex since it requires in principle complete knowledge of the dynamics and structure of the plasma in question. Both of these are unknown in general and even if they were known, the solution would be computationally complex. Methods that recognise both the non-linearity and coupling of these equations exist (radiative transfer techniques) but are restricted to particular source configurations that are generally very simple such as 1-D or 2-D isobaric and/or isothermal slabs.

Presented and developed here are escape probability and absorption factor techniques for solving the radiative transfer and statistical balance equations in a regime within which they naturally linearise and decouple. These methods have the benefit of being simple to use and are easily integrated within arbitrarily complex geometric plasma models. Thus they are desirable for studying the solar chromosphere and TR which are both highly structured.

Escape probability and absorption factor techniques were introduced in chapter 2 and were applied to spectral measurements of the east solar limb made by the SUMER instrument on board the SOHO spacecraft. Using these techniques, optical depths of spectral lines of C II and C III were extracted at the limb from observed branching

ratios of lines arising from a common upper level. Escape probabilities were coupled with some simple atmosphere models to predict the branching ratio variations from which optical depths at disk centre were deduced. These optical depths allowed all the lines of C II and C III to be classified according to the effects of opacity on both emergent intensities (via $\bar{g}\{\tau_0\}$) and the excited state population structure (via $\bar{\bar{g}}\{\tau_0/2\}$). It was found that certain lines were optically thin but had opacity modified upper levels due to absorption in other lines.

A predicted limb brightening curve for the C III $2s2p^3P_2 - 2p^2\,^3P_2$ line at 1175.711 Å was calculated based on the most effective fit to the observed branching ratios. Unlike the fits to the ratios, the fit to the fluxes, though effective on the disk and well beyond the limb, was poor in the vicinity of the limb itself. This fact, coupled with the inability of the line-of-sight escape probability to extract optical depths for the C III 1175.711 Å line in this region, illustrate weaknesses in the escape probability expressions and/or the stratified atmosphere models.

To resolve these discrepancies, and to investigate the applicability of the escape probability approach in general, the assumptions underpinning these methods have been addressed. The key areas studied relate to

1. the variation of the source function with respect to space and frequency
2. the effects of atmospheric structure
3. instrumental effects

In chapter 3 the spatial variation of the source function was considered. The source function varies spatially for two reasons: firstly, due to the spatial variation of (T_e, N_e) which leads to a dependence of the population structure on position, and secondly due to the influence of photo-absorption on the population structure. The first source of variation, though significant, was initially neglected in order to focus on the effect of opacity on the source function variation. This may otherwise be described as scattering into the line-of-sight. For a number of perpendicular optical depths, the population structure was calculated throughout model emitting layers using a spatially dependent absorption factor, $\Lambda(\tau_0, x)$. This calculation led to the identification

of a disk centre optical depth regime within which the modification to the source function due to opacity impinges negligibly on the validity of the line-of-sight averaged escape probability. The maximum optical depth for which $\bar{g}\{\tau_0\}$ is valid was found to be ~ 10.

As part of this study, the quantity $\mathcal{G}(\tau_0, x) \equiv 1/2(\bar{\bar{g}}\{\tau_0^-\}+\bar{\bar{g}}\{\tau_0^+\})$, was introduced. It was found that the range of optical depths within which this quantity is valid is smaller than that for $\bar{g}\{\tau_0\}$. This is due to indirect effects which mostly influence lines that share an upper level with lines that are more optically thick than themselves. The maximum optical depth for which $\mathcal{G}(\tau_0, x)$ is effective is ~ 0.5. However, the indirect effects are most significant at the layer edges and thus the optical depth range for which $\bar{\bar{g}}\{\tau_0/2\}$ is greater (~ 1).

In chapter 4 the effects of line blending were considered. Line blending fits naturally within the escape probability/absorption factor framework from an algebraic point of view. However, it introduces non-linearity into the $\bar{\bar{g}}\{\tau_0/2\}$ expression through an explicit dependence on upper level population densities which are opacity sensitive. Consequently $\bar{\bar{g}}\{\tau_0/2\}$ must be calculated iteratively when blending is included. If it is calculated in this way then, as in the blended case, it is effective for a range of optical depths although this range is restricted in comparison with the unblended case. This restriction is dependent on the degree of blending. As before, the spatially dependent equivalent, $\mathcal{G}(\tau_0, x)$, fails at layer edge for lines that share an upper level with a thicker line.

If $\bar{\bar{g}}\{\tau_0/2\}$ is not calculated iteratively its range of validity is severely reduced and is most markedly in error for the most severely blended lines.

Again a disk centre optical depth regime was identified within which the line-of-sight averaged escape probability, $\bar{g}^{(i)}\{\tau_0\}$ is valid. The upper optical depth limit was found to be ~ 4.

Spectral line profiles were considered in a blended context and it was found that opacity can lead to significant distortion of individual line profiles and can severely alter the intensity envelope of multiplets affected by blending. Opacity can also lead to perceived Doppler shifts in overlapped components.

In chapter 5 the effects of atmospheric structure and plasma flow were addressed.

It was demonstrated that for a structured, dynamic, optically thick plasma, an appropriate stratified, static model can be found from which an optical depth regime may be identified within which $\bar{g}^{(i)}\{\tau_0\}$ is valid in *both* the stratified, static and the structured, dynamic cases. This follows since the presence of structure and flow serve to minimise the effects of photo-absorption on the source function.

The spectral data discussed in chapter 2 was reconsidered from both a modelling and diagnostic perspective in chapter 6. Revised models were constructed that include correct treatment of line-of-sight optical depths, line blending and instrumentally scattered light. The resultant fits to observed limb-brightening curves and branching ratio variations were partially improved and partially worsened compared with the fits achieved in chapter 2. It was concluded that the structural detail ignored in the stratified models is critical for modelling effectively the emergent fluxes. It was also concluded that at heights above $\sim$ 970 arc sec, the signals are not dominated by instrumentally scattered light as had been expected. Rather structural issues are responsible for the failure of the models at and beyond the limb.

Observed fluxes were analysed in comparison with $f_{los}\{\tau_0\}\bar{g}^{(i)}\{\tau_0\}$ from which it was discovered that the quantities $f_{los}\{\tau_0\}$ show no dependence on optical depth. This implies that the spatial variation of the source function due to the variation of (T_e, N_e) with position may be neglected in the moderate optical depth regime of interest here, as asserted in chapter 3. It follows that $\bar{g}^{(i)}\{\tau_0\}$ is accurate for moderate optical depths.

The $f_{los}\{\tau_0\}$ terms, which may be written simply as f_{los}, are interpreted as filling factors, representing the area of the slit occupied by emitting structures. The variability of these factors for the two multiplets of C II and the multiplet of C III considered in this work, indicates that at all pointing positions, both on disk and off-limb, there exist emitting structures that are observationally unresolved. In an attempt to resolve these structures, the data was separated based on the visual identification of spicular and intra-spicular regions. The stratified models were found to be much more effective for the intra-spicular data than in both the spicular and combined cases. However, filling factors were deduced from both sets of data suggesting the presence of structures within both regions that have diameters less than $\sim$ 1 arc sec

The effectiveness of the line-of-sight escape probability demonstrated here illustrates its potential for use within structurally complex, dynamic plasma models. Moreover, the applicability of $\bar{g}^{(i)}\{\tau_0\}$, and its independence of model structure make it a powerful tool for diagnosing plasma parameters such as optical depth, and filling factors of emitting structures. It is possible to extend such techniques to incorporate bound-free absorption factors (Loch, 2001) and to consider the effects of opacity on ionisation balance. This fact, coupled with the flexibility of escape probability and absorption factor techniques from a structural perspective, suggest that these models may be applied to the study of radiative power loss from complex plasma geometries.

The branching ratio analysis is effective for diagnosing optical depths and filling factors providing the corresponding optical depths at disk centre are not too great. The cut-off is $\sim \tau_{0,dc} = 10$ for unblended lines. For blended lines this cut-off is lower and is dependent on the degree of overlap. Currently no simple formula exists to compute the cut-off for blended lines but further studies may reveal a simple connection between it and the optical depth of the line in question, along with those of the overlapped components and their overlap parameters $((\nu_0^{(i)} - \nu_0^{(n)})/\Delta\nu)$. Disk centre optical depths may be obtained by direct measurement or by model based extrapolation as demonstrated in chapters 2 and 6.

The filling factor diagnostic may be used in conjunction with a line-of-sight filling factor analysis such as that of Mariska et al. (1978). Such methods compare electron densities deduced from emission measure analyses which yield the line-of-sight integrated electron density, and local density diagnostics using line ratios. Together the two could be used to diagnose the 3-D structure of spicule-like features.

The escape probability methods presented in this work are not limited to use with quiet sun observations at the limb but may be applied anywhere, both on disk and off-limb and to features such as active regions and prominences. Furthermore, there are not restricted to use with stratified static models but may be coupled with complex geometric and dynamic plasma models to predict optically thick emission for comparison with observation. Providing the optical depths are moderate, such predictions represent realistic solutions to the radiative transfer and statistical balance equations.

Bibliography

1. Anzer U., Heinzel P., 1999, A&A 349, 974
2. Anzer U., Heinzel P., 2000, A&A 358, L75
3. Athay R.G., Dere K.P., 1989, ApJ 346, 514
4. Athay R.G., Holzer T.E., 1982, ApJ 225, 743
5. Auer L.H., Paletou F., 1994, A&A 285, 675
6. Bates D.R., Kingston A.E., McWhirter R.W.P., 1962, Proc. Royal Society London, 267A, 297
7. Beckers J.M., 1972, Ann. Rev. Astron. Astrophys. 10, 73
8. Behringer K.H., 1997, Max Plank Institut fuer Plasmaphysik report IPP 10/5
9. Bhatia A.K., Kastner S.O., 1997, J. Quant. Spectrosc. Radiat. Transfer 58, 347
10. Bhatia A.K., Kastner S.O., 1999, ApJ 516, 482
11. Brekke P., Hassler D.M., Wilhelm K., 1997, Solar Phys. 175, 349
12. Brooks D.H., 1997, Ph.D. Thesis, Univ. of Strathclyde
13. Brooks D.H., Fischbacher G.A., Fludra A., 2000, A&A 357, 697
14. Brooks D.H., Summers H.P., Harrison R.A. et al., 1998, Astrophys Space Sci. 261, 91

15. Budnik F., Schröder K.-P., Wilhelm K. et al., 1998, A&A 334, L77

16. Burgess A., Summers H.P., 1969, ApJ 157, 1007

17. Carlsson M., 1986, Technical Report 33, Uppsala Astronomical Observatory

18. Carlsson M., 1997, Proceedings of a Summer School Held in Orsay, France, 1-13 September 1997

19. Chae J., Yun H.S., Poland, A.I., 1998, ApJS, 114,151

20. Code A.D., Whitney B.A., 1995, ApJ 441, 400

21. Craig I.J.D., Brown J.C., 1973, Solar Phys. 49, 239

22. David C., Gabriel A.H., Bely-Debau, 1997, Proceedings of the Fifth SOHO Workshop, Oslo, Norway, 17-30 June, 1997

23. Domingo V., Fleck B., Poland A.I., 1995, Solar Phys. 162, 1

24. Doschek G.A., Vanhoosier M.B., Bartoe J.-D.R. et al., 1976, ApJS 31, 417

25. Doyle J.G., McWhirter R.W.P., 1980, MNRAS 193, 947

26. Doyle J.G., Teriaca L., Banerjee D., 2000, A&A 356, 335

27. Fledman U., Cohen L., Doschek G.A., 1982, ApJ 255, 325

28. Feldman U., Lamming J.M., 1994, ApJ 434, 370

29. Feutrier P., 1964, C.R. Acad. Sci. Paris, 258, 3189

30. Fontenla J.M, Rovira M., Vial J.-C. et al., 1996, ApJ 466, 496

31. Gontikakis C., Vial J.-C., Gouttebroze P., 1997, A&A 325, 803

32. Gouttebroze P., Heinzel P., Vial J.-C., 1993, A&AS 99, 513

33. Gouttebroze P., Vial J.-C., Tsiropoula G., 1986, A&A, 154, 154

34. Heasley J.N., Mihalas D., 1976, ApJ 210, 827

35. Heinzel P., 1995, A&A 299, 563

36. Heinzel P., Brommier V., Vial J.-C., 1996, Solar Phys. 164, 211

37. Heinzel P., Gouttebroze P., Vial J.-C., 1987, A&A 183, 351

38. Henze W., Engvold O., 1992, Solar Phys. 141, 51

39. Holstein T., 1947, Phys. Rev. 72, 1212

40. Hubeny I., Lites B.W., 1995, ApJ 455, 376

41. Hummer D.G., Rybicki G.B., 1982, ApJ 263, 925

42. Irons F.E., 1979, J. Quant. Spectrosc. Radiat. Transfer 22, 1

43. Ishizawa T., 1971, Publ. Astron. Soc. Japan 23, 75

44. Jordan C., 1967, Solar Phys. 2, 441

45. Kastner S.O., 1999, Physica Scripta 60, 381

46. Kastner S.O., 1981, J. Quant. Spectrosc. Radiat. Transfer 26, No. 4, 377

47. Kastner S.O., Bhatia A.K., 1989, ApJS 71, 665

48. Kastner S.O., Bhatia A.K., 1992, ApJ 401, 416

49. Kastner S.O., Kastner R.E., 1990, J. Quant. Spectrosc. Radiat. Transfer 44, No. 2, 275

50. Keenan R.P., Kingston A.B., 1986, MNRAS 220, 493

51. Lanzafame A.C., 1994, A&A 287, 792

52. Lemaire P., 1998, private communication

53. Loch S.D., 2001, Ph.D. Thesis, Univ. of Strathclyde

54. Lorrain P., Koutchmy S., 1993, A&A 269, 518

55. Lorrain P., Koutchmy S., 1996, Solar Physics 165, 115

56. Mariska J.T., Feldman U., Doschek G.A., 1978, ApJ 226, 698

57. McWhirter R.W.P., 1965, In: Huddlestone R.H., Leonard D.H. (eds), Plasma Diagnostic Techniques, Accademic Press, Inc.

58. McWhirter R.W.P., Summers H.P., 1984, In: Masset H.S.W., McDaniel E.W., Bederson B. (eds), Applied Atomic Collision Physics, Accademic Press, Inc.

59. Mein N., Mein P., Heinzel et al., 1996, A&A 309, 275

60. Mihalas D., 1978, Stellar Atmospheres (2nd ed.), W.H. Freeman & Co., San Fransisco

61. Mitchell A.C.G., Zemansky M.W., 1961, Resonance radiation and excited atoms, Cambridge University Press

62. Olson G.L., Auer L.H., Buchler J.R., 1986, J. Quant. Sectrosc. Radiat. Transfer 35, 431

63. Orrall F.Q., Schmahl E.J., 1980, ApJ 240, 908

64. Paletou F., 1995, A&A 302, 587

65. Paletou F., 1996, A&A 311, 708

66. Paletou F., Vial J.-C., Auer L.H., 1993, A&A 274, 571

67. Papushev P.G., Salakhutdinov R.T., 1994, Space Science Rev. 70, 47

68. Phillips K.J.H., 1992, Guide to the Sun, Cambridge University Press

69. Poland A., Skumanich A., Athay R.G. et al., 1971, Solar Phys. 18,391

70. Roberts W.O., 1945, ApJ 101, 136

71. Rybicki G.B., Hummer D.G., 1991, A&A 245,171

72. Rybicki G.B., Hummer D.G., 1992, A&A 262, 209

73. Secchi P.A., 1877, Le Soleil, Vol. 2, Chap II, Paris, Gauthier-Villars

74. Spadaro D., Lanza A.F., Antiochos S.K., 1996, Ap.J. 462, 1011

75. Spitzer L., 1956, 'Physics of Fully Ionised Gases', Interscience, NY

76. Vernazza J.B., Avrett B.H., Loeser R., 1981, ApJS 45, 635

77. Wilhelm K., Curdt W., Marsch B. et al., 1995, Solar Phys. 162, 189

78. Withbroe G.L., 1983, ApJ 267, 825

79. Withbroe G.L., Mariska J.T., 1976, Solar Phys. 48, 21

80. Wood K., Raymond J., 2000, ApJ 540, 563

81. Zheng W., Davidsen A.F., Kriss G.A., 1998, ApJ 115, 391

Appendix A

The assumption of constant source function: results for the exponential density case

The absorption factor analysis described in sec. 3.4 applies to a stratified, plane parallel atmosphere and may be performed using any density distribution, $N_l(x)$. The absorption factors shown in figs 3.5 and 3.6 and the corresponding density distributions shown in figs 3.8 $\rightarrow$ 3.11 are shown here for an exponential density model (model 3). The agreement between $\Lambda(\tau_0, x)$ and $\mathcal{G}(\tau_0, x)$ is not greatest at layer centre but in between layer centre and the point of peak emission. Thereafter, however, the same conclusions follow as in chapter 3. The agreement between $\Lambda(\tau_0, x)$ and $\mathcal{G}(\tau_0, x)$ decreases toward the layer edges and with optical depth. The $\Lambda(\tau_0, x)$ versus x trends deviate from those of $\mathcal{G}(\tau_0, x)$ most markedly for lines that share an upper level with a line thicker than themselves. The density distributions do not display these indirect effects and are modified in a similar manner to those in the constant density case but with the point of most significant modification begin between layer centre and the point of peak emission. The corresponding limb-brightening curves are shown in figs 3.12b and 3.13b.

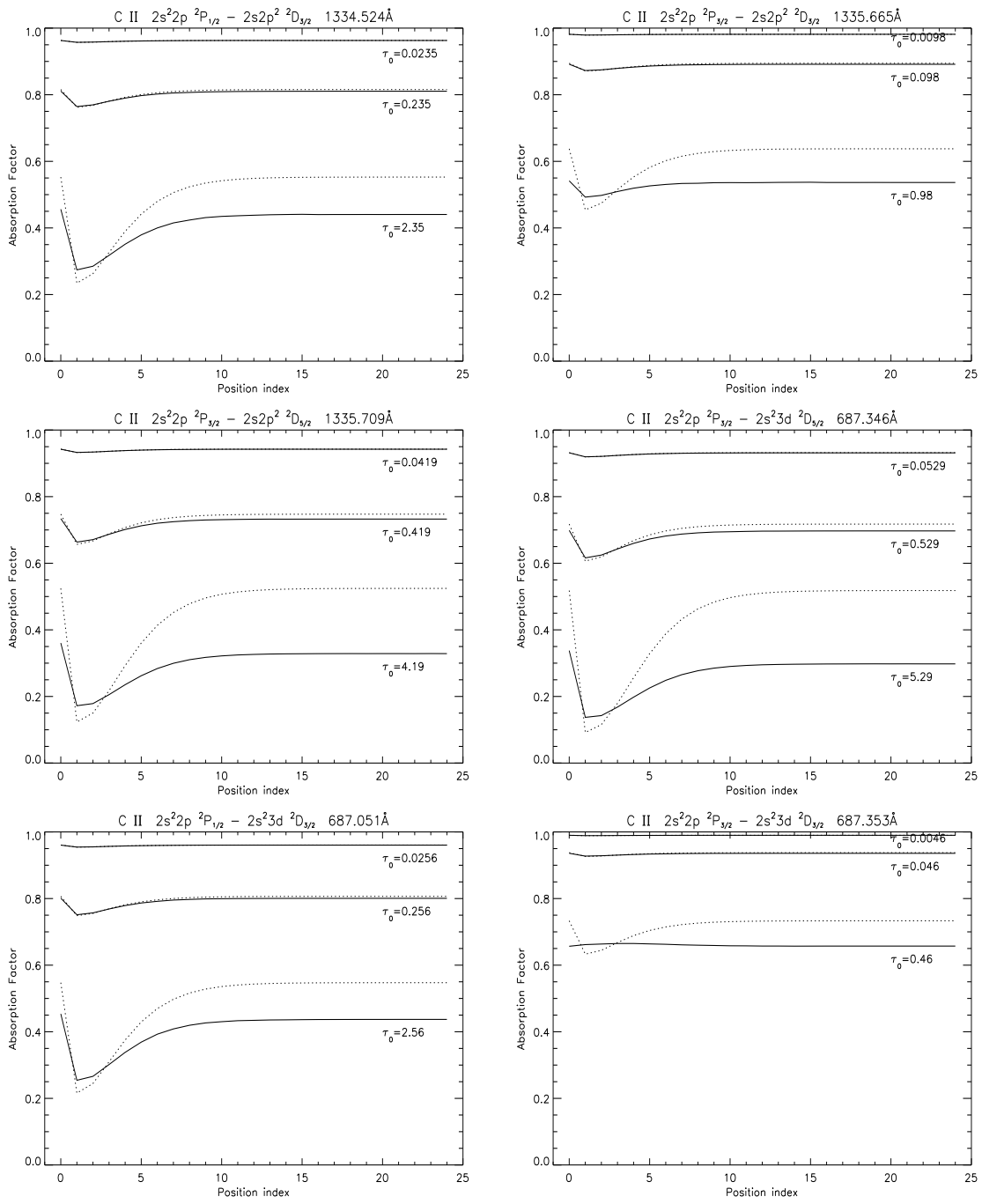

Figure A.1: Absorption factors versus position for selected lines of C II corresponding to three sets of optical depths. Absorption factors are calculated iteratively via eqs 3.15 and 2.8 in an exponential density model. The solid lines are $\Lambda(\tau_0, x)$ and the dotted lines are $\mathcal{G}\{\tau_0, x\}$. These plots are comparable with those in fig. 3.5

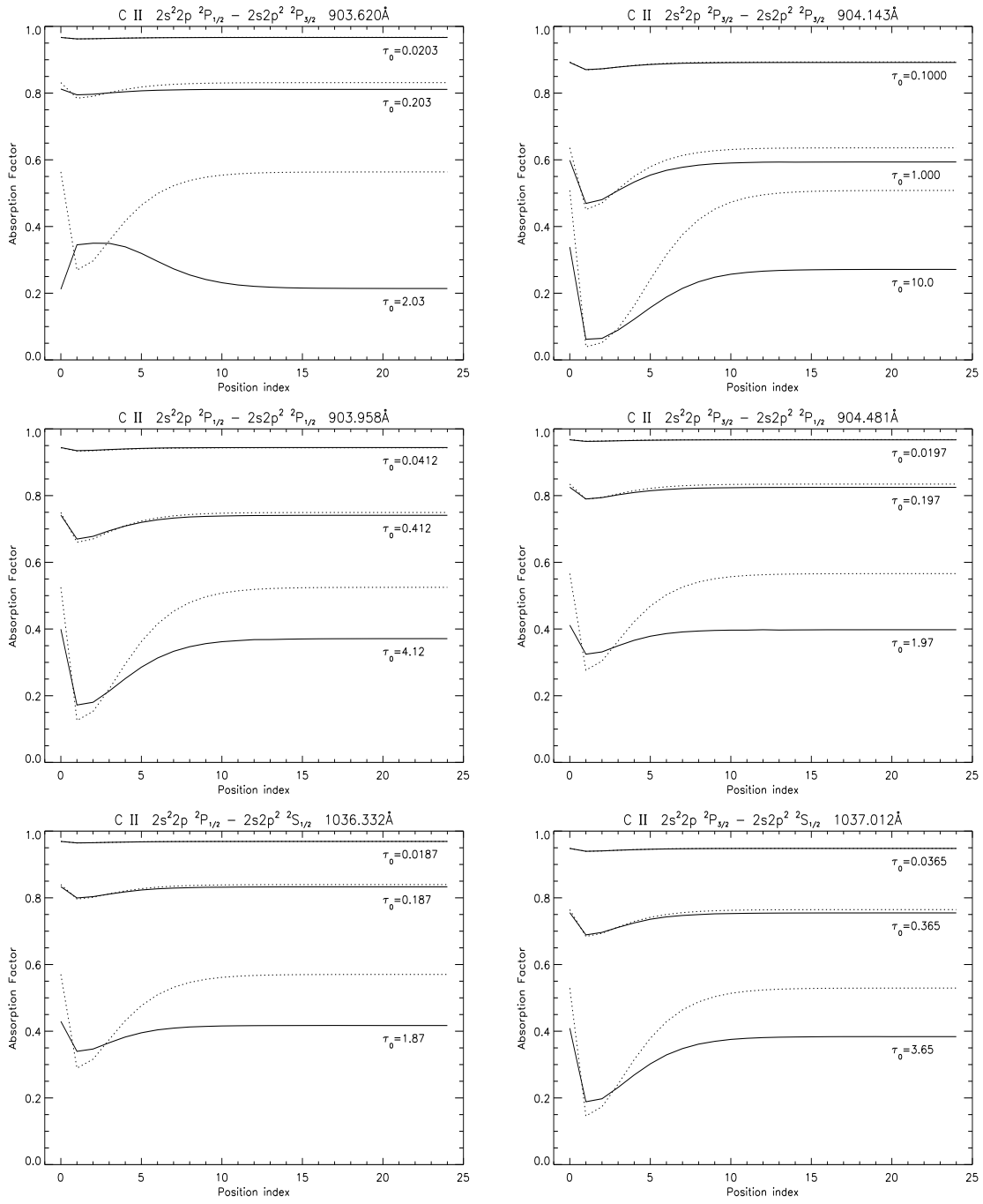

Figure A.2: Absorption factors versus position for selected lines of C II as in fig A.1. These plots are comparable with those in fig. 3.6.

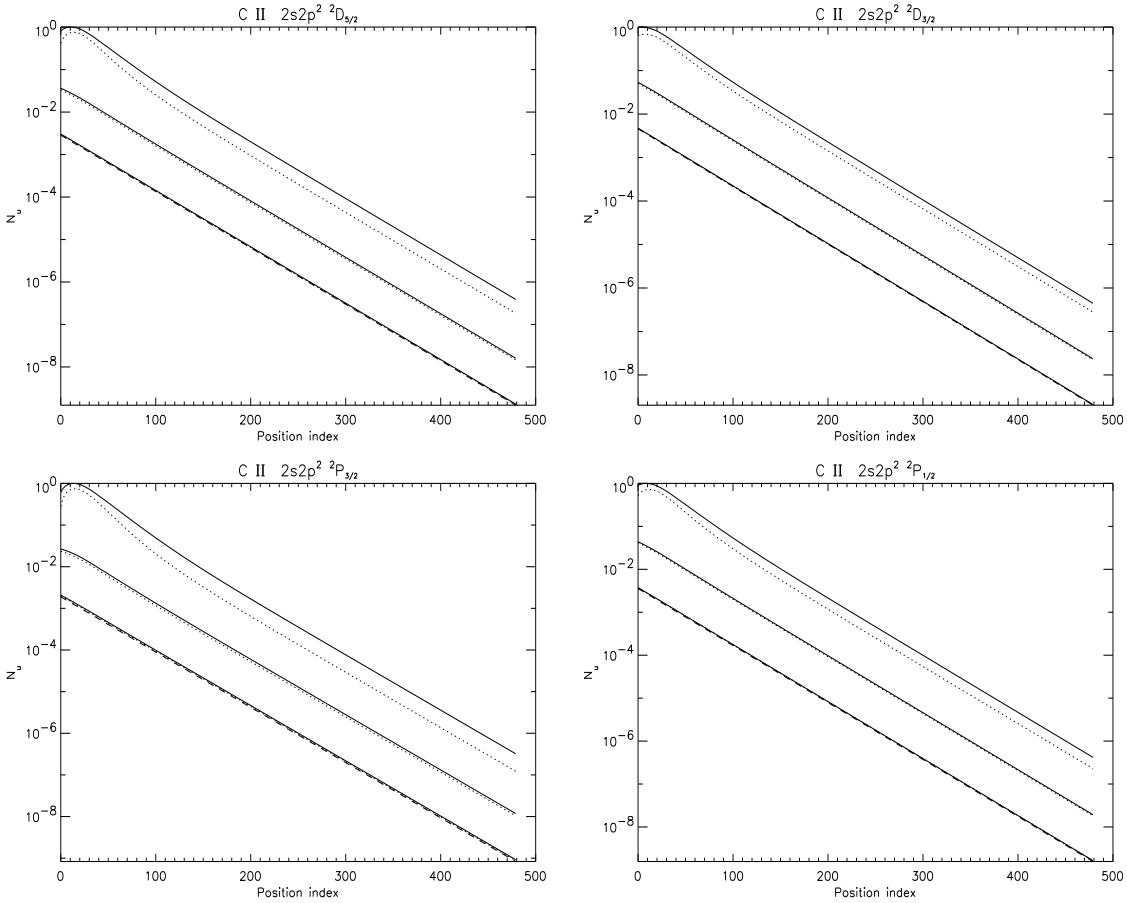

Figure A.3: Upper level population densities versus spatial position for selected levels of C II calculated in an exponential density model. The solid lines correspond to calculations based on $\Lambda(\tau_0, x)$ for the same three sets of optical depths as in figs A.1 and A.2. The dotted lines represent the $\mathcal{G}(\tau_0, x)$ based calculations. Values are not absolute but are scaled so that the maximum population density value is unity. These plots are comparable with those in fig. 3.8

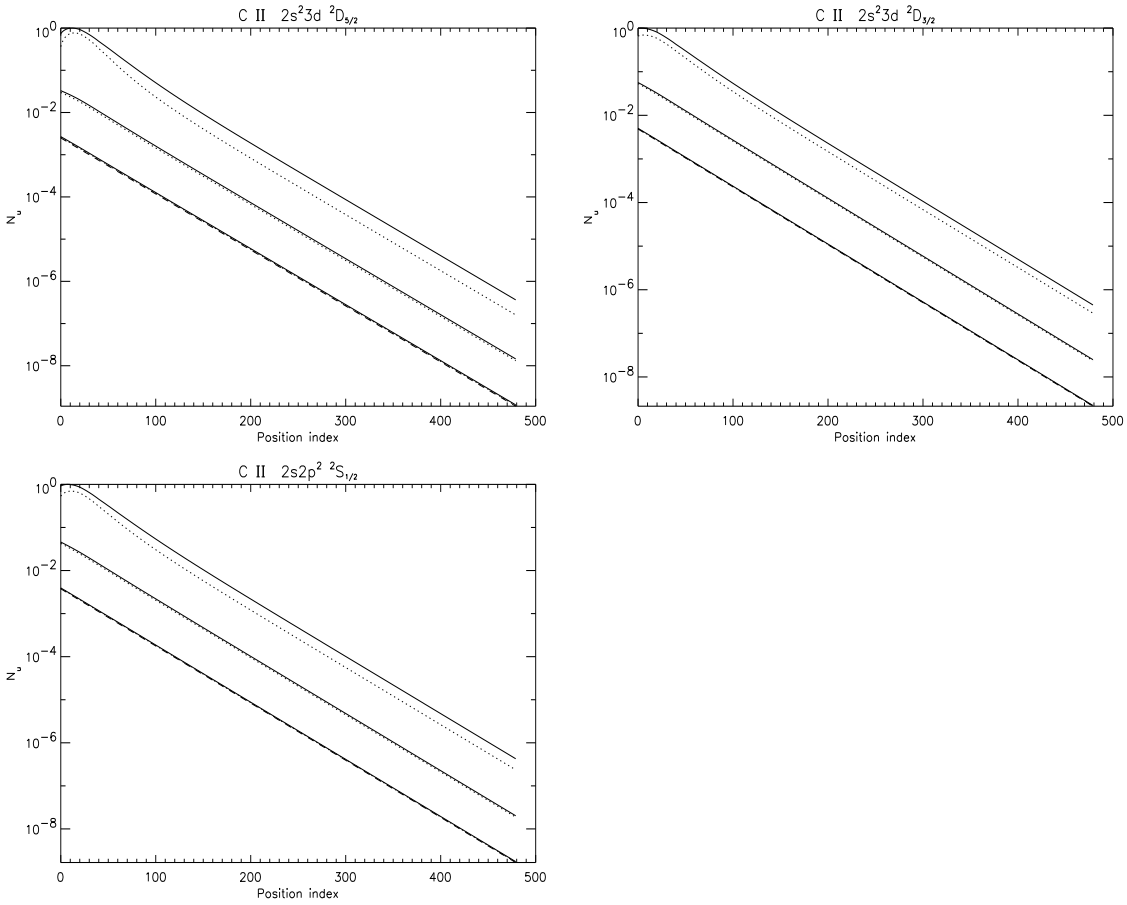

Figure A.4: Upper level population densities versus spatial position for selected lines of C II calculated in an exponential density model. The solid and dotted lines are as in fig. A.3. Values are not absolute but are scaled so that the maximum population density value is unity. These plots are comparable with those in fig. 3.9

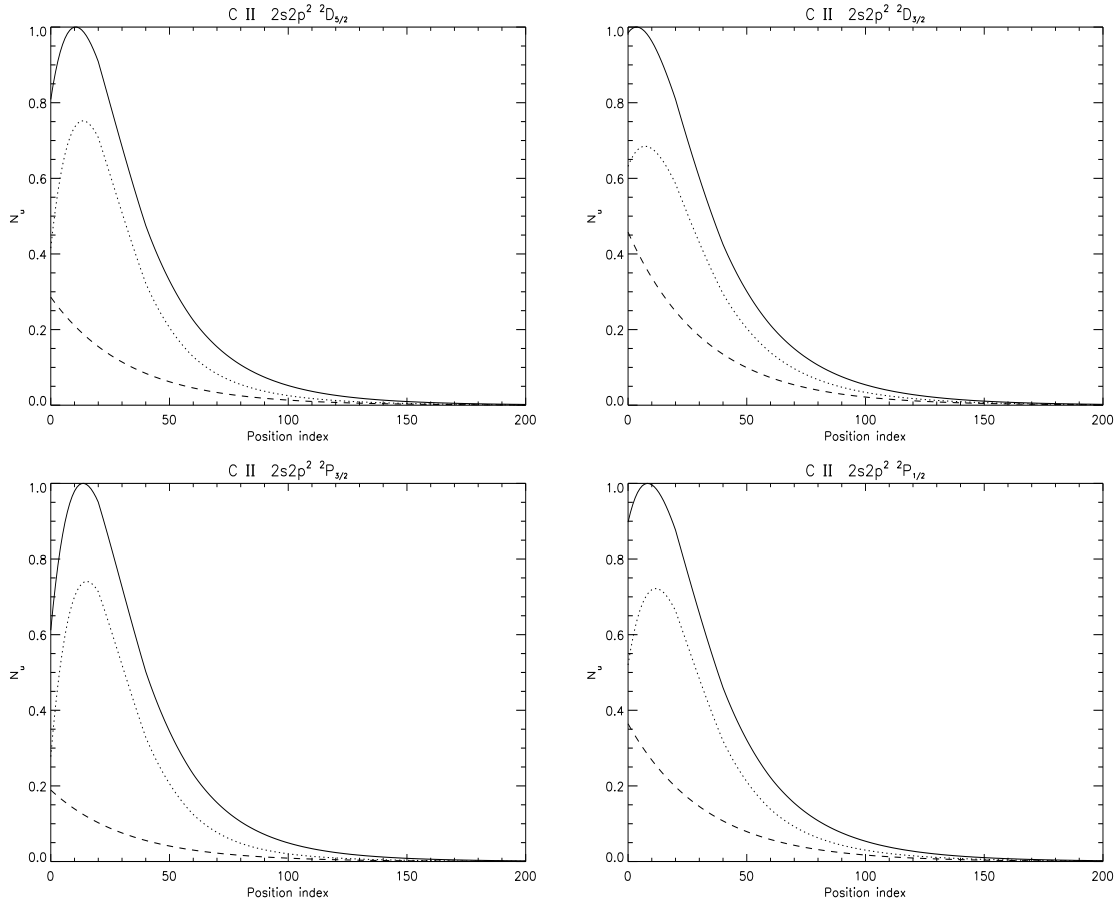

Figure A.5: Upper level population densities versus spatial position for selected lines of C II calculated in an exponential density model as in figs A.3 and A.4 but just in the most optically thick case. The solid and dotted lines are as in figs A.3 and A.4

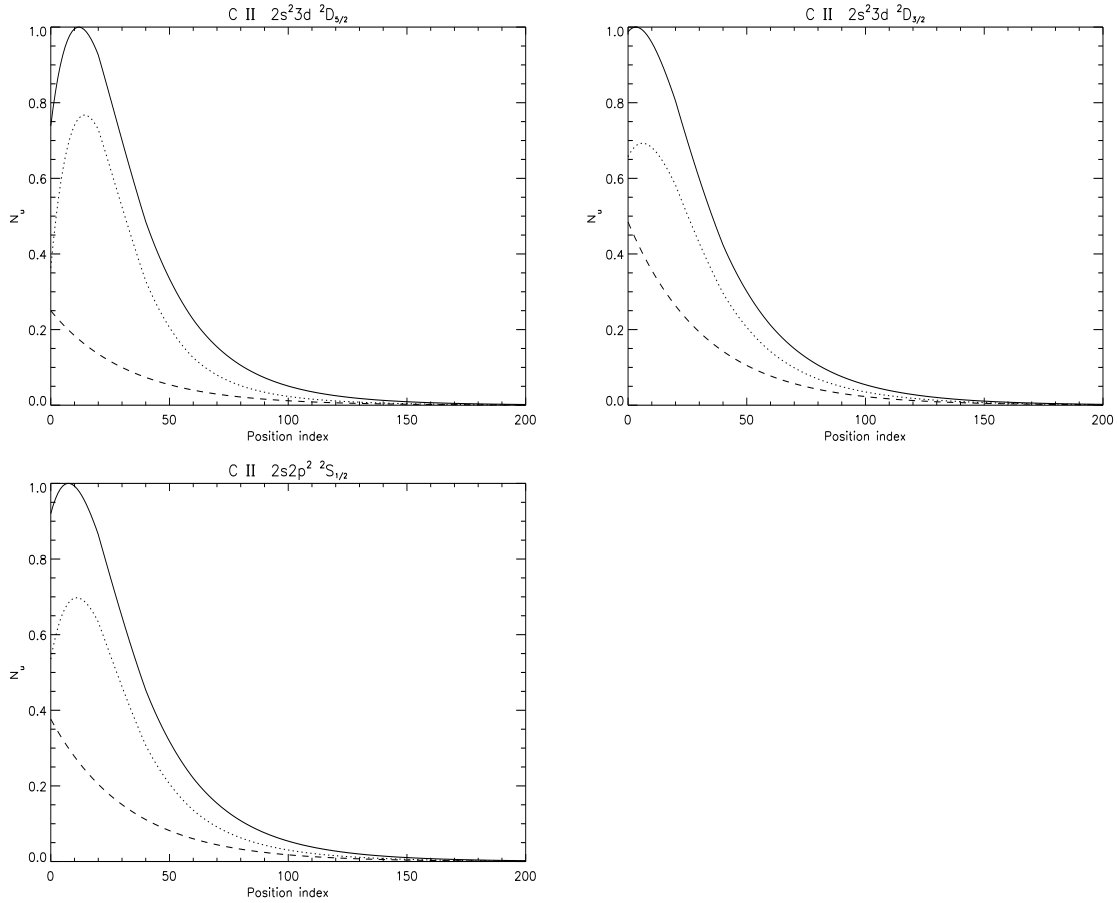

Figure A.6: Upper level population densities versus spatial position for selected lines of C II calculated in an exponential density model as in fig. A.5. These plots are comparable with those in fig. 3.11

Appendix B

The effect of line blending: results for the exponential density case

The absorption factors shown in figs 4.7 and 4.8 and the corresponding density distributions shown in figs 4.10 $\rightarrow$ 4.13 are shown here for an exponential density model (model 3). The agreement between $\Lambda^{(i)}(\tau_0, x)$ and $\mathcal{G}^{(i)}(\tau_0, x)$ is not greatest at layer centre but in between layer centre and the point of peak emission. Thereafter, however, the same conclusions follow as in chapter 4. The agreement between $\Lambda^{(i)}(\tau_0, x)$ and $\mathcal{G}^{(i)}(\tau_0, x)$ decreases toward the layer edges and with optical depth. There is a downward shift in the $\Lambda^{(i)}(\tau_0, x)$ values with respect to the $\mathcal{G}^{(i)}(\tau_0, x)$ ones in the blended lines. This is due to the dependence of $\Lambda^{(i)}(\tau_0, x)$ on opacity sensitive upper level population densities of overlapped components. This shift would be removed if $\mathcal{G}^{(i)}(\tau_0, x)$ were calculated iteratively. The $\Lambda^{(i)}(\tau_0, x)$ versus x trends deviate from those of $\mathcal{G}(\tau_0, x)$ most markedly for lines that share an upper level with a line thicker than themselves. The density distributions do not display these indirect effects and are modified in a similar manner to those in the constant density case but with the point of most significant modification begin between layer centre and the point of peak emission. The corresponding limb-brightening curves are shown in figs 4.14b and 4.15b.

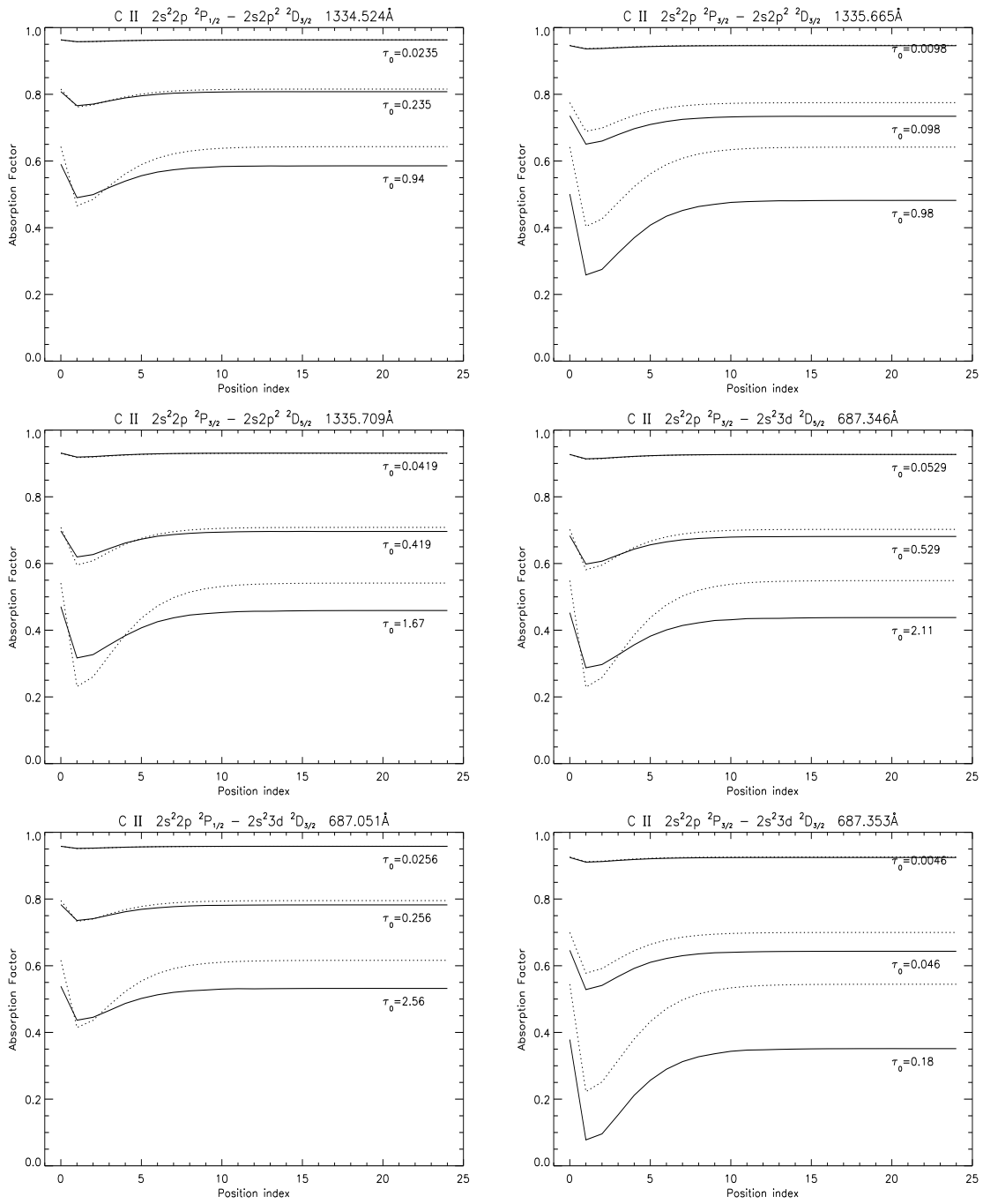

Figure B.1: Absorption factors with blending included versus position for selected lines of C II corresponding to three sets of optical depths. Absorption factors are calculated iteratively via eqs 4.18 and 2.8 in an exponential density model. The solid lines are $\Lambda^{(i)}(\tau_0, x)$ and the dotted lines are $\mathcal{G}^{(i)}\{\tau_0, x\}$. These plots are comparable with those in fig. 4.7.

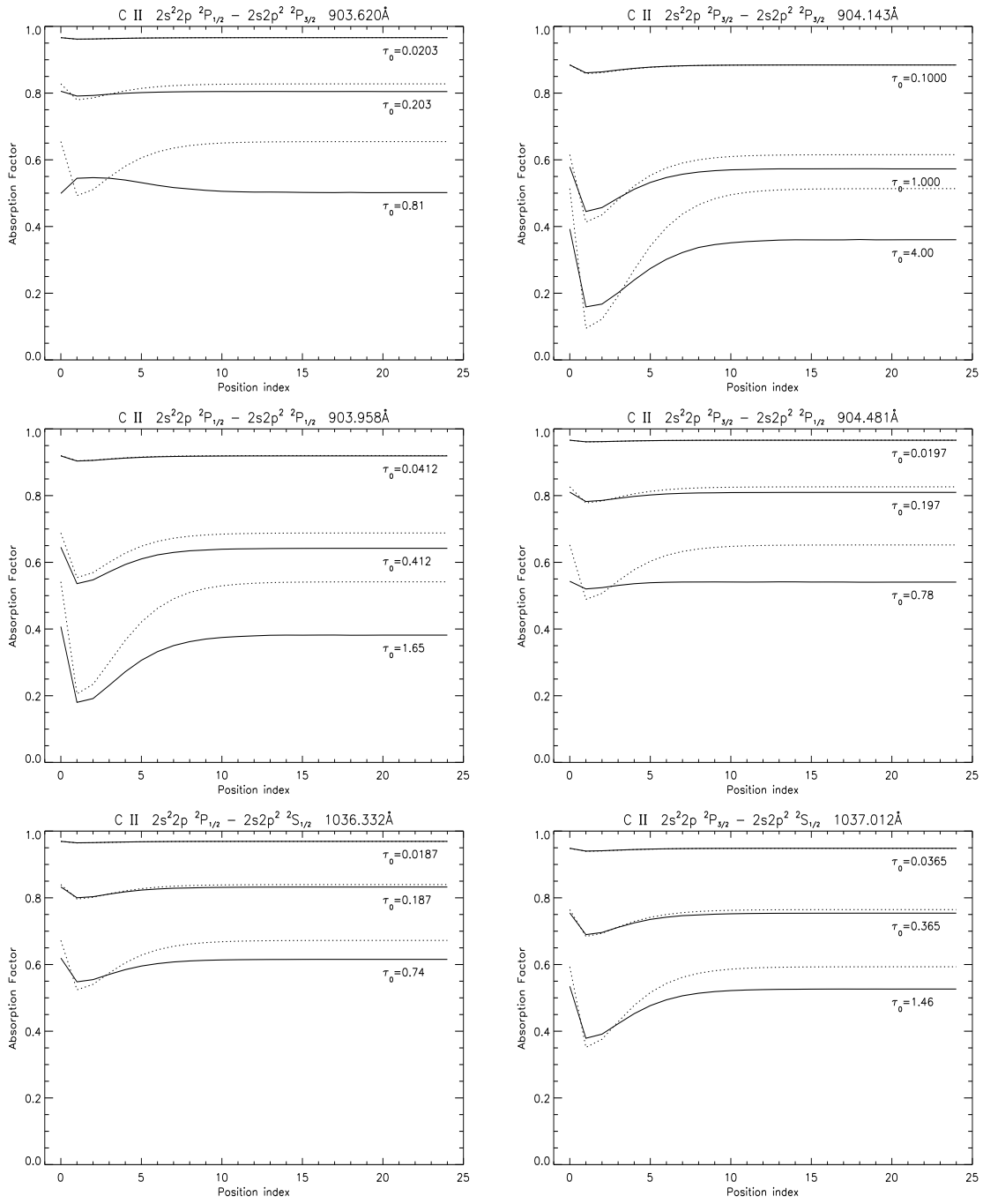

Figure B.2: Absorption factors with blending included versus position for selected lines of C II as in fig A.1. These plots are comparable with those in fig. 4.8.

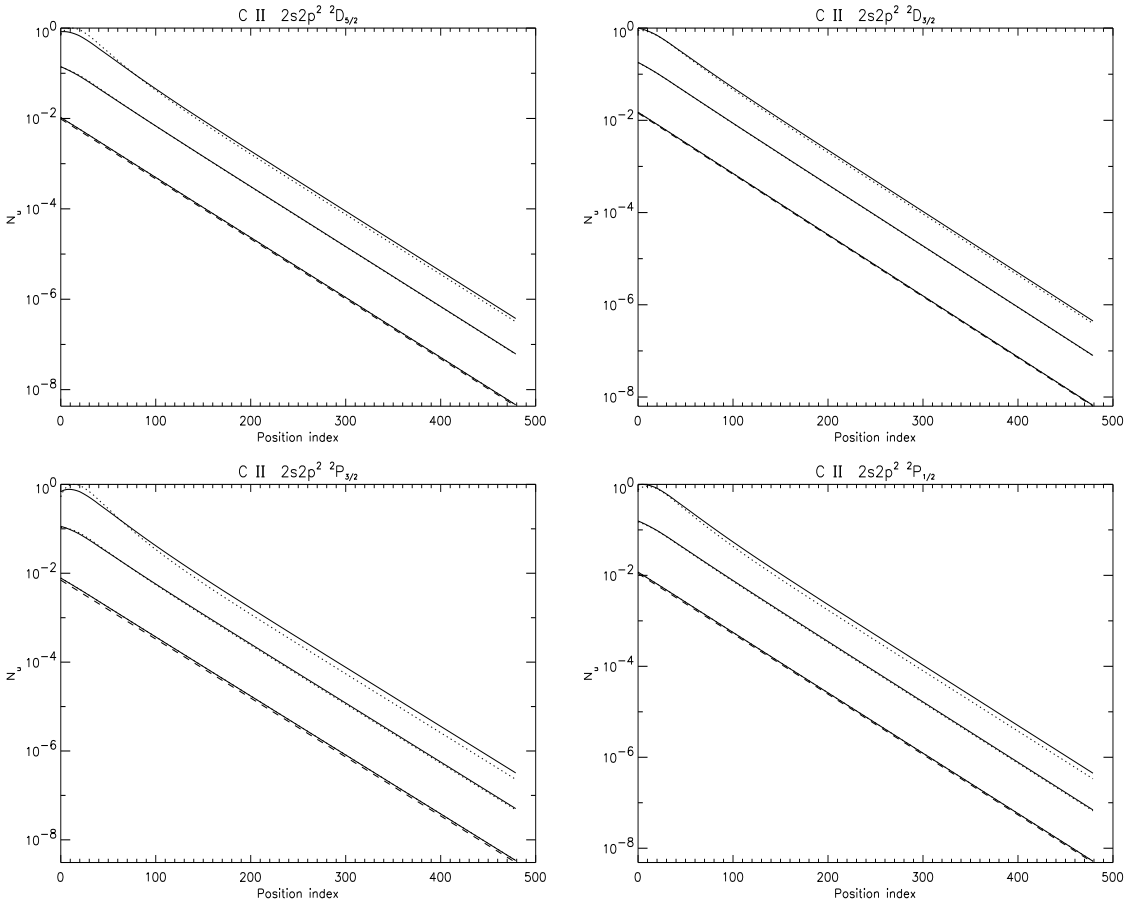

Figure B.3: Upper level population densities versus spatial position for selected lines of C II with blending effects included, calculated in an exponential density model. The solid lines correspond to calculations based on $\Lambda^{(i)}(\tau_0, x)$ for the same three sets of optical depths as in figs B.1 and B.2. The dotted lines represent the $\mathcal{G}^{(i)}(\tau_0, x)$ based calculations. These plots are comparable with those in fig. 4.10.

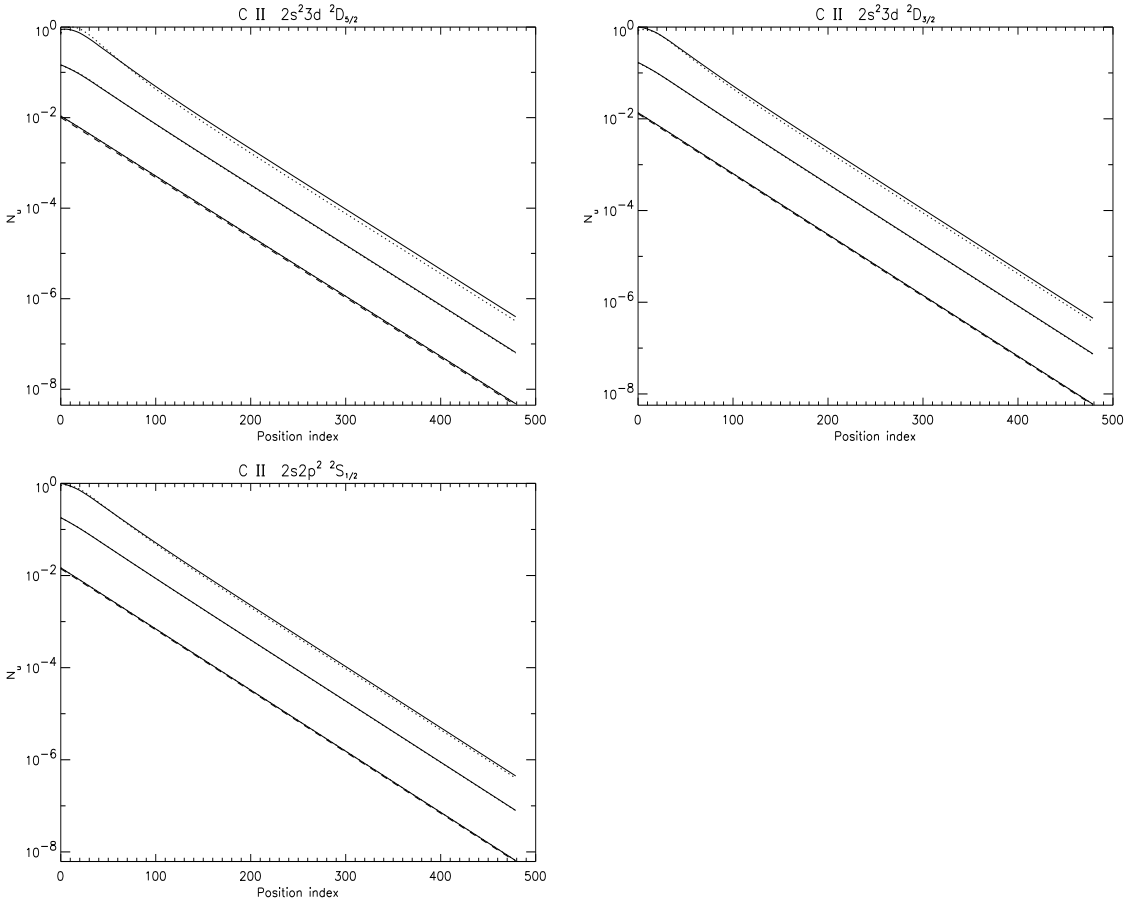

Figure B.4: Upper level population densities versus spatial position for selected lines of C II with blending effects included, calculated in an exponential density model. The solid and dotted lines are as in fig. B.3. These plots are comparable with those in fig. 4.11.

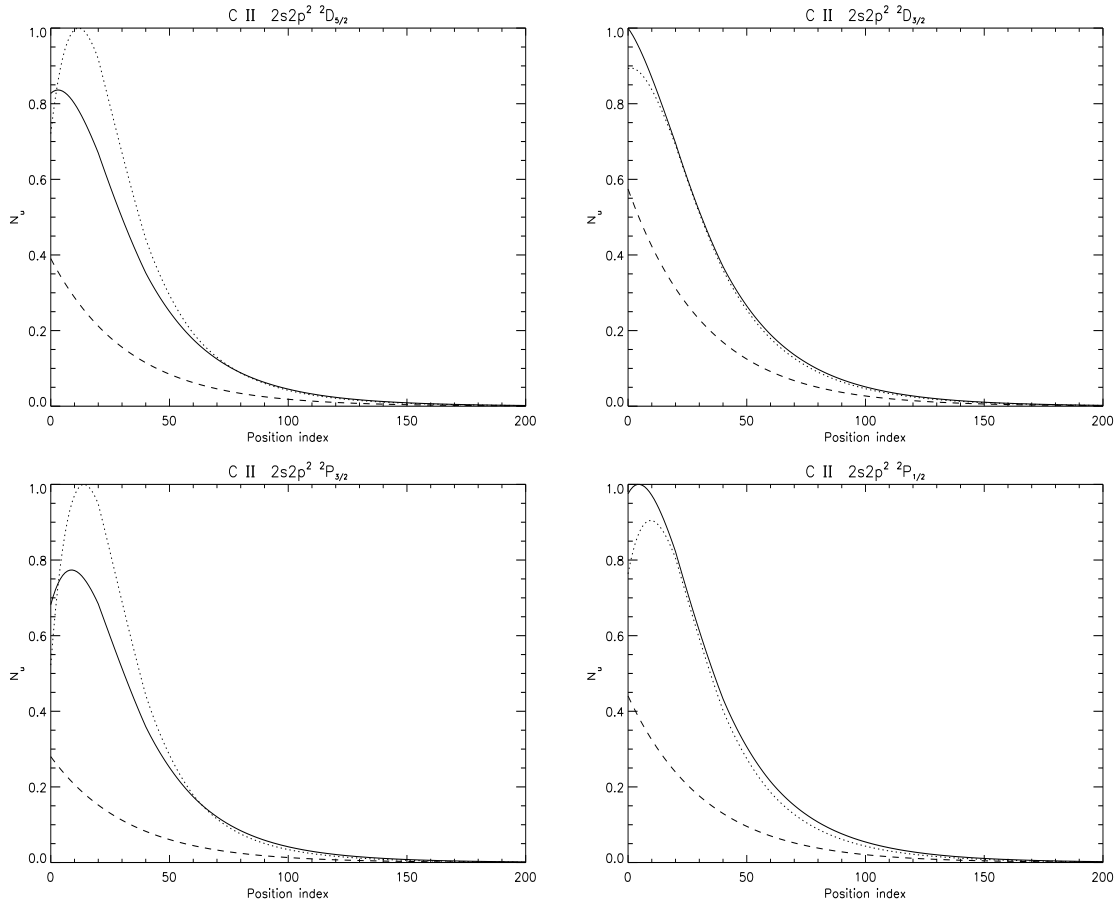

Figure B.5: Upper level population densities versus spatial position including blending effects, for selected lines of C II as in figs B.3 and B.4 but just in the most optically thick case. The solid and dotted lines are as in figs B.3 and B.4. Values are not absolute but are scaled so that the maximum population density value is unity. These plots are comparable with those in fig. 4.12.

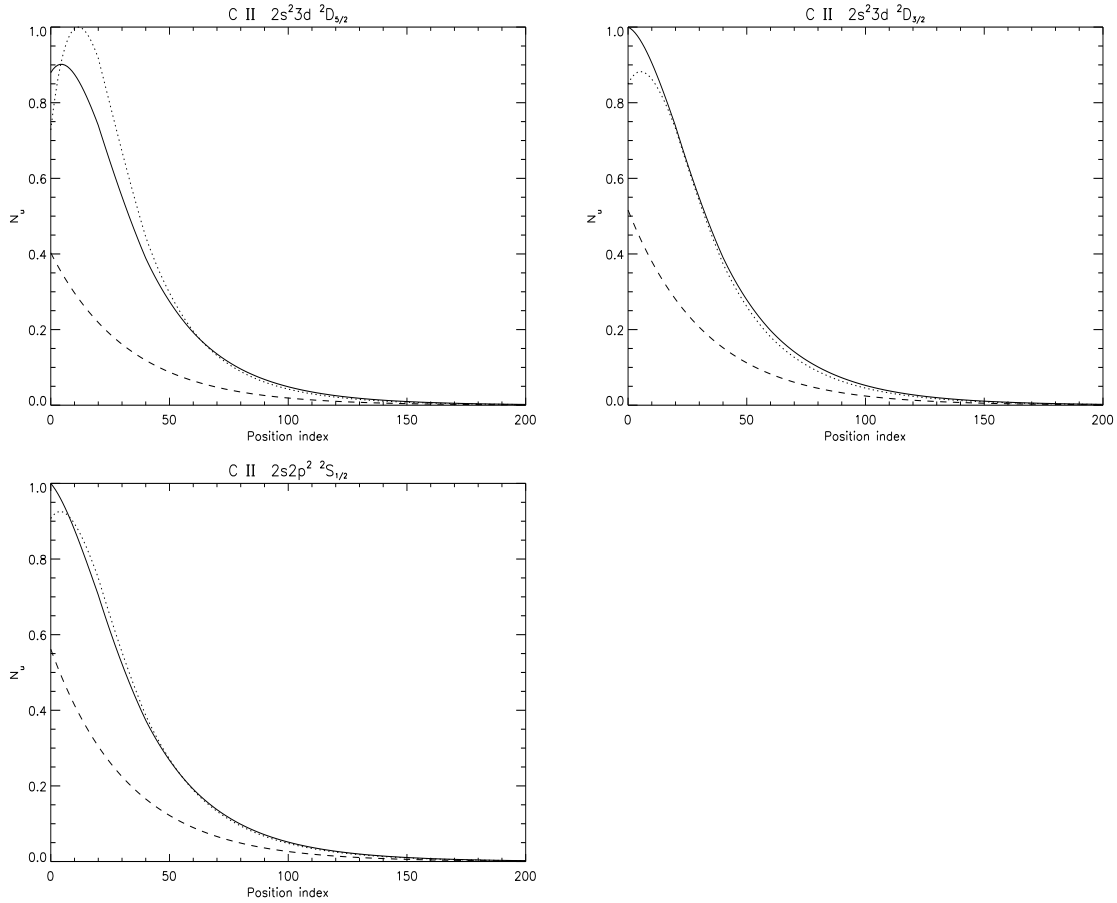

Figure B.6: Upper level population densities versus spatial position including blending effects, for selected lines of C II as in fig. B.5. Values are not absolute but are scaled so that the maximum population density value is unity. These plots are comparable with those in fig. 4.13.